

**THEORETICAL, SIMULATED, AND EXPERIMENTAL  
PHOTOACOUSTIC APPROACHES TO DETECT THE INTERNAL  
CAROTID ARTERY DURING MINIMALLY INVASIVE  
NEUROSURGERY**

by  
Michelle T. Graham

A dissertation submitted to Johns Hopkins University in conformity with the  
requirements for the degree of Doctor of Philosophy

Baltimore, Maryland  
July 2022

©2022 Michelle T. Graham  
All rights reserved

# Abstract

Real-time intraoperative guidance during the minimally invasive neurosurgical procedure known as endonasal transsphenoidal surgery is often limited to endoscopy and computed tomography. These imaging options are suboptimal when localizing internal carotid arteries (ICAs) either obscured by tissue or shifted relative to preoperative locations due to anatomical disruptions during surgery. Accidental damage to these critical structures has severe surgical complications, such as patient hemorrhage, stroke, and death.

Photoacoustic imaging is a promising imaging technique to provide real-time intraoperative guidance of the subsurface ICAs. However, interactions with bone along the optical and acoustic pathways degrade photoacoustic image quality. In this dissertation, novel theoretical, simulated, and experimental approaches are employed to address image quality limitations, yielding the following three fundamental contributions to the proposed photoacoustic technology.

First, a new photoacoustic-specific spatial coherence theory was derived and developed, followed by the development of PhocoSpace, an open-source software package to utilize this theory. This foundational theory supports the implementation of advanced coherence-based beamforming techniques to enable ICA detection and generally improve photoacoustic image quality in bony environments, with broader applications that extend beyond these tasks. Second, intraoperative ICA tracking tasks most beneficial for coherence-based beamforming were differentiated from those

better suited to more traditional amplitude-based beamforming techniques. Third, a novel approach employing patient-specific simulations is presented to identify naturally occurring acoustic windows for photoacoustic receiver placements that minimize acoustic interactions with bone.

These contributions demonstrate that strategic use of acoustic windows and coherence-based beamforming techniques address photoacoustic image degradation in the presence of bone and ultimately generate interpretable photoacoustic images of the ICAs. From presurgical planning to intraoperative monitoring, a new paradigm for photoacoustic detection of the ICAs during minimally invasive neurosurgery is established. Beyond ICA detection, the contributions herein extend to photoacoustic-based detection of other critical structures (e.g., nerves or other blood vessels) lying within optically and acoustically challenging environments.

## **Thesis Committee**

Muyinatu A. Lediju Bell (Primary Reader, Advisor)  
John C. Malone Associate Professor  
Department of Electrical and Computer Engineering  
Johns Hopkins Whiting School of Engineering

Jin U. Kang (Secondary Reader)  
Jacob Suter Jammer Professor  
Department of Electrical and Computer Engineering  
Johns Hopkins Whiting School of Engineering

Xingde Li  
Professor  
Department of Biomedical Engineering  
Johns Hopkins University School of Medicine

# Acknowledgements

I would like to express my deepest gratitude to my advisor Dr. Muyinatu (Bisi) Bell for her invaluable patience, feedback, and mentorship. As one of her inaugural PhD advisees, it has been a rewarding experience to grow as a researcher alongside the growth of her lab. I would like to extend additional thanks to my dissertation committee, Dr. Jin Kang, Dr. Xingde Li, and Dr. Francis (Pete) Creighton, who generously served on key milestones within the PhD program as well as provided expertise and collaborations. Furthermore, this endeavor would not have been possible without the collaborations of Peter Kazantzides, Jonathan Chrispin, Fabrizio Assis, Kai Ding, Sami Tuffaha, Visakha Suresh, Nick von Guionneau, Susanna Thon, and Arlene Chiu.

I am also exceedingly grateful to my fellow PULSE Lab members, past and present: Arun (Aurous) Nair, Josh Shubert, Derek (D-man) Allman, Alycen (Steed) Wiacek, Eduardo (Edu) Gonzalez, Mardava (Arranis) Gubbi, Kelley Kempinski, (“Who would have thought that I-”) Theron Palmer, Huayu Hou, Jiaqi (Justina) Huang, Lingyi Zhao, Arunima Sharma, Junior Arroyo, and Jiaxin Zhang. The environment this group of individuals created was one of unwavering support and comradery, full of insightful discussion within the office, helping hands within in the lab, and a fun-loving spirit within the city of Baltimore and beyond. Thank you all for having confidence in me when I lacked it in myself, and helping me charge onward.

I would be remiss in not mentioning other members of the Electrical and Computer

Engineering department. The staff were always ready to offer their assistance as well as engage in friendly conversation. Jasper Stroud and Milad Alemohammad, senior PhD students when I joined the department, were ever-present to provide guidance as I learned the ropes of being a PhD student. I could also not forget the dogs of the ECE department, Paco, Shadow, Blackjack, Pinot, Stella, and Violet. They truly were a PhD student's best friend and brightened up each day! Thanks should also go to those I have mentored during my tenure at Hopkins, especially Reese Dunne. You made me strive to be a better mentor, project manager, and researcher.

Lastly, I could not have undertaken this journey without the support of my family and friends, especially Jesse and Bisco. Your belief in me is a source of inspiration and at the foundation of my successes in life.

# Contents

<b>Abstract</b> . . . . .	<b>ii</b>
<b>Acknowledgements</b> . . . . .	<b>iv</b>
<b>List of Tables</b> . . . . .	<b>xii</b>
<b>List of Figures</b> . . . . .	<b>xiv</b>
<b>List of Symbols</b> . . . . .	<b>xxxii</b>
<b>List of Abbreviations</b> . . . . .	<b>xxxiv</b>
<b>Chapter 1 Introduction</b> . . . . .	<b>1</b>
1.1 Biomedical photoacoustic imaging overview . . . . .	1
1.1.1 Discovery and medical adoption of the photoacoustic effect . . . . .	1
1.1.2 Photoacoustic signal generation . . . . .	2
1.1.3 Photoacoustic signal processing . . . . .	3
1.2 Intraoperative photoacoustic imaging of the internal carotid arteries during endonasal transsphenoidal surgery . . . . .	3
1.2.1 Significance of localizing the internal carotid arteries . . . . .	3
1.2.2 Challenges with current image-guidance techniques . . . . .	5
1.2.3 Emergence of photoacoustic image guidance . . . . .	5

1.3	Challenges with photoacoustic image guidance . . . . .	6
1.3.1	Optical interactions with bone . . . . .	6
1.3.2	Acoustic interactions with bone . . . . .	7
1.3.3	DAS and SLSC beamforming challenges . . . . .	8
1.4	Dissertation overview . . . . .	9
	References . . . . .	11
<b>Chapter 2 Photoacoustic Spatial Coherence Theory . . . . .</b>		<b>20</b>
2.1	Introduction . . . . .	20
2.2	Theory . . . . .	23
2.2.1	Photoacoustic Spatial Coherence . . . . .	23
2.2.2	Photoacoustic Short-Lag Spatial Coherence Imaging . . . . .	30
2.2.3	Modeling Point Targets . . . . .	33
2.3	Methods . . . . .	34
2.3.1	Theory-Based Simulations . . . . .	34
2.3.2	k-Wave Simulations . . . . .	37
2.3.3	India Ink and Point Target Experiments . . . . .	38
2.3.4	In Vivo Experiment . . . . .	39
2.3.5	Empirical Methods to Add Noise to Simulated Datasets . . . . .	40
2.3.6	Exploring Theoretical Implications for SLSC Imaging . . . . .	42
2.4	Results . . . . .	43
2.4.1	Comparison of Delay-and-Sum and SLSC Images . . . . .	43
2.4.2	Theoretical Photoacoustic Spatial Coherence Functions . . . . .	45
2.4.3	Comparison of SLSC Lateral Profiles . . . . .	48
2.4.4	Effect of the Light Beam Profile on SLSC Image Contrast . . . . .	51
2.4.5	Effect of the Light Beam Profile on SLSC Image FWHM . . . . .	53
2.4.6	Optimal M Value for Photoacoustic SLSC Images . . . . .	54
2.5	Discussion . . . . .	57

2.6	Conclusion . . . . .	61
2.7	Acknowledgements . . . . .	61
	References . . . . .	62
<b>Chapter 3</b>	<b>PhocoSpace: An Open-Source Simulation Package to Im-</b>	
	<b>plement Photoacoustic Spatial Coherence Theory . . . . .</b>	<b>69</b>
3.1	Introduction . . . . .	70
3.2	Photoacoustic Spatial Coherence Theory . . . . .	71
3.3	PhocoSpace Workflow . . . . .	73
3.4	PhocoSpace Use Cases and Examples . . . . .	75
	3.4.1 Default imaging properties and parameters . . . . .	75
	3.4.2 SLSC images of diverse target geometries . . . . .	76
	3.4.3 Multiple customizable fluence profiles . . . . .	77
	3.4.4 Transducer bandwidth variations . . . . .	79
3.5	Conclusion . . . . .	80
	References . . . . .	81
<b>Chapter 4</b>	<b>Integrated Simulation and Human Cadaver Head Investi-</b>	
	<b>gations . . . . .</b>	<b>85</b>
4.1	Introduction . . . . .	85
4.2	Materials and Methods . . . . .	89
	4.2.1 k-Wave Simulations . . . . .	89
	4.2.2 Photoacoustic Imaging System . . . . .	90
	4.2.3 Intact Human Skull Experiments . . . . .	93
	4.2.3.1 Pre-experiment Specimen Preparations . . . . .	93
	4.2.3.2 Temporal Bone Feasibility Study . . . . .	95
	4.2.3.3 Probe Location Comparison . . . . .	96
	4.2.3.4 Ocular Imaging Experiments with Filled Skull . . . . .	97



4.2.4	Fresh Cadaver Head Studies . . . . .	98
4.2.5	Validation with CT Registration . . . . .	101
4.2.6	Image Quality Metrics . . . . .	101
4.3	Results . . . . .	102
4.3.1	k-Wave Simulations of Empty Skull . . . . .	102
4.3.1.1	Identification of Potential Ultrasound Probe Locations	102
4.3.1.2	Acoustic Signal Trapping Due to Skull Anatomy . .	103
4.3.1.3	Localized Acoustic Pressure Analysis . . . . .	105
4.3.2	k-Wave Simulations of Fresh Cadaver Head . . . . .	106
4.3.3	Empty Skull Experimental Results . . . . .	106
4.3.3.1	Temporal Probe Location is Not Optimal . . . . .	106
4.3.3.2	Probe Location Comparison . . . . .	109
4.3.4	Filled Skull Results and Spacer Design Requirements . . . . .	112
4.3.5	Fresh Cadaver Head Results . . . . .	112
4.4	Discussion . . . . .	116
4.5	Conclusion . . . . .	120
4.6	Acknowledgements . . . . .	121
	References . . . . .	121

<b>Chapter 5</b>	<b>Validation of Patient-Specific Simulation Methods to De-</b>	
	<b>termine Acoustic Windows . . . . .</b>	<b>130</b>
5.1	Intoduction . . . . .	130
5.2	Methods . . . . .	132
5.3	Results . . . . .	133
5.4	Discussion . . . . .	136
5.5	Conclusion . . . . .	137
5.6	Acknowledgements . . . . .	137
	References . . . . .	137

<b>Chapter 6 Workflow and Vision for Clinical Translation of Acoustic Windows Identified with Presurgical, Patient-Specific Simulations . . . . .</b>	<b>141</b>
6.1 Introduction . . . . .	141
6.2 Methods . . . . .	144
6.2.1 Simulation Configuration . . . . .	144
6.2.2 Image Formation and Analysis . . . . .	148
6.3 Results . . . . .	149
6.4 Discussion . . . . .	154
6.5 Conclusion . . . . .	157
6.6 Acknowledgements . . . . .	158
References . . . . .	158
<b>Chapter 7 Conclusions and Future Directions . . . . .</b>	<b>163</b>
7.1 Summary . . . . .	163
7.2 From ICA detection to nerve detection . . . . .	164
7.2.1 Rationale . . . . .	164
7.2.2 Experimental methods . . . . .	166
7.2.3 Results from multispectral measurements of nerve tissue . . . . .	167
7.2.4 Interpretation of preliminary application to nerves and proposed next steps . . . . .	168
7.3 Additional Possible Directions . . . . .	170
7.3.1 Novel transducer designs . . . . .	170
7.3.2 Comparison to alternative image quality improvement solutions . . . . .	171
7.3.3 Photoacoustic spatial coherence theory applied to brachytherapy seed detection . . . . .	171
7.4 Outlook . . . . .	173
References . . . . .	173

Biography . . . . . 178

# List of Tables

<b>Table 2.1</b> $\sigma_N$ (mean $\pm$ one standard deviation of ten measurements) for the results reported in Figs. 5, 7-11, and 14 . . . . .	42
<b>Table 3.1</b> Summary of the fields contained within the output structure, -, which is generated by the theoretical photoacoustic spatial coherence and SLSC image computation executed with -. . . . .	74
<b>Table 4.1</b> Summary of light delivery design parameters and corresponding maximum allowable output laser energy at the tip of each light delivery method, using a 25.2 mJ/cm <sup>2</sup> safety limit for 750 nm wavelength light. The maximum allowable energy reported for the 2 mm-core-diameter fiber bundle with quartz spacer was calculated using the area of light shown in Fig. 4.4(c). . . . .	93
<b>Table 4.2</b> Summary of the five waypoints investigated during the skull experiment with brain tissue, including x-z coordinates with respect to sphenoid bone surface, Euclidean distance between each waypoint and the sphenoid bone surface, calculated laser spot diameter incident on sphenoid surface (based on geometrical optical principles), and the resulting maximum allowable energy. . . . .	98
<b>Table 6.1</b> Transcranial photoacoustic simulation parameters. . . . .	147

<b>Table 6.2</b>	Simulated tissue properties of the homogeneous and heterogeneous volumetric maps [19], [21]–[26]. The two shear wave properties of sound speed in brain and absorption power law prefactors in bone and brain are not explicitly known. However, these properties can be estimated as approximately half the corresponding compressional speed of sound and approximately double the corresponding compressional absorption power law prefactor [25], [27]. . . . .	147
<b>Table 6.3</b>	Comparison of execution times and memory usage for the compressional and elastic k-Wave simulations. . . . .	150

# List of Figures

<b>Figure 1.1</b>	Diagram of endonasal transsphenoidal surgery for pituitary tumor resection. Surgical tools, such as endoscopes and drills are inserted through the nasal cavity to gain access to the surgical site. The outset image is an axial CT scan of a patient with a pituitary tumor. The scan is annotated to demonstrate the proximity of the internal carotid arteries to the tumor. . . . .	4
<b>Figure 1.2</b>	During photoacoustic visualization of the internal carotid arteries, optical and acoustic interactions that occur with the bone present along the photoacoustic imaging pathway include optical attenuation and acoustic attenuation, aberration, and reverberation. Each of these interactions contributes to degradation in photoacoustic image quality. This dissertation presents three new methods to improve photoacoustic image quality of the ICAs in the presence of bone. These contributions span both presurgical planning and intraoperative monitoring tasks. . . . .	6

**Figure 2.1** Illustration of the Fresnel approximation for an aperture (rectangle) and source (circle) located at the aperture center  $\mathbf{X}_0$ . The distance from the source to a point on the aperture is  $r_n$ . The lateral distance  $X_1 - X_2 \ll z$ , where  $z$  is the axial position of the source. Therefore,  $r \approx z$ . . . . . 28

**Figure 2.2** Steering direction from the aperture center to a focal point  $(x_k, z)$  in the image, illustrated with the assumption that Eq. (2.17) represents an initial focus located at lateral position  $x_k = 0$ . . . . . 31

**Figure 2.3** (a) Optical absorption ( $\mu_a$ ) distribution for a circular cross-section of a simulated 6 mm-diameter blood vessel with high optical absorption surrounded by tissue of low optical absorption, (b) Grünesen parameter ( $\Gamma$ ) distribution, (c) corresponding photoacoustic pressure distribution ( $A_N$ ), and (d) a lateral profile of  $A_N$  taken from the axial depth indicated by the dashed white line. . . . . 35

**Figure 2.4** Experimental setup showing tubing of inner diameters 4.5 mm, 6 mm, 8 mm, and 10 mm (1.3 mm-, 2 mm-, and 4 mm-diameter tubing not shown) fixed in an acrylic scaffold and suspended in a water bath. The light source shown is the 1 mm-core-diameter optical fiber which was later interchanged with the 5 mm-diameter fiber bundle in the same position relative to the ultrasound transducer. An Alpinion L3-8 transducer is placed with its imaging plane viewing a circular cross-section of the tubing. . . . . 40

**Figure 2.5** (a) Experimental delay-and-sum (DAS) image, (b) experimental short-lag spatial coherence (SLSC) image, (c) theoretical SLSC simulation (with added noise), and (d) k-Wave simulation (with added noise) of 1.3 mm- and 8 mm-diameter targets. The circles in the experimental DAS and SLSC images denote the inner (solid line) and outer (dotted line) diameters of the Tygon tubing filled with India ink. SLSC images are normalized to the brightest pixel and limited to display a minimum value of zero for  $M = 11\%$  of the aperture. DAS images are displayed with a 25 dB dynamic range. . . . . 44

**Figure 2.6** Noiseless theoretical coherence functions of at the center of targets ranging in size from a point to 10 mm in diameter using (a) light sheet and (b) 1 mm Gaussian beam profiles as the illuminating sources. The x-axis represents lag (i.e.,  $m$  or  $\mathbf{m}$ ) as a percentage of the receive aperture. . . . . 45

**Figure 2.7** Coherence functions from a point target center. (a) Simulated point target data without noise ( $N_A = 0$ ) shows coherence functions that are relatively constant across the aperture, indicating a coherent source. (b) Simulated point target data with noise compared with experimental point target data, demonstrating partially coherent source functions when noise is present. The x-axis represents lag (i.e.,  $m$  or  $\mathbf{m}$ ) as a percentage of the receive aperture. . . . . 47



**Figure 2.8** Comparison of theoretical, k-Wave, and experimental coherence functions at the location corresponding to the center of (a) 1.3 mm-diameter and (b) 4.5 mm-diameter targets. The x-axis represents lag (i.e.,  $m$  or  $\mathbf{m}$ ) as a percentage of the receive aperture. . . . . 48

**Figure 2.9** Root mean square error (RMSE) comparing both k-Wave data with noise and experimental data to theoretical coherence functions with noise in the (a) short-lag and (b) long-lag regions. 49

**Figure 2.10** (a,e) Theoretical, (b,f) k-Wave, and (c,g) experimental photoacoustic SLSC images of a point target and 12 mm-diameter target. The experimental image of the 12 mm-diameter target is derived from the *in vivo* hepatic blood vessel data. Images are displayed with  $M = 11\%$  of the aperture, with the exception of the 12 mm *in vivo* experimental target, which is displayed with  $M = 1\%$  of the aperture. Images were normalized and thresholded to a minimum value of 0.3 in (a)-(c) and (g) and 0 in (e) and (f). (d,h) The corresponding lateral profiles demonstrate comparable resolution, target width, and coherence. . . . . 50

**Figure 2.11** Lateral SLSC profiles at axial depths corresponding to the target center of (a) theoretical, (b) k-Wave, and (c) experimental SLSC images of the point, 4.5 mm, and 12 mm targets, each displayed with three different values of  $M$  represented as a percentage of the receive aperture. The experimental profiles are derived from SLSC images of the thread (point target), India ink (4.5 mm target), and *in vivo* vessel (12 mm target). The 12 mm *in vivo* target lateral SLSC profiles were normalized to the maximum value in each line plot. . . . . 51

**Figure 2.12** Theoretical measurements of contrast in SLSC images as a function of target diameter for three illuminating beam profiles (light sheet, 1 mm- and 5 mm-diameter Gaussian beam). These theoretical predictions in the presence of noise are compared to experimental India ink data acquired with the fiber bundle ( $\times$ ) and the optical fiber (o). For the larger targets, theory and experimental data show improved contrast with the narrower illumination beam profile. All SLSC images are computed with  $M = 11\%$  of the aperture. . . . . 52

**Figure 2.13** Theoretical full width at half maximum (FWHM) measurements of SLSC lateral profiles as a function of target diameter for three illuminating beam profiles (light sheet, 1 mm-, and 5 mm-diameter Gaussian beams). These theoretical predictions in the presence of noise are compared to India ink experimental data acquired with the fiber bundle ( $\times$ ) and the optical fiber (o). The ideal 1:1 relationship is shown as a dashed line. SLSC lateral profiles were computed with  $M = 11\%$  of the aperture. . . . . 54

<b>Figure 2.14</b>	Lateral resolution calculated with theoretical, k-Wave, and experimental point target data sets as a function of $M$ , which is represented as a percentage of the receive aperture. . . . .	55
<b>Figure 2.15</b>	Theoretical measurements of contrast in SLSC images as a function of target diameter for four $M$ values (2%, 4%, 8%, and 11% of the receive aperture). These theoretical predictions in the presence of noise are compared with experimental data of SLSC images displayed with the same four $M$ values ( $\times$ , $\circ$ , $*$ , and $\triangle$ , respectively). . . . .	56
<b>Figure 3.1</b>	Graphical illustration and associated MATLAB code demonstrating the two-stage PhocoSpace workflow for an 8 mm diameter circular blood vessel target. . . . .	73
<b>Figure 3.2</b>	Example photoacoustic imaging target geometries and associated theoretical SLSC images computed with PhocoSpace, including (a,b) a single 4 mm diameter target, (c,d) six circular targets with diameters ranging 2-7 mm, (e,f) a blood vessel vasculature model, and (g,h) the Johns Hopkins University crest. . . . .	76
<b>Figure 3.3</b>	Fluence profiles and corresponding SLSC images computed with PhocoSpace, including (a,b) a light sheet with a uniform fluence value of $F = 5 \text{ mJ/cm}^2$ and Gaussian profiles with (c,d) 25 mm, (e,f) 5 mm, and (g,h) 1 mm initial beam diameters. . . . .	78
<b>Figure 3.4</b>	Coherence functions extracted from the center of the (a) 2 mm diameter and (b) 7 mm diameter target in the six-circle target geometry when excited with the four fluence profiles shown in Fig. 3.3. . . . .	79

**Figure 3.5** SLSC images of the vasculature target geometry shown in Fig. 3.2, computed with transducer bandwidths of (a) 8-17 MHz (12.0 MHz center frequency), (b) 3-8 MHz (5.5 MHz center frequency), and (c) 1-5 MHz (3.0 MHz center frequency). (d) Corresponding lateral SLSC profiles at the location indicated by the white arrows, compared to a lateral profile taken from the same position within the vasculature target map geometry. 80

**Figure 4.1** Annotated slice of the density distribution for k-Wave simulations, derived from a corresponding axial CT slice of the fresh human cadaver head. Acoustic sensors were distributed across the eyelid surfaces as shown. The location of simulated photoacoustic sources for the LCA and RCA are also shown. Each source was simulated independently. . . . . 91

**Figure 4.2** Optical absorption spectra of endogenous biological chromophores [42]–[49]. A wavelength of 750 nm was chosen to excite our experimental blood. . . . . 92

**Figure 4.3** Experimental setups for the intact skull, cleaned from tissue attachments. (a) Empty skull with the 5 mm-core-diameter fiber bundle as the optical source and the ultrasound probe placed on the 1 mm-thick temporal bone fragment. (b) Empty skull with the 1 mm-core-diameter optical fiber as the optical source and the ultrasound probe placed on the nasal cavity. (c) Empty skull with the 5 mm-core-diameter fiber bundle as the optical source and the ultrasound probe placed on the right ocular region. (d) Skull filled with brain tissue and eye sockets filled with ovine eyes with the 2 mm-core-diameter fiber bundle as the optical source and the ultrasound probe placed on the right ovine eye. The Tygon tubing was filled with whole human blood for this experiment. . . . . 94

**Figure 4.4** (a) Endoscopic image of the sphenoid sinus of the fresh cadaver head. The left and right carotid arteries (LCA and RCA, respectively) are located on either side of the sphenoid bone to be removed. The quartz spacer attached to the terminal end of the fiber bundle is visualized in the endoscopic field of view and is directed to illuminate the RCA. (b) Photograph of the 2 mm-core-diameter fiber bundle with quartz spacer, emitting 690 nm light (for visualization only). (c) Expected beam profile incident on the sphenoid surface when emitting 750 nm light during the fresh cadaver head experiments. . . . 100

<b>Figure 4.5</b>	(a) k-Wave simulation results from acoustic sensors distributed across the external surface of the empty skull, showing the maximum pressure received by each sensor (over the entire simulation duration). (b) Summary of the maximum pressure received by each sensor exceeding 3% of the initial source pressure, mapped as red-shaded surfaces on the 3D CT reconstruction. The axial plane intersecting the nasal cavity corresponds to the image plane of Fig. 4.6. . . . . .	103
<b>Figure 4.6</b>	Axial slices from 3D k-Wave simulations demonstrating acoustic wave propagation within the complex bony anatomy of the empty skull overlaid on the simulated density map, spanning times $t_0$ to $t_3$ . Time $t_0$ shows the initial pressure distribution of the carotid sources. Time $t_3$ shows the photoacoustic signals after traveling to the temporal bone. The photoacoustic signals in each image are normalized by the maximum photoacoustic amplitude at time $t_0$ . . . . .	104
<b>Figure 4.7</b>	Photoacoustic pressure signals from k-Wave simulations of the empty skull, each measured from a single sensor location (a) within the nasal cavity and ocular regions and (b) within the nasal cavity and temporal regions. The nasal sensor locations were identical for each plot and replicated to simplify comparisons. . . . .	105

**Figure 4.8** Visualization of k-Wave acoustic sensor data for sensors placed on the left and right eyelids of the fresh cadaver head when the photoacoustic source is (a) the LCA and (b) the RCA. The colors indicate the total signal energy received by each sensor at the completion of each simulation, normalized by the maximum of the total signal energy for each simulation. . . . . 107

**Figure 4.9** (a) 3D CT reconstruction of the empty skull highlighting the axial-lateral ultrasound imaging planes and lateral-elevation ultrasound probe locations used for the temporal region, nasal cavity, and ocular regions. Co-registered photoacoustic and CT images of the empty skull with the axial-lateral dimension of the ultrasound probe placed on the (b) temporal region (with no temple bone), (c) nasal cavity region, and (d) ocular region. (e) Co-registered photoacoustic and CT images of the skull filled with brain tissue and ultrasound probe placed on the right ocular region. The CT images are displayed in grayscale, and the photoacoustic images are displayed in color with 20 dB dynamic range. Photoacoustic targets include the LCA, RCA, and optical source (S). The Tygon tubing phantom ICAs appear as hollow circles on CT images. . . . . 108

**Figure 4.10** Empty skull experiments: (a) RCA contrast in DAS images with temporal bone thicknesses ranging 0-4.4 mm, and pulse energies ranging 0.08-75.0 mJ (displayed on a log scale). (b) Minimum energy required to visualize the RCA in DAS and SLSC images when the probe was placed on temple region. The dashed line represents the 4.95 mJ maximum allowable energy for the 5 mm-core-diameter fiber bundle, as reported in Table 4.1. Arrows ( $\uparrow$ ) represent minimum required energies which exceeded the maximum capable pulse energy of the optical source. Filled skull experiments: (c) RCA contrast in DAS images when the laser tip was located at waypoint C (1.64 cm away from sphenoid) for sphenoid bone thicknesses ranging 0-3.3 mm. Pulse energies ranged 0.10-13.8 mJ and are displayed on a log scale. (d) Minimum energy required to visualize the RCA in DAS images at waypoints A, B, and C when the probe was placed on the ocular region with sphenoid bone thicknesses ranging 0-3.3 mm. The dashed lines represent the maximum allowable energy calculated for the 2 mm-core-diameter fiber bundle without the quartz spacer attached, as reported in Table 4.2. A 3D visualization of waypoints A, B, and C with respect to the sphenoid bone surface is shown for reference. . . . . 110



<b>Figure 4.11</b>	DAS and SLSC photoacoustic images of the empty skull overlaid on co-registered ultrasound images acquired with (a) nasal, (b) ocular, and (c) temporal probe locations. The optical source (S) emitted 3, 5, and 4 mJ per pulse, respectively. Each photoacoustic image was normalized to its brightest pixel and displayed with 10 dB dynamic range. The sphenoid and temporal bone thicknesses were 0 mm and 1 mm, respectively. The RCA signal labeled with the yellow arrow was used to compute contrast. . . . .	111
<b>Figure 4.12</b>	(a,c) DAS and (b,d) SLSC photoacoustic images from the fresh cadaver, overlaid on co-registered ultrasound images acquired with (a,b) left and (c,d) right ocular probe locations. The light source operated at 5.4 mJ per pulse and was placed on the LCA (visualized through the left eye) or RCA (visualized through the right eye). (e) Co-registered CT (gray scale) and photoacoustic image (color) images acquired with the ultrasound probe placed on the right eyelid of the cadaver head. .	113
<b>Figure 4.13</b>	Contrast of the ICAs in DAS and SLSC photoacoustic images from the fresh cadaver head when the ultrasound probe was located on the left or right eye (as indicated in the legend), and the light source illuminated the ICA located on the same side as the probe. . . . .	114
<b>Figure 4.14</b>	Minimum energy required to visualize the ICAs with 5 dB contrast with DAS and SLSC imaging when the optical source was placed at stationary distances of 0 cm and 1.5 cm away from the ICA target located on the same side as the probe (which is indicated in the legend). . . . .	115

<b>Figure 4.15</b>	DAS contrast measurements from photoacoustic images of the right ocular region as the light source was navigated in the sphenoid sinus of the fresh cadaver head and the distance between the light source and RCA was increased. . . . .	116
<b>Figure 5.1</b>	Annotated slices of the speed of sound distribution, derived from axial CT slices of the same human cadaver head. (a) The simulation consisted of acoustic sensors distributed across the eyelids and photoacoustic sources independently placed in the left carotid artery (LCA) or right carotid artery (RCA) position. (b) The corollary experimental setup consisted of transducers placed on the eyelids, an optical source inserted through the nasal cavity, and independently illuminated LCA and RCA photoacoustic sources. . . . .	132
<b>Figure 5.2</b>	Visualization of k-Wave acoustic sensor data for sensors placed on the left and right eyelids of the cadaver head when the photoacoustic source is the (a) LCA and (b) RCA. (c) Histograms of the probability of a left or right eyelid sensor receiving a log-compressed total signal energy in the range 0 to -45 dB. Each histogram represents energies from sensors on a singular eyelid when illuminating the corresponding carotid artery independently, calculated using Eq. 5.2. . . . .	134

**Figure 5.3** DAS photoacoustic images from the fresh cadaver, overlaid on co-registered ultrasound images when the transducer location and photoacoustic source are the (a) left eyelid and LCA and (b) right eyelid and RCA. The images were normalized to the brightest pixel within the image. (c) Histograms of the probability of an image pixel within a region of interest inside the photoacoustic source in the DAS images having an amplitude in the range 0 to -45 dB, calculated using Eq. 5.3. . . . . 135

**Figure 6.1** Surgical workflow with and without the use of patient-specific simulations. Without photoacoustic simulations, a surgeon will likely have to test multiple ultrasound receiver locations and their feasibility. Simulations have the potential to efficiently identify these locations before the surgical procedure. 143

**Figure 6.2** Axial slice from the CT volume of the human cadaver skull demonstrating a 2-D cross-section of the 3-D simulation configuration. Spherical photoacoustic sources were placed within the left internal carotid artery (LCA) and at distances of 6-13 mm from the LCA to represent a the tip of a surgical instrument (a distance of 6 mm is shown). Green lines illustrate locations of independently placed ultrasound transducers. . . 145

**Figure 6.3** Two-dimensional cross-section of acoustic wave propagation at various time points (i.e.,  $t_0$  through  $t_3$ ) during the homogeneous (top) and heterogeneous (bottom) three-dimensional simulations. There is no bone present in the homogeneous simulation, as represented by the greyscale background. In both cases, the acoustic wave propagates spherically outward from the initial pressure distribution (location of left ICA). In the heterogeneous simulations, acoustic interactions with cranial bone cause distortions (i.e., aberrations, attenuation, scattering, reverberations) in the waveform which ultimately degrade image quality. See Video 1 for the evolution of wave propagation for these two simulations. . . . . 146

**Figure 6.4** Simulated (a) compressional and (b) elastic photoacoustic channel data of the left internal carotid artery obtained with the temporal acoustic window. (c) Difference image of the elastic channel data subtracted from the compressional channel data. 151

**Figure 6.5** (a) Simulated photoacoustic images of the left internal carotid artery obtained with the ocular, nasal, and temporal acoustic windows, from left to right respectively. The top and bottom rows show compressional and elastic simulation results, respectively. The single target and multiple background ellipsoidal regions of interest are outlined in blue and orange, respectively. Images are displayed with 10 dB dynamic range. (b) Corresponding mean  $\pm$  one standard deviation of contrast, signal-to-noise ratio (SNR), contrast-to-noise ratio (CNR), and generalized contrast-to-noise ratio (gCNR)[33], [34] measurements. 152

<b>Figure 6.6</b>	Point spread function -6 dB contours for the (a) homogeneous and (b) heterogeneous point target simulations. (c) Corresponding areas of the point spread function -6 dB contours. Homogeneous simulation measurements provide baseline resolution measurements without the negative effects of tissue heterogeneity. . . . .	153
<b>Figure 6.7</b>	(a) Heterogeneous simulated photoacoustic images of the two sources representing the LCA and instrument tip, obtained with the ocular acoustic window at a relative distance of 11.27 mm. The target-to-instrument distance is the length of the line between the source centers in the image. (b) Comparison of measured target-to-instrument distances as a function of the true target-to-instrument distances for compressional ( $\circ$ ) and elastic ( $\Delta$ ) measurements in the ocular, nasal, and temporal acoustic windows. The ideal 1:1 relationship is shown as the dashed black line, with $\pm 1.4$ mm boundaries, representing the best possible resolution of the system, indicated by the dashed gray lines. . . . .	154
<b>Figure 7.1</b>	New paradigm for photoacoustic detection of the ICAs during minimally invasive neurosurgery. . . . .	165
<b>Figure 7.2</b>	Schematic of the combined amplitude- and coherence-based multispectral imaging methodology indicating four key phases (1) experimental setup for data acquisition, (2) ROI identification with SLSC imaging (3) extraction of DAS pixel amplitude with SLSC-identified ROIs, and (4) generation of photoacoustic amplitude spectra. . . . .	167

**Figure 7.3** Absorptivity spectra of cholesterol, water, nerve, and plasti-  
 sol measured at wavelengths (a) 1200-1420 nm and (b) 1600-  
 1820 nm . (c,d) Corresponding photoacoustic amplitude spec-  
 tra measured from SLSC-indicated regions in DAS images at  
 wavelengths (c) 1200-1420 nm and (d) 1600-1820 nm. The top  
 and bottom boundaries of the shaded regions represent the  
 maximum and minimum, respectively, amplitude measured  
 from the DAS image pixels within the SLSC-identified region  
 at that wavelength. . . . . 169

**Figure 7.4** Theoretical explanation of the effect of  $M$  value in the ex-  
 perimental visualization of two cross sections of brachyther-  
 apy seeds with SLSC imaging. (top row) Schematic diagrams  
 of a brachytherapy seed, showing seed dimensions and out-  
 lines of the cross sections imaged within each column. (middle  
 row) Theoretical spatial coherence functions and lateral pro-  
 files from the corresponding theoretical SLSC image when the  
 indicated cross section of the brachytherapy seed was simu-  
 lated. (bottom row) Experimental images of the brachyther-  
 apy seeds displayed with  $M=2$  and  $M=10$  [22]. . . . . 172

# List of Symbols

## Symbols

$A_N$	initial pressure distribution
$A_t$	mean amplitude of the initial pressure distribution inside the target in the absence of noise
$\beta$	thermal coefficient of volume expansion
$C$	spatial covariance in the spatial frequency domain
$C_p$	specific heat capacity at constant pressure
$c$	speed of sound
$E_s$	signal energy
$\hat{E}_s$	log compressed signal energy
$F$	fluence
$F_o$	initial fluence
$f$	acoustic frequency
$f_c$	transducer center frequency
$f_H$	highest frequency within $-6$ dB bandwidth of the transducer frequency response
$f_L$	lowest frequency within $-6$ dB bandwidth of the transducer frequency response
$\Delta f$	frequency increments
$\Gamma$	Grüneisen parameter
$H_{rx}$	spherical propagation of a sound wave from a photoacoustic source to a point on the receiving transducer
$h_b$	histogram of signal amplitude within a background region

$h_t$	histogram of signal amplitude within a target region
$K$	coherence value at lag zero
$\Lambda$	wavelength of light
$\lambda$	acoustic wavelength
$\lambda_c$	wavelength corresponding to transducer center frequency (i.e., inverse of $f_c$ )
$\lambda_H$	highest wavelength within $-6$ dB bandwidth of the transducer frequency response
$\lambda_L$	lowest wavelength within $-6$ dB bandwidth of the transducer frequency response
$\Delta\lambda$	wavelength increments
$M$	limit of integration over the spatial lag axis
$\mathbf{m}$	spatial lag (i.e., distance between two transducer elements) in units of space
$m$	spatial lag in units of number of elements
$\mu_a$	optical absorption coefficient
$\mu_b$	mean amplitude of signals within a background region
$\mu'_s$	reduced optical scattering coefficient
$\mu_t$	mean amplitude of signals within a target region
$N_t$	total simulation time
$N_h$	number of bins in histogram
$N$	total number of elements
$N_A$	zero-mean Gaussian distributed additive noise
$N_o$	variance of the Gaussian distributed noise
$N_{sc}$	scaling factor of zero-mean Gaussian distributed additive noise
$N_a$	number of absorbers
$\mathbf{n}$	sample depth in units of samples
$P$	measured photoacoustic pressure field
$P_i$	amplitude of the $i$ th image pixel
$\hat{P}_i$	log compressed pixel amplitude
$p_0$	initial photoacoustic pressure



$\Delta p$	amplitude of photoacoustic signal
$R_p$	photoacoustic spatial covariance
$\hat{R}_p$	normalized spatial correlation
$\overline{R_p}$	least-squares best fit polynomial for the first 35 lags of the photoacoustic spatial coherence function
$r_n$	travel distance from the source to the aperture
$SLSC_{pixel}$	pixel in SLSC image
$\sigma_N$	standard deviation
$s_i$	time-delayed acoustic signal received by the $i$ th element
$\sigma_t$	standard deviation of signals within a target region
$\sigma_b$	standard deviation of signals within a background region
$t$	time
$u$	spatial frequency in the lateral dimension
$v$	spatial frequency in the elevation dimension
$w_o$	initial optical beam diameter
$\mathbf{X}_0$	photoacoustic source location
$\mathbf{X}_n$	location on receiving aperture
$\mathbf{X}'_{0n}$	independent variables for pressure field integration
$x_k$	lateral focal point
$x_s$	time domain pressure signal at sensor index, $s$
$\chi$	photoacoustic source function
$\chi_0$	average power of the photoacoustic source function
$y$	elevation dimension
$z$	depth of the imaging plane
$z_r$	Rayleigh length

# List of Abbreviations

## Abbreviations

2D	Two dimensional
ANSI	American National Standards Institute
CF	Coherence Factor
CNR	Contrast-to-noise ratio
CT	Computed tomography
DAS	Delay-and-sum
FWHM	Full width at half maximum
gCNR	Generalized contrast-to-noise ratio
GPU	Graphical processing unit
ICA	Internal carotid artery
LCA	Left internal carotid artery
MPE	Maximum permissible exposure
MR	Magnetic resonance
NIR	Near infrared
OPO	Optical parametric oscillator
PSF	Point spread function
RCA	Right internal carotid artery
RMSE	Root mean square error
ROI	Region of interest
SLSC	Short-lag spatial coherence

SNR      Signal-to-noise ratio  
VCZ      van Cittert-Zernike

# Chapter 1

## Introduction

### 1.1 Biomedical photoacoustic imaging overview

#### *1.1.1 Discovery and medical adoption of the photoacoustic effect*

On February 26th, 1880, Alexander Graham Bell excitedly exclaimed in a letter to his father, “I have heard articulate speech produced by sunlight! I have heard a ray of the sun laugh and cough and sing! ... I have been able to hear a shadow, and I have even perceived by ear the passage of a cloud across the sun’s disk” [1]. Inspired by this new observation, A.G. Bell as well as scientists Wilhelm Röntgen and John Tyndall independently conducted experiments on a myriad of liquid, solid, and gaseous matter and observed similar production of sound during exposure to intermittent optical energy [2]–[4]. These scientists had discovered the phenomenon today known as the photoacoustic effect.

The photoacoustic effect was adopted in the medical imaging field to assist in a myriad of clinical applications such as disease diagnosis and surveillance, therapeutic treatment monitoring, and intraoperative image guidance [5]–[13]. Specifically, in biomedical photoacoustic imaging, a light source excites an optically absorbing target of interest to produce acoustic signals that can be received by a standard ultrasound

transducer and reconstructed into an image using a process known as beamforming [7], [14]. Due to the high optical absorption of hemoglobin (i.e., the oxygen carrying protein in blood), blood vessels are an ideal candidate for photoacoustic visualization. This dissertation focuses on photoacoustic imaging as a technique for visualization of the internal carotid arteries, the primary vessels which supply blood to the brain.

### 1.1.2 Photoacoustic signal generation

To efficiently generate a rise in pressure, two conditions are imposed upon the irradiated volume - stress confinement and thermal confinement. Stress confinement is satisfied when the duration of the irradiating pulse does not exceed the time for the sound wave to transmit beyond the irradiated volume. Additionally, when the pulse duration is short enough such that heat conduction beyond the irradiated volume is negligible for the duration of the pulse, thermal confinement is satisfied [15]. Under these conditions, the initial amplitude of a photoacoustic signal  $\Delta p$ , can be written as:

$$\Delta p = \Gamma \mu_a(\Lambda) F(\mu_a, \mu'_s) \quad (1.1)$$

where  $\mu_a$ ,  $\mu'_s$ , and  $\Gamma$  are the tissue-specific properties of optical absorption coefficient, reduced optical scattering coefficient, and Grüneisen parameter, respectively,  $F$  is the fluence of the excitation light incident on the target, and  $\Lambda$  is the wavelength of the incident light. The Grüneisen parameter is a dimensionless, temperature-dependent factor proportional to the fraction of thermal energy converted into mechanical stress and is defined as:

$$\Gamma = \frac{\beta c^2}{C_p} \quad (1.2)$$

where  $\beta$  is the thermal coefficient of volume expansion,  $C_p$  is the specific heat capacity at constant pressure, and  $c$  is the speed of sound [16], [17].

### *1.1.3 Photoacoustic signal processing*

Ultrasound transducers employ piezoelectric materials to detect photoacoustic signals by converting the mechanical energy of the acoustic waves into electrical energy. Techniques such as backprojection, time-reversal, and beamforming are used to spatially localize these received signals and reconstruct an image [6], [18], [19]. Beamforming takes advantage of the hardware, electronics, and principles of ultrasound image formation such that photoacoustic imaging can be smoothly incorporated into existing ultrasound systems and their associated transducer arrays. The first step in the beamforming process is to time-delay the received signals, an operation which corrects the time-of-arrival differences of the acoustic signal along the array. Subsequent steps are unique to the beamformer being used for the image reconstruction. Specifically, this dissertation utilizes the delay-and-sum (DAS) and short-lag spatial coherence (SLSC) beamformers.

## **1.2 Intraoperative photoacoustic imaging of the internal carotid arteries during endonasal transsphenoidal surgery**

### *1.2.1 Significance of localizing the internal carotid arteries*

The internal carotid arteries (ICAs) originate bilaterally in the neck, enter the skull, and traverse a torturous path along the anterior skull base. Due to their complex anatomical positioning within the skull base, the ICAs are at risk of injury during skull base interventions. In a 2018 survey, 20% of participating skull base surgeons report causing at least one ICA injury within the last 12 months with 50.9% of these injuries occurring during endonasal transsphenoidal surgery for pituitary tumor resection [20].

Fig. 1.1 demonstrates the endonasal transsphenoidal approach in which instruments are inserted through the nasal cavities to drill away the posterior face of the

sphenoid sinus, gain access to the skull base, and resect tumors [21], [22]. The axial CT scan in Fig. 1.1 highlights the proximity of the ICAs to the surgical site. The ICAs often lie within millimeters of the tumor and, in the case of aggressive and advanced tumors, the ICAs can even be invaded by and embedded within the tumor [23]. In addition, the left and right ICAs are separated by an average of 1.2 - 2.8 cm [24], [25], with high anatomical variability of the region leading to ICA separations as minimal as 0.4 cm [26], [27].

Intraoperative monitoring of the ICAs is paramount to prevent iatrogenic injury to the ICAs and avoid the associated severe surgical complications such as hemorrhage, hypotension, stroke, aneurysm, carotid cavernous fistula, cranial nerve deficits (e.g, visual loss or paralysis), and death. Morbidity and mortality rates are as high as 14% and 24–26%, respectively, each time an accidental injury occurs [28]–[32].

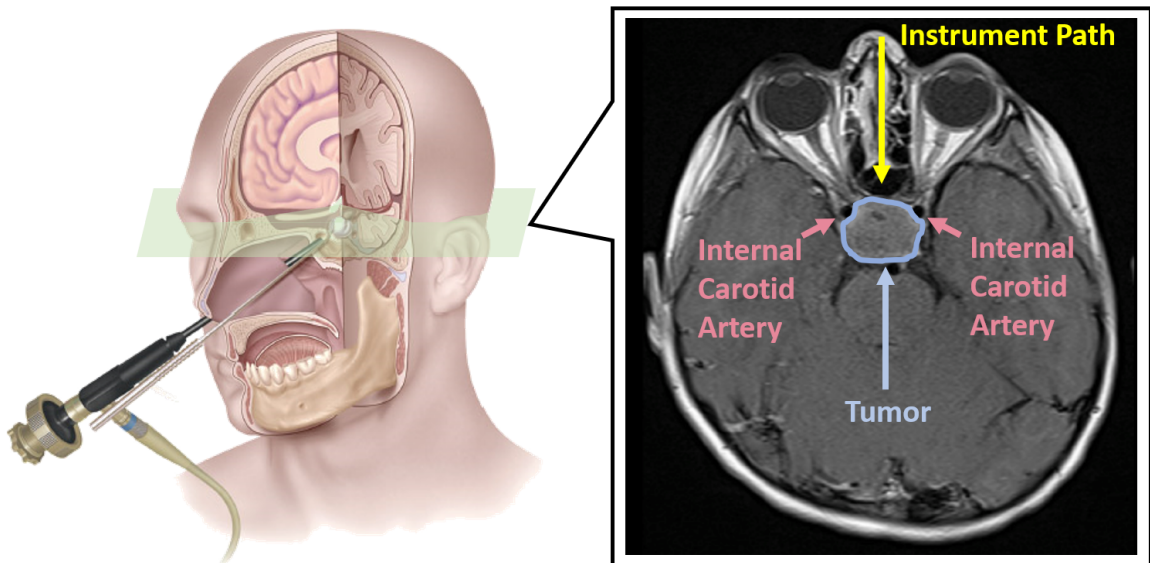


Figure 1.1: Diagram of endonasal transsphenoidal surgery for pituitary tumor resection. Surgical tools, such as endoscopes and drills are inserted through the nasal cavity to gain access to the surgical site. The outset image is an axial CT scan of a patient with a pituitary tumor. The scan is annotated to demonstrate the proximity of the internal carotid arteries to the tumor.

### *1.2.2 Challenges with current image-guidance techniques*

Current image-guidance techniques for intraoperative monitoring of the ICAs include stereotactic guidance, Doppler ultrasound, and endoscopy [33]. Although stereotactic guidance provides anatomical information for surgical planning, intraoperatively it is subject to registration errors which can become increasingly large as patient anatomy is disrupted during surgery and as the anatomy significantly deviates from that shown in preoperative x-ray computed tomography (CT) or magnetic resonance (MR) images. Doppler ultrasound can exploit blood flow to visualize the ICAs, however, is restricted by limited penetration depth due to high attenuation rates from the two-way propagation through bony structures. Endoscopes inserted through the nasal cavity enable real-time visualization of the surgical field, but are unable to locate critical structures underlying bone, brain matter, or muscle in the operative path [34], [35].

### *1.2.3 Emergence of photoacoustic image guidance*

Photoacoustic imaging is a promising intraoperative imaging technique for real-time visualization of the ICAs [13], [36]–[40]. This technique is implemented by inserting a light source into the nasal cavity, similar to the insertion of other instruments during endonasal surgery. An optical pulse emitted from the light source transmits through superficial structures such bone and dura and illuminates the ICAs. Through the photoacoustic effect, the hemoglobin in the ICAs absorb the optical energy, thermally expand, and generate an acoustic signal. The acoustic signal propagates through tissues (e.g., brain, bone, and skin) to an externally placed ultrasound transducer. Both optical and acoustic energy interact with bone at multiple points along the optical (i.e., optical source to ICA) and acoustic (i.e., ICA to transducer) pathways.



### 1.3 Challenges with photoacoustic image guidance

#### 1.3.1 Optical interactions with bone

Fig. 1.2 demonstrates interactions that occur with bone present in the optical and acoustic pathways, resulting in photoacoustic image quality degradation [41]. As light propagates along the optical pathway, the high absorption and scattering properties of bone attenuate the total optical energy and decrease the fluence incident on the underlying ICAs [42]–[46]. The direct relationship between the generated photoacoustic signal amplitude and fluence indicates that photoacoustic detection of targets underlying bone suffers from poor target contrast when using strictly amplitude-based

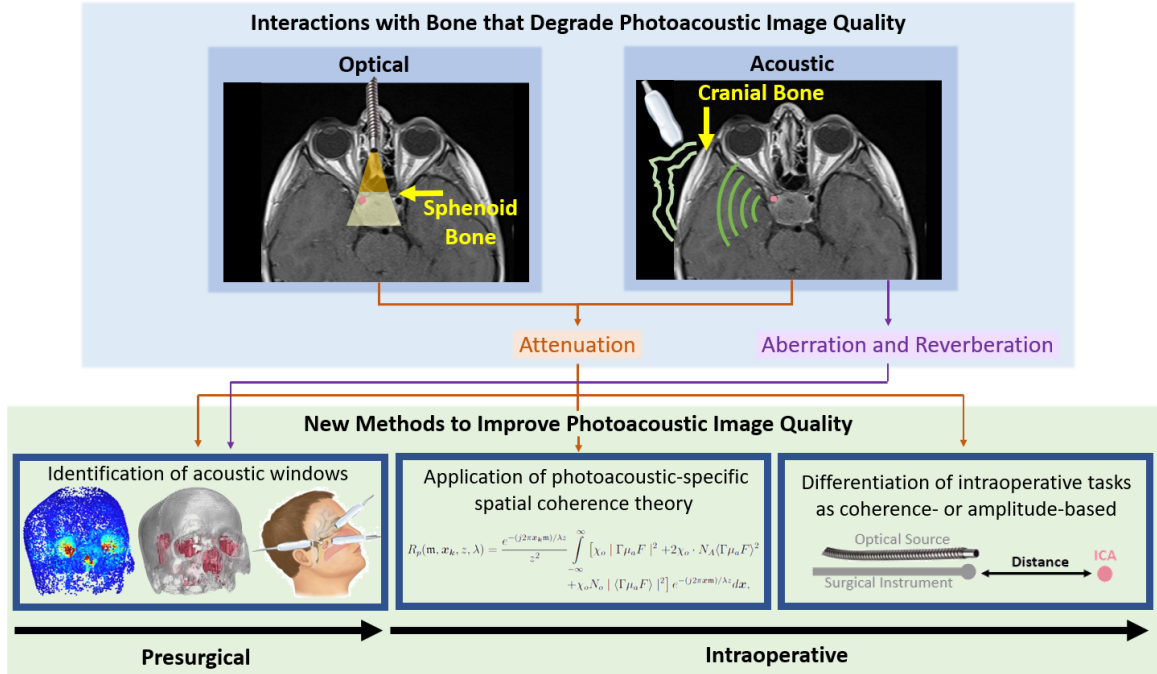


Figure 1.2: During photoacoustic visualization of the internal carotid arteries, optical and acoustic interactions that occur with the bone present along the photoacoustic imaging pathway include optical attenuation and acoustic attenuation, aberration, and reverberation. Each of these interactions contributes to degradation in photoacoustic image quality. This dissertation presents three new methods to improve photoacoustic image quality of the ICAs in the presence of bone. These contributions span both presurgical planning and intraoperative monitoring tasks.

approaches [47]. Overcoming this amplitude-based challenge is further complicated by maximum permissible exposure limits established for skin and eyes by the American National Standards Institute [48]. Because of these safety limits, it is often not a feasible solution to mitigate optical attenuation by increasing the total optical energy in the imaging environment and other solutions must be explored.

### *1.3.2 Acoustic interactions with bone*

Similar to the optical pathway, sound propagating along the acoustic pathway will be scattered and absorbed by bone, thereby significantly attenuating the acoustic signal [42], [49]–[54]. Additional image-degrading acoustic effects arise from the acoustic heterogeneity which bone introduces into the acoustic pathway. The acoustic impedance mismatches at the brain-bone, cortical-cancellous bone, and bone-skin interfaces cause acoustic interactions such as reverberation (i.e., multiple reflections back and forth between two interfaces) and mode conversion (i.e., bidirectional longitudinal to shear wave conversion) [47], [55], [56]. In addition, heterogeneities in acoustic velocity cause aberrations (i.e., phase distortion) along the propagating wavefront [56], [57].

In photoacoustic images, these acoustic interactions with bone cause poor target visualization, incorrect target localization, reduced resolution, and reflection artifacts [45], [47], [58], [59]. The severity of photoacoustic image degradation depends on the anatomy of the bone (e.g., thickness and proportion of cancellous and cortical layers) and the angle of the acoustic wave incident to the bone [60], [61], with the bone thickness being the dominant variable affecting the severity of image degradation [58], [62].

### 1.3.3 DAS and SLSC beamforming challenges

DAS and SLSC are two examples of beamforming techniques for photoacoustic image reconstruction. DAS is a low-complexity algorithm which sums the delayed channel data across the array. Constructive and destructive interference will localize the origins of the targets in the image plane. Mathematically, DAS beamforming is described as:

$$DAS_{pixel} = \sum_{i=1}^N s_i(\mathbf{n}), \quad (1.3)$$

where  $s_i(\mathbf{n})$  is the time-delayed acoustic signal received by the  $i$ th element,  $\mathbf{n}$  is the sample depth in units of samples,  $N$  is the number of elements in the receiving array, and  $DAS_{pixel}$  is one pixel in the DAS image. DAS beamforming generates images of photoacoustic signal amplitude.

SLSC beamforming is a more advanced, coherence-based beamforming technique. SLSC beamforming computes the spatial coherence of the received signals as a function of element spacing (i.e., spatial lag, or  $m$ ) and sums these coherence functions,  $\hat{R}_p(m)$ , up to a specific short-lag value,  $M$ , to directly display measured spatial coherence values. Mathematically, the SLSC beamformer can be described as follows:

$$\hat{R}_p(m) = \frac{1}{N-m} \sum_{i=1}^{N-m} \frac{\sum_{\mathbf{n}=\mathbf{n}_1}^{\mathbf{n}_2} s_i(\mathbf{n})s_{i+m}(\mathbf{n})}{\sqrt{\sum_{\mathbf{n}=\mathbf{n}_1}^{\mathbf{n}_2} s_i^2(\mathbf{n}) \sum_{\mathbf{n}=\mathbf{n}_1}^{\mathbf{n}_2} s_{i+m}^2(\mathbf{n})}}, \quad (1.4)$$

$$SLSC_{pixel} = \sum_{m=1}^M \hat{R}_p(m), \quad (1.5)$$

where  $\mathbf{n}_1$  to  $\mathbf{n}_2$  is the axial correlation kernel length, and  $SLSC_{pixel}$  is one pixel in the short-lag spatial coherence image [63]. SLSC beamforming generates images which are independent of signal amplitude. As a result, SLSC beamforming of photoacoustic images in high noise environments demonstrates notable improvements in contrast and signal-to-noise ratios, in comparison to traditional DAS beamforming [64]–[70].

Although Eqs. 1.4 and 1.5 describe the implementation of the SLSC beamformer, these equations do not describe the theoretical foundations of this beamformer when applied to photoacoustic data. Without a theory, it is difficult to ascertain cases when SLSC beamforming would be more beneficial than the more traditional DAS beamformer. As a result, theoretical development of photoacoustic spatial coherence is a critical step toward realizing the full potential of these different beamforming options.

#### 1.4 Dissertation overview

This dissertation addresses challenges surrounding photoacoustic visualization of the ICAs in the presence of bone, with applications from presurgical to intraoperative use, as illustrated in Fig. 1.2. Combining theoretical, simulated, and experimental approaches, the contributions of this dissertation include: (1) development and validation of a photoacoustic-specific spatial coherence theory, (2) differentiation of intraoperative ICA tracking tasks most beneficial for SLSC beamforming from those better suited to more traditional DAS beamforming, and (3) identification of new photoacoustic windows to optimize signal visualization. These contributions are described according to the following structure:

- Chapter 2 derives and validates a novel photoacoustic-specific spatial coherence theory. We demonstrate the utility of this theory to optimize photoacoustic SLSC images of circular targets (with diameters encompassing the typical sizes of adult ICAs) and point targets (which can represent nearby surgical instrument tips illuminated with the photoacoustic effect). This foundational theory supports the implementation of advanced coherence-based beamforming techniques for ICA (and nearby instrument tip) detection, improving photoacoustic image quality in bony environments with high optical and acoustic attenuation.

- Recognizing the broad potential of our theoretical derivation in Chapter 2, we developed PhocoSpace, an open-source photoacoustic toolbox to simulate the coherence of photoacoustic signals. Chapter 3 demonstrates PhocoSpace as a flexible *in silico* tool to execute and accelerate photoacoustic spatial coherence investigations for clinical applications such as blood vessel detection.
- With a strong theoretical foundation developed, Chapter 4 transitions from theoretical applications in the absence of bone to SLSC imaging implementations in the presence of bone in human cadaver heads. We classify intraoperative ICA tracking tasks into those most beneficial for SLSC beamforming (or other coherence-based signal processing techniques) and those better suited for traditional DAS beamforming (or related amplitude-based techniques). Additionally, we identify naturally occurring acoustic windows to reduce the overall attenuating, reverberation, and aberration acoustic interactions with bone. We then demonstrate the feasibility of one newly identified window, the ocular cavity, in a cadaver head experiment with a light delivery design that ensures safety.
- Chapter 5 further validates the newly identified ocular cavity acoustic window for ICA detection. These investigations demonstrate the promise of photoacoustic simulations as a tool for patient-specific pre-operative surgical planning of optimal receiver locations when using photoacoustic imaging as an intraoperative navigation technique.
- Chapter 6 presents a vision for the workflow of photoacoustic image-based ICA and instrument tip detection, from presurgical planning to intraoperative use. We discuss options for minimizing barriers to clinical translation of intraoperative photoacoustic imaging of the ICAs. Additionally, we demonstrate the reduction of one of these barriers by fine-tuning a presurgical, simulation-based, patient-specific acoustic window identification methodology.

- Chapter 7 concludes this dissertation with a summary of the work contained herein and offers a discussion of potential future directions.

This dissertation relies on the content of individual, peer-reviewed publications. Multiple chapters replicate these manuscripts in their original, unaltered forms. As a result, there are redundancies regarding the explanation of recurring principles in separate chapters. However, these redundancies are essential to the flow and content of the individual chapters.

## References

- [1] A. G. Bell, *Letter from alexander graham bell to alexander melville bell, february 26, 1880, with transcript*, Library of Congress, Feb. 1880.
- [2] —, “The production of sound by radiant energy,” *American Journal of Science*, pp. 242–253, 1881.
- [3] W. C. Röntgen, “On tones produced by the intermittent irradiation of a gas,” *The London, Edinburgh, and Dublin Philosophical Magazine and Journal of Science*, vol. 11, no. 68, pp. 308–311, 1881.
- [4] J. Tyndall, “Iii. action of an intermittent beam of radiant heat upon gaseous matter,” *Proceedings of the Royal Society of London*, vol. 31, no. 206-211, pp. 307–317, 1881.
- [5] A. Wiacek and M. A. L. Bell, “Photoacoustic-guided surgery from head to toe,” *Biomedical Optics Express*, vol. 12, no. 4, pp. 2079–2117, 2021.
- [6] P. Beard, “Biomedical photoacoustic imaging,” *Interface Focus*, vol. 1, no. 4, pp. 602–631, 2011.
- [7] M. Xu and L. V. Wang, “Photoacoustic imaging in biomedicine,” *Review of Scientific Instruments*, vol. 77, no. 4, p. 041 101, 2006.

- [8] A. B. E. Attia, G. Balasundaram, M. Moothanchery, U. Dinish, R. Bi, V. Ntzichristos, and M. Olivo, “A review of clinical photoacoustic imaging: Current and future trends,” *Photoacoustics*, vol. 16, p. 100 144, 2019.
- [9] D. Das, A. Sharma, P. Rajendran, and M. Pramanik, “Another decade of photoacoustic imaging,” *Physics in Medicine & Biology*, vol. 66, no. 5, 05TR01, 2021.
- [10] S. Mallidi, G. P. Luke, and S. Emelianov, “Photoacoustic imaging in cancer detection, diagnosis, and treatment guidance,” *Trends in Biotechnology*, vol. 29, no. 5, pp. 213–221, 2011.
- [11] S. Zackrisson, S. Van De Ven, and S. Gambhir, “Light in and sound out: Emerging translational strategies for photoacoustic imaging,” *Cancer Research*, vol. 74, no. 4, pp. 979–1004, 2014.
- [12] M. A. L. Bell, “Photoacoustic vision for surgical guidance,” in *2020 IEEE International Ultrasonics Symposium (IUS)*, IEEE, 2020, pp. 1–6.
- [13] M. A. Lediju Bell, “Photoacoustic imaging for surgical guidance: Principles, applications, and outlook,” *Journal of Applied Physics*, vol. 128, no. 6, p. 060 904, 2020.
- [14] R. Bouchard, O. Sahin, and S. Emelianov, “Ultrasound-guided photoacoustic imaging: Current state and future development,” *IEEE Transactions on Ultrasonics, Ferroelectrics, and Frequency Control*, vol. 61, no. 3, pp. 450–466, 2014.
- [15] G. Paltauf and P. E. Dyer, “Photomechanical processes and effects in ablation,” *Chemical Reviews*, vol. 103, no. 2, pp. 487–518, 2003.
- [16] B. T. Cox and P. C. Beard, “Fast calculation of pulsed photoacoustic fields in fluids using k-space methods,” *The Journal of the Acoustical Society of America*, vol. 117, no. 6, pp. 3616–3627, 2005.

- [17] V. E. Gusev and A. A. Karabutov, "Laser optoacoustics," *Nasa Sti/recon Technical Report A*, vol. 93, p. 16 842, 1991.
- [18] E. Hysi, M. J. Moore, E. M. Strohm, and M. C. Kolios, "A tutorial in photoacoustic microscopy and tomography signal processing methods," *Journal of Applied Physics*, vol. 129, no. 14, p. 141 102, 2021.
- [19] Y. Zhou, J. Yao, and L. V. Wang, "Tutorial on photoacoustic tomography," *Journal of biomedical optics*, vol. 21, no. 6, p. 061 007, 2016.
- [20] N. R. Rowan, M. T. Turner, B. Valappil, J. C. Fernandez-Miranda, E. W. Wang, P. A. Gardner, and C. H. Snyderman, "Injury of the carotid artery during endoscopic endonasal surgery: Surveys of skull base surgeons," *Journal of Neurological Surgery Part B: Skull Base*, vol. 79, no. 03, pp. 302–308, 2018.
- [21] P. Cappabianca, L. M. Cavallo, and E. de Divitiis, "Endoscopic endonasal transsphenoidal surgery," *Neurosurgery*, vol. 55, pp. 933–941, 2004.
- [22] X. Zhang, Z. Fei, W. Zhang, J. Zhang, W. Liu, L. Fu, W. Cao, and S. Jiang XF and Song, "Endoscopic endonasal transsphenoidal surgery for invasive pituitary adenoma," *Journal of Clinical Neuroscience*, vol. 15, pp. 241–245, 2008.
- [23] E. R. Laws, "Vascular complications of transsphenoidal surgery," *Pituitary*, vol. 2, no. 2, pp. 163–170, 1999.
- [24] M. A. Mascarella, R. Forghani, S. D. Maio, D. Sirhan, A. Zeitouni, G. Mohr, and M. A. Tewfik, "Indicators of a reduced intercarotid artery distance in patients undergoing endoscopic transsphenoidal surgery," *Journal of Neurological Surgery, Part B, Skull Base*, vol. 76, no. 3, pp. 195–201, 2015.
- [25] W. H. Renn and A. L. Rhoton, "Microsurgical anatomy of the sellar region," *Journal of neurosurgery*, vol. 43, no. 3, pp. 288–298, 1975.



- [26] R. M. Bergland, B. S. Ray, and R. M. Torack, "Anatomical variations in the pituitary gland and adjacent structures in 225 human autopsy cases," *Journal of Neurosurgery*, vol. 28, no. 2, pp. 93–99, 1968.
- [27] R. L. Dolci, L. F. Ditzel Filho, C. R. Goulart, S. Upadhyay, L. Buohliqah, P. R. Lazarini, D. M. Prevedello, and R. L. Carrau, "Anatomical nuances of the internal carotid artery in relation to the quadrangular space," *Journal of Neurosurgery*, vol. 128, no. 1, pp. 174–181, 2017.
- [28] I. Ciric, A. Ragin, C. Baumgartner, and D. Pierce, "Complications of transsphenoidal surgery: Results of a national survey, review of the literature, and personal experience," *Neurosurgery*, vol. 40, no. 2, pp. 225–237, 1997.
- [29] M. O. Perry, W. H. Snyder, and E. R. Thal, "Carotid artery injuries caused by blunt trauma," *Annals of Surgery*, vol. 192, no. 1, pp. 74–77, 1980.
- [30] J. Raymond, J. Hardy, R. Czepko, and D. Roy, "Arterial injuries in transsphenoidal surgery for pituitary adenoma; the role of angiography and endovascular treatment," *American Journal of Neuroradiology*, vol. 18, no. 4, pp. 655–665, 1997.
- [31] R. Valentine and P.-J. Wormald, "Carotid artery injury after endonasal surgery," *Otolaryngologic Clinics of North America*, vol. 44, no. 5, pp. 1059–1079, 2011.
- [32] O. Y. Chin, R. Ghosh, C. H. Fang, S. Baredes, J. K. Liu, and J. A. Eloy, "Internal carotid artery injury in endoscopic endonasal surgery: A systematic review," *The Laryngoscope*, vol. 126, no. 3, pp. 582–590, 2016.
- [33] A. R. Javer, O. Marglani, A. Lee, M. Matishak, and K. A. Genoway, "Image-guided endoscopic transsphenoidal removal of pituitary tumours.," *Journal of Otolaryngology–Head & Neck Surgery*, vol. 37, no. 4, 2008.

- [34] K. Kitazawa, H. Okudera, T. Takemae, and S. Kobayashi, “CT guided transsphenoidal surgery: Report of nine cases,” *Neurological Surgery*, vol. 21, no. 147, 1993.
- [35] P. Cappabianca, A. Alfieri A.and Colao, L. M. Cavallo, M. Fusco, C. Peca, G. Lombardi, and E. de Divitiis, “Endoscopic endonasal transsphenoidal surgery in recurrent and residual pituitary adenomas: Technical note,” *Minimally Invasive Neurosurgery*, vol. 43, pp. 38–43, 2000. DOI: [10.1055/s-2000-8814](https://doi.org/10.1055/s-2000-8814).
- [36] M. A. L. Bell, A. K. Ostrowski, K. Li, P. Kazanzides, and E. M. Boctor, “Localization of transcranial targets for photoacoustic-guided endonasal surgeries,” *Photoacoustics*, vol. 3, no. 2, pp. 78–87, 2015.
- [37] —, “Quantifying bone thickness, light transmission, and contrast interrelationships in transcranial photoacoustic imaging,” in *Proceedings of SPIE, Photons Plus Ultrasound: Imaging and Sensing*, vol. 9323, 2015.
- [38] M. A. L. Bell, A. B. Dagle, P. Kazanzides, and E. M. Boctor, “Experimental assessment of energy requirements and tool tip visibility for photoacoustic-guided endonasal surgery,” in *Proceedings of SPIE, Photons Plus Ultrasound: Imaging and Sensing*, vol. 9708, 2016, p. 97080D.
- [39] M. A. L. Bell, A. K. Ostrowski, P. Kazanzides, and E. M. Boctor, “Feasibility of transcranial photoacoustic imaging for interventional guidance of endonasal surgeries,” in *Proceedings of SPIE, Photons Plus Ultrasound: Imaging and Sensing*, vol. 8943, 2014, p. 894307.
- [40] T. Kirchner, J. Gröhl, N. Holzwarth, M. A. Herrera, A. Hernández-Aguilera, E. Santos, and L. Maier-Hein, “Photoacoustic monitoring of blood oxygenation during neurosurgical interventions,” in *Proceedings of SPIE, Photons Plus Ultrasound: Imaging and Sensing*, vol. 10878, 2019, pp. 14–18.

- [41] R. Manwar, K. Kratkiewicz, and K. Avanaki, “Investigation of the effect of the skull in transcranial photoacoustic imaging: A preliminary ex vivo study,” *Sensors*, vol. 20, no. 15, p. 4189, 2020.
- [42] A. N. Bashkatov, E. A. Genina, V. I. Kochubey, and V. V. Tuchin, “Optical properties of human cranial bone in the spectral range from 800 to 2000 nm,” in *Saratov Fall Meeting 2005: Optical Technologies in Biophysics and Medicine VII*, SPIE, vol. 6163, 2006, pp. 306–316.
- [43] X. Wang, D. L. Chamberland, and G. Xi, “Noninvasive reflection mode photoacoustic imaging through infant skull toward imaging of neonatal brains,” *Journal of neuroscience methods*, vol. 168, no. 2, pp. 412–421, 2008.
- [44] S. Golovynskiy, I. Golovynska, L. I. Stepanova, O. I. Datsenko, L. Liu, J. Qu, and T. Y. Ohulchanskyy, “Optical windows for head tissues in near-infrared and short-wave infrared regions: Approaching transcranial light applications,” *Journal of Biophotonics*, vol. 11, no. 12, e201800141, 2018.
- [45] L. Nie, X. Cai, K. I. Maslov, A. Garcia-Uribe, M. A. Anastasio, and L. V. Wang, “Photoacoustic tomography through a whole adult human skull with a photon recycler,” *Journal of Biomedical Optics*, vol. 17, no. 11, p. 110 506, 2012.
- [46] Q. Xu, B. Volinski, A. Hariri, A. Fatima, and M. Nasiriavanaki, “Effect of small and large animal skull bone on photoacoustic signal,” in *Proceedings of SPIE, Photons Plus Ultrasound: Imaging and Sensing*, vol. 10064, 2017, 100643S.
- [47] M. Kneipp, J. Turner, H. Estrada, J. Rebling, S. Shoham, and D. Razansky, “Effects of the murine skull in optoacoustic brain microscopy,” *Journal of Biophotonics*, vol. 9, no. 1-2, pp. 117–123, 2016.
- [48] American National Standards Institute, *American national standard for the safe use of lasers*, 2007.

- [49] B. E. Treeby and B. T. Cox, “Modeling power law absorption and dispersion for acoustic propagation using the fractional laplacian,” *The Journal of the Acoustical Society of America*, vol. 127, no. 5, pp. 2741–2748, 2010.
- [50] B. E. Treeby, “Acoustic attenuation compensation in photoacoustic tomography using time-variant filtering,” *Journal of biomedical optics*, vol. 18, no. 3, p. 036 008, 2013.
- [51] G. Pinton, J.-F. Aubry, E. Bossy, M. Muller, M. Pernot, and M. Tanter, “Attenuation, scattering, and absorption of ultrasound in the skull bone,” *Medical Physics*, vol. 39, no. 1, pp. 299–307, 2012.
- [52] F. J. Fry and J. E. Barger, “Acoustical properties of the human skull,” *The Journal of the Acoustical Society of America*, vol. 63, no. 5, pp. 1576–1590, 1978.
- [53] S. Pichardo, V. W. Sin, and K. Hynynen, “Multi-frequency characterization of the speed of sound and attenuation coefficient for longitudinal transmission of freshly excised human skulls,” *Physics in Medicine & Biology*, vol. 56, no. 1, p. 219, 2010.
- [54] J. Lee, D.-G. Paeng, and K. Ha, “Attenuation of the human skull at broadband frequencies by using a carbon nanotube composite photoacoustic transducer,” *The Journal of the Acoustical Society of America*, vol. 148, no. 3, pp. 1121–1129, 2020.
- [55] B. Liang, S. Wang, F. Shen, Q. H. Liu, Y. Gong, and J. Yao, “Acoustic impact of the human skull on transcranial photoacoustic imaging,” *Biomedical optics express*, vol. 12, no. 3, pp. 1512–1528, 2021.
- [56] H. Estrada, J. Rebling, J. Turner, and D. Razansky, “Broadband acoustic properties of a murine skull,” *Physics in Medicine & Biology*, vol. 61, no. 5, p. 1932, 2016.

- [57] B. Liang, W. Liu, Q. Zhan, M. Li, M. Zhuang, Q. H. Liu, and J. Yao, “Impacts of the murine skull on high-frequency transcranial photoacoustic brain imaging,” *Journal of biophotonics*, vol. 12, no. 7, e201800466, 2019.
- [58] L. Mohammadi, R. Manwar, H. Behnam, J. Tavakkoli, and M. R. N. Avanaki, “Skull’s aberration modeling: Towards photoacoustic human brain imaging,” in *Photons Plus Ultrasound: Imaging and Sensing 2019*, SPIE, vol. 10878, 2019, pp. 518–528.
- [59] C. Huang, L. Nie, R. W. Schoonover, Z. Guo, C. O. Schirra, M. A. Anastasio, and L. V. Wang, “Aberration correction for transcranial photoacoustic tomography of primates employing adjunct image data,” *Journal of Biomedical Optics*, vol. 17, no. 6, p. 066 016, 2012.
- [60] X. Yang and L. V. Wang, “Monkey brain cortex imaging by photoacoustic tomography,” *Journal of biomedical optics*, vol. 13, no. 4, p. 044 009, 2008.
- [61] E. W. Stein, K. Maslov, and L. V. Wang, “Noninvasive, in vivo imaging of the mouse brain using photoacoustic microscopy,” *Journal of applied physics*, vol. 105, no. 10, p. 102 027, 2009.
- [62] R. W. Schoonover, L. V. Wang, and M. A. Anastasio, “Numerical investigation of the effects of shear waves in transcranial photoacoustic tomography with a planar geometry,” *Journal of biomedical optics*, vol. 17, no. 6, p. 061 215, 2012.
- [63] M. A. L. Bell, Trahey, G. E., Byran, B. C., and J. J. Dahl, “Short-lag spatial coherence of backscattered echoes: Imaging characteristics,” *IEEE Transactions on Ultrasonics, Ferroelectrics, and Frequency Control*, vol. 58, no. 7, pp. 1377–1388, 2011.
- [64] M. A. L. Bell, N. Ku, D. Y. Song, and E. M. Boctor, “Short-lag spatial coherence beamforming of photoacoustic images for enhanced visualization of prostate brachytherapy seeds,” *Biomedical Optics Express*, vol. 4, no. 10, p. 1964, 2013.

- [65] M. A. L. Bell, N. P. Kuo, D. Y. Song, J. U. Kang, and E. M. Boctor, “In vivo visualization of prostate brachytherapy seeds with photoacoustic imaging,” *Journal of Biomedical Optics*, vol. 19, no. 12, p. 126 011, 2014.
- [66] M. A. L. Bell, D. Y. Song, and E. M. Boctor, “Coherence-based photoacoustic imaging of brachytherapy seeds implanted in a canine prostate,” in *Medical Imaging 2014: Ultrasonic Imaging and Tomography*, SPIE, vol. 9040, 2014, pp. 166–171.
- [67] M. A. L. Bell, X. Guo, H. J. Kang, and E. Boctor, “Improved contrast in laser-diode-based photoacoustic images with short-lag spatial coherence beamforming,” in *2014 IEEE International Ultrasonics Symposium*, IEEE, 2014, pp. 37–40.
- [68] B. Pourebrahimi, S. Yoon, D. Dopsa, and M. C. Kolios, “Improving the quality of photoacoustic images using the short-lag spatial coherence imaging technique,” in *Photons Plus Ultrasound: Imaging and Sensing 2013*, International Society for Optics and Photonics, vol. 8581, 2013, 85813Y.
- [69] M. T. Graham, J. Huang, F. Creighton, and M. A. L. Bell, “Simulations and human cadaver head studies to identify optimal acoustic receiver locations for minimally invasive photoacoustic-guided neurosurgery,” *Photoacoustics*, p. 100 183, 2020.
- [70] E. A. Gonzalez and M. A. L. Bell, “GPU implementation of photoacoustic short-lag spatial coherence imaging for improved image-guided interventions,” *Journal of Biomedical Optics*, vol. 25, no. 7, p. 077 002, 2020.

# Chapter 2

## Photoacoustic Spatial Coherence Theory

*The work presented in this chapter was published in the following manuscript:*

M. T. Graham and M. A. L. Bell, “Photoacoustic spatial coherence theory and applications to coherence-based image contrast and resolution,” *IEEE Transactions on Ultrasonics, Ferroelectrics, and Frequency Control*, vol. 67, no. 10, pp. 2069–2084, 2020.

### 2.1 Introduction

Photoacoustic imaging techniques rely on the photoacoustic effect to generate acoustic signals. To achieve the photoacoustic effect, pulsed light is transmitted and an acoustic wave is generated from the thermal expansion and contraction of an optically absorbing target. By tuning the wavelength of the incident light, techniques using this effect exploit the optical absorption spectrum of biologic chromophores to achieve high target sensitivity [2]. Common clinical targets include hemoglobin, nerves, and metal with major application areas in blood flow measurement [3], flow cytometry [4], vascular imaging [5], [6], surgical navigation and guidance [7]–[13], and

implant placement [14], [15].

Coherence-based photoacoustic techniques are increasingly popular due to their ability to improve resolution and imaging depth. For example, changes in the volume of red blood cells flowing through an artery tend to generate fluctuations in the resulting photoacoustic pressure signal. The temporal coherence of these pressure signals can be used to implement photoacoustic correlation spectroscopy to estimate blood flow with better resolution and higher imaging depth than Doppler imaging methods [3].

Similarly, when imaging deep structures, conventional amplitude-based photoacoustic imaging is often challenged by low signal-to-noise ratios due to insufficient fluence at the target depth, optical scattering in tissues, and depth-dependent acoustic attenuation. Lateral resolution also suffers due to the depth-dependent acoustic beam widths. As a result, coherence-based imaging techniques have been introduced, primarily to reduce side-lobes and acoustic clutter. One example of a spatial coherence technique to improve image quality is coherence factor (CF) weighting, which improves spatial resolution and contrast [16]. CF weighting has been combined with other methods, such as synthetic aperture focusing [17] and an adaptive minimum variance method [18] to achieve additional improvements in spatial resolution and contrast. SNR-dependent CF weighting was also introduced to preserve contrast in high-noise scenarios [19]. Similar success was achieved when weighting traditional amplitude-based images with other types of coherence-based metrics, including coherence weighting to improve resolution in the elevation dimension [20] and short-lag spatial coherence (SLSC) weighting to reduce clutter in amplitude-based images [21].

Initial implementations of SLSC imaging to photoacoustic data demonstrate that weighting with amplitude-based images is not a requirement to achieve the benefits of reduced clutter and improved contrast and resolution [15], [22]–[25]. SLSC images directly display measured coherence values, and these measurements are independent



of signal amplitude. As a result, SLSC images are particularly beneficial for photoacoustic imaging in high-noise environments, which can be caused by insufficient laser fluence incident on a target of interest. Insufficient laser fluence often results from low-energy sources (e.g., when using pulsed laser diodes [24], [26] or light emitting diodes [27]–[29]) or when imaging structures that are far away from the light source (e.g., when imaging brachytherapy seeds with an interstitial or transurethral approach [15], [22], [23], [30]). In these cases, photoacoustic SLSC images demonstrate considerable improvements in border delineations, contrast, contrast-to-noise ratios, and signal-to-noise ratios when compared to traditional delay-and-sum (DAS) beamforming and Fourier-based reconstruction techniques.

Although these benefits of coherence-based signal processing are based on experimental observations, a well-developed theory to describe expected spatial coherence has multiple additional benefits. For example, this theory can be used to study a wide range of potential optimizations that would otherwise require lengthy experimental testing, which is not always feasible. This theory may also be used to gain insight into potential unexpected and counterintuitive optimizations. We derived an initial narrowband photoacoustic spatial coherence theory in our associated conference paper [31] and updated this narrowband theory to consider frequencies within the bandwidth of an ultrasound probe [32]. In addition, we derived and tested additive noise models to further improve our initial theory [33]. This journal paper presents a complete mathematical description of our theory in the presence of noise, including validation with experimental data from multiple target sizes. We also discuss how our photoacoustic spatial coherence theory can be applied to optimize photoacoustic SLSC image display.

The remainder of article is organized as follows: Section 2.2 provides a complete description of our theory for photoacoustic spatial coherence and details how it can be used to create theoretical photoacoustic SLSC images. Section 2.3 lists our validation

methods using SLSC images that are derived from theoretical equations, k-Wave simulations [34], and experimental data consisting of thread, ink-filled tubes, and an *in vivo* hepatic blood vessel. Section 2.4 shows the results of our validation methods and demonstrates the utility of our theory when selecting photoacoustic-based parameters to optimize the contrast and resolution of SLSC images. Finally, Section 2.5 discusses the major insights and implications derived from this work, and Section 2.6 contains our concluding remarks.

## 2.2 Theory

### 2.2.1 Photoacoustic Spatial Coherence

A linear systems approach is used to describe the measured photoacoustic pressure field,  $P$ . The first component of the linear system is  $\chi$ , which is the random, nonuniform distribution of moderately dense, spatially incoherent absorbers (also known as the source function or source distribution function) at source location  $\mathbf{X}_0 = (\mathbf{x}, \mathbf{y}, z)$ . The moderately dense requirement (with moderate defined as 3.18 absorbers/mm<sup>2</sup> and dense defined as 318.3 absorbers/mm<sup>2</sup> in [35]) is introduced based on our observations that photoacoustic absorbers generally respond as an incoherent source function when their distribution is moderately dense and as a coherent source function when their distribution is dense. Guo *et al.* [36] similarly observed a coherent photoacoustic source when visualizing a dense ensemble of photoacoustic absorbers.

The second component of the linear system is  $A_N$ , the initial pressure distribution of absorbers located at position  $\mathbf{X}_o$  in the presence of noise [33]:

$$A_N(\mathbf{X}_o, f) = A + N_{sc}, \quad (2.1)$$

where  $N_{sc}$  scales zero-mean, Gaussian distributed, additive noise,  $N_A$ , by the expected value of the amplitude of the initial pressure distribution,  $A$ , as described by the

equation:

$$N_{sc} = \langle A \rangle N_A, \quad (2.2)$$

where  $\langle \cdot \rangle$  represents the expected value, and  $\langle A \rangle$  may be interpreted as an average over uncorrelated pressure signals generated from a microscopic distribution of moderately dense photoacoustic absorbers. To avoid confusion with the description provided in [33], we clarify here that  $N_{sc}$  in Eq. (2.1) is equivalent to the  $N_A$  term introduced in Eq. 8 of [33]. Although  $N_A$  has the same definition in both manuscripts, the scaling term  $\langle A \rangle$  is introduced in this manuscript in order for us to relate noise amplitudes to pressure amplitudes.

$A$  is a function of the fluence,  $F$ , at depth  $z$  and two tissue properties (i.e., the Grüneisen parameter,  $\Gamma$ , and the optical absorption coefficient,  $\mu_a$ ), as defined by the following equation:

$$A = \mu_a \Gamma F. \quad (2.3)$$

Based on the definitions provided in Eqs. (2.1)-(2.3),  $A_N$  takes the following form:

$$A_N = \begin{cases} \mu_a \Gamma F, & N_A = 0 \\ \mu_a \Gamma F + \langle \mu_a \Gamma F \rangle N_A, & N_A \neq 0 \end{cases} \quad (2.4)$$

The uncorrelated source-related noise,  $N_A$ , originates from random fluctuations in the source distribution (e.g., variations in fluence at the absorber surface [33] and variations in the optical absorption within the absorber). This additive noise model is based on our observations of experimental data (as described in detail in our previous publication [33]). Note that Ref. [33] also describes an additional noise term related to the channel noise-to-signal ratio, which we assume to be negligible throughout this paper.

The third component of the linear system is  $H_{rx}$ , which is the spherical propagation of the sound wave from the source to a point,  $n$ , on the transducer:

$$H_{rx}(\mathbf{X}_0, \mathbf{X}_n, f) = \frac{e^{j2\pi fr_n/c}}{r_n},$$

$$r_n = |\mathbf{X}_0 - \mathbf{X}_n|, \quad (2.5)$$

where  $\mathbf{X}_n$  is a point on the aperture (e.g.,  $\mathbf{X}_n = (\mathbf{x}_n, \mathbf{y}_n, 0)$ ),  $c$  is the speed of sound,  $r_n$  is the travel distance from the source to the aperture, and  $f$  is the acoustic frequency, which is related to the bandwidth of the ultrasound transducer.

The acoustic pressure measured from a single target is, therefore, defined as:

$$P(\mathbf{X}_0, \mathbf{X}_n, f) = \chi(\mathbf{X}_0, f) A_N(\mathbf{X}_0, f) H_{rx}(\mathbf{X}_0, \mathbf{X}_n, f). \quad (2.6)$$

The total received pressure at a point on the aperture,  $\mathbf{X}_n$ , is found by integrating the pressure field over  $\mathbf{X}_0$ , as described by:

$$P(\mathbf{X}_n, f) = \iiint_V P(\mathbf{X}_0, \mathbf{X}_n, f) d^3 \mathbf{X}_0. \quad (2.7)$$

To relate this derivation to previous derivations of photoacoustic pressure, note that Eq. (2.7) is similar to Eq. (2) in Ref. [37]. The photoacoustic spatial covariance,  $R_p$ , is the correlation of the pressure field at two lateral receiving positions  $\mathbf{X}_1$  and  $\mathbf{X}_2$ :

$$R_p(\mathbf{X}_1, \mathbf{X}_2, f) = \langle P(\mathbf{X}_1, f), P^*(\mathbf{X}_2, f) \rangle, \quad (2.8)$$

where  $P^*$  represents the complex conjugate of  $P$ . Expansion of Eq. (2.8) yields:

$$\begin{aligned}
R_p(\mathbf{X}_1, \mathbf{X}_2, f) = & \iiint_V \iiint_V \chi(\mathbf{X}'_{01}, f) \chi^*(\mathbf{X}'_{02}, f) \\
& \cdot H_{rx}(\mathbf{X}'_{01}, \mathbf{X}_1, f) H_{rx}^*(\mathbf{X}'_{02}, \mathbf{X}_2, f) \\
& \cdot A_N(\mathbf{X}'_{01}, f) A_N^*(\mathbf{X}'_{02}, f) d^3 \mathbf{X}'_{01} d^3 \mathbf{X}'_{02}, \quad (2.9)
\end{aligned}$$

where  $\mathbf{X}'_{01}$  and  $\mathbf{X}'_{02}$  are independent variables over which the pressure field is integrated to determine the total received pressure at aperture positions  $\mathbf{X}_1$  and  $\mathbf{X}_2$ , respectively.

Insertion of Eqs. (2.1) and (2.2) into Eq. (2.9) yields:

$$\begin{aligned}
R_p(\mathbf{X}_1, \mathbf{X}_2, f) = & \iiint_V \iiint_V \chi(\mathbf{X}'_{01}, f) \chi^*(\mathbf{X}'_{02}, f) \\
& \cdot H_{rx}(\mathbf{X}'_{01}, \mathbf{X}_1, f) H_{rx}^*(\mathbf{X}'_{02}, \mathbf{X}_2, f) \\
& \cdot [A(\mathbf{X}'_{01}, f) A^*(\mathbf{X}'_{02}, f) \\
& + A(\mathbf{X}'_{01}, f) \langle A^* \rangle N_A^*(\mathbf{X}'_{02}, f) \\
& + \langle A \rangle A^*(\mathbf{X}'_{02}, f) N_A(\mathbf{X}'_{01}, f) \\
& + \langle A \rangle \langle A^* \rangle N_A(\mathbf{X}'_{01}, f) N_A^*(\mathbf{X}'_{02}, f)] \\
& \cdot d^3 \mathbf{X}'_{01} d^3 \mathbf{X}'_{02}. \quad (2.10)
\end{aligned}$$

Because the source function,  $\chi$ , has a random, nonuniform, moderately dense, spatially incoherent distribution, note that:

$$\langle \chi(\mathbf{X}'_{01}, f), \chi^*(\mathbf{X}'_{02}, f) \rangle = \chi_o \delta(\mathbf{X}'_{01} - \mathbf{X}'_{02}), \quad (2.11)$$

where  $\chi_o$  represents the average power of the absorber distribution. Similarly, because

$N_A$  is also a random variable,

$$\langle N_A(\mathbf{X}'_{01}, f), N_A^*(\mathbf{X}'_{02}, f) \rangle = N_o \delta(\mathbf{X}'_{01} - \mathbf{X}'_{02}), \quad (2.12)$$

where  $N_o$  is the variance of the Gaussian distribution of  $N_A$ . According to Eqs. (2.11) and (2.12), the expected value of the source distribution and the associated noise within the source term are equal to zero except when  $\mathbf{X}'_{01} = \mathbf{X}'_{02}$ .

The expressions in Eqs. (2.11) and (2.12) reduce the expression for spatial covariance in Eq. (2.10) to a single volume integral:

$$\begin{aligned} R_p(\mathbf{X}_1, \mathbf{X}_2, f) = & \iiint_V [ \chi_o | A(\mathbf{X}'_0, f) |^2 + 2\chi_o N_A(\mathbf{X}'_0, f) \langle A \rangle^2 \\ & + \chi_o N_o | \langle A \rangle |^2 ] \frac{e^{j2\pi f(r_1 - r_2)/c}}{r_1 r_2} d^3 \mathbf{X}'_0, \\ r_i = & |\mathbf{X}_i - \mathbf{X}'_0|. \end{aligned} \quad (2.13)$$

The initial photoacoustic response is assumed to reside within an isochronous volume; thus the spatial covariance over a short depth,  $z$ , within this volume is taken to be constant, which reduces the volume integral in Eq. (2.13) to a surface integral [38]–[40]. This assumption is satisfied in photoacoustic imaging for multiple reasons (e.g., short nanosecond-duration laser pulses, laser pulse repetition frequencies on the order of several Hz as opposed to hundreds of kHz [24], and acoustic temporal frequencies limited by the transducer bandwidth). We then apply the paraxial and Fresnel approximations to the amplitude and phase terms, respectively. The paraxial approximation assumes that we are primarily interested in the received response near the axis of each transducer element:

$$r_i \approx z. \quad (2.14)$$

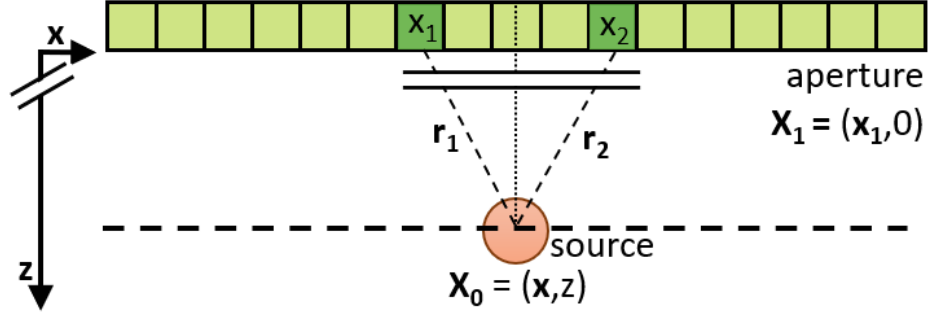


Figure 2.1: Illustration of the Fresnel approximation for an aperture (rectangle) and source (circle) located at the aperture center  $\mathbf{X}_0$ . The distance from the source to a point on the aperture is  $r_n$ . The lateral distance  $X_1 - X_2 \ll z$ , where  $z$  is the axial position of the source. Therefore,  $r \approx z$ .

The Fresnel approximation assumes that the axial distance between the aperture and source (i.e.,  $z$ ) is orders of magnitude larger than the lateral and elevation distances between a position on the aperture and a source, as illustrated in Fig. 2.1 for the lateral dimension. This approximation also supports the separability of the lateral and elevation dimensions and yields the following approximations in the lateral dimension:

$$r_1 \approx z + \frac{(\mathbf{x}_1 - \mathbf{x})(\mathbf{x}_1 - \mathbf{x})}{2z}, \quad (2.15)$$

$$r_2 \approx z + \frac{(\mathbf{x}_2 - \mathbf{x})(\mathbf{x}_2 - \mathbf{x})}{2z}. \quad (2.16)$$

Using the approximations described in Eqs. (2.14)-(2.16) yields an equation for photoacoustic spatial covariance that only depends on lateral position:

$$\begin{aligned} R_p(\mathbf{x}_1, \mathbf{x}_2, z, \lambda) = & \frac{e^{j\pi(\mathbf{x}_1\mathbf{x}_1 - \mathbf{x}_2\mathbf{x}_2)/\lambda z}}{z^2} \cdot \int_{-\infty}^{\infty} \left[ \chi_o \left| \Gamma(\mathbf{x}, z) \mu_a(\mathbf{x}, z) F(\mathbf{x}, z) \right|^2 \right. \\ & + 2\chi_o N_A \langle \Gamma(\mathbf{x}, z) \mu_a(\mathbf{x}, z) F(\mathbf{x}, z) \rangle^2 \\ & \left. + \chi_o N_o \left| \langle \Gamma(\mathbf{x}, z) \mu_a(\mathbf{x}, z) F(\mathbf{x}, z) \rangle \right|^2 \right] \\ & \cdot e^{-j2\pi(\mathbf{x}(\mathbf{x}_1 - \mathbf{x}_2))/\lambda z} d\mathbf{x}, \end{aligned} \quad (2.17)$$

where  $\lambda = c/f$ . Because broadband photoacoustic signals are sensed and filtered by a transducer with finite bandwidth, the  $\lambda$  term is primarily related to the acoustic frequency of the transducer [2], [41]. To evaluate Eq. (2.17) and obtain a spatial covariance,  $\lambda$  can be approximated as the wavelength corresponding to the center frequency of the transducer,  $\lambda_c$ . Note that Eq. (2.17) represents the product of a constant term, a phase term, and a Fourier transform that depends on both the initial pressure distribution (i.e.,  $A$ ) and scaled noise terms. The spatial frequencies in this Fourier transform are given by  $u = (\mathbf{x}_1 - \mathbf{x}_2)/\lambda z$ .

There are two options to eliminate the phase term in Eq. (2.17)[42], [43] (i.e., the two points  $x_1$  and  $x_2$  are symmetric with respect to the lateral center of the transducer when receiving unfocused data, or delays were applied to focus the received channel data and align responses at one point of interest in the image field). With either option, the new expression for spatial covariance in the lateral dimension depends only on spatial frequency  $u$ :

$$\mathcal{C}(\mathbf{u}) = \frac{1}{z^2} \int_{-\infty}^{\infty} \left[ \chi_o |\Gamma \mu_a F|^2 + 2\chi_o N_A \langle \Gamma \mu_a F \rangle^2 + \chi_o N_o |\langle \Gamma \mu_a F \rangle|^2 \right] e^{-j2\pi \mathbf{x} \mathbf{u}} d\mathbf{x}, \quad (2.18)$$

where  $\mathcal{C}$  represents the spatial covariance in the spatial frequency domain.

Eq. (2.18) is similar to the equation describing the van Cittert-Zernike (VCZ) theorem applied to pulse-echo measurements [42], with the optics-related terms (i.e.,  $\Gamma$ ,  $\mu_a$ , and  $F$ ) replacing the term that would describe an acoustic transmit pressure amplitude (or acoustic receive pressure amplitude when the equation is derived using acoustic reciprocity [44]). The VCZ theorem requires incoherent source distributions; therefore, this analogy for our photoacoustic spatial coherence theory applies to moderately dense absorber distributions.



A similar equation applies to the elevation dimension, considering that the lateral and elevation dimensions are separable. Therefore, a spatial covariance equation that includes both dimensions can be written as follows:

$$\mathcal{C}(\mathbf{u}, \mathbf{v}) = \frac{1}{z^2} \int_{-\infty}^{\infty} \int_{-\infty}^{\infty} \left[ \chi_o |\Gamma \mu_a F|^2 + 2\chi_o N_A \langle \Gamma \mu_a F \rangle^2 + \chi_o N_o |\langle \Gamma \mu_a F \rangle|^2 \right] e^{-j2\pi(\mathbf{u}\mathbf{x} + \mathbf{v}\mathbf{y})} d\mathbf{x}d\mathbf{y}, \quad (2.19)$$

where  $\mathbf{y}$  is the elevation dimension and  $\mathbf{v}$  is the spatial frequency in the elevation dimension. Let  $\mathbf{y}_1$  and  $\mathbf{y}_2$  be defined as the equivalent terms to  $\mathbf{x}_1$  and  $\mathbf{x}_2$ , respectively, in the elevation dimension rather than lateral dimension. Then, the spatial frequency in the elevation dimension is defined as  $\mathbf{v} = (\mathbf{y}_1 - \mathbf{y}_2)/\lambda z$ . Note that Eq. (2.19) uses one of the two assumptions for phase term elimination described above (i.e., either  $\mathbf{y}_1$  and  $\mathbf{y}_2$  are symmetric about the center of the transducer in the elevation dimension or the data are focused in the elevation plane of the transducer, which can typically be accomplished with a transducer lens). Although spatial covariance is inherently 2D, as described by Eq. (2.19), throughout this manuscript, we evaluate our theory in the separable lateral dimension of the transducer using Eqs. (2.17) and (2.18).

### 2.2.2 Photoacoustic Short-Lag Spatial Coherence Imaging

To make photoacoustic SLSC images, we consider the array steering vector, which encodes the steering direction from the aperture center to a focal point of interest,  $(x_k, z)$ , in the photoacoustic image. Shifting the focal point along the lateral image dimension changes the steering direction, as illustrated in Fig. 2.2. Alternatively, with a fixed steering direction, the image target may be laterally shifted relative to a fixed aperture to build lateral image pixels. This alternative is mathematically

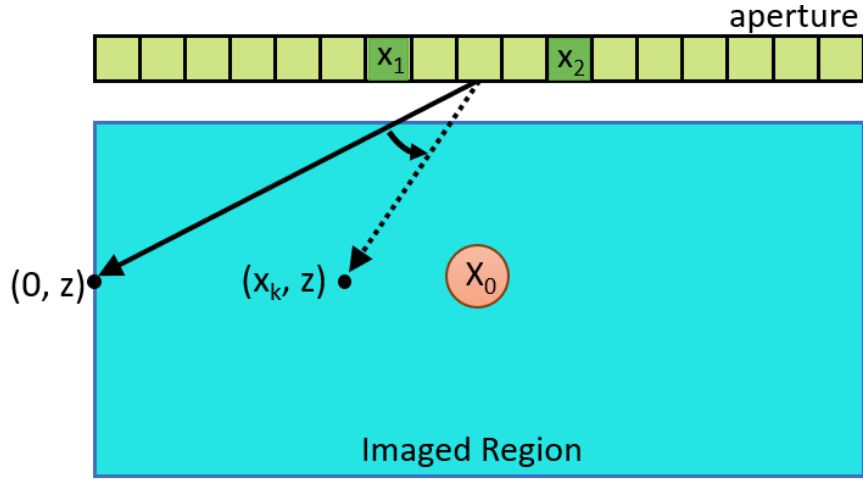


Figure 2.2: Steering direction from the aperture center to a focal point  $(x_k, z)$  in the image, illustrated with the assumption that Eq. (2.17) represents an initial focus located at lateral position  $x_k = 0$ .

described using the shifting property of Fourier transforms, which states that a shift in space by  $x_k$  corresponds to multiplication by a phase term in the spatial frequency domain, resulting in our final photoacoustic spatial covariance equation:

$$R_p(\mathbf{m}, \mathbf{x}_k, z, \lambda) = \frac{e^{-(j2\pi\mathbf{x}_k\mathbf{m})/\lambda z}}{z^2} \int_{-\infty}^{\infty} \left[ \chi_o |\Gamma\mu_a F|^2 + 2\chi_o \cdot N_A \langle \Gamma\mu_a F \rangle^2 + \chi_o N_o |\langle \Gamma\mu_a F \rangle|^2 \right] e^{-(j2\pi\mathbf{x}\mathbf{m})/\lambda z} d\mathbf{x}, \quad (2.20)$$

where the additional dependencies on  $\mathbf{x}$  and  $z$  (shown in Eq. (2.17)) are omitted for simplicity. The lag in Eq. (2.20) is defined in units of distance as:

$$\mathbf{m} = \mathbf{x}_1 - \mathbf{x}_2, \quad (2.21)$$

and  $\mathbf{m}$  is related to spatial frequency as defined by:

$$\mathbf{u} = \frac{\mathbf{m}}{\lambda z}, \quad (2.22)$$

where  $\lambda$  depends on the bandwidth of the probe, as described in Section 2.2.1.

Eq. (2.20) may be expressed in terms of spatial frequency as:

$$\mathcal{C}(\mathbf{u}, \mathbf{x}_k) = \frac{e^{-j2\pi\mathbf{x}_k\mathbf{u}}}{z^2} \int_{-\infty}^{\infty} \left[ \chi_o |\Gamma\mu_a F|^2 + 2\chi_o N_A \langle \Gamma\mu_a F \rangle^2 + \chi_o N_o |\langle \Gamma\mu_a F \rangle|^2 \right] e^{-j2\pi\mathbf{x}\mathbf{u}} d\mathbf{x}. \quad (2.23)$$

Note that the phase term in Eqs. (2.20) and (2.23) is generalizable because the definition of lag is represented in spatial units (i.e.,  $\mathbf{m}$ ) rather than units of element number (i.e.,  $m$ , as in previous derivations for ultrasound spatial coherence [42], [44], [45]), which makes this definition independent of the transducer pitch. An additional benefit of this independence includes applicability to transducers with variable pitch. The relationship between  $\mathbf{m}$  and  $m$  is:

$$m = \frac{\mathbf{m}}{\text{pitch}}, \quad (2.24)$$

where pitch is the transducer pitch.

To obtain a theoretical SLSC image, the dependency on the entire bandwidth of the transducer was included by integrating Eq. (2.20) over wavelengths that correspond to the highest and lowest acoustic frequencies within the -6 dB bandwidth of the transducer frequency response (i.e.,  $\lambda_H$  and  $\lambda_L$ , respectively, approximating equal weights for each wavelength), normalizing the result by the value obtained at lag zero (i.e.,  $K(x_k, z)$ ), then integrating over the first  $M$  lags to obtain each pixel in the theoretical SLSC image, as defined by the equation:

$$\begin{aligned} SLSC_{\text{pixel}}(x_k, z) &= \frac{1}{K(x_k, z)} \int_0^M \int_{\lambda_L}^{\lambda_H} R_p(m', x_k, z, \lambda') d\lambda' dm', \\ &\approx \frac{1}{K(x_k, z)} \sum_{m=1}^M \sum_{\lambda=\lambda_L}^{\lambda_H} R_p(m, x_k, z, \lambda). \end{aligned} \quad (2.25)$$

The dependence on transducer pitch is introduced in Eq. (2.25) in order to maintain consistency with previous descriptions of the integration process. As an aside, if transducer pitch is variable, the relationship between  $\mathbf{m}$  and  $m$  described in Eq. (2.24) would need to be updated, but this update would not change the format of Eq. (2.25).

### 2.2.3 Modeling Point Targets

Considering that point targets are defined as any target smaller than the resolution of the imaging system, we modify Eq. (2.6) to model point targets by first defining the source function as a delta function:

$$\chi(\mathbf{x}, f) = \delta(\mathbf{X}_o, f). \quad (2.26)$$

The correlation of the source function in Eq. (2.26) is defined as:

$$\langle \delta(\mathbf{X}'_{01}, f), \delta^*(\mathbf{X}'_{02}, f) \rangle = \delta(\mathbf{X}'_{01} - \mathbf{X}'_{02}), \quad (2.27)$$

which states that the expected value of the point source is equal to zero except when  $\mathbf{X}'_{01} = \mathbf{X}'_{02}$ .

Next, Eq. (2.12) can be implemented to demonstrate that the noise associated with this point source is also equal to zero except when  $\mathbf{X}'_{01} = \mathbf{X}'_{02}$ . Using a similar derivation and the same assumptions that follow after Eq. (2.12), we arrive at a mathematical expression for the spatial covariance of a point target:

$$R_{p,point}(\mathbf{m}, \mathbf{x}_k, z, \lambda) = \frac{e^{-(j2\pi\mathbf{x}_k\mathbf{m})/\lambda z}}{z^2} \int_{-\infty}^{\infty} \left[ |\Gamma\mu_a F|^2 + 2N_A \langle \Gamma\mu_a F \rangle^2 + N_o |\langle \Gamma\mu_a F \rangle|^2 \right] e^{-(j2\pi\mathbf{x}\mathbf{m})/\lambda z} d\mathbf{x}. \quad (2.28)$$

Eq. (2.28) may also be expressed in terms of spatial frequency:

$$\mathcal{C}_{point}(\mathbf{u}, \mathbf{x}_k) = \frac{e^{-j2\pi\mathbf{x}_k\mathbf{u}}}{z^2} \int_{-\infty}^{\infty} \left[ |\Gamma\mu_a F|^2 + 2N_A \langle \Gamma\mu_a F \rangle^2 + N_o |\langle \Gamma\mu_a F \rangle|^2 \right] e^{-j2\pi\mathbf{x}\mathbf{u}} d\mathbf{x}. \quad (2.29)$$

Eqs. (2.28) and (2.29) each represent a Fourier transform multiplied by a phase term, similar to Eqs. (2.20) and (2.23), respectively. To create theoretical SLSC images of point targets,  $R_p$  in Eq. (2.25) was replaced with Eq. (2.28).

## 2.3 Methods

### 2.3.1 Theory-Based Simulations

A 2D phantom was simulated in MATLAB with its lateral dimension corresponding to the lateral dimension of an ultrasound transducer and axial dimension corresponding to the depth of the imaging plane. An ultrasound transducer was modeled with most properties similar to the Alpinion L3-8 transducer (i.e., 128 elements, 0.3 mm pitch, and 3.84 cm total length) with the exception of the kerf being equal to 0 mm. This transducer was placed at depth  $z = 0$  cm. The simulated targets for theoretical testing included a point target and circular targets with diameters ranging from 0.2 mm to 12 mm. The circular targets were modeled as a distribution of randomly positioned absorbers, as shown in Fig. 2.3(a) for a simulated blood vessel surrounded by tissue.

Two types of fluence profiles were simulated to obtain  $F$ . The first profile was a light sheet with a uniform fluence value of  $F = 5$  mJ/cm<sup>2</sup> illuminating the entire phantom. The second profile was a Gaussian beam with an initial diameter,  $w_o$ , of 1 mm or 5 mm, initial depth  $z = 6.8$  mm, and a beam width that increased with depth. This Gaussian beam profile was simulated using the light propagation model defined

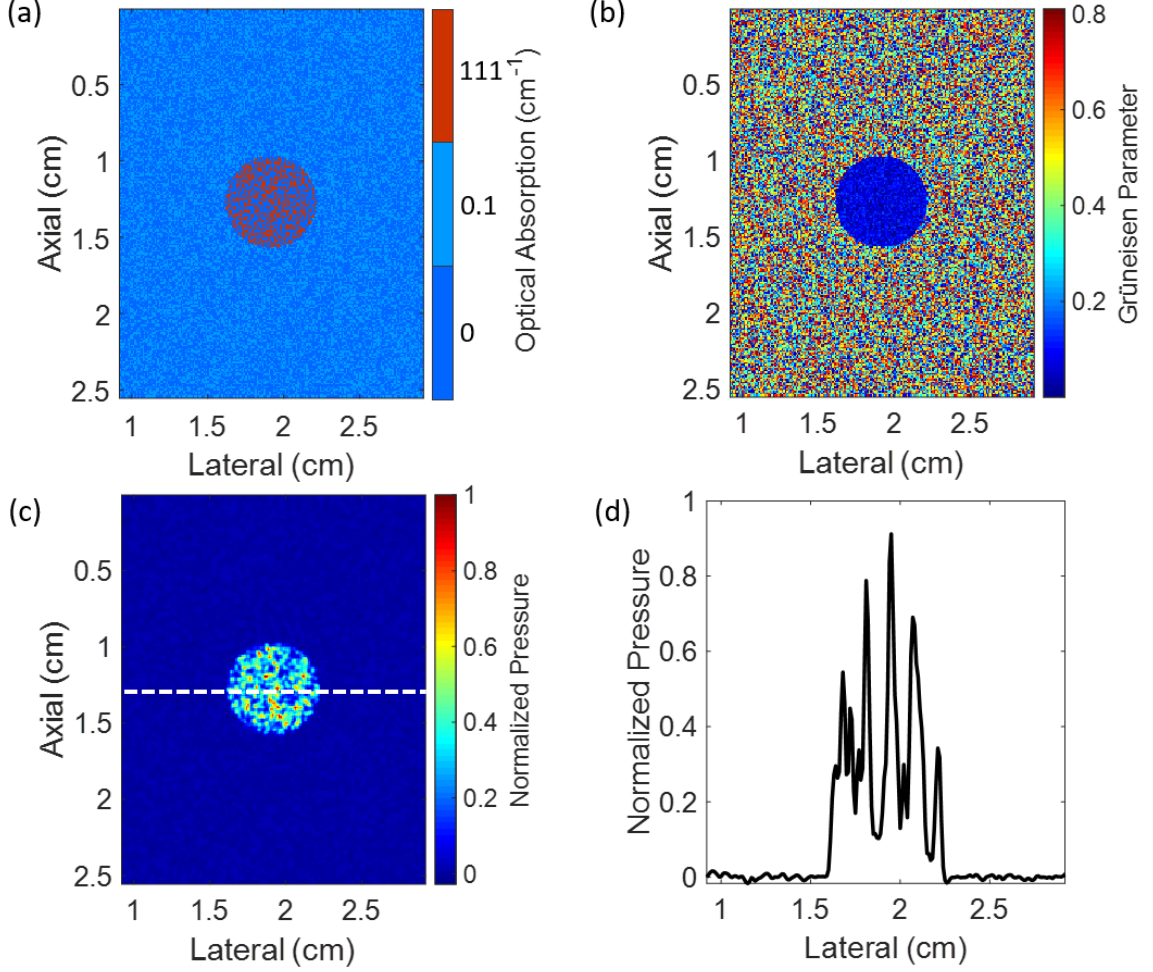


Figure 2.3: (a) Optical absorption ( $\mu_a$ ) distribution for a circular cross-section of a simulated 6 mm-diameter blood vessel with high optical absorption surrounded by tissue of low optical absorption, (b) Grüneisen parameter ( $\Gamma$ ) distribution, (c) corresponding photoacoustic pressure distribution ( $A_N$ ), and (d) a lateral profile of  $A_N$  taken from the axial depth indicated by the dashed white line.

as [46]:

$$F(\mathbf{x}, z) = F_o e^{-2x^2 / (w_o \sqrt{1 + (\frac{z}{z_r})^2})}. \quad (2.30)$$

where  $F_o$  is the initial fluence (set to 5 mJ/cm<sup>2</sup>) and  $z_r$  is the Rayleigh length (set to 1.2 mm and 6.2 mm for the 1 mm and 5 mm initial beam diameters, respectively).

Unless otherwise stated, the following values were used to define  $\mu_a$ ,  $\chi$ ,  $\Gamma$ ,  $N_o$ , and

$N_A$  in Eqs. (2.20) and (2.28). The mean magnitude of  $\mu_a$  was  $111 \text{ cm}^{-1}$  inside the photoacoustic target (to model hemoglobin in blood),  $0.1 \text{ cm}^{-1}$  outside the target (to model tissue), and  $0 \text{ cm}^{-1}$  when no absorbers were present [47]. The total number of absorbers,  $N_a$ , for the phantom with the circular targets was determined by the density of absorbers, which was fixed at  $40 \text{ absorbers/mm}^2$ . Because the Grünesien parameter is known to vary locally due to the composite nature of biological tissue [47],  $\Gamma$  was modeled as random values ranging 0-0.81 and 0-0.144 in tissue and in blood, respectively [47], as shown in Fig. 2.3(b). The average power of the absorber distribution,  $\chi_o$  was modeled as an arbitrary constant. The variance ( $N_o$ ) of the added noise ( $N_A$ ) was empirically determined, resulting in the values reported in Table 2.1. This combination of parameters produced a photoacoustic pressure distribution ( $A_N$ ), as shown in Figs. 2.3(c) and 2.3(d).

To obtain theoretical spatial coherence functions, Eqs. (2.20) and (2.28) were evaluated with an acoustic wavelength,  $\lambda \approx \lambda_c = 269 \mu\text{m}$  (which corresponds to a transducer with center frequency,  $f_c = 5.5 \text{ MHz}$ ). This result was then normalized by the value obtained at lag zero. For each target size, Eqs. (2.20) and (2.28) were evaluated with ten unique  $\mu_a$ ,  $\Gamma$ , and  $N_A$  distributions (with constant  $N_o$ ) in order to provide statistical measurements summarizing the mean and standard deviation of presented results.

To implement theoretical SLSC imaging, Eq. (2.25) (including the point source simplification described in Section 2.2.3) was evaluated over a discrete set of wavelengths that correspond to the -6 dB bandwidth of the frequency response of the Alpinion L3-8 ultrasound transducer (i.e.,  $\lambda_L = 211 \mu\text{m}$  to  $\lambda_H = 395 \mu\text{m}$  for multiple lateral positions (i.e.,  $x_k$ ) and for a specific  $M$  value. The wavelengths were incremented using a fixed  $\Delta f = 0.25 \text{ MHz}$ , which resulted in a variable  $\Delta\lambda = \lambda_{n+1} - \lambda_n = \frac{\Delta f}{c}(\lambda_n \lambda_{n+1})$ .

### 2.3.2 *k*-Wave Simulations

In order to compare our theoretical model to existing simulation methods for studying coherence-based beamformers, photoacoustic data were additionally simulated using the k-Wave software package [34]. The k-Wave acoustic receiver was modeled with most properties similar to the Alpinion L3-8 transducer (i.e., 128 elements, 3.84 cm total length, 0.3 mm pitch, 5.5 center frequency) with the exception of 0 mm kerf and 49 MHz sampling frequency. The targets were circular regions of moderately dense absorbers with diameters ranging from 0.1 mm (i.e. a point source) to 12 mm. Absorber locations within the circular region were randomly chosen (with the exception of the point source). These locations were constant between k-Wave and theoretical simulations of equally sized targets.

After creating ten unique absorber maps for each target size, each absorber map was combined with one of ten randomly generated Gaussian noise distributions created with the empirically determined standard deviations reported in Table 2.1 (in order to model the randomness of the initial pressure distribution associated with variations in fluence). In particular, each zero-mean Gaussian noise profile was added to the initial pressure distribution created with k-Wave simulations to create ten initial pressure distributions for each target size. For each pressure distribution, a time domain simulation was performed to generate 2D photoacoustic channel data, which was subsequently bandpass filtered to model the band-limiting effects of an Alpinion L3-8 ultrasound transducer with a center frequency of 5.5 MHz.

Spatial coherence functions and SLSC images were calculated from k-Wave data as described by the following equations from previous publications [7], [15], [48]:

$$\hat{R}_p(m) = \frac{1}{N - m} \sum_{i=1}^{N-m} \frac{\sum_{\mathbf{n}=n_1}^{n_2} s_i(\mathbf{n})s_{i+m}(\mathbf{n})}{\sqrt{\sum_{\mathbf{n}=n_1}^{n_2} s_i^2(\mathbf{n}) \sum_{\mathbf{n}=n_1}^{n_2} s_{i+m}^2(\mathbf{n})}}, \quad (2.31)$$



$$SLSC_{pixel} = \sum_{m=1}^M \hat{R}_p(m), \quad (2.32)$$

where  $\hat{R}_p(m)$  represents the normalized spatial correlation measured from received signals,  $m$  and  $N$  are defined in Section 2.2.2,  $s_i(\mathbf{n})$  is the time-delayed acoustic signal received by the  $i$ th element,  $\mathbf{n}$  is the sample depth in units of samples,  $\mathbf{n}_1$  to  $\mathbf{n}_2$  is the correlation kernel length, which was chosen to be  $2.4\lambda_c$  (with some numerical implementation differences due to rounding), and  $SLSC_{pixel}$  is one pixel in the short-lag spatial coherence image. The actual correlation kernel length (after rounding) was 23 samples. Unless otherwise stated, the value of  $M$  was set to 14, which corresponds to 11% of the number of elements in the receive aperture.

### 2.3.3 India Ink and Point Target Experiments

Two photoacoustic phantoms were used to validate the theoretical predictions of our model, particularly with regard to the effects of the illuminating beam diameter, target diameter, and varying  $M$ . The first photoacoustic phantom consisted of tubing of inner diameters ranging from 1.3 mm to 10 mm submerged in a water bath, as illustrated in Fig. 2.4. This tubing was rigidly fixed in an acrylic plate and initially filled with water to obtain the photoacoustic signal of the tubing alone. The water was aspirated and subsequently replaced with a 0.067 % India ink solution without altering the tubing position, enabling discrimination of signals from the tubing walls relative to signals from the India ink. The second photoacoustic phantom was a black thread of diameter 0.2 mm, which was suspended in a water bath.

Ten frames of photoacoustic channel data of each target were acquired with an Alpinion (Bothell, WA) E-Cube 12R ultrasound scanner connected to an Alpinion L3-8 linear array transducer. The sampling frequency of the ultrasound system was 40 MHz. The transducer was positioned to visualize the circular cross section of the thread or tubing diameter in the image plane. In this transducer orientation, the

thread was considered to be a point target.

Two different light delivery methods were coupled to the output port of a Phocus Mobile laser (Opotek, Inc., Carlsbad, CA) and independently used to acquire photoacoustic images with an optical wavelength of 760 nm. The first light delivery method was a 1-mm-core-diameter, multimode optical fiber with 0.5 numerical aperture (shown in Fig. 2.4). The laser output energy was 1.5 mJ/pulse. The second light delivery method was a larger 5 mm-diameter fiber bundle. The laser output energy was 125 mJ/pulse. Both light delivery methods were approximated to produce Gaussian-shaped beams.

Spatial coherence functions and SLSC images of the experimental data were calculated using Eqs. (2.31) and (2.32), respectively. The actual correlation kernel length (after rounding) was 17 samples. Unless otherwise stated, the value of  $M$  was set to 14, which corresponds to 11% of the number of elements in the receive aperture.

#### 2.3.4 *In Vivo Experiment*

*In vivo* photoacoustic data were used to assess the performance of our theoretical framework in a more complex environment that represents a clinical or surgical scenario of interest. These data were acquired from a major vein in a porcine liver study approved by the Johns Hopkins Animal Care and Use Committee, as described in our previous publications [12], [33]. To briefly summarize the imaging procedure, a laparotomy was performed to gain access to the liver, and the same photoacoustic imaging system described in Section 2.3.3 was utilized. The Alpinion L3-8 linear array transducer and 5 mm-diameter fiber bundle were both in direct contact with the liver tissue to visualize a circular cross section of the hepatic vein. The laser was operated at 750 nm with an incident energy of 40.5 mJ per pulse on the tissue surface. The vein was approximately 12 mm in diameter in the cross-sectional view of the ultrasound image.

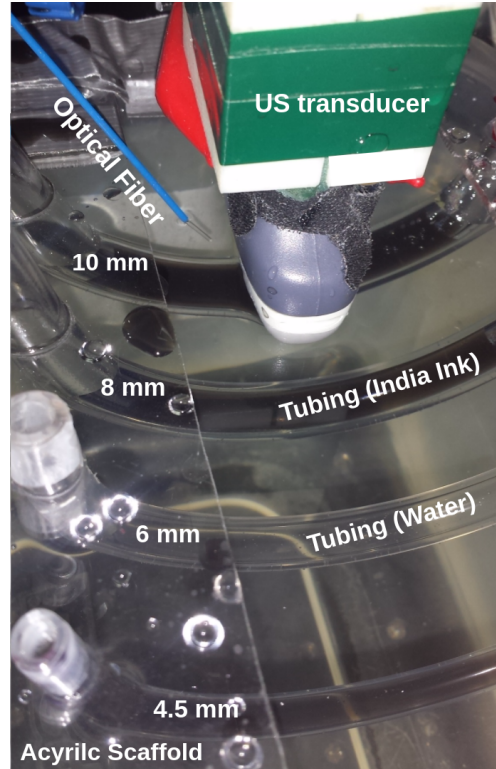


Figure 2.4: Experimental setup showing tubing of inner diameters 4.5 mm, 6 mm, 8 mm, and 10 mm (1.3 mm-, 2 mm-, and 4 mm-diameter tubing not shown) fixed in an acrylic scaffold and suspended in a water bath. The light source shown is the 1 mm-core-diameter optical fiber which was later interchanged with the 5 mm-diameter fiber bundle in the same position relative to the ultrasound transducer. An Alpinion L3-8 transducer is placed with its imaging plane viewing a circular cross-section of the tubing.

Spatial coherence functions and SLSC images of the *in vivo* data were calculated using Eqs. (2.31) and (2.32), respectively. The actual correlation kernel length (after rounding) was 17 samples. Unless otherwise stated, the value of  $M$  was set to 14, which corresponds to 11% of the number of elements in the receive aperture.

### 2.3.5 Empirical Methods to Add Noise to Simulated Datasets

The magnitude of the noise added to the theoretical and k-Wave simulated datasets was empirically determined based on the definition of  $\sigma_N$  reported in [33], which describes a phenomenological model of the deviation from a mean value at each lag in

a coherence function. To determine the value of  $\sigma_N$ , theoretical and k-Wave datasets were first simulated with the SNR of the initial pressure distribution,  $SNR_p$ , varied from 10 dB to 45 dB in 5 dB increments.  $SNR_p$  is related to  $N_o$  (i.e., the variance of the Gaussian distribution of the additive noise in the initial pressure distribution, as introduced in Eq. (2.12)) based on the following definition:

$$SNR_p = 20 \log_{10} \left( \frac{A_t}{\sqrt{N_o}} \right), \quad (2.33)$$

where  $A_t$  is the mean amplitude of the initial pressure distribution inside the target in the absence of noise (i.e.,  $A$  in Eq. (2.1)).

The following equation was then evaluated to calculate  $\sigma_N$  for the theoretical datasets:

$$\sigma_N = \sqrt{\frac{\sum_{m=0}^k (\hat{R}_p(m) - \overline{R}_p(m))^2}{k-1}}, \quad (2.34)$$

where  $\hat{R}_p$  is the normalized coherence function generated by evaluating and normalizing the result of Eq. (2.28) or Eq. (2.20) for a theoretical point target or for theoretical targets larger than a point target, respectively. Otherwise,  $\hat{R}_p$  was obtained by evaluating Eq. (2.32) for k-Wave and experimental results.  $\overline{R}_p$  is the least-squares best fit polynomial for the first 35 lags of the coherence function at the center of the target and  $k$  is the number of lags used in the fit.

For each target size with multiple theoretical and k-Wave  $SNR_p$  values simulated, the  $SNR_p$  chosen for the  $\sigma_N$  values reported in Table 2.1 was the  $SNR_p$  which generated a coherence function with the closest  $\sigma_N$  match to the  $\sigma_N$  measured from experimental data. The  $\sigma_N$  values measured from experimental data and chosen for theoretical and k-Wave simulations are reported in Table 2.1. The blank entries in Table 2.1 indicate experimental coherence functions that contained noise less consistent with the associated phenomenological model (likely due to the presence of strong coherent reverberations from the tubing in the experimental data). Therefore, the

Table 2.1:  $\sigma_N$  (mean  $\pm$  one standard deviation of ten measurements) for the results reported in Figs. 5, 7-11, and 14

Target Diameter (mm)	Theory	k-Wave	Experiment
Point	$0.044 \pm 0.005$	$0.037 \pm 0.008$	$0.056 \pm 0.011$
1.3	$0.017 \pm 0.005$	$0.014 \pm 0.004$	$0.016 \pm 0.005$
4.5	$0.014 \pm 0.002$	$0.012 \pm 0.004$	–
8	$0.002 \pm 0.000$	$0.004 \pm 0.003$	–
12	$0.084 \pm 0.004$	$0.082 \pm 0.008$	$0.080 \pm 0.000$

$SNR_p$  value chosen for each simulated dataset in these cases was the  $SNR_p$  which generated coherence functions with the most similar  $\sigma_N$  values between the theoretical and k-Wave simulations.

In addition to the  $\sigma_N$  values reported in Table 2.1 and due to notable differences between k-Wave and theoretical results, we were additionally interested in comparing theoretical results directly to experimental data. For these cases,  $\sigma_N$  values ranging 0.002 to 0.020 (which corresponded to  $SNR_p$  ranging 40 dB to 20 dB, respectively) were compared. These ranges were consistent with the range of  $\sigma_N$  values reported in Table 2.1.

For completeness, we note that the theoretical value of  $\sigma_N$  is related to  $N_A$  (i.e., the additive noise in the initial pressure distribution) and  $N_o$  (i.e., the variance of the Gaussian distribution of  $N_A$ ) by relating Eqs. (2.34) and (2.20) (or Eqs. (2.34) and (2.28) for the point target case).

### 2.3.6 Exploring Theoretical Implications for SLSC Imaging

To explore notable trends derived from our photoacoustic spatial coherence theory, SLSC image contrast and resolution were characterized as functions of the light beam profile diameter and the target size, for various  $M$  values using Eq. (2.25). Contrast was defined as:

$$\text{Contrast} = 20 \log_{10} \left( \frac{\mu_t}{\mu_b} \right), \quad (2.35)$$

where  $\mu_t$  and  $\mu_b$  are the mean amplitude of signals within the a target and background region, respectively, of the SLSC image. Resolution trends were quantified by measuring the full width at half maximum (FWHM) of lateral profiles created with multiple target sizes and illumination profile diameters. These theoretical results were compared to the controlled phantom results from the experiments described in Section 2.3.3.

## 2.4 Results

### 2.4.1 Comparison of Delay-and-Sum and SLSC Images

Fig. 2.5 compares traditional DAS beamforming with coherence-based SLSC images of experimental 1.3 mm- and 8 mm-diameter targets comprised of India ink. The 1 mm-diameter optical fiber was used to acquire the photoacoustic image of the 1.3 mm target. The 5 mm-diameter fiber bundle was used to acquire the photoacoustic image of the 8 mm target. Theoretical SLSC data was simulated with a Gaussian beam fluence profile with 1 mm and 5 mm initial beam diameters for the 1.3 mm- and 8 mm-diameter targets, respectively.

SLSC beamforming more clearly delineates the target content and boundaries farthest from the light source when compared to DAS beamforming. The DAS photoacoustic images of the targets may appear smaller than their actual sizes due to the depth-dependent fluence distribution that is known to impact a majority of photoacoustic images reconstructed with DAS beamforming. However, although the amplitude decreases with depth, the boundaries are better delineated in the SLSC images because the spatial coherence of the received signals is independent of amplitude, which is one of the known benefits of the SLSC beamformer applied to photoacoustic data. As the tubing surrounding the experimental targets produces spatially coherent signals, the proximal and distal tubing and structural boundaries are more clearly

visualized in the SLSC images, while signals above above the tubing are possibly due to a photoacoustic effect generated by the laser beam from the 1 mm-diameter optical fiber (1.3 mm target) or the 5 mm-diameter fiber bundle (8 mm target) interacting with the water surrounding the tubing.

Boundary delineation is a known benefit of SLSC imaging (compared to DAS and similar amplitude-based beamformers) applied to photoacoustic data, particularly when the target boundary is located at a considerable distance from the light source [9], [15], [22]. This enhanced target boundary delineation emphasizes the usefulness of coherence-based beamformers and highlights the importance of developing photoacoustic-specific spatial coherence theory to support their implementation.

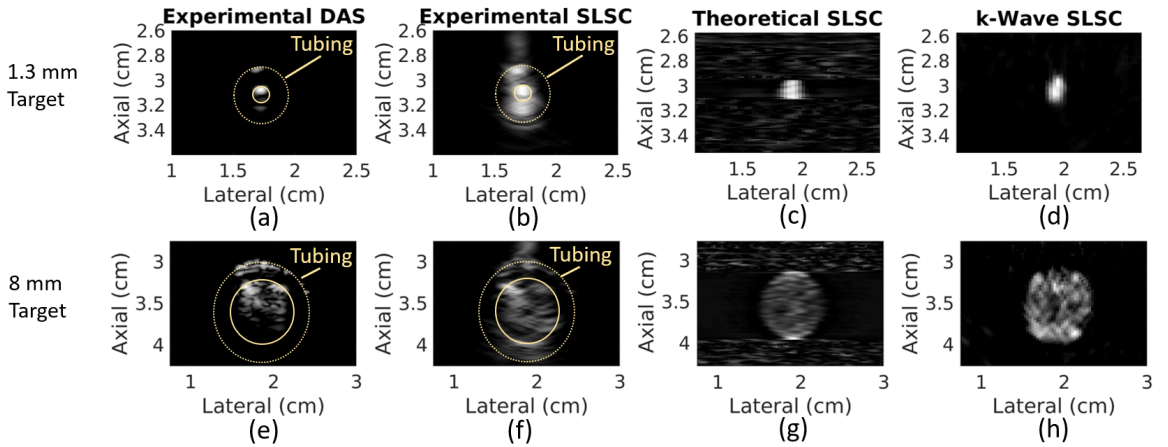


Figure 2.5: (a) Experimental delay-and-sum (DAS) image, (b) experimental short-lag spatial coherence (SLSC) image, (c) theoretical SLSC simulation (with added noise), and (d) k-Wave simulation (with added noise) of 1.3 mm- and 8 mm-diameter targets. The circles in the experimental DAS and SLSC images denote the inner (solid line) and outer (dotted line) diameters of the Tygon tubing filled with India ink. SLSC images are normalized to the brightest pixel and limited to display a minimum value of zero for  $M = 11\%$  of the aperture. DAS images are displayed with a 25 dB dynamic range.

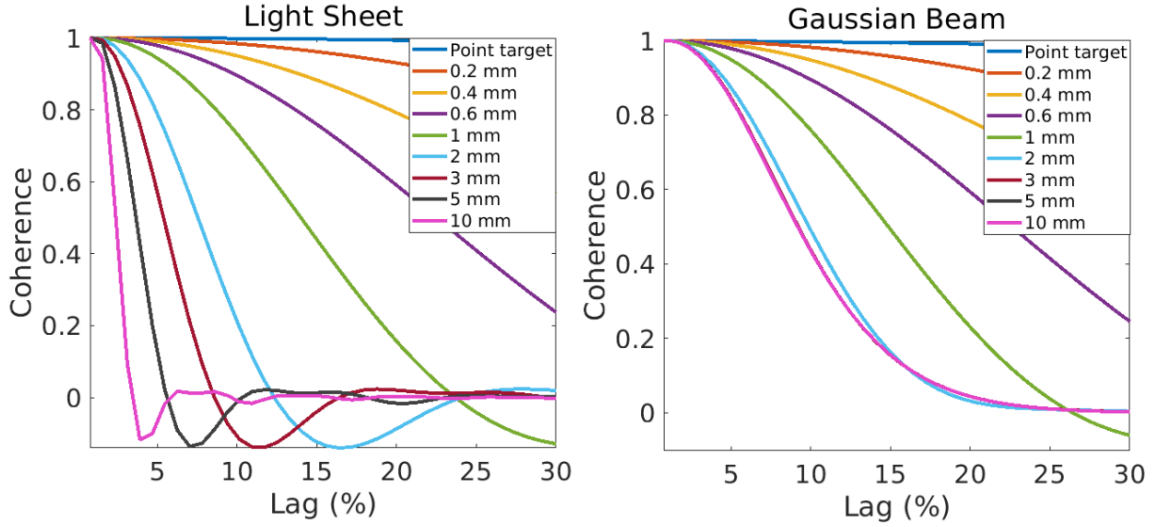


Figure 2.6: Noiseless theoretical coherence functions of at the center of targets ranging in size from a point to 10 mm in diameter using (a) light sheet and (b) 1 mm Gaussian beam profiles as the illuminating sources. The x-axis represents lag (i.e.,  $m$  or  $\mathbf{m}$ ) as a percentage of the receive aperture.

#### 2.4.2 Theoretical Photoacoustic Spatial Coherence Functions

Although experimental spatial coherence functions are expected to have some level of noise [33], theoretical spatial coherence functions were first simulated in the absence of noise (i.e.,  $N_A = 0$ ), to better understand expected trends. When a light sheet profile is used in theoretical simulations, the width of the coherence function continuously decreases from constant across the aperture for a point target to a significantly shorter coherence length for the 10 mm target, as shown in Fig. 2.6(a). In comparison, when a narrow-beam Gaussian profile is used (1 mm initial beam diameter), the width of the coherence function follows the same trend as a light sheet until the target size exceeds the maximum beam diameter, as shown in Fig. 2.6(b), where the 2-10 mm targets have coherence functions that are similar to (and in some cases overlapping) each other. These noiseless theoretical results indicate that both the target size and the fluence profile of the illuminating light source affect photoacoustic spatial coherence.



Theoretical photoacoustic spatial coherence functions (simulated with a Gaussian beam fluence profile with 5 mm initial beam diameter) were compared to k-Wave simulated and experimental photoacoustic coherence functions created from multiple targets sizes. The light source for the experimental data was the 5 mm-diameter fiber bundle. Fig. 2.7(a) shows the agreement between coherence functions for point targets created with theory and k-Wave in the absence of noise. Both results have relatively constant coherence across the aperture.

Fig. 2.7(b) demonstrates that the addition of noise yields a point target coherence function that decays as a function of lag. The theoretical, k-Wave, and experimental photoacoustic spatial coherence functions decrease at a similar rate as a function of lag and have qualitatively similar  $\sigma_N$  (i.e., deviation from a mean value at each lag in the coherence function).

The short-lag region was previously defined as the region of the coherence function extending to a fixed percentage the receive aperture. However, when comparing results from targets larger than a point target, we define the short-lag region as the region from lag 0 to the lag defined by the first zero-crossing of the theoretical coherence function. This new definition is introduced to account for the dependence of photoacoustic spatial coherence on both target size and the width of the light profile (demonstrated in Fig. 2.6). Our following results focus on the short-lag region.

Fig. 2.8 shows coherence functions from theoretical simulated datasets in the presence of noise compared with experimental and k-Wave results for targets with diameters of 1.3 mm and 4.5 mm. Theoretical data was simulated with a Gaussian beam fluence profile with 1 mm and 5 mm initial beam diameters, for the 1.3 mm- and 4.5 mm-diameter targets, respectively. The experimental light source was the 1 mm-diameter optical fiber and 5 mm-diameter fiber bundle for the 1.3 mm and 4.5 mm targets, respectively.

In Fig. 2.8(a), the theoretical, k-Wave, and experimental photoacoustic spatial

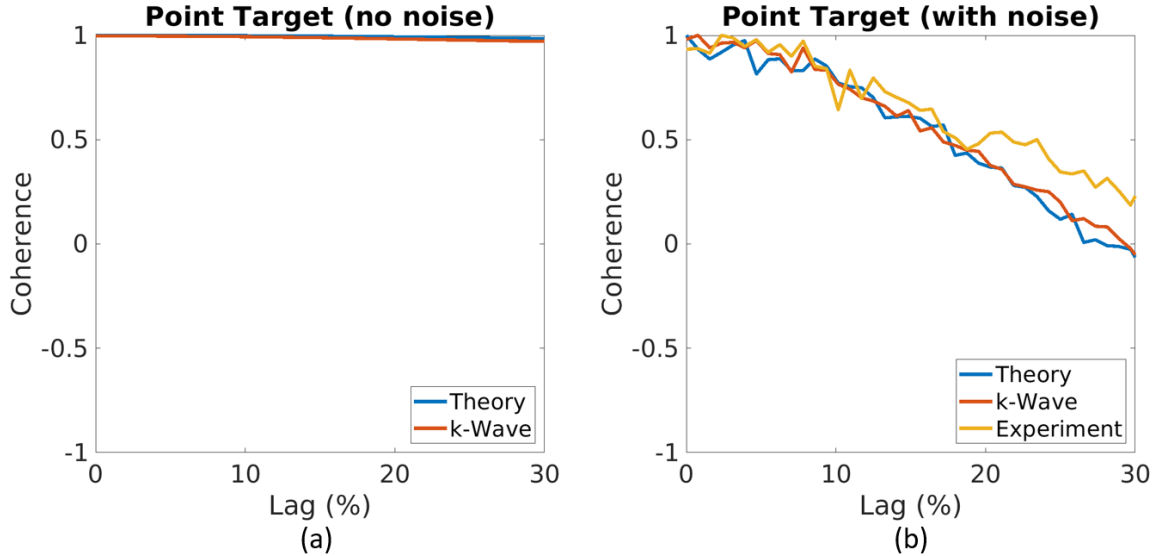


Figure 2.7: Coherence functions from a point target center. (a) Simulated point target data without noise ( $N_A = 0$ ) shows coherence functions that are relatively constant across the aperture, indicating a coherent source. (b) Simulated point target data with noise compared with experimental point target data, demonstrating partially coherent source functions when noise is present. The x-axis represents lag (i.e.,  $m$  or  $\mathbf{m}$ ) as a percentage of the receive aperture.

coherence functions have general qualitative agreement (i.e., similar rate of decrease with increasing lag and similar  $\sigma_N$ ). Fig. 2.8(b) shows a similar result for the the 4.5 mm-diameter target, as the three coherence functions generally agree in the short-lag region. However, values outside of the short-lag region, which should ideally have zero coherence in the absence of noise (as demonstrated in Fig. 2.6), produce significant deviations between datasets with values that seem to hover near zero. In addition, the experimental coherence function demonstrates what appears to be coherent reverberations artifacts at higher lags, which are not modeled in theoretical or k-Wave simulations and appear to dominate the noise described by  $\sigma_N$ .

The agreement between theoretical results and k-Wave or experimental results was quantified with the root mean square error (RMSE) of coherence function differences measured at each lag value. This RMSE was calculated separately for the short-lag region (defined as 30% of the receive aperture for the point target and the first zero-crossing for larger targets) and the long-lag region (defined as all results outside of

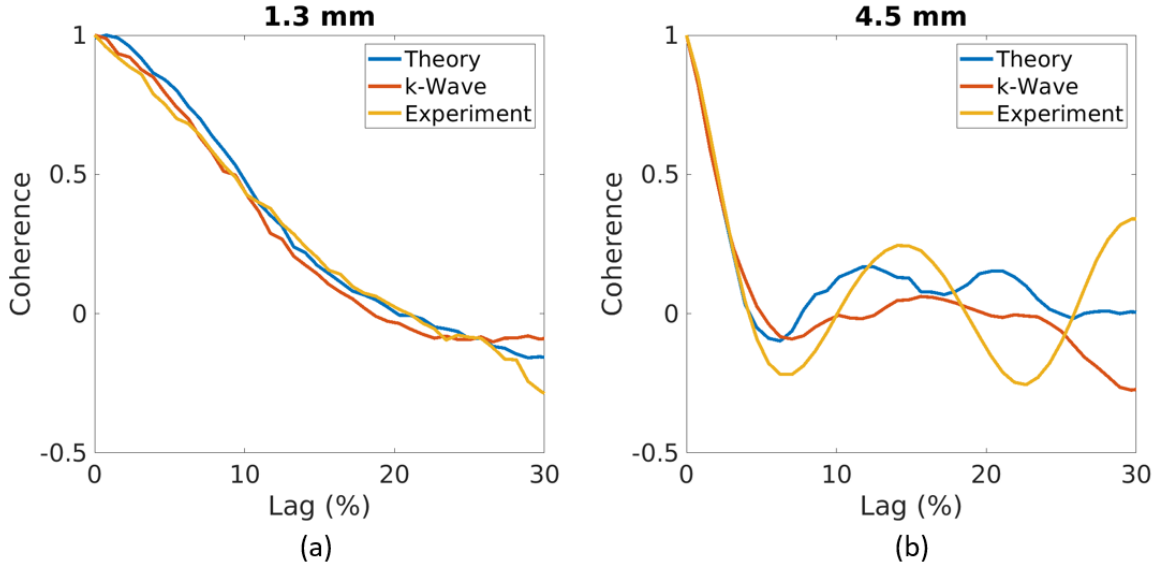


Figure 2.8: Comparison of theoretical, k-Wave, and experimental coherence functions at the location corresponding to the center of (a) 1.3 mm-diameter and (b) 4.5 mm-diameter targets. The x-axis represents lag (i.e.,  $m$  or  $\mathbf{m}$ ) as a percentage of the receive aperture.

the short-lag region), as displayed in Fig. 2.9.

Figs. 2.9(a) and 2.9(b) confirm the qualitative observation that RMSE is consistently lower in the short-lag region (RMSE  $< 0.05$  when theory is compared with k-Wave and RMSE  $< 0.1$  when theory is compared with experiment) than in the long-lag region.

### 2.4.3 Comparison of SLSC Lateral Profiles

Fig. 2.10 shows photoacoustic SLSC images and corresponding lateral profiles for a point target and 12 mm-diameter target. For the theoretical simulations, the light profiles were a Gaussian with 5 mm initial beam diameter when simulating the point target and a light sheet when simulating the 12 mm target. The experimental results for the point target and the 12 mm target were derived from the thread and *in vivo* data, respectively. The inclusion of *in vivo* data enables the comparison of images without the effects of the tubing and surrounding water previously shown in Fig.

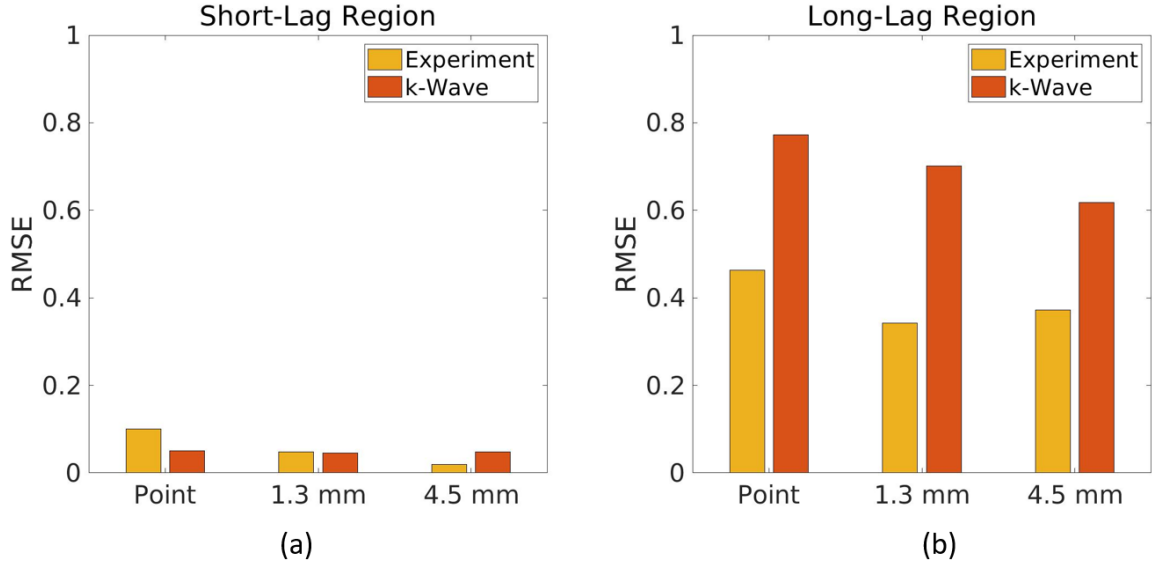


Figure 2.9: Root mean square error (RMSE) comparing both k-Wave data with noise and experimental data to theoretical coherence functions with noise in the (a) short-lag and (b) long-lag regions.

2.5. The theoretical, k-Wave, and experimental images in Fig. 2.10 generally show comparable lateral resolution for the 12 mm target. However, the k-Wave image has better resolution than the theoretical and experimental images for the point target. These similarities and differences are particularly evident with the alignment of the lateral profiles through each target center.

Fig. 2.11 shows lateral profiles for three target sizes and multiple  $M$  values. The experimental results for the point target, 4.5 mm target, and 12 mm target were derived from SLSC images of the thread, India ink, and *in vivo* hepatic blood vessel, respectively. For the point target and 4.5 mm target, theoretical data was simulated with a Gaussian beam fluence profile with 5 mm initial beam diameter. A light sheet fluence profile was used for theoretical simulations of the 12 mm target.

Some differences were required to make comparisons across theory, k-Wave, and experimental datasets in Figs. 2.10 and 2.11. For example, dynamic range was adjusted to best display amplitudes within these targets.  $M$  values were different for

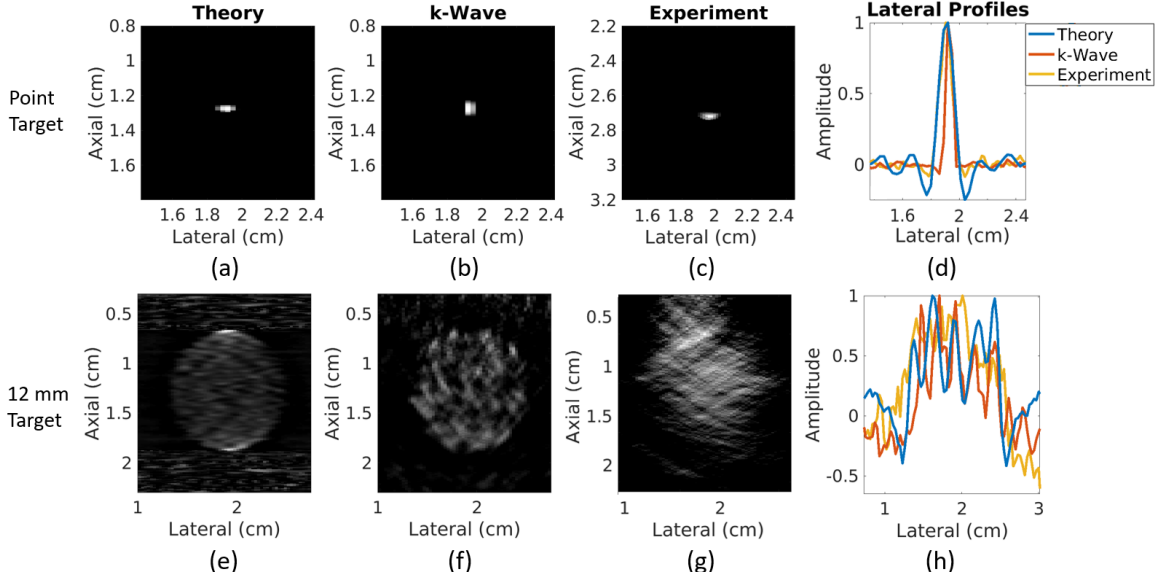


Figure 2.10: (a,e) Theoretical, (b,f) k-Wave, and (c,g) experimental photoacoustic SLSC images of a point target and 12 mm-diameter target. The experimental image of the 12 mm-diameter target is derived from the *in vivo* hepatic blood vessel data. Images are displayed with  $M = 11\%$  of the aperture, with the exception of the 12 mm *in vivo* experimental target, which is displayed with  $M = 1\%$  of the aperture. Images were normalized and thresholded to a minimum value of 0.3 in (a)-(c) and (g) and 0 in (e) and (f). (d,h) The corresponding lateral profiles demonstrate comparable resolution, target width, and coherence.

the 12 mm *in vivo* target likely due to differences in the absorber distribution in the experimental data. Lateral profiles for this target were normalized because of the large amplitude differences within the target that dominate without normalization. In addition, lateral axes were adjusted to place the target at the center. There are also differences in the absorber appearances across the three datasets in Fig. 2.10.

Despite differences in display methods and appearance, the following two trends were nonetheless observed when comparing these datasets in Fig. 2.11. First, the contrast of the point target increases with an increase in  $M$  for both simulated data with noise and experimental data. Second, a low  $M$  value (i.e., 1 - 3 % of the aperture) generally excludes high spatial frequency content from the SLSC image and results in blurred target boundaries. As  $M$  increases, more high spatial frequency content is

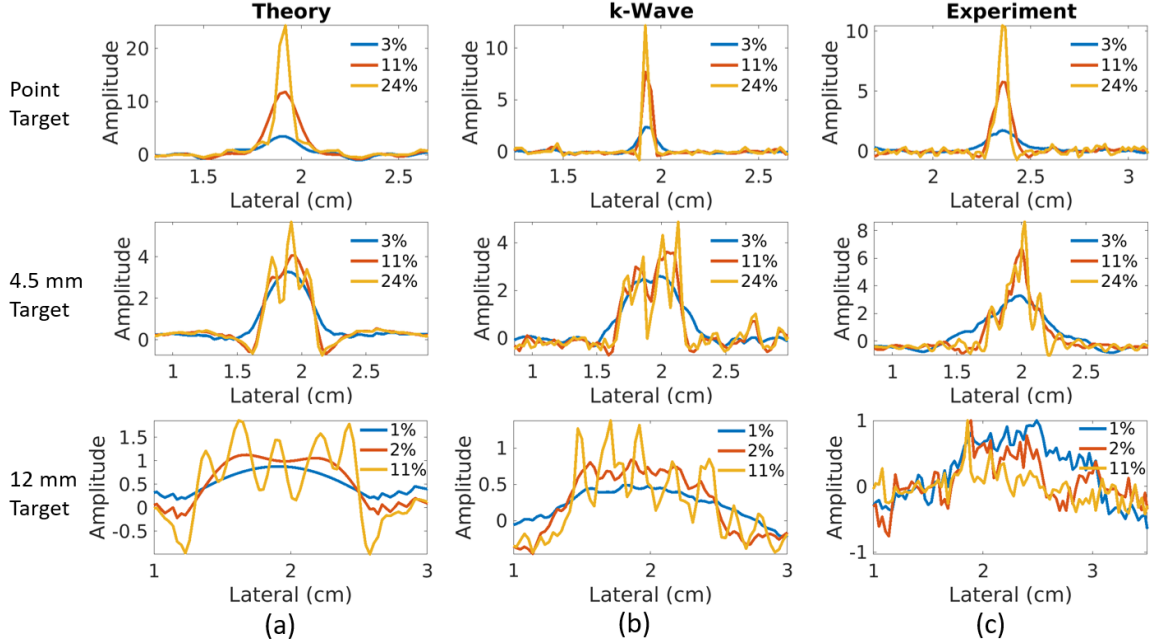


Figure 2.11: Lateral SLSC profiles at axial depths corresponding to the target center of (a) theoretical, (b) k-Wave, and (c) experimental SLSC images of the point, 4.5 mm, and 12 mm targets, each displayed with three different values of  $M$  represented as a percentage of the receive aperture. The experimental profiles are derived from SLSC images of the thread (point target), India ink (4.5 mm target), and *in vivo* vessel (12 mm target). The 12 mm *in vivo* target lateral SLSC profiles were normalized to the maximum value in each line plot.

included in the SLSC image and target boundary delineation improves.

#### 2.4.4 Effect of the Light Beam Profile on SLSC Image Contrast

Fig. 2.6 indicates that the light beam profile affects the spatial coherence function, as the narrower light profile increases the coherence length of larger targets. This trend suggests that we can improve the SLSC image contrast of larger targets by using a narrow laser beam. To explore this effect that is based on our newly derived theory, the contrast of targets in theoretical and experimental SLSC images was measured as a function of diameter, resulting in Fig. 2.12.

For the theoretical results in Fig. 2.12, the upper and lower bounds of each illumination profile width (i.e., 1 mm, 5 mm, and light sheet) correspond to the mean

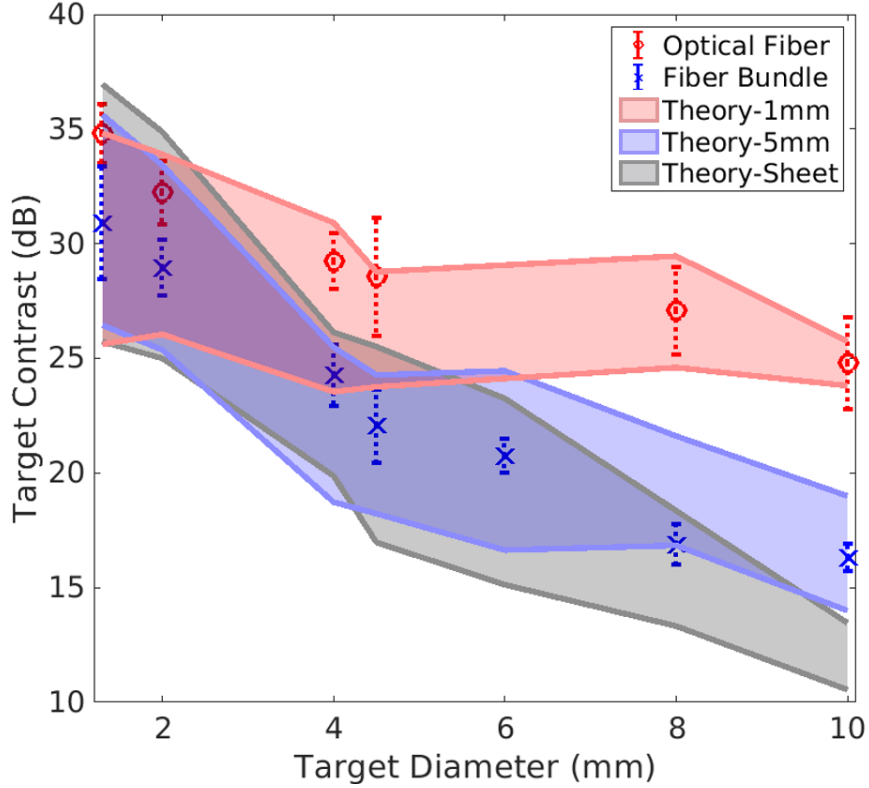


Figure 2.12: Theoretical measurements of contrast in SLSC images as a function of target diameter for three illuminating beam profiles (light sheet, 1 mm- and 5 mm-diameter Gaussian beam). These theoretical predictions in the presence of noise are compared to experimental India ink data acquired with the fiber bundle ( $\times$ ) and the optical fiber ( $\circ$ ). For the larger targets, theory and experimental data show improved contrast with the narrower illumination beam profile. All SLSC images are computed with  $M = 11\%$  of the aperture.

contrast measurements of ten theoretical simulation results with  $SNR_p = 20$  dB and  $SNR_p = 40$  dB, respectively. The target contrast with the 1 mm Gaussian beam illumination profile decreased from 25.6–35.0 dB at a target diameter of 1.3 mm to 23.8–25.2 dB as target diameter increased to 10 mm. For the 5 mm Gaussian beam illumination profile, target contrast decreased from 26.5–36.2 dB to 14.0–19.0 dB as target diameter increased. For the light sheet illumination profile, target contrast decreased from 25.7–35.4 dB to 10.5–13.7 dB as target diameter increased.

The theoretical results in Fig. 2.12 were compared to experimental photoacoustic SLSC images acquired with a 1 mm-core-diameter optical fiber (for comparison with

the 1 mm narrow-beam Gaussian profile) and a 5 mm-diameter fiber bundle (for comparison with the 5 mm broader Gaussian profile). The experimental data (shown as data points in Fig. 2.12) generally agree with the theoretical results, as the smaller light beam profiles generate images with higher contrast for the same targets. In addition, the mean contrasts for experimental datasets are within the range of the theoretical prediction for the corresponding light source. The results in Fig. 2.12 demonstrate that the SLSC image contrast of targets can be improved by limiting the illuminating beam to a size that is smaller than the target size.

#### 2.4.5 Effect of the Light Beam Profile on SLSC Image FWHM

Although SLSC image contrast can be increased by narrowing the width of the light beam profile (see Fig. 2.12), intuition suggests that only the portion of a large target that is illuminated with the narrow beam will be visible in the SLSC image. Fig. 2.13 explores this expectation with FWHM measurements of SLSC lateral profiles ( $M = 11\%$ ) created with target sizes ranging from 1.3 mm to 11 mm in diameter. Ideally, a one-to-one relationship would exist between these two measurements as indicated by the dashed line in Fig. 2.13. The upper and lower bounds of each illumination profile correspond to the mean FWHM measurements for ten theoretical simulations with  $SNR_p = 20$  dB and  $SNR_p = 40$  dB, respectively. With the light sheet illumination, the theoretical result in Fig. 2.13 generally follows the ideal expectation. When the light beam diameter is decreased to 5 mm, the measured FWHM no longer follows this ideal trend for targets  $\geq 4.5$  mm. Similarly, when the light beam diameter is further decreased to 1 mm, the theory shows more of a deviation from the ideal result. The data points in Fig. 2.13 show our experimental measurements for comparison with theoretical predictions. The experimental measurements generally follow the predicted trends.



#### 2.4.6 Optimal $M$ Value for Photoacoustic SLSC Images

The optimal choice for the number of lags summed to create SLSC images (i.e.,  $M$ ) is known to be correlated with the photoacoustic image lateral resolution (as shown in Fig. 2.11). To quantify this resolution, Fig. 2.14 shows the mean FWHM of SLSC lateral profiles of theoretical, k-Wave, and experimental point targets as a function of  $M$  with  $\pm$  one standard deviation of the mean shown as shaded error bars. A 5 mm Gaussian fluence profile was used for theoretical simulations and the 5 mm-diameter fiber bundle was used as the experimental light source. Lateral resolution generally decays as a function of the  $M$  value used to create the SLSC images. As noted in

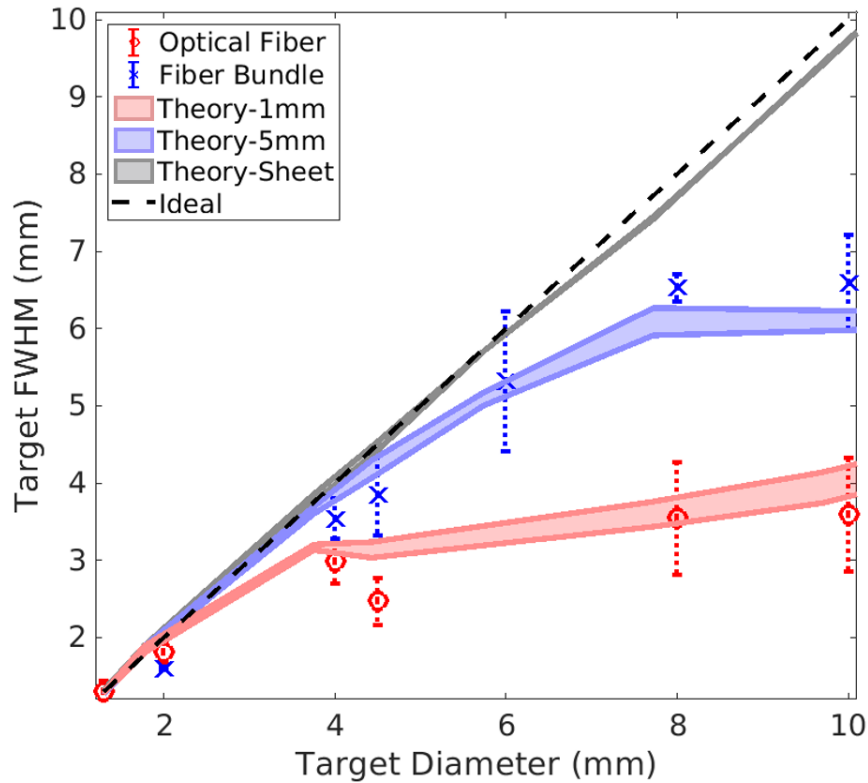


Figure 2.13: Theoretical full width at half maximum (FWHM) measurements of SLSC lateral profiles as a function of target diameter for three illuminating beam profiles (light sheet, 1 mm-, and 5 mm-diameter Gaussian beams). These theoretical predictions in the presence of noise are compared to India ink experimental data acquired with the fiber bundle ( $\times$ ) and the optical fiber ( $o$ ). The ideal 1:1 relationship is shown as a dashed line. SLSC lateral profiles were computed with  $M = 11\%$  of the aperture.

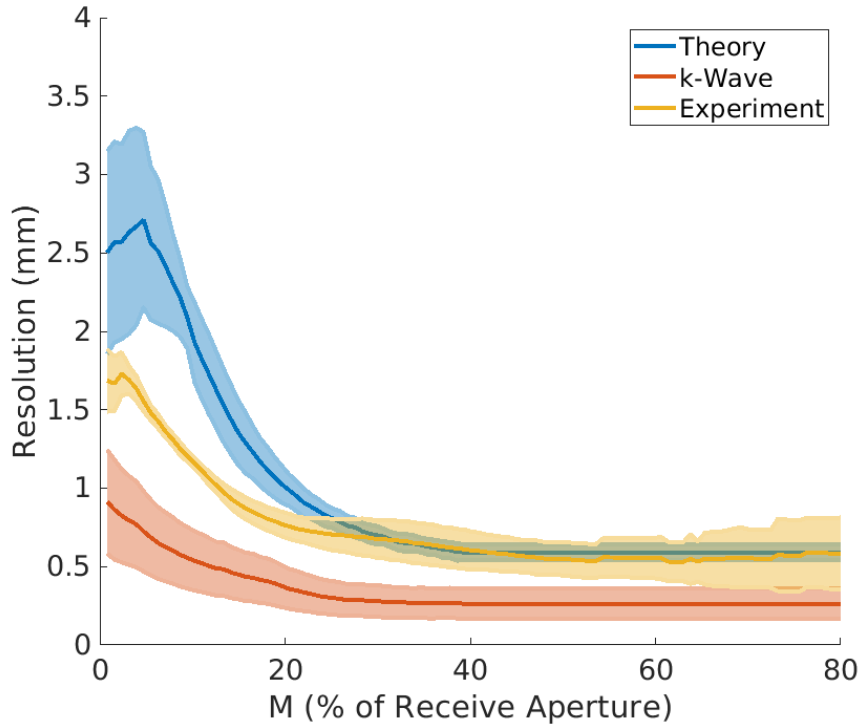


Figure 2.14: Lateral resolution calculated with theoretical, k-Wave, and experimental point target data sets as a function of  $M$ , which is represented as a percentage of the receive aperture.

Section 2.4.3, because coherence functions are a function of spatial frequency, they encode higher frequency content at higher  $M$  values resulting in SLSC images created with higher  $M$  values having improved target boundary delineation and resolution.

In Fig. 2.14, the mean lateral resolution measured with theoretical and experimental data overlap when  $M \geq 31\%$ , and the best mean lateral resolution measurements were 0.6 mm for both theoretical and experimental data, which occurred when  $M \geq 35\%$  of the aperture. Consistent with the results in Fig. 10, the best resolution was generally achieved with k-Wave simulations, which is true regardless of the  $M$  value, although the reason for this lower resolution with k-Wave results is unclear. The fundamental reason for the theoretical deviation from experimental results in the short-lag region is also unclear. However, when comparing mean theoretical results to mean experimental and k-Wave results, these deviations were  $\leq 1.1$  mm and

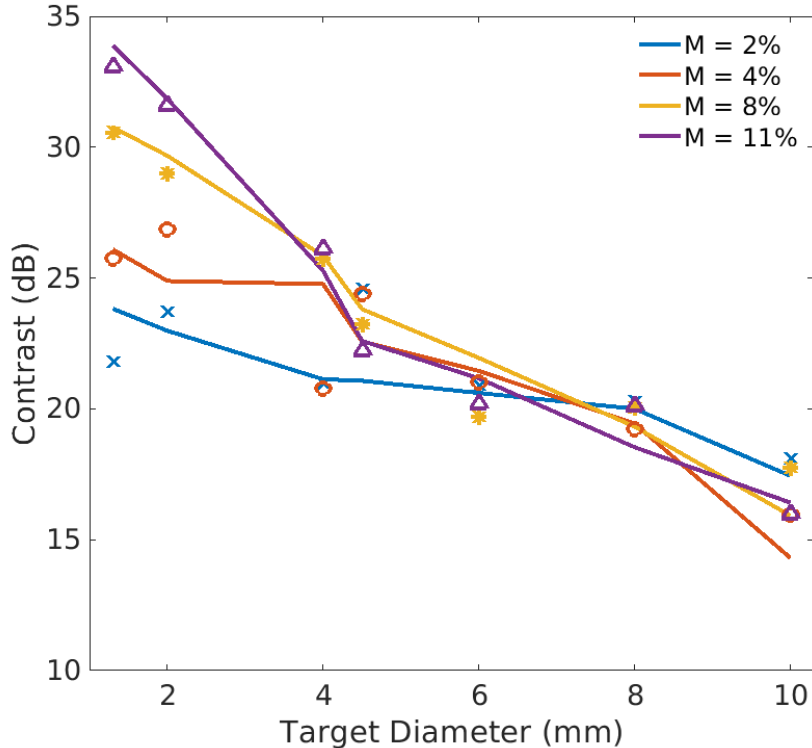


Figure 2.15: Theoretical measurements of contrast in SLSC images as a function of target diameter for four  $M$  values (2%, 4%, 8%, and 11% of the receive aperture). These theoretical predictions in the presence of noise are compared with experimental data of SLSC images displayed with the same four  $M$  values ( $\times$ ,  $o$ ,  $*$ , and  $\Delta$ , respectively).

$\leq 1.9$  mm, respectively. Despite these differences across the three datasets, there is a general trend of higher  $M$  values providing the best lateral resolution within each dataset, which is consistent with previous results [15].

The contrast of photoacoustic SLSC images was previously shown to be relatively constant as a function of  $M$  (albeit with a large standard deviation of measurements from multiple laser firings to image the same target) [15], [33]. However, lateral profiles from images of point targets (see Fig. 2.11) indicate that the optimal choice of  $M$  may depend on target size, as the smaller point target benefits from higher  $M$  values to improve target contrast. This dependence is also shown in our previous publication for multiple simulated noise levels [33].

Fig. 2.15 shows contrast as a function of target diameter for four  $M$  values (ex-

pressed as a percentage of the receive aperture) in order to compare theoretical simulations relating SLSC image contrast,  $M$ , and target size with experimental data. Theoretical predictions using a 5 mm Gaussian fluence profile are shown with solid lines, which represent the mean contrast of simulations with  $SNR_p$  values ranging 20 dB to 40 dB. Experimental results obtained with a 5 mm fiber bundle as a light source are shown as the data points with the same colors as the corresponding theoretical predictions. The 1.3 mm target achieves higher contrast at  $M = 11\%$  when compared to its contrast at  $M = 4\%$  and  $M = 8\%$ . This difference is less apparent for the 4 mm-diameter target. Discrepancies between the contrast predictions and the experimental results in Fig. 2.15 likely exist because the specific noise and absorber characteristics needed to match experimental data are unknown. Despite this discrepancy, the overall trends (i.e., higher contrast with smaller targets and larger  $M$  values) are generally consistent across either theoretical or experimental data. Thus, the presented theory can be used to predict the optimal choice of  $M$  values, based on target size, light profile diameter, and desired resolution. In general, smaller targets can be imaged with larger  $M$  values in order to boost target contrast and resolution.

## 2.5 Discussion

This work is the first to present a complete photoacoustic spatial coherence theory for point targets and moderately dense optical absorber distributions. We developed and validated our theory with experimental and k-Wave data, then explored applications of this theory to optimize photoacoustic SLSC image contrast and resolution. Due to the lower accuracy of theory-based simulations in the long-lag region than the short-lag region as shown in Fig. 2.9, we propose the use of this theoretical method primarily for predictions within the short-lag region of the acoustic receiver aperture.

The inclusion of both k-Wave and experimental data in our analyses were critical to the validation of our theoretical models for five reasons. First, the controlled

phantom experiment with varied illuminating beam diameters and target diameters enabled us to gain insights into the effects of these variables on SLSC image quality, as described in Sections 2.4.4 through 2.4.6. Second, including k-Wave data enabled us to compare theoretical simulation results to an existing simulation method for studying coherence-based beamformers for photoacoustics. Third, support for our theoretical approach was achieved by showing that we can arrive at similar conclusions with k-Wave simulations (e.g., for the short-lag region of spatial coherence functions in Figs. 2.7 and 2.8 and for SLSC lateral profiles in Figs. 2.10 and 2.11), particularly in cases where we suffered from experiment-related artifacts (such as reverberations from tubing in Fig. 2.5 or the the large amplitude differences within the *in vivo* target, which required normalization of the associated line profiles in Fig. 2.11). Fourth, the similarities achieved with k-Wave data in cases where experimental similarity was not completely achieved (e.g., Fig. 2.5) enabled us to confirm that our theoretical derivation is a viable method to study photoacoustic spatial coherence. Fifth, the inclusion of *in vivo* data enabled us to introduce more complexity than capable with our phantom setup (e.g., optical scattering, acoustic scattering, absorbers and noise sources of clinical interest) without including confounding effects from experimental tubing. This inclusion of *in vivo* data also enabled us to determine if our major conclusions would be altered for this more realistic surgical scenario. Although there were some differences (such as in the appearance of the final SLSC images in Figs. 2.5 and 2.10), these differences did not affect the theory-based insights provided in Sections 2.4.4 through 2.4.6.

Based on these insights, we conclude that there are two primary advantages of this photoacoustic spatial coherence theory. First, with the introduction of this theory, experiments are no longer necessary to explore how light profile designs will affect SLSC image contrast and resolution. A summary of the various effects that are supported by this theory include observations that SLSC image contrast can be improved

by limiting the size of the illumination beam, the lateral width of the illumination beam limits visualization of the full lateral extent of target sizes larger than the illumination beam, and smaller targets can be imaged with higher  $M$  values to improve target contrast and resolution.

The second advantage is that our theory-based method is a more direct route to create SLSC simulation images without requiring simulations of channel data received by the acoustic aperture. Based on Eq. 2.25 and with consideration that  $\lambda$  is related to temporal frequency,  $m$  is related to spatial frequency, and integration is a linear filter, the SLSC image pixel can be interpreted as a joint spatial and temporal frequency filter applied to a scaled, noisy version of the square of the traditional initial pressure distribution expression in photoacoustic imaging. Using this implementation, our theory-based methods combine the simulations of a light profile and associated pressure distribution in one straightforward step. Implementation of this theory does not require Monte Carlo simulations to model the light profile incident on the target and the associated fluence distribution within the target in order to create a custom initial pressure distribution based on the incident light profile [49].

The presented theory was derived for a moderately dense distribution of absorbers, which enabled an analogous mathematical representation to the VCZ theorem applied to pulse-echo measurements [42]. This mathematical relationship can be considered as the VCZ theorem applied to photoacoustic imaging of moderately dense absorber distributions, and it appropriately explains the inverse relationship between target size and coherence length, which ultimately affects SLSC image contrast as a function of the number of lags summed. Thus, based on this theory, it is evident that larger targets, which produce shorter coherence lengths, will have the best contrast when SLSC images are created with lower  $M$  values.

Similarly, there is an inverse relationship between the lateral width of the light profile and the coherence length, which explains why limiting the size of an illumina-

tion beam will provide higher-contrast SLSC images of targets that are larger than the beam profile. This light profile adjustment is one potential method to compensate for our inability to control target sizes in most imaging cases of interest (e.g., *in vivo* imaging) in order to produce optimal-contrast SLSC images.

Alternatively, this theory also supports an adaptive pixel-wise approach to choosing the optimal  $M$  value, which may be based on known regional target sizes and illumination profiles. For example, in photoacoustic-guided surgery, locally changing the  $M$  value with the known position of a tool tip has the potential to optimize visualization of the tool tip relative to larger anatomical structures [7]–[10]. An additional perspective is to potentially utilize the measured spatial coherence properties to predict target sizes based on the presented theory, which will be the focus of future work.

While it was previously shown that large targets containing a higher density of individual absorbers produce photoacoustic images with strong boundary contrast and minimal signal inside the target [36], [50], this representation is not shown in our theoretical and k-Wave simulation images, because the associated data sets are based on a moderately dense distribution of absorbers. In this moderately dense case, boundary signals do not dominate interior speckle and the entire target can be visualized with similar intensity throughout the target interior, as demonstrated with India ink in a 8 mm-diameter tube (Fig. 2.5) and with the 12 mm-diameter *in vivo* blood vessel (Fig. 2.10). These examples demonstrate that photoacoustic targets of interest can realistically contain a moderately dense distribution of absorbers and will not always produce signals only at the target boundaries.

As indicated by theory and confirmed with experimental measurements, there is a trade-off between target contrast and target boundary detection when optimizing the fluence profile incident on the target (see Figs. 2.12 and 2.13, respectively, which show better contrast with smaller optical beam widths and better FWHM measurements

with larger optical beam widths). This trade-off can be resolved by raster scanning a narrow light beam and combining resulting images to improve both SLSC contrast and resolution. There is also a limit to the narrowness of the light profile based on laser safety limits and the incident laser fluence (which is inversely proportional to the diameter of the incident light profile). As noted earlier, the presented theoretical expressions are advantageous as they provide a new method to explore these potential tradeoffs prior to conducting experiments. One example of an application that will benefit from this exploration of tradeoffs is the design of specialized light delivery systems that attach to surgical tools, where there is a wide range of possible configurations that are more efficient to test *in silico* compared to designing and building prototypes for experimental testing [8], [51], [52].

## 2.6 Conclusion

This manuscript describes a theoretical photoacoustic spatial coherence framework that generally agrees with experimental data from target sizes spanning point targets to a 12 mm-diameter *in vivo* target. The proposed theory and associated theory-based simulation methods offer benefits over previously available methods, including the ability to predict SLSC image contrast, lateral resolution, and lateral FWHM values based on target size and the incident light beam profile. In addition, this theory provides insights into optimizing photoacoustic SLSC image display based on light profile width, contrast, and resolution measurements. This theory also establishes a foundation for future explorations to optimize other coherence-based photoacoustic techniques.

## 2.7 Acknowledgements

This work is supported by NSF CAREER Award ECCS-1751522, NIH R00 EB018994, and NSF Graduate Research Fellowship DGE1746891. The authors thank Kelley



Kempski and Dr. Jin He for assistance with *in vivo* data collection, and Nicholas Louloudis, Sue Eller, and Ivan George for animal care and surgery support.

## References

- [1] M. T. Graham and M. A. L. Bell, “Photoacoustic spatial coherence theory and applications to coherence-based image contrast and resolution,” *IEEE Transactions on Ultrasonics, Ferroelectrics, and Frequency Control*, vol. 67, no. 10, pp. 2069–2084, 2020.
- [2] P. Beard, “Biomedical photoacoustic imaging,” *Interface Focus*, vol. 1, no. 4, pp. 602–631, 2011.
- [3] S. L. Chen, T. Ling, S. W. Huang, H. W. Baac, and J. Guo, “Photoacoustic correlation spectroscopy and its application to low-speed flow measurement,” *Optics Letters*, vol. 72, no. 2, pp. 181–204, 2010.
- [4] E. I. Galanzha and V. P. Zharov, “Photoacoustic flow cytometry,” *Methods*, vol. 57, no. 3, pp. 280–296, 2012.
- [5] E. Z. Zhang, J. G. Laufer, R. B. Pedley, and P. C. Beard, “In vivo high-resolution 3d photoacoustic imaging of superficial vascular anatomy,” *Physics in Medicine and Biology*, vol. 54, no. 4, 2009.
- [6] Y. Lao, D. Xing, S. Yang, and L. Xiang, “Noninvasive photoacoustic imaging of the developing vasculature during early tumor growth,” *Physics in Medicine and Biology*, vol. 53, no. 15, 2008.
- [7] N. Gandhi, M. Allard, S. Kim, P. Kazanzides, and M. A. L. Bell, “Photoacoustic-based approach to surgical guidance performed with and without a da vinci robot,” *Journal of Biomedical Optics*, vol. 22, no. 12, p. 121 606, 2017.

- [8] M. Allard, J. Shubert, and M. A. L. Bell, “Feasibility of photoacoustic-guided teleoperated hysterectomies,” *Journal of Medical Imaging*, vol. 5, no. 2, p. 021 213, 2018.
- [9] M. A. L. Bell, A. K. Ostrowski, K. Li, P. Kazanzides, and E. M. Boctor, “Localization of transcranial targets for photoacoustic-guided endonasal surgeries,” *Photoacoustics*, vol. 3, no. 2, pp. 78–87, 2015.
- [10] D. Piras, C. Grijzen, P. Schütte, W. Steenbergen, and S. Manohar, “Photoacoustic needle: Minimally invasive guidance to biopsy,” *Journal of Biomedical Optics*, vol. 18, no. 7, p. 070 502, 2013.
- [11] J. M. Mari, S. West, P. C. Beard, and A. E. Desjardins, “Multispectral photoacoustic imaging of nerves with a clinical ultrasound system,” in *Photons Plus Ultrasound: Imaging and Sensing 2014*, International Society for Optics and Photonics, vol. 8943, 2014, 89430W.
- [12] K. Kempfski, A. Wiacek, M. Graham, E. Gonzalez, B. Goodson, D. Allman, J. Palmer, H. H. S. Beck, J. He, and M. A. L. Bell, “In vivo photoacoustic imaging of major blood vessels in the pancreas and liver during surgery,” *Journal of Biomedical Optics*, vol. 24, no. 12, 2019.
- [13] M. Graham, F. Assis, D. Allman, A. Wiacek, E. Gonzalez, M. Gubbi, J. Dong, H. Hou, S. Beck, J. Chrispin, and M. A. L. Bell, “In vivo demonstration of photoacoustic image guidance and robotic visual servoing for cardiac catheter-based interventions,” *IEEE Transactions on Medical Imaging*, vol. 39, no. 4, pp. 1015–1029, 2020.
- [14] J. L. Su, B. Wang, and S. Y. Emelianov, “Photoacoustic imaging of coronary artery stents,” *Optics Express*, vol. 17, no. 2, pp. 19 894–19 901, 2009.

- [15] M. A. L. Bell, N. Ku, D. Y. Song, and E. M. Boctor, “Short-lag spatial coherence beamforming of photoacoustic images for enhanced visualization of prostate brachytherapy seeds,” *Biomedical Optics Express*, vol. 4, no. 10, p. 1964, 2013.
- [16] K. Hollman, K. Rigby, and M. O’donnell, “Coherence factor of speckle from a multi-row probe,” in *1999 IEEE Ultrasonics Symposium. Proceedings. International Symposium (Cat. No. 99CH37027)*, IEEE, vol. 2, 1999, pp. 1257–1260.
- [17] C. K. Liao, M. L. Li, and P. C. Li, “Optoacoustic imaging with synthetic aperture focusing and coherence weighting,” *Optics Letters*, vol. 29, no. 21, pp. 2506–2508, 2004.
- [18] S. Park, A. B. Karpouk, S. R. Aglyamov, and S. Y. Emelianov, “Adaptive beamforming for photoacoustic imaging,” *Optics Letters*, vol. 33, no. 12, pp. 1291–1293, 2008.
- [19] Y. H. Wang and P. C. Li, “SNR-dependent coherence-based adaptive imaging for high-frame-rate ultrasonic and photoacoustic imaging,” *IEEE Transactions on Ultrasonics, Ferroelectrics, and Frequency Control*, vol. 61, no. 8, pp. 1419–1432, 2014.
- [20] D. Wang, Y. Wang, Y. Zhou, J. Lovell, and J. X, “Coherent-weighted three-dimensional image reconstruction in linear-array-based photoacoustic tomography,” *Biomedical Optics Express*, vol. 7, pp. 1957–1965, 2016.
- [21] E. J. Alles, M. Jaeger, and J. C. Bamber, “Photoacoustic clutter reduction using short-lag spatial coherence weighted imaging,” in *2014 IEEE International Ultrasonics Symposium*, IEEE, 2014, pp. 41–44.
- [22] M. A. L. Bell, N. P. Kuo, D. Y. Song, J. U. Kang, and E. M. Boctor, “In vivo visualization of prostate brachytherapy seeds with photoacoustic imaging,” *Journal of Biomedical Optics*, vol. 19, no. 12, p. 126 011, 2014.

- [23] M. A. L. Bell, D. Y. Song, and E. M. Boctor, “Coherence-based photoacoustic imaging of brachytherapy seeds implanted in a canine prostate,” in *Medical Imaging 2014: Ultrasonic Imaging and Tomography*, SPIE, vol. 9040, 2014, pp. 166–171.
- [24] M. A. L. Bell, X. Guo, H. J. Kang, and E. Boctor, “Improved contrast in laser-diode-based photoacoustic images with short-lag spatial coherence beamforming,” in *2014 IEEE International Ultrasonics Symposium*, IEEE, 2014, pp. 37–40.
- [25] B. Pourebrahimi, S. Yoon, D. Dopsa, and M. C. Kolios, “Improving the quality of photoacoustic images using the short-lag spatial coherence imaging technique,” in *Photons Plus Ultrasound: Imaging and Sensing 2013*, International Society for Optics and Photonics, vol. 8581, 2013, 85813Y.
- [26] R. Kolkman, W. Steenbergen, and T. van Leeuwen, “In vivo photoacoustic imaging of blood vessels with a pulsed laser diode,” *Lasers in Medical Science*, 2006.
- [27] R. S. Hansen, “Using high-power light emitting diodes for photoacoustic imaging,” in *Medical Imaging 2011: Ultrasonic Imaging, Tomography, and Therapy*, International Society for Optics and Photonics, vol. 7968, 2011, 79680A.
- [28] T. J. Allen and P. C. Beard, “High power visible light emitting diodes as pulsed excitation sources for biomedical photoacoustics,” *Biomedical Optics Express*, vol. 7, pp. 1260–1270, 2016.
- [29] A. Hariri, J. Lemaster, J. Wang, A. Jeevarathinam, D. Chao, and J. Jokerst, “The characterization of an economic and portable led-based photoacoustic imaging system to facilitate molecular imaging,” *Photoacoustics*, vol. 9, pp. 10–20, 2018.

- [30] M. A. L. Bell, X. Guo, D. Y. Song, and E. M. Boctor, “Transurethral light delivery for prostate photoacoustic imaging,” *Journal of Biomedical Optics*, vol. 20, no. 3, p. 036 002, 2015.
- [31] M. T. Graham and M. A. L. Bell, “Theoretical application of short-lag spatial coherence to photoacoustic imaging,” in *2017 IEEE International Ultrasonics Symposium (IUS)*, IEEE, 2017, pp. 1–4.
- [32] —, “Development and validation of a short-lag spatial coherence theory for photoacoustic imaging,” in *Photons Plus Ultrasound: Imaging and Sensing 2018*, International Society for Optics and Photonics, vol. 10494, 2018, 104945K.
- [33] B. Stephanian, M. T. Graham, H. Hou, and M. A. L. Bell, “Additive noise models for photoacoustic spatial coherence theory,” *Biomedical Optics Express*, vol. 9, no. 11, 2018.
- [34] B. E. Treeby and B. T. Cox, “K-Wave: MATLAB toolbox for the simulation and reconstruction of photoacoustic wave fields,” *Journal of Biomedical Optics*, vol. 15, no. 2, p. 021 314, 2010.
- [35] X. Dean-Bean and D. Razansky, “On the link between the speckle free nature of optoacoustics and visibility of structures in limited-view tomography,” *Photoacoustics*, 2016.
- [36] Z. Guo, L. Li, and L. V. Wang, “On the speckle-free nature of photoacoustic tomography,” *Medical Physics*, vol. 36, no. 9, pp. 4084–4088, 2009.
- [37] M. Xu and L. V. Wang, “Universal back-projection algorithm for photoacoustic computed tomography,” *Physical Review*, 2005.
- [38] J.-F. Cardoso and M. Fink, “Echographic diffraction filters and the diffraction function for random media through an instantaneous time-frequency approach,” *The Journal of the Acoustical Society of America*, vol. 90, no. 2, pp. 1074–1084, 1991. DOI: [10.1121/1.402296](https://doi.org/10.1121/1.402296).

- [39] A. Derode and M. Fink, “The notion of coherence in optics and its application to acoustics,” *European Journal of Physics*, vol. 15, no. 2, pp. 81–90, 1994.
- [40] M. Fink and J.-F. C. Cardoso, “Diffraction effects in pulse-echo measurement,” *IEEE Transactions on Sonics and Ultrasonics*, vol. 31, no. 4, pp. 313–329, 1984.
- [41] K. Irisawa, T. Hirasawa, K. Hirota, K. Tsujita, and M. Ishihara, “Influence of laser pulse width to the photoacoustic temporal waveform and the image resolution with a solid-state excitation laser,” in *Photons Plus Ultrasound: Imaging and Sensing 2012*, SPIE, vol. 8223, 2012, pp. 544–551.
- [42] R. Mallart and M. Fink, “The van Cittert-Zernike theorem in pulse echo measurements,” *Journal of the Acoustical Society of America*, 1991.
- [43] J. Goodman, *Statistical Optics*. John Wiley & Sons, 2015.
- [44] N. Bottenus and K. F. Ustuner, “Acoustic reciprocity of spatial coherence in ultrasound imaging,” *IEEE Transactions on Ultrasonics, Ferroelectrics, and Frequency Control*, 2015.
- [45] D. Liu and R. Waag, “About the application of the van cittert-zernike theorem in ultrasonic imaging,” *IEEE Transactions on Ultrasonics and Ferroelectrics Frequency Control*, vol. 42, no. 4, pp. 590–601, 1995.
- [46] R. Fischer, B. Tadic-Galeb, and P. Yoder, *Optical System Design, Second Edition*. The McGraw-Hill companies, Inc., 2000.
- [47] D. K. Yao, C. Yang, K. Maslov, and L. V. Wang, “Photoacoustic measurement of the grüneisen parameter of tissue,” *Journal of Biomedical Optics*, vol. 19, no. 1, 2014.
- [48] M. A. L. Bell, Trahey, G. E., Byran, B. C., and J. J. Dahl, “Short-lag spatial coherence of backscattered echoes: Imaging characteristics,” *IEEE Transactions on Ultrasonics, Ferroelectrics, and Frequency Control*, vol. 58, no. 7, pp. 1377–1388, 2011.

- [49] S. L. Jacques, “Coupling 3d monte carlo light transport in optically heterogeneous tissues to photoacoustic signal generation,” *Photoacoustics*, vol. 2, no. 4, pp. 137–142, 2014.
- [50] X. L. Dean-Ben and D. Razansky, “On the link between the speckle free nature of optoacoustics and visibility of structures in limited-view tomography,” *Photoacoustics*, vol. 4, no. 4, pp. 133–140, 2016.
- [51] B. Eddins and M. A. L. Bell, “Design of a multifiber light delivery system for photoacoustic-guided surgery,” *Journal of Biomedical Optics*, vol. 22, no. 4, pp. 1–11, 2017.
- [52] J. Shubert and M. A. L. Bell, “A novel drill design for photoacoustic guided surgeries,” *Proc. of SPIE, Photons Plus Ultrasound: Imaging and Sensing*, vol. 10494, 2018.

## Chapter 3

# PhocoSpace: An Open-Source Simulation Package to Implement Photoacoustic Spatial Coherence Theory

*The work presented in this chapter is based on the following manuscript:*

M. Graham and M. Bell, “PhocoSpace: An open-source simulation package to implement photoacoustic spatial coherence theory,” in *2022 IEEE International Ultrasonics Symposium (IUS)*, accepted, IEEE, 2022





### 3.1 Introduction

Photoacoustic imaging relies on the photoacoustic effect, which is initiated by pulsed light incident on an optically absorbing target generating an acoustic wave through thermal expansion followed by contraction. By tuning the wavelength of the incident light to maximize the optical absorption of a target of interest, chromophores (e.g., hemoglobin in blood, lipids in atherosclerotic plaques) can be selectively visualized with high contrast [2]. However, amplitude-based photoacoustic images tend to suffer from poor image quality when there is insufficient fluence at the target depth.

Spatial coherence-based imaging techniques have been introduced to improve amplitude-based photoacoustic image quality. The majority of these techniques weight the amplitude image by measured spatial coherence values [3]–[9]. Short-lag Spatial Coherence (SLSC) beamforming, a technique initially developed for ultrasound imaging [10], differs by directly displaying measured spatial coherence values to generate an image that is independent of signal amplitude. As a result, SLSC beamforming of photoacoustic images in high noise environments demonstrates notable improvements in contrast and signal-to-noise ratios, in comparison to traditional delay-and-sum beamforming [11]–[17].

To systematically characterize these and other empirical observations surrounding the photoacoustic SLSC beamformer, we developed a photoacoustic-specific spatial coherence theory [18]. We then implemented our theory with simulations, followed by validation with experimental data from multiple photoacoustic target sizes and incident fluence profiles. In addition, we demonstrated that these simulations were useful to study a wide range of potential optimizations that would otherwise require lengthy experimental testing.

To maximize the full potential of our recently introduced spatial coherence theory, we developed PhocoSpace, an open-source toolbox to simulate and characterize

multiple possible coherence-based photoacoustic image investigations for clinical applications (e.g., blood vessel and instrument tip detection, with additional possible uses described in [19]). PhocoSpace is implemented as a MATLAB-based simulation package available at <https://gitlab.com/pulselab/phocospace>. This paper is organized as a user manual for PhocoSpace, beginning with a brief theoretical overview, followed by descriptions of the toolbox workflow with use case examples.

### 3.2 Photoacoustic Spatial Coherence Theory

To develop the photoacoustic spatial coherence theory described in [18], the photoacoustic pressure field received by a transducer,  $P$ , is modeled as a linear system, defined as:

$$P(\mathbf{X}_0, \mathbf{X}_n, f) = \chi(\mathbf{X}_0, f)A_N(\mathbf{X}_0, f)H_{rx}(\mathbf{X}_0, \mathbf{X}_n, f), \quad (3.1)$$

where  $\chi$  is the random distribution of incoherent photoabsorbers,  $H_{rx}$  is the spherical propagation of the pressure wave from the source to a point on the transducer,  $f$  is the acoustic frequency, and  $\mathbf{X}_n$  is a point on the receiving aperture.  $A_N$  is the initial pressure distribution of absorbers located at position  $\mathbf{X}_o$  in the presence of noise and is defined as:

$$A_N = \begin{cases} \mu_a \Gamma F, & N_A = 0 \\ \mu_a \Gamma F + \langle \mu_a \Gamma F \rangle N_A, & N_A \neq 0 \end{cases} \quad (3.2)$$

where  $\langle \cdot \rangle$  represents the expected value and  $N_A$  is a zero-mean, Gaussian-distributed, additive noise term which originates from random fluctuation in the source distribution (e.g., variations in the fluence at the absorber surface [20] and variations in the optical absorption within the absorber).

Photoacoustic spatial covariance,  $R_p$ , is defined as the correlation of the received

pressure field at two lateral receiving positions  $\mathbf{X}_1$  and  $\mathbf{X}_2$ :

$$R_p(\mathbf{X}_1, \mathbf{X}_2, f) = \langle P(\mathbf{X}_1, f), P^*(\mathbf{X}_2, f) \rangle, \quad (3.3)$$

where  $P^*$  represents the complex conjugate of  $P$ .

Eqs. (3.1)-(3.3) are foundational to the derivation of the following description, which predicts that photoacoustic spatial coherence is expressed as a phase term multiplied by the Fourier transform of the initial pressure distribution squared and scaled by noise terms:

$$R_p(\mathbf{m}, \mathbf{x}_k, z, f) = \frac{e^{-(j2\pi\mathbf{x}_k\mathbf{m}f)/cz}}{z^2} \int_{-\infty}^{\infty} \left[ \chi_o |\Gamma\mu_a F|^2 + 2\chi_o \cdot N_A \langle \Gamma\mu_a F \rangle^2 + \chi_o N_o |\langle \Gamma\mu_a F \rangle|^2 \right] e^{-(j2\pi\mathbf{x}\mathbf{m}f)/cz} d\mathbf{x} \quad (3.4)$$

where  $\chi_o$  is the average power of the absorber distribution,  $N_o$  is the variance of the Gaussian distribution of  $N_A$ ,  $x_k$  is the lateral shift between the lateral location of interest in the imaging plane and the center of the imaging plane,  $z$  is the depth in the imaging plane,  $c$  is the speed of sound, and  $m$  is the spatial lag between two elements on the receiving aperture.

To obtain a theoretical SLSC image, the dependence on the entire bandwidth of the transducer was included by performing the following three steps. First, Eq. (3.4) was integrated over wavelengths that correspond to the highest and lowest acoustic frequencies within the -6 dB bandwidth of a traditional ultrasound transducer frequency response (i.e.,  $f_H$  and  $f_L$ , respectively, approximating equal weights for each wavelength). Second, the result was normalized by the value obtained at lag zero (i.e.,  $K(x_k, z)$ ). Finally, we integrated over the first  $M$  lags to obtain each pixel in

the theoretical SLSC image. These three steps are defined by the equation:

$$SLSC_{pixel}(x_k, z) = \frac{1}{K(x_k, z)} \int_0^M \int_{f_L}^{f_H} R_p(m', x_k, z, f') df' dm',$$

$$\approx \frac{1}{K(x_k, z)} \sum_{m=1}^M \sum_{f=f_L}^{f_H} R_p(m, x_k, z, f). \quad (3.5)$$

### 3.3 PhocoSpace Workflow

The PhocoSpace workflow is implemented in two stages: (1) definition of imaging plane properties, followed by (2) evaluation of photoacoustic spatial coherence theory. Fig. 3.1 illustrates these two stages for an 8 mm diameter circular blood vessel target, represented as a graphical representation alongside associated MATLAB code.

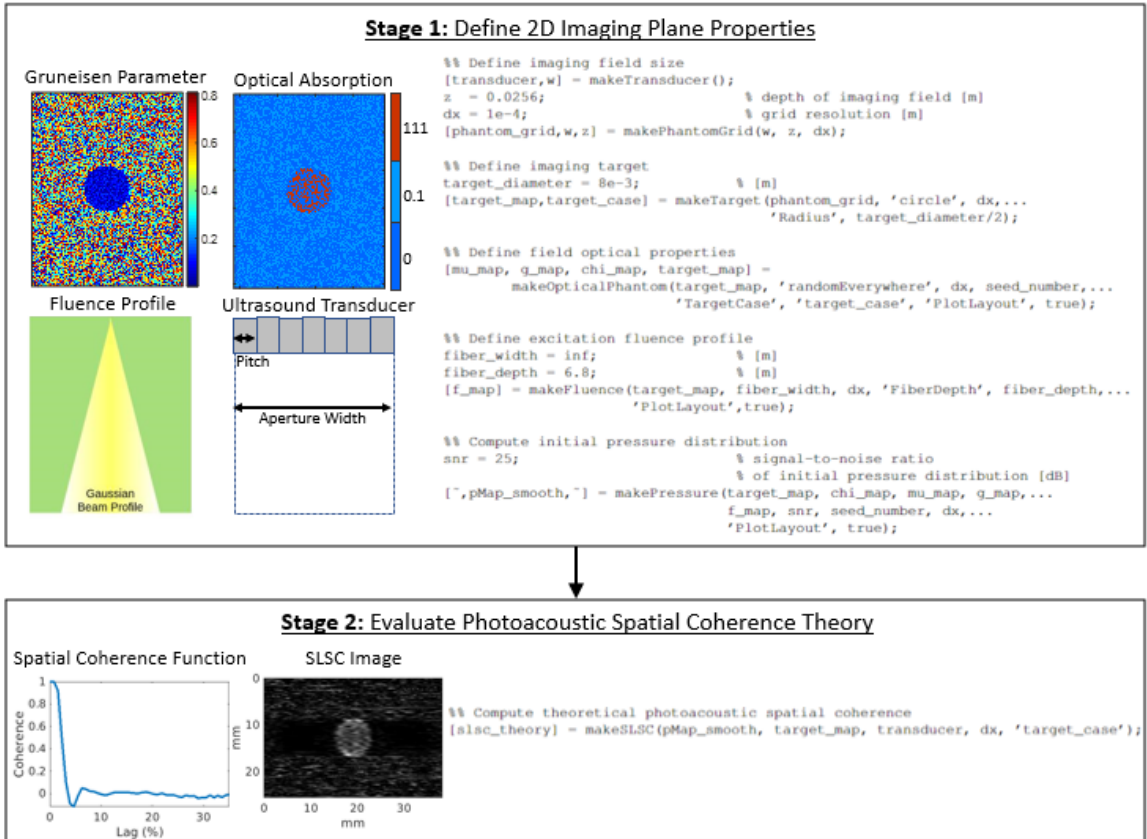


Figure 3.1: Graphical illustration and associated MATLAB code demonstrating the two-stage PhocoSpace workflow for an 8 mm diameter circular blood vessel target.

In the first stage, the lateral dimension of the imaging plane corresponds to the lateral dimension of an ultrasound transducer, and the axial dimension corresponds to image depth. User-defined properties for Stage 1 include medium characteristics (e.g., target geometry, Grüneisen parameter, optical absorption) and properties of the imaging equipment (e.g., excitation fluence profile, transducer aperture width, transducer bandwidth, transducer pitch, variance of the additive Gaussian noise). The functions used to define these properties include `makeTransducer.m`, `makePhantomGrid.m`, `makeTarget.m`, `makeOpticalPhantom.m`, `makeFluence.m`, and `makePressure.m`.

In the second stage, the properties defined in the first stage are employed to evaluate Eqs. (3.4) and (3.5) to obtain theoretical spatial coherence functions and theoretical SLSC images, respectively. These computations are executed by the function `makeSLSC.m`. Table 3.1 summarizes the fields contained within the output

Table 3.1: Summary of the fields contained within the output structure, `slsc_theory`, which is generated by the theoretical photoacoustic spatial coherence and SLSC image computation executed with `makeSLSC.m`.

Field	Description
<code>N_ele</code>	Number of elements in transducer
<code>pitch</code>	Center-to-center distance between two transducer elements
<code>freq</code>	Transducer -6 dB bandwidth array
<code>x_axis</code>	Lateral image axis array
<code>z_axis</code>	Axial image axis array
<code>cc</code>	Computed coherence functions for each lateral location at an indicated depth and for each frequency in the field "freq"
<code>cc_avg</code>	Computed coherence functions for each lateral location at an indicated depth and averaged over the transducer bandwidth
<code>slsc</code>	Computed SLSC images for each M value and for each frequency in the field "freq"
<code>slsc_avg</code>	Computed SLSC images for each M value and averaged over the transducer bandwidth

structure `slsc_theory`.

### 3.4 PhocoSpace Use Cases and Examples

#### 3.4.1 Default imaging properties and parameters

Customizations of PhocoSpace are demonstrated in the following sections, including modeling a diverse range of target geometries (Section 3.4.2), fluence profiles (Sections 3.4.3), and transducer bandwidths (Section 3.4.4). Unless otherwise noted, in each of these examples, the following eight default imaging plane definitions were employed as follows. First, an ultrasound transducer with 128 elements, 0.3-mm pitch, 3.84-cm total length, and -6 dB bandwidth of 3.75-7.0 MHz was placed at depth  $z = 0$  cm. Second, the fluence profile ( $F$ ) was a light sheet with a uniform fluence value of  $F = 5$  mJ/cm<sup>2</sup>, illuminating the entire phantom. Third, the optically absorbing targets were modeled as a distribution of randomly positioned absorbers with a spatial density of 40 absorbers per mm<sup>2</sup> within the target region. Fourth, the mean magnitude of the optical absorption coefficient ( $\mu_a$ ) was 111  $cm^{-1}$  inside the photoacoustic target (to model hemoglobin in blood), 0.1  $cm^{-1}$  outside the target (to model tissue), and 0  $cm^{-1}$  when no absorbers were present [21], as illustrated in Fig. 3.1. Fifth, the Grünesien parameter ( $\Gamma$ ) was modeled as random values ranging 0-0.81 and 0-0.144 in tissue and in blood, respectively [21], as illustrated in Fig. 3.1. Sixth, the average power of the absorber distribution,  $\chi_o$  was modeled as an arbitrary constant. Seventh, the variance ( $N_o$ ) of the added noise ( $N_A$ ) was  $8e^{-5}$ . Finally, the discrete set of frequencies indicating the -6 dB bandwidth of the frequency response of the transducer (i.e.,  $f_L = 3.25$  to  $f_H = 7.0$  MHz) were incremented using a fixed  $\Delta f = 0.25$  MHz. All SLSC images are displayed with  $M = 8\%$  of the receive aperture.

### 3.4.2 SLSC images of diverse target geometries

Fig. 3.2 shows the predicted SLSC images of the four example target geometries currently contained within the PhocoSpace package. These geometries include a 4 mm diameter circular target (`circle_4mm.mat`, Fig. 3.2(a)), a combination of six circular targets with diameters ranging 2-7 mm (`polkadots2.mat`, Fig. 3.2(c)), a model of blood vessel vasculature[22] (`vasculature_kwave.mat`, Fig. 3.2(e)), and the

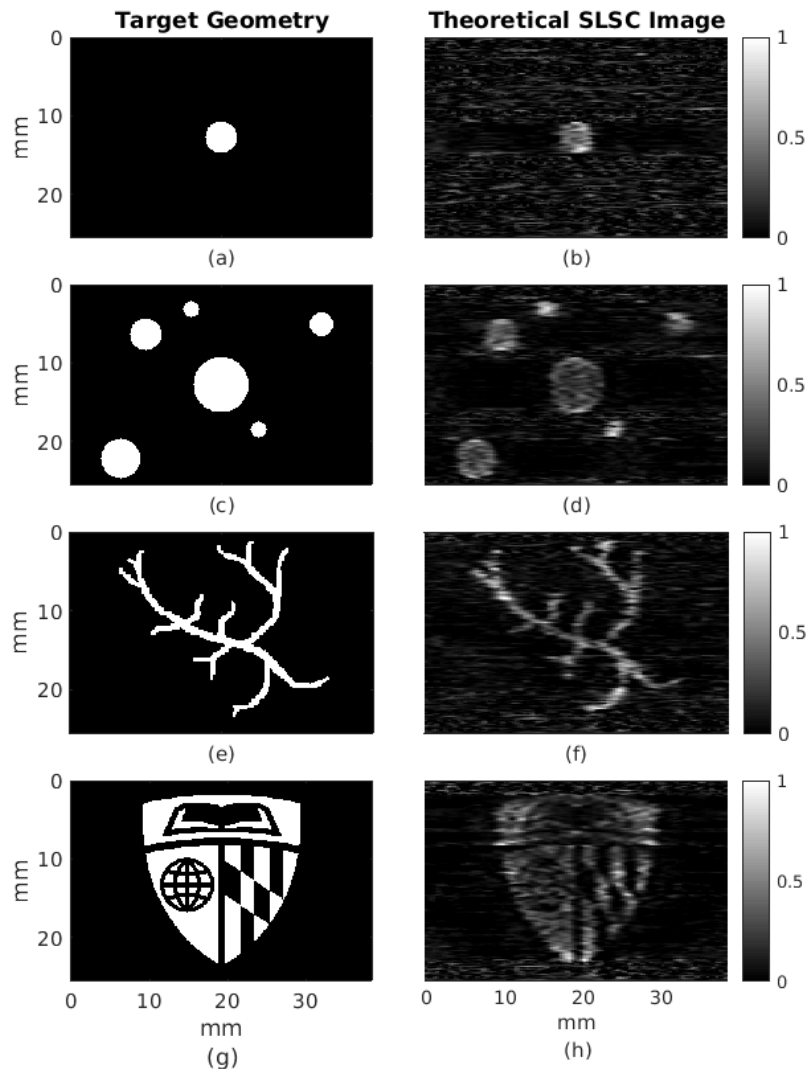


Figure 3.2: Example photoacoustic imaging target geometries and associated theoretical SLSC images computed with PhocoSpace, including (a,b) a single 4 mm diameter target, (c,d) six circular targets with diameters ranging 2-7 mm, (e,f) a blood vessel vasculature model, and (g,h) the Johns Hopkins University crest.

Johns Hopkins University crest (`jhu_crest.mat`, Fig. 3.2(g)). Corresponding theoretical photoacoustic SLSC images produced by PhocoSpace are also shown. Overall, Fig. 3.2 demonstrates the flexibility of PhocoSpace to model a wide range of target geometries, and this example may be replicated using `demonstrate_target_maps.m` in the PhocoSpace package.

### 3.4.3 Multiple customizable fluence profiles

Fig. 3.3 demonstrates the predicted SLSC images of the six-circle target geometry (Fig. 3.2(c)) when excited with four fluence profiles. These profiles include the default light sheet with uniform fluence (Fig. 3.3(a)), as well as Gaussian profiles with 25 mm (Fig. 3.3(c)), 5 mm (Fig. 3.3(e)), and 1 mm (Fig. 3.3(g)) initial beam diameters, each with 6.8 mm initial depth. The Gaussian beam profiles were simulated using the light propagation model described in [18], [23]. The associated theoretical SLSC images demonstrate the portions of the target geometries visualized with each fluence profile. Fig. 3.3 can be replicated using the example `demonstrate_fluence_maps.m` in the PhocoSpace package.

Fig. 3.4 shows predicted theoretical coherence functions of the six-circle target geometry (Fig. 3.2(c)) when excited with four fluence profiles. Specifically, the coherence functions displayed are computed at the centers of the 2 mm and 7 mm diameter targets (Figs. 3.4(a) and 3.4(b), respectively). As stated in [18], two inverse relationships exist between (1) the lateral width of the target illuminated and the coherence length (i.e., the spatial lag coinciding with the first zero crossing of the coherence function), and (2) the target size and the coherence length. These relationships are mathematically dictated by the Fourier transform in Eq. (3.4), which can be considered as the van Cittert-Zernike theorem applied to photoacoustic imaging [18], [24], [25]. As the spatial frequency term of the Fourier transform in Eq. (3.4) is encoded in the x-axes of Fig. 3.4, these coherence functions confirm that increasing



the width of the light profile or the target size (i.e., in the space dimension), decreases the coherence length (i.e., in the spatial frequency dimension). However, when the entire target width is illuminated, additional broadening of the light profile beyond the target width does not impact coherence length, as demonstrated by the overlapping coherence functions obtained with the light sheet and 25 mm Gaussian beam for each target.

Figs. 3.3 and 3.4 demonstrate that PhocoSpace successfully models multiple light

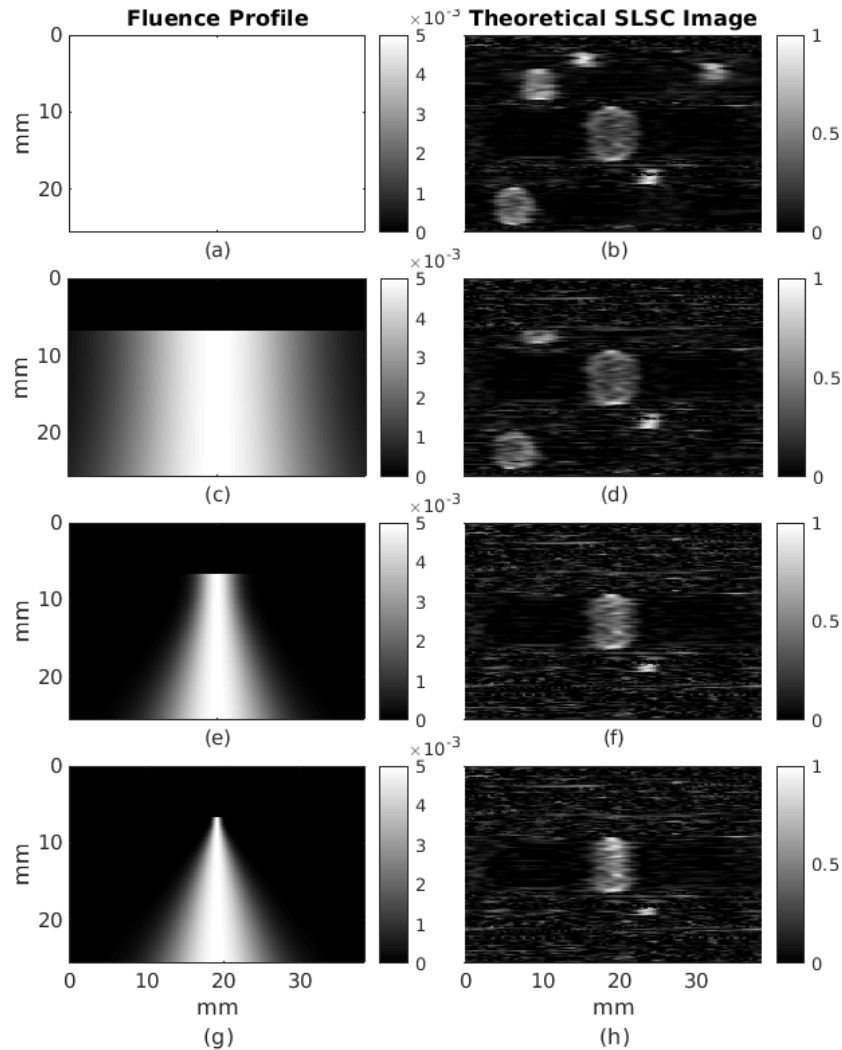


Figure 3.3: Fluence profiles and corresponding SLSC images computed with PhocoSpace, including (a,b) a light sheet with a uniform fluence value of  $F = 5 \text{ mJ/cm}^2$  and Gaussian profiles with (c,d) 25 mm, (e,f) 5 mm, and (g,h) 1 mm initial beam diameters.

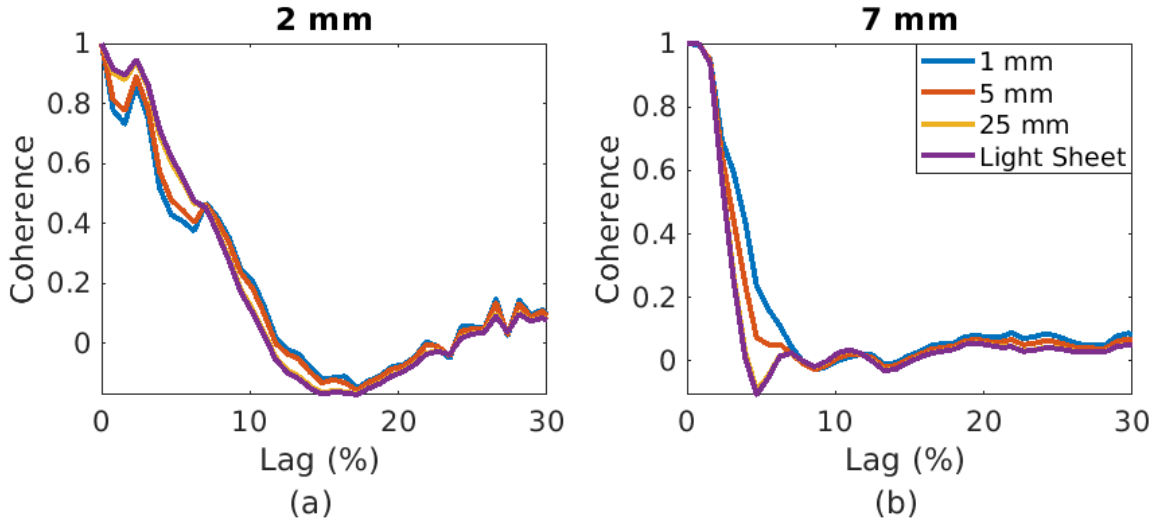


Figure 3.4: Coherence functions extracted from the center of the (a) 2 mm diameter and (b) 7 mm diameter target in the six-circle target geometry when excited with the four fluence profiles shown in Fig. 3.3.

profiles to investigate the effects of light illumination on photoacoustic spatial coherence functions and corresponding SLSC images.

#### 3.4.4 Transducer bandwidth variations

Fig. 3.5 shows the predicted SLSC images of the vasculature geometry in Fig. 3.2(e), computed with -6dB transducer bandwidths of 8-17 MHz (Fig. 3.5(a)), 3-8 MHz (Fig. 3.5(b)), and 1-5 MHz (Fig. 3.5(c)). Fig. 3.5(d) shows corresponding lateral SLSC profiles (and the lateral target geometry profile) at the location indicated by the arrows in Fig. 3.5(a), which corresponds to depth  $z = 8.1$  mm. Fig. 3.5 demonstrates that PhocoSpace successfully models the degradation of SLSC image resolution as transducer center frequency decreases, which is promising for additional customization based on common ultrasound transducer specifications. The output in Fig. 3.5 can be replicated using the example `demonstrate_transducer_bandwidth.m` in the PhocoSpace package.

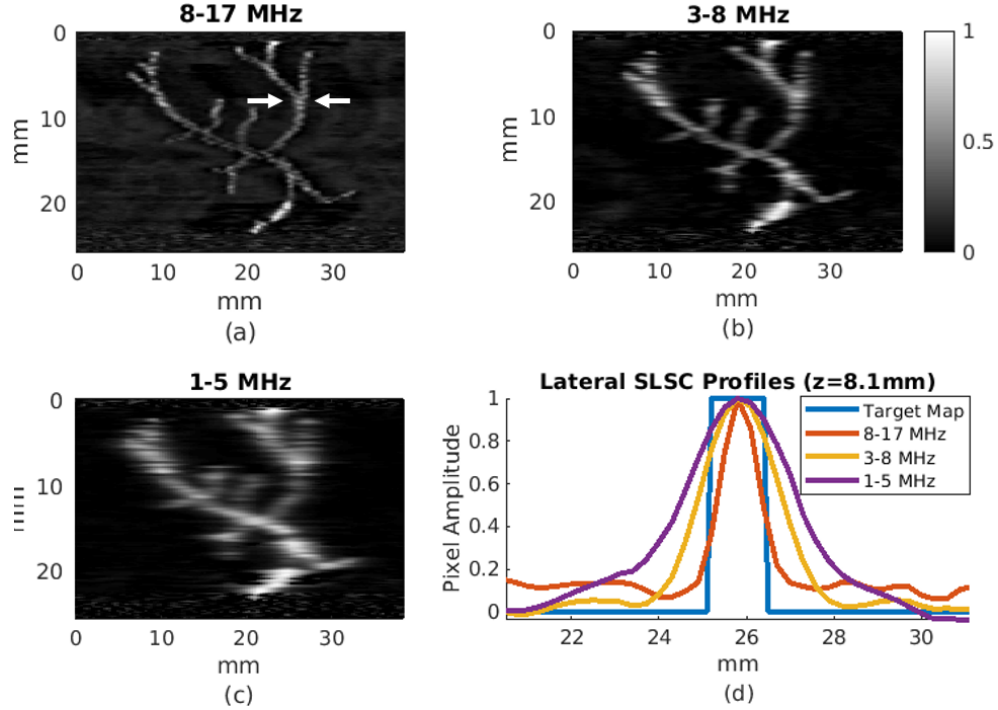


Figure 3.5: SLSC images of the vasculature target geometry shown in Fig. 3.2, computed with transducer bandwidths of (a) 8-17 MHz (12.0 MHz center frequency), (b) 3-8 MHz (5.5 MHz center frequency), and (c) 1-5 MHz (3.0 MHz center frequency). (d) Corresponding lateral SLSC profiles at the location indicated by the white arrows, compared to a lateral profile taken from the same position within the vasculature target map geometry.

### 3.5 Conclusion

Our previously derived photoacoustic spatial coherence theory established a foundation for exploration of coherence-based photoacoustic signal processing techniques without lengthy experimental testing. Based on this theory, we developed the PhocoSpace a simulation package to provide the imaging community with a flexible toolbox to execute and accelerate photoacoustic spatial coherence investigations. With customizable parameters (e.g., target geometry, incident light beam profile, transducer bandwidth), PhocoSpace is a promising approach to characterizing photoa-

coustic spatial coherence functions, photoacoustic SLSC images, and other coherence-based photoacoustic biomedical applications. Future innovations that require coherence-based photoacoustic techniques, analyses, and comparisons are additionally anticipated to benefit from this software release.

## Acknowledgments

This research is supported by NSF CAREER Award ECCS 1751522 and NSF SCH Award IIS 2014088.

## References

- [1] M. Graham and M. Bell, “PhocoSpace: An open-source simulation package to implement photoacoustic spatial coherence theory,” in *2022 IEEE International Ultrasonics Symposium (IUS)*, accepted, IEEE, 2022.
- [2] M. Xu and L. V. Wang, “Photoacoustic imaging in biomedicine,” *Review of Scientific Instruments*, vol. 77, no. 4, p. 041 101, 2006.
- [3] C. K. Liao, M. L. Li, and P. C. Li, “Optoacoustic imaging with synthetic aperture focusing and coherence weighting,” *Optics Letters*, vol. 29, no. 21, pp. 2506–2508, 2004.
- [4] M.-L. Li, H. F. Zhang, K. Maslov, G. Stoica, and L. V. Wang, “Improved in vivo photoacoustic microscopy based on a virtual-detector concept,” *Optics Letters*, vol. 31, no. 4, pp. 474–476, 2006.
- [5] S. Park, A. B. Karpiouk, S. R. Aglyamov, and S. Y. Emelianov, “Adaptive beamforming for photoacoustic imaging,” *Optics Letters*, vol. 33, no. 12, pp. 1291–1293, 2008.

- [6] Y. H. Wang and P. C. Li, “SNR-dependent coherence-based adaptive imaging for high-frame-rate ultrasonic and photoacoustic imaging,” *IEEE Transactions on Ultrasonics, Ferroelectrics, and Frequency Control*, vol. 61, no. 8, pp. 1419–1432, 2014.
- [7] D. Wang, Y. Wang, Y. Zhou, J. Lovell, and J. X, “Coherent-weighted three-dimensional image reconstruction in linear-array-based photoacoustic tomography,” *Biomedical Optics Express*, vol. 7, pp. 1957–1965, 2016.
- [8] S. Jeon, E.-Y. Park, W. Choi, R. Managuli, K. J. Lee, and C. Kim, “Real-time delay-multiply-and-sum beamforming with coherence factor for in vivo clinical photoacoustic imaging of humans,” *Photoacoustics*, vol. 15, p. 100 136, 2019.
- [9] E. J. Alles, M. Jaeger, and J. C. Bamber, “Photoacoustic clutter reduction using short-lag spatial coherence weighted imaging,” in *2014 IEEE International Ultrasonics Symposium*, IEEE, 2014, pp. 41–44.
- [10] M. A. L. Bell, Trahey, G. E., Byran, B. C., and J. J. Dahl, “Short-lag spatial coherence of backscattered echoes: Imaging characteristics,” *IEEE Transactions on Ultrasonics, Ferroelectrics, and Frequency Control*, vol. 58, no. 7, pp. 1377–1388, 2011.
- [11] M. A. L. Bell, N. Ku, D. Y. Song, and E. M. Boctor, “Short-lag spatial coherence beamforming of photoacoustic images for enhanced visualization of prostate brachytherapy seeds,” *Biomedical Optics Express*, vol. 4, no. 10, p. 1964, 2013.
- [12] M. A. L. Bell, N. P. Kuo, D. Y. Song, J. U. Kang, and E. M. Boctor, “In vivo visualization of prostate brachytherapy seeds with photoacoustic imaging,” *Journal of Biomedical Optics*, vol. 19, no. 12, p. 126 011, 2014.
- [13] M. A. L. Bell, D. Y. Song, and E. M. Boctor, “Coherence-based photoacoustic imaging of brachytherapy seeds implanted in a canine prostate,” in *Medi-*

- cal Imaging 2014: Ultrasonic Imaging and Tomography*, SPIE, vol. 9040, 2014, pp. 166–171.
- [14] M. A. L. Bell, X. Guo, H. J. Kang, and E. Boctor, “Improved contrast in laser-diode-based photoacoustic images with short-lag spatial coherence beamforming,” in *2014 IEEE International Ultrasonics Symposium*, IEEE, 2014, pp. 37–40.
- [15] B. Pourebrahimi, S. Yoon, D. Dopsa, and M. C. Kolios, “Improving the quality of photoacoustic images using the short-lag spatial coherence imaging technique,” in *Photons Plus Ultrasound: Imaging and Sensing 2013*, International Society for Optics and Photonics, vol. 8581, 2013, 85813Y.
- [16] M. T. Graham, J. Huang, F. Creighton, and M. A. L. Bell, “Simulations and human cadaver head studies to identify optimal acoustic receiver locations for minimally invasive photoacoustic-guided neurosurgery,” *Photoacoustics*, p. 100 183, 2020.
- [17] E. A. Gonzalez and M. A. L. Bell, “GPU implementation of photoacoustic short-lag spatial coherence imaging for improved image-guided interventions,” *Journal of Biomedical Optics*, vol. 25, no. 7, p. 077 002, 2020.
- [18] M. T. Graham and M. A. L. Bell, “Photoacoustic spatial coherence theory and applications to coherence-based image contrast and resolution,” *IEEE Transactions on Ultrasonics, Ferroelectrics, and Frequency Control*, vol. 67, no. 10, pp. 2069–2084, 2020.
- [19] M. A. L. Bell, “Photoacoustic vision for surgical guidance,” in *2020 IEEE International Ultrasonics Symposium (IUS)*, IEEE, 2020, pp. 1–6.
- [20] B. Stephanian, M. T. Graham, H. Hou, and M. A. L. Bell, “Additive noise models for photoacoustic spatial coherence theory,” *Biomedical Optics Express*, vol. 9, no. 11, 2018.

- [21] D. K. Yao, C. Yang, K. Maslov, and L. V. Wang, “Photoacoustic measurement of the grüneisen parameter of tissue,” *Journal of Biomedical Optics*, vol. 19, no. 1, 2014.
- [22] B. E. Treeby and B. T. Cox, “K-Wave: MATLAB toolbox for the simulation and reconstruction of photoacoustic wave fields,” *Journal of Biomedical Optics*, vol. 15, no. 2, p. 021 314, 2010.
- [23] R. Fischer, B. Tadic-Galeb, and P. Yoder, *Optical System Design, Second Edition*. The McGraw-Hill companies, Inc., 2000.
- [24] R. Mallart and M. Fink, “The van Cittert-Zernike theorem in pulse echo measurements,” *Journal of the Acoustical Society of America*, 1991.
- [25] J. Goodman, *Statistical Optics*. John Wiley & Sons, 2015.

# Chapter 4

## Integrated Simulation and Human Cadaver Head Investigations

*The work presented in this chapter was published in the following manuscript:*

M. T. Graham, J. Huang, F. Creighton, and M. A. L. Bell, “Simulations and human cadaver head studies to identify optimal acoustic receiver locations for minimally invasive photoacoustic-guided neurosurgery,” *Photoacoustics*, p. 100 183, 2020.

### 4.1 Introduction

Endoscopic transsphenoidal surgery is a minimally invasive technique frequently used to remove pituitary tumors and access the anterior skull base [2]–[4]. Instruments are inserted through the nasal cavities to drill away the posterior face of the sphenoid sinus, gain access the skull base and dura of the cavernous sinus, and resect tumors [5], [6]. This procedure is generally safe, with mortality rates of 0.2-1.2% for experienced to novice surgeons [7]. Nonetheless, critical structures such as the internal carotid arteries (ICAs), optic nerves, and cranial nerves are within millimeters of the surgical site and are therefore susceptible to iatrogenic injury at a rate of 6.8% [8], which can have surgical complications including paralysis, visual loss, stroke, cerebral spinal



fluid leaks, hemorrhage, and death [8], with morbidity and mortality rates as high as 14% and 24 - 26%, respectively, each time an accidental injury occurs [7], [9]–[11]. In addition, over 50% of patients with residual disease or growth hormone-secreting tumors undergo re-operations [12], which increases the risk to individual patients experiencing this surgery more than once in their lifetimes. Revision surgeries also tend to have increased scarring, loss of natural anatomical markers, and disruption of ICA locations, which increase the risk of surgical complications from 6.8% to 11.4% in these cases [8].

Within the surgical site, the left and right ICAs are typically separated by 1.24 - 2.67 cm [13], which highlights the tight surgical workspace and motivates the need to closely monitor the location of the ICAs. While stereotactic guidance and endoscopy are primary monitoring techniques for endonasal transsphenoidal surgeries, these techniques suffer from two known limitations. First, stereotactic guidance is subject to registration errors which can become increasingly large as patient anatomy is disrupted during surgery and as the anatomy significantly deviates from that shown in preoperative x-ray computed tomography (CT) or magnetic resonance (MR) images. The second limitation is that endoscopy is unable to identify critical structures underlying bone or other tissues in the operative path [14]. An intraoperative imaging technique that provides real-time navigation of the complex, subsurface anatomy of the anterior skull would greatly assist surgeons with avoiding severe complications caused by these two well-known limitations.

Photoacoustic imaging has been demonstrated as a promising intraoperative imaging technique for neurological and neurosurgical [15]–[21] procedures. In photoacoustic imaging, optical energy incident on an optically absorbing target is converted into acoustic energy [22]. In transcranial photoacoustic imaging, a light delivery system inserted into the nasal cavity can cause photoacoustic excitation of naturally occurring chromophores, such as hemoglobin in blood vessels and lipids within the

myelin sheath of nerves [23]. An externally placed ultrasound probe can receive the photoacoustic signals to create photoacoustic images.

Transcranial photoacoustic imaging is challenged by the reverberation, aberration, and attenuation of acoustic waves, which combine to degrade image quality. These adverse effects are primarily caused by the heterogeneity of cranial bone and the acoustic impedance mismatch between bone and cranial tissues [24]–[26]. Limited optical penetration through bone additionally complicates transcranial photoacoustic imaging [24], [27]–[29]. Image processing techniques specific to transcranial photoacoustic imaging have been developed to improve target resolution, contrast, and localization in the presence of skull bone [30]–[32].

Previous work additionally explored imaging requirements specific to applying transcranial photoacoustic imaging as an endonasal intraoperative surgical navigation technique. In these studies, blood vessel mimicking targets composed of Tygon tubing and *ex vivo* bovine blood were imaged through varying thicknesses of cranial bone in plastisol and brain tissue phantoms [16]–[19]. These studies proposed the temporal region as the location of the ultrasound probe, considering that the temporal bone is generally accepted as the ideal acoustic window for transcranial ultrasound imaging [33]. In addition, Purkayastha *et al.* [33] investigated three potential ultrasound probe locations for transcranial imaging, including the transorbital, submandibular, and suboccipital windows. To the authors’ knowledge, no similar comparative studies of external acoustic windows have been performed for transcranial photoacoustic imaging.

Considering the initially proposed temporal probe placement, minimum energy requirements for visualization of photoacoustic targets with delay-and-sum (DAS) beamforming were determined to be 1.2 - 5.9 mJ in the presence of 0 - 2 mm-thick temporal and sphenoid bones [18]. Short-lag spatial coherence (SLSC) imaging, an advanced beamforming technique previously shown to enhance target contrast when

compared to DAS beamforming [34]–[36], was applied to transcranial photoacoustic imaging when penetrating thicker bone [16], [19]. In addition, simultaneous visualization of a neurosurgery drill bit tip and phantom ICAs indicated that photoacoustic imaging has the potential to provide necessary spatial information to avoid ICA damage [18], [37], [38].

In this paper, we build on previous experimental setups by performing transcranial photoacoustic imaging with intact adult human skulls. These intact skulls provide insights into the relationships between complex bony skull anatomy and acoustic wave propagation challenges (e.g., sound reverberation and attenuation), and the effects of these challenges on photoacoustic image quality. In addition, we reassess previously defined bone thickness and contrast interrelationships and minimum energy requirements for ICA visualization in the presence of this complex skull anatomy. We also analyze the feasibility of temporal probe placement for transcranial photoacoustic imaging. Our reassessments and analyses include both amplitude-based (i.e., DAS) and coherence-based (i.e., SLSC) beamformers. An additional contribution of this paper is the first known comparative exploration of three acoustic windows for transcranial photoacoustic imaging (i.e., ocular, nasal, and temporal).

This chapter is organized as follows. Section 4.2 describes our simulation and experimental methods, including the rationale and demonstration of a novel light delivery design for clinical translation. Section 4.3 presents our results, where simulations of an empty skull serve the three-fold purpose of identifying optimal external ultrasound probe locations (Section 4.3.1.1), explaining the acoustic sound trapping observed inside the skull (Section 4.3.1.2), and analyzing the localized acoustic pressure on the surface of the skull (Section 4.3.1.3). Simulations of a fresh cadaver head were additionally implemented to perform localized acoustic pressure analyses (Section 4.3.2). A comparative experimental study with the same empty skull that was simulated is then presented to confirm simulation results showing that the nasal

cavity and ocular region are more feasible probe locations (Section 4.3.3.2) than the temple region (Section 4.3.3.1). Adding brain and eye tissue to the empty skull setup introduced additional acoustic material to confirm simulation results regarding the ocular probe location and to investigate light delivery design requirements for imaging the ICA targets within laser safety limits (Section 4.3.4). We then present results from a complete human cadaver head, which validate the ocular region as a feasible ultrasound probe location for clinical translation with our novel light delivery design (Section 4.3.5). In Section 4.4, we discuss probe location comparisons from the perspectives of image quality, image interpretability, and practical feasibility. We also discuss future opportunities and challenges for integrating optimal ultrasound probe locations into current practice. Section 4.5 summarizes our major conclusions.

## 4.2 Materials and Methods

### 4.2.1 *k-Wave Simulations*

Three-dimensional photoacoustic simulations were performed using the k-Wave toolbox [39], [40], based on CT volumes of two intact human cadaver specimens. The first specimen was an empty human skull that was cleaned from tissue attachments and provided by The Phantom Laboratory (Salem, NY). The second specimen was a fresh, formalin-fixed cadaver head obtained from the Maryland Department of Health Anatomy Board. The CT volumes of these two specimens were converted into heterogeneous density and sound speed volumetric maps to generate the simulation medium. For the empty skull specimen, the skull surface was segmented from the CT volume and acoustic sensors were distributed across the external skull surface. For the fresh cadaver head, CT images were acquired before the surgical procedure was performed, and acoustic sensors were distributed across the eyelid and eye surfaces of these preoperative images.

To illustrate the relationship between sensor and source locations and general anatomy of interest, Fig. 4.1 shows an axial slice of the simulated density distribution derived from the CT of the fresh cadaver head and annotated with anatomical landmarks, acoustic sensor locations, and photoacoustic source locations. The right and left ICAs are approximately 4 mm in diameter and reside on either side of the sella turcica, a bony saddle-like structure composed of the anterior sphenoid, the hypophyseal fossa (i.e., the depression where the pituitary gland rests), and the dorsum sellae (i.e., the bony wall dividing the sella turcica from the cranial cavity).

For each specimen simulation, photoacoustic sources were placed within the left and right ICAs. We assumed an equivalent fluence incident on each ICA, resulting in an initial pressure amplitude of 403 Pa for each source. The signal energy received by each sensor location was calculated as:

$$E_s = \sum_{n=0}^{N_t} |x(t)|^2 \quad (4.1)$$

where  $x(t)$  is the time domain pressure signal and  $N_t$  is the total simulation time in seconds. The Courant-Friedrichs-Lewy numbers (which influence simulation accuracy and overall simulation times [40], [41]) were 0.15 and 0.10 for the empty skull and cadaver head specimens, respectively. No shear waves were included in this simulation.

#### 4.2.2 Photoacoustic Imaging System

The photoacoustic imaging system used for experimental studies consisted of a Phocus Mobile laser (Opotek, Carlsbad, CA, USA) and E-Cube 12R ultrasound scanner connected to an SP1-5 phased array transducer (Alpinion Medical Systems, Seoul, South Korea). Four light delivery methods were individually coupled to the OPO output of the laser in order to investigate three system design components: (1) energy requirements, (2) ability to image within safety limits, and (3) ability to meet these

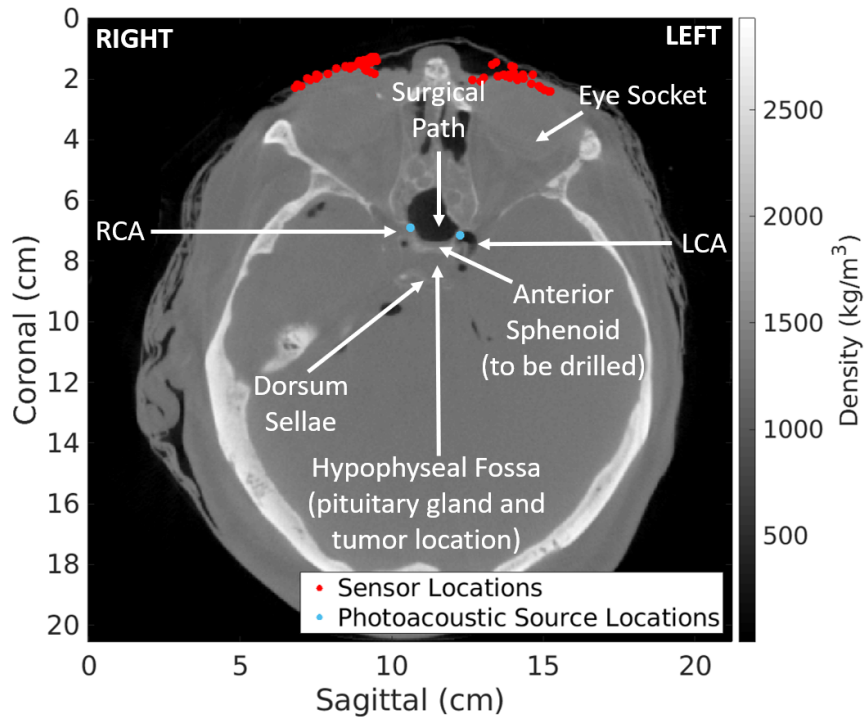


Figure 4.1: Annotated slice of the density distribution for k-Wave simulations, derived from a corresponding axial CT slice of the fresh human cadaver head. Acoustic sensors were distributed across the eyelid surfaces as shown. The location of simulated photoacoustic sources for the LCA and RCA are also shown. Each source was simulated independently.

energy and safety requirements while maintaining a sufficiently small form factor to operate within the nasal cavity.

Three of the light delivery methods were commercially available, including a 5 mm-core-diameter fiber bundle, a 1 mm-core-diameter optical fiber, and a 2 mm-core-diameter fiber bundle, as shown in Figs. 4.3(a,c), 4.3(b), and 4.3(d), respectively. The fourth light delivery method was the 2 mm-core-diameter fiber bundle, with its terminal end modified for insertion into a 1.67 cm length, 4 mm inner diameter, and 6 mm outer diameter hollow quartz tube as shown in Fig. 4.4(b) (more details about the rationale for this fourth design appear in Section 4.3.4).

The OPO of the laser was tuned to a fixed wavelength of 750 nm in order to excite deoxyhemoglobin (which we assume to be the endogenous chromophore in our experimental blood). Fig. 4.2 shows that there are multiple wavelength options to excite oxyhemoglobin in the ICAs during surgery, which has an optical absorption spectra that is orders of magnitude greater than that of other tissues surrounding the surgical site (e.g., bone, brain matter, collagen, lipids, and water [42]–[47]). At

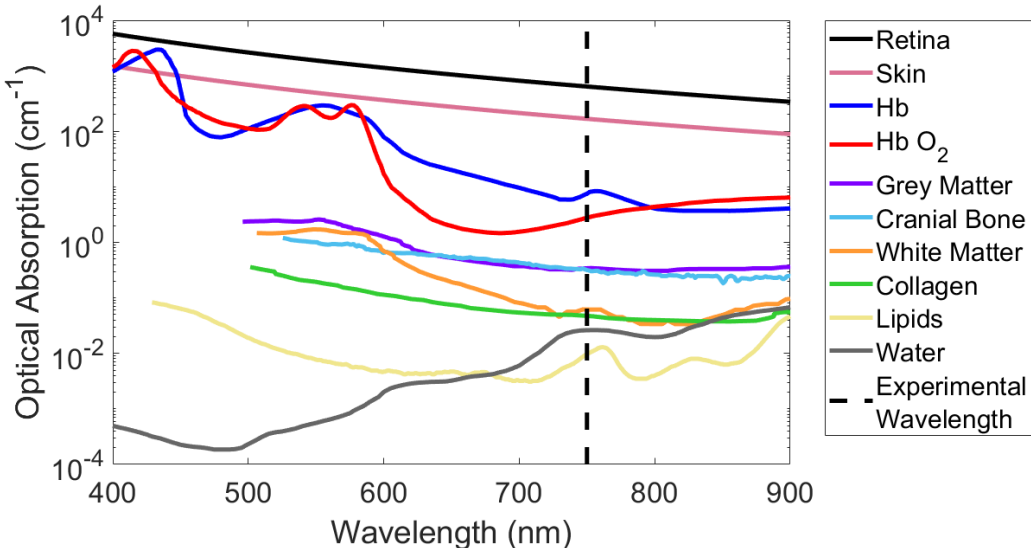


Figure 4.2: Optical absorption spectra of endogenous biological chromophores [42]–[49]. A wavelength of 750 nm was chosen to excite our experimental blood.

our chosen wavelength of 750 nm, the American National Standards Institute (ANSI) only defines the maximum permissible exposure (MPE) for two biological organs (i.e., human skin and retinal tissue). Considering the orders of magnitude higher optical absorption of retina and skin compared to other tissues within the surgical site, as shown in Fig. 4.2, the established safety limits are likely conservative for other biological tissues [42]–[50]. Therefore, we chose to benchmark our methods against the MPE for skin, which is 25.2 mJ/cm<sup>2</sup> for 750 nm light [51]. Table 4.1 summarizes the maximum allowable energy using this MPE for each light delivery method.

### 4.2.3 Intact Human Skull Experiments

#### 4.2.3.1 Pre-experiment Specimen Preparations

Experiments were performed with the intact human skull shown in Fig. 4.3 and used for the simulations described in Section 4.2.1. The anterior sphenoid bone was

Table 4.1: Summary of light delivery design parameters and corresponding maximum allowable output laser energy at the tip of each light delivery method, using a 25.2 mJ/cm<sup>2</sup> safety limit for 750 nm wavelength light. The maximum allowable energy reported for the 2 mm-core-diameter fiber bundle with quartz spacer was calculated using the area of light shown in Fig. 4.4(c).

Light Delivery Method	Outer Diameter (mm)	Numerical Aperture	Maximum Allowable Energy (mJ)
5 mm-core-diameter fiber bundle	15	0.22	4.95
1 mm-core-diameter fiber bundle	6.1	0.50	0.20
2 mm-core-diameter fiber bundle	6.8	0.22	0.80
2 mm-core-diameter fiber bundle with quartz spacer	6.8	0.22	9.32



removed to expose the skull base (as is typical in transsphenoidal procedures). Phantom ICAs were created by fixing 4 mm inner diameter Tygon tubing inside the skull in the correct anatomical location on either side of the sella turcica.

The phantom ICAs were injected with either India ink solution or whole human blood. India ink mixed with water was previously demonstrated to mimic the optical absorption of blood in the concentration range 0.03-0.13% [52], [53]. We repeated

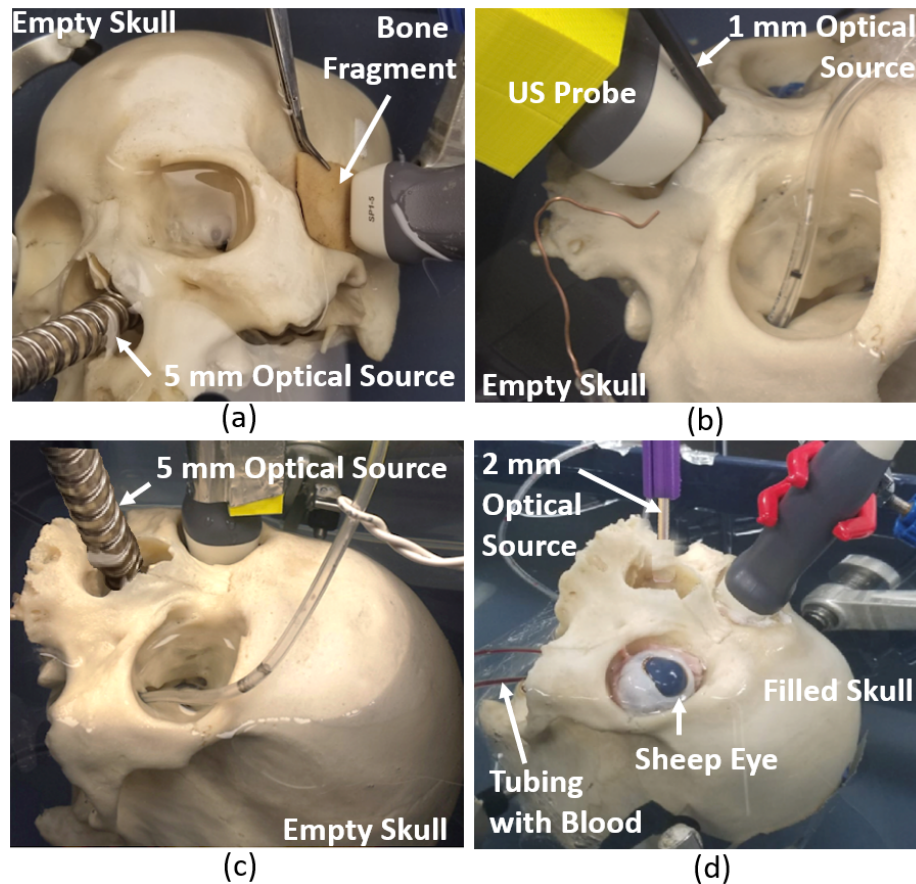


Figure 4.3: Experimental setups for the intact skull, cleaned from tissue attachments. (a) Empty skull with the 5 mm-core-diameter fiber bundle as the optical source and the ultrasound probe placed on the 1 mm-thick temporal bone fragment. (b) Empty skull with the 1 mm-core-diameter optical fiber as the optical source and the ultrasound probe placed on the nasal cavity. (c) Empty skull with the 5 mm-core-diameter fiber bundle as the optical source and the ultrasound probe placed on the right ocular region. (d) Skull filled with brain tissue and eye sockets filled with ovine eyes with the 2 mm-core-diameter fiber bundle as the optical source and the ultrasound probe placed on the right ovine eye. The Tygon tubing was filled with whole human blood for this experiment.

similar experiments to determine the concentration that matched the contrast of photoacoustic signals originating from the whole human blood of Johns Hopkins Hospital patients (with approval from the Institutional Review Board), and determined that 0.5% India ink solution provided the best match. Therefore, to perform the experiments described in Sections 4.2.3.2 and 4.2.3.3, a solution of 0.5% India ink and water was injected into the phantom ICAs. To perform the experiments in Section 4.2.3.4, the phantom ICAs were injected with whole human blood from Johns Hopkins Hospital patients.

For each experiment described in Sections 4.2.3.2 - 4.2.3.4, the prepared skull was fixed in a Mayfield clamp and submerged in a water bath for acoustic coupling. The skull was degassed for 30 minutes after submersion and prior to imaging. In addition, the chosen light delivery method was inserted into the nasal cavity to illuminate the phantom ICAs.

#### 4.2.3.2 Temporal Bone Feasibility Study

Building on the previous work of Bell *et al.* [18], which demonstrates an experimental phantom study to image blood through 0 - 2.5 mm-thick temporal bone fragments in the presence of ovine brain tissue, we performed a similar study with the intact human skull. The purpose of our study was to reassess energy requirements for transcranial photoacoustic imaging of phantom ICAs in this more complex acoustic environment.

In addition to the anterior sphenoid bone removed from the intact skull, a 2 cm x 3 cm region of the temporal bone was removed from this skull via a middle fossa craniotomy to create a variable thickness temporal bone window. This variable thickness window was created by covering the area of the removed bone window with one of five approximately 3 cm x 3.3 cm human cadaver skull bone fragments, as shown in Fig. 4.3(a). The skull fragments were cut from formalin-fixed temporal

bone specimens, manually cleaned from tissue attachments, and sanded to a desired thicknesses. The thickness of each fragment measured 0 mm (no fragment present), 1.0 mm, 1.3 mm, 3.0 mm, or 4.4 mm. For each thickness, the ultrasound probe was fixed in the same location, as shown in Fig. 4.3(a), to control the thickness of the transcranial acoustic pathway for this systematic study.

The 5 mm-core-diameter fiber bundle was inserted in the nasal cavity, as shown in Fig. 4.3(a). The following pulse energies were emitted from the tip of the fiber bundle for each temporal bone thickness: 0.08, 0.28, 4.20, 11.0, 21.0, 34.0, 47.0, 61.0, and 75.0 mJ. For this study, results are reported as functions of the five temporal bone thicknesses and these nine laser energies.

#### *4.2.3.3 Probe Location Comparison*

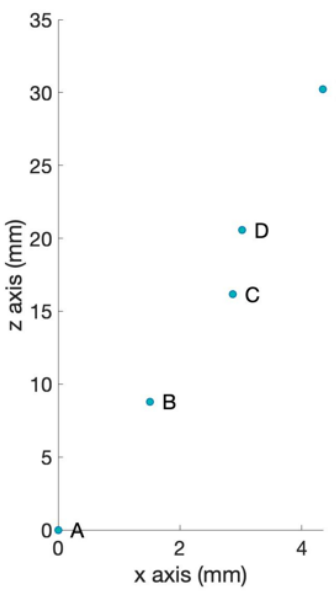
To experimentally confirm results from the k-Wave simulations described in Section 4.2.1, the ultrasound probe was placed on two additional regions of the intact skull: (1) the nasal cavity and (2) the ocular region, as shown in Figs. 4.3(b) and 4.3(c), respectively. These two additional probe locations were investigated prior to drilling away the temporal bone for the study described in Section 4.2.3.2. Due to space constraints, the 1 mm-core-diameter fiber was utilized to image through the nasal cavity, with an energy limited to 3 mJ per pulse at the fiber tip. Otherwise, the 5 mm-core-diameter fiber bundle was utilized, and it emitted 5 mJ per pulse for the ocular probe location. The results from these ocular and nasal probe placements were compared to results obtained from the study described in Section 4.2.3.2, with the thickness of the temporal bone window fixed at 1 mm and the laser energy fixed at 4.2 mJ per pulse.

#### 4.2.3.4 *Ocular Imaging Experiments with Filled Skull*

To assess the combined impact of tissue attenuation, space constraints, and fluence limits on photoacoustic image quality and their relationship to light delivery design requirements, ovine brain tissue was placed to fill the frontal cranium, ovine eyes were placed in the ocular region, and whole human blood was injected into the phantom ICAs, as shown in Fig. 4.3(d). The drilled away anterior sphenoid bone was used as a variable thickness sphenoid window by covering the area with one of five total 1.5 cm diameter circular human cadaver skull bone fragments which were prepared using the same methods as the fragments described in Section 4.2.3.2. The thickness of each fragment was 0 mm (no fragment present), 0.5 mm, 1.3 mm, 2.1 mm, or 3.3 mm.

The light delivery system was downsized from the 5 mm-core-diameter (15 mm-outer-diameter) fiber bundle to the 2 mm-core-diameter fiber bundle to enable navigation in the average adult nasal cavity for this experiment. In order to explore the feasibility of obtaining suitable images while maintaining laser safety limits with this smaller light delivery system, the laser spot size incident on the tissue was increased by increasing the distance between the laser tip and sphenoid bone surface. For repeatable laser tip placement, this fiber bundle was affixed to the end effector of a UR5e robot arm (Universal Robots Company, Odense, Denmark). After touching the sphenoid bone, the laser tip was retracted, pausing at the five waypoints listed in Table 4.2. This table cross-references waypoint locations, their associated spot sizes incident on the sphenoid bone (calculated using geometrical optical principles), and maximum allowable energy output per pulse. At each waypoint and each sphenoid bone thickness, the RCA was imaged with the following pulse energies: 0.10 mJ, 0.90 mJ, 1.30 mJ, 2.20 mJ, 5.40 mJ, 7.50 mJ, 10.6 mJ and 13.8 mJ. For this experiment, results are reported as functions of sphenoid bone thickness, waypoint positions, and the eight laser energies.

Table 4.2: Summary of the five waypoints investigated during the skull experiment with brain tissue, including x-z coordinates with respect to sphenoid bone surface, Euclidean distance between each waypoint and the sphenoid bone surface, calculated laser spot diameter incident on sphenoid surface (based on geometrical optical principles), and the resulting maximum allowable energy.

Laser Tip Location	Waypoint	Laser Tip to Sphenoid Bone Distance	Laser Spot Diameter (cm)	Maximum Allowable Energy (mJ)
	E	3.05 cm	1.02	25.57
	D	2.08 cm	0.55	13.93
	C	1.64 cm	0.39	9.80
	B	0.89 cm	0.18	4.43
	A	0.00 mm	0.03	0.80

#### 4.2.4 Fresh Cadaver Head Studies

Experiments with a complete human cadaver head were performed to test the translatability of results from the experiments described in Sections 4.2.1 - 4.2.3. After obtaining CT images and noticing air cavities in the ICAs of this cadaver head (e.g., see Fig. 4.1), an additional 10 - 14 mL of whole human blood was injected in each ICA, superior to the common carotid. These carotid arteries in the neck were sutured after this injection. An endonasal surgery was performed on this fresh human cadaver head in order to expose the anterior face of the sphenoid bone.

After fixing the cadaver head in a Mayfield clamp, a 3 mm diameter, 30 degree

nasal endoscope (Karl Storz, Tuttlingen, Germany) was inserted into the sphenoid sinus to produce the image shown in Fig. 4.4(a). This image is annotated to highlight sphenoid bone that would be removed in a surgical procedure to access the skull base. Similarly, the white bounded areas highlight the visually determined locations of the LCA and RCA, which have an intracarotid distance of 1.5 cm and are covered by 0.8 - 1.4 mm-thick and 1.1 - 2 mm-thick bone, respectively, as measured in the preoperative CT images. These ICAs were visually identified using anatomical landmarks and the subtle color visible through the thin bone covering these ICAs.

The 2 mm-core-diameter fiber bundle terminated with the quartz tube (mentioned in Section 4.2.2 and shown in Fig. 4.4(b)) was inserted through the nasal cavity, stopping at the anterior face of the sphenoid bone in the sphenoid sinus, as shown in Fig. 4.4(a). Without the quartz spacer, this fiber bundle is limited to a maximum energy of 0.80 mJ per pulse at the fiber tip in order to operate within safety limits, as indicated in Table 4.1. However, the results in Section 4.3.4 describe that 2.2 mJ per pulse is the minimum energy for ICA visualization with the ocular probe position. Therefore, the quartz spacer was added to increase the incident  $1/e$  spot area to  $0.37 \text{ cm}^2$  at the spacer tip, as shown in Fig. 4.4(c). This spot size was measured with a beam profiler (Edmund Optics, Barrington, New Jersey, USA) and allows a maximum operable energy of 9.32 mJ per pulse to satisfy laser safety limits. Therefore, the threefold purpose of the spacer is to provide a physical barrier to ensure that the desired distance is maintained, decrease the likelihood of exceeding safety limits, and relieve the operator from the burden of manually maintaining a minimum spot size without the spacer, which overall improves device safety and usability.

The fiber bundle was positioned to independently illuminate the left and right ICAs, as shown in Fig. 4.4(a) for the RCA. The laser energy was varied from 0.9 to 13.1 mJ. The ultrasound probe was placed on either the left or right closed eyelid of the human cadaver head.

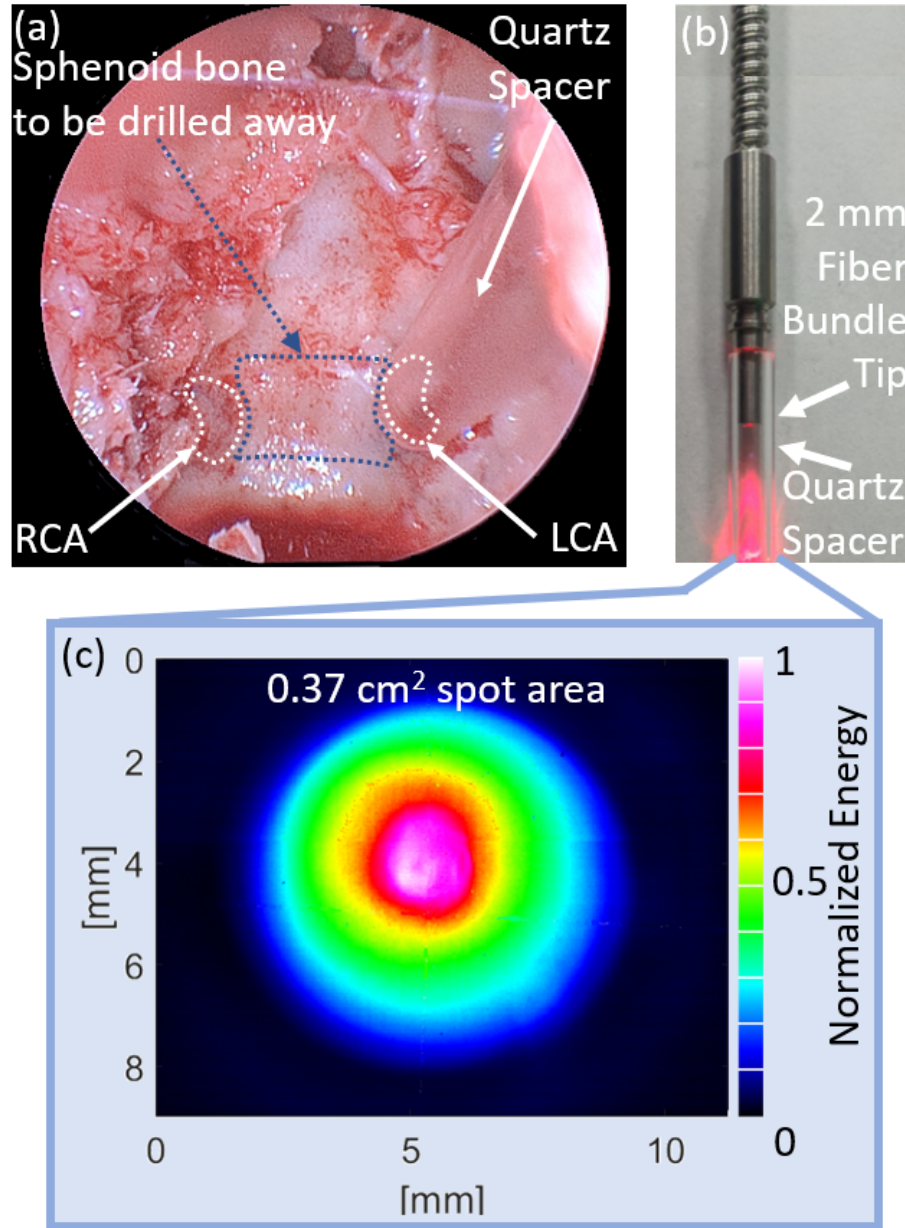


Figure 4.4: (a) Endoscopic image of the sphenoid sinus of the fresh cadaver head. The left and right carotid arteries (LCA and RCA, respectively) are located on either side of the sphenoid bone to be removed. The quartz spacer attached to the terminal end of the fiber bundle is visualized in the endoscopic field of view and is directed to illuminate the RCA. (b) Photograph of the 2 mm-core-diameter fiber bundle with quartz spacer, emitting 690 nm light (for visualization only). (c) Expected beam profile incident on the sphenoid surface when emitting 750 nm light during the fresh cadaver head experiments.

#### 4.2.5 Validation with CT Registration

The signals in the photoacoustic images obtained during the experiments described in Sections 4.2.3-4.2.4 were validated using CT registration. Ultrasound images were acquired for anatomical reference after each photoacoustic image acquisition. The CT slices corresponding to the ultrasound imaging planes in the empty skull, filled skull, and fresh head experiments were manually extracted from the CT volume based on an estimate of the ultrasound probe imaging plane used in each experiment. Anatomical features in ultrasound images were then used to perform landmark registration between ultrasound images and CT slices using 3D Slicer [54]. This ultrasound-to-CT image registration was sufficient to produce the final photoacoustic-to-CT image registration, because photoacoustic imaging utilizes the same acoustic receiver and therefore, the resulting photoacoustic images are inherently co-registered to the ultrasound images.

#### 4.2.6 Image Quality Metrics

Photoacoustic images were reconstructed with DAS and SLSC beamformers. Photoacoustic DAS and SLSC image contrast was measured for experimental images, defined as follows:

$$\text{Contrast} = 20 \log_{10} \left( \frac{\mu_t}{\mu_b} \right) \quad (4.2)$$

where  $\mu_t$  and  $\mu_b$  are the mean values within rectangular regions of interest (ROIs) corresponding to the photoacoustic signal and background regions of the beamformed data. The signal ROI was centered on the brightest pixel in the photoacoustic image. The rectangular ROI size was chosen to encompass the photoacoustic signal (i.e., approximately 2 mm x 0.7 mm). Each background ROI was the same size as the signal ROI and laterally shifted by 21 - 29 mm from the signal ROI. Visual inspection confirmed that the background ROIs primarily contained photoacoustic signals



representative of the electronic noise of the system. When analyzing photoacoustic image contrast as a function of pulse energy, ROIs were selected once for each bone thickness, using the photoacoustic image acquired with the highest pulse energy. This selection was then maintained for the remaining pulse energies.

Each photoacoustic image was normalized by the brightest pixel and displayed with -10 dB dynamic range. The short-lag value  $M$ , which is described in more detail in previous papers [34], [55] was fixed at 15 for the SLSC images (i.e., 23% of the receive aperture). A minimum target contrast of 5 dB for DAS beamformed images was determined to be the threshold for ICA visualization in each DAS beamformed image. Similarly, contrast thresholds of 10 dB and 5 dB were visually determined from SLSC images of the intact human skull and fresh cadaver head, respectively. Plots of contrast as a function of energy for each temporal or sphenoid bone thickness were used to determine the minimum energy required for visibility by selecting the minimum tested pulse energy at which contrast exceeded the threshold in each plot.

### 4.3 Results

#### 4.3.1 *k*-Wave Simulations of Empty Skull

##### 4.3.1.1 Identification of Potential Ultrasound Probe Locations

Fig. 4.5(a) shows the maximum pressure received by each acoustic sensor distributed across the empty skull surface at the completion of the simulation. Fig. 4.5(b) summarizes this result by showing the locations of sensors that received a maximum pressure signal greater than or equal to 3% of the initial source pressure. The regions on the skull surface which met this pressure threshold were the nasal, ocular, and temple regions, which received 9.2%, 4.7%, and 3.8% of the initial photoacoustic pressure, respectively. These regions were identified as potential ultrasound probe locations.

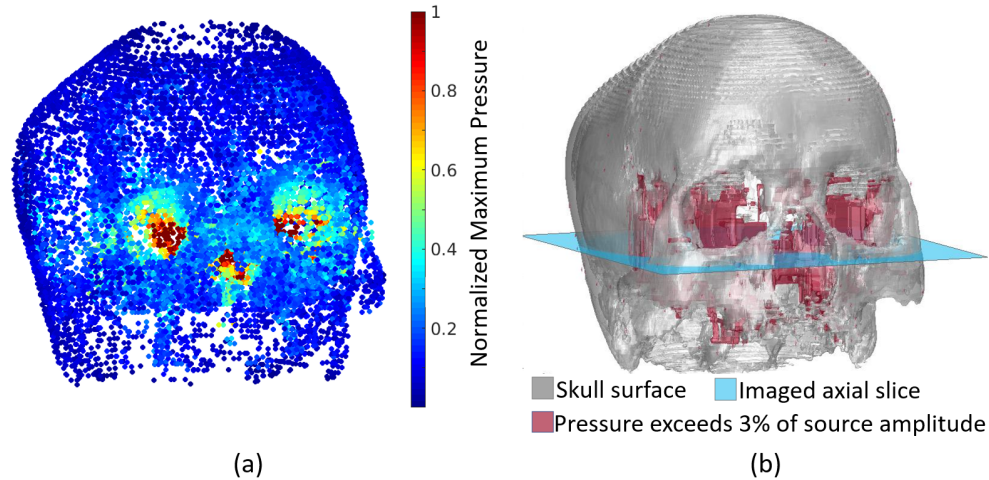


Figure 4.5: (a) k-Wave simulation results from acoustic sensors distributed across the external surface of the empty skull, showing the maximum pressure received by each sensor (over the entire simulation duration). (b) Summary of the maximum pressure received by each sensor exceeding 3% of the initial source pressure, mapped as red-shaded surfaces on the 3D CT reconstruction. The axial plane intersecting the nasal cavity corresponds to the image plane of Fig. 4.6.

#### 4.3.1.2 Acoustic Signal Trapping Due to Skull Anatomy

Fig. 4.6 demonstrates how the complex bony anatomy of the empty skull affects the propagation of acoustic waves. At time  $t_0$ , the axial slice through the simulation medium shows the circular cross-sections of the two initial pressure distributions located at the position of the ICAs. At time  $t_1$ , the pressure from the LCA and RCA propagated spherically outward from the initial location, and an acoustic reflection from the right anterior sphenoid region of the sella turcica is also observed. At time  $t_2$ , multiple acoustic reflections are observed, primarily originating from the anterior sphenoid bone and dorsa sellae, which reflect the acoustic signal back into the hypophyseal fossa. The reflected waves from the rounded edges of the dorsa sellae were observed to be spherically propagating as if the reflective surface were another photoacoustic source, which is an expected source of artifacts in photoacoustic images. In addition, these reflections trap acoustic signal in the sella turcica, and acoustic signal attenuates as it reverberates within the sella turcica. At time  $t_3$ , photoacoustic signals

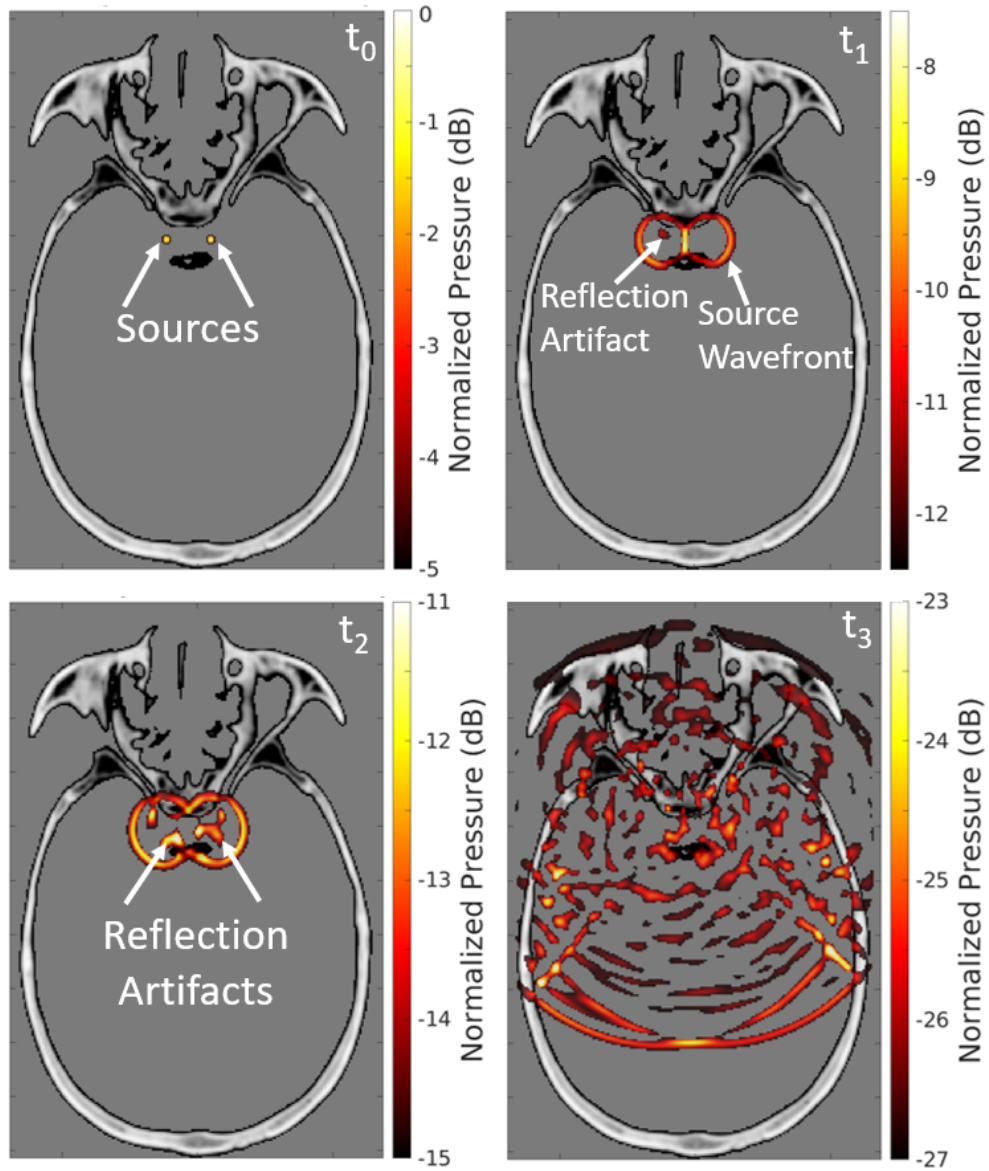


Figure 4.6: Axial slices from 3D k-Wave simulations demonstrating acoustic wave propagation within the complex bony anatomy of the empty skull overlaid on the simulated density map, spanning times  $t_0$  to  $t_3$ . Time  $t_0$  shows the initial pressure distribution of the carotid sources. Time  $t_3$  shows the photoacoustic signals after traveling to the temporal bone. The photoacoustic signals in each image are normalized by the maximum photoacoustic amplitude at time  $t_0$ .

have traveled to the external skull surfaces, while acoustic signal also remains near the initial pressure distribution positions and within the sella turcica, and reverberations are observed throughout the cranial cavity.

### 4.3.1.3 Localized Acoustic Pressure Analysis

Fig. 4.7 shows pressure signals received by a single acoustic sensor positioned in the nasal cavity, on the left and right ocular regions, and on the left and right temples of the empty skull. Sensors receiving the maximum pressure were chosen for each of these examples. The maximum received pressure of the sensor in the nasal cavity exceeds that of either the ocular (Fig. 4.7(a)) or temple (Fig. 4.7(b)) region by 16 Pa and 22 Pa, respectively. In addition, Fig. 4.7(a) shows that the sensors on the right and left eyes receive equivalent maximum pressures of 13 Pa. Fig. 4.7(b) shows that the sensors on the left temple received a maximum pressure that was 0.6 Pa greater than those on the right temple. Thus, there is minimal to no left-right asymmetry in these acoustic pathways (i.e., between the source and temple or between the source and ocular regions), making the left and right side equally preferable ultrasound probe locations for the simulated anatomy. Note that the maximum pressure received by these five sensor locations indicate a pressure decrease as the source-to-sensor distance

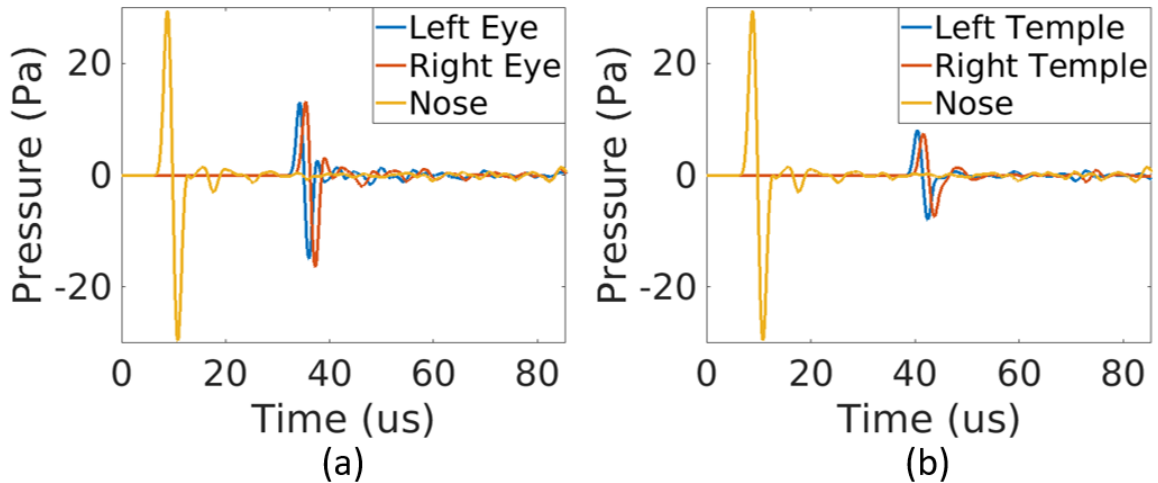


Figure 4.7: Photoacoustic pressure signals from k-Wave simulations of the empty skull, each measured from a single sensor location (a) within the nasal cavity and ocular regions and (b) within the nasal cavity and temporal regions. The nasal sensor locations were identical for each plot and replicated to simplify comparisons.

increased, which is expected.

### 4.3.2 *k-Wave Simulations of Fresh Cadaver Head*

Fig. 4.8 shows the distribution of photoacoustic signal energy received by acoustic sensors located on the left and right eyes in the 3D k-Wave simulation of the fresh cadaver head, with signal energy calculated using Eq. 4.1. When the LCA was illuminated (Fig. 4.8(a)), the average signal energy received by all sensors located on the left and right eyes were  $12.8 \times 10^3 \text{ Pa}^2$  and  $9.2 \times 10^3 \text{ Pa}^2$ , respectively. When the RCA was illuminated (Fig. 4.8(b)), the average signal energy received by all sensors located on the left and right eyes were  $9.6 \times 10^3 \text{ Pa}^2$  and  $12.4 \times 10^3 \text{ Pa}^2$ , respectively.

### 4.3.3 *Empty Skull Experimental Results*

#### 4.3.3.1 *Temporal Probe Location is Not Optimal*

Fig. 4.9(a) shows a 3D CT reconstruction of the empty skull, axial-lateral ultrasound imaging planes, and lateral-elevation ultrasound probe locations used for the temporal region, nasal cavity, and ocular regions. A corresponding photoacoustic-to-CT image registration when the ultrasound probe was placed on the temple region is shown in Fig. 4.9(b). This registration shows that the photoacoustic signals originate from the same locations as the ICAs which confirms visualization of the ICA targets.

When compared to Bell *et al.*'s previous study [18] with 1 mm temporal bone fragments, the reported target contrast ranged 9.0-19.2 dB when the laser operated with 2.0-9.3 mJ per pulse. Our new experimental results with the empty skull and 1 mm temporal bone resulted in ICA target contrast ranging 7.8-14.3 dB when the laser operated with 4.2-11.0 mJ per pulse. Although there is an overlap of contrast values reported for the two experiments, our newer experiment generally reports lower contrast values, which motivates additional investigation of the temporal region as a probe location using the intact skull, as presented in Fig. 4.10.

Fig. 4.10(a) shows ICA target contrast in DAS images from the empty skull experiment as a function of energy for temporal bone thicknesses ranging 0 - 4.4 mm. The ICA target contrast increased as laser energy increased and as temporal bone thickness decreased. For the range of energies tested, the ICA target contrast was consistently less than the empirically determined 5 dB visualization threshold when the temporal bone thickness was greater than 1.3 mm. Fig. 4.10(b) shows the corresponding minimum required energy to visualize the ICA targets in the presence of temporal bone, using the visually determined contrast threshold defined in Section 4.2.6. The dashed line in Fig. 4.10(b) shows the 4.95 mJ maximum allowable energy

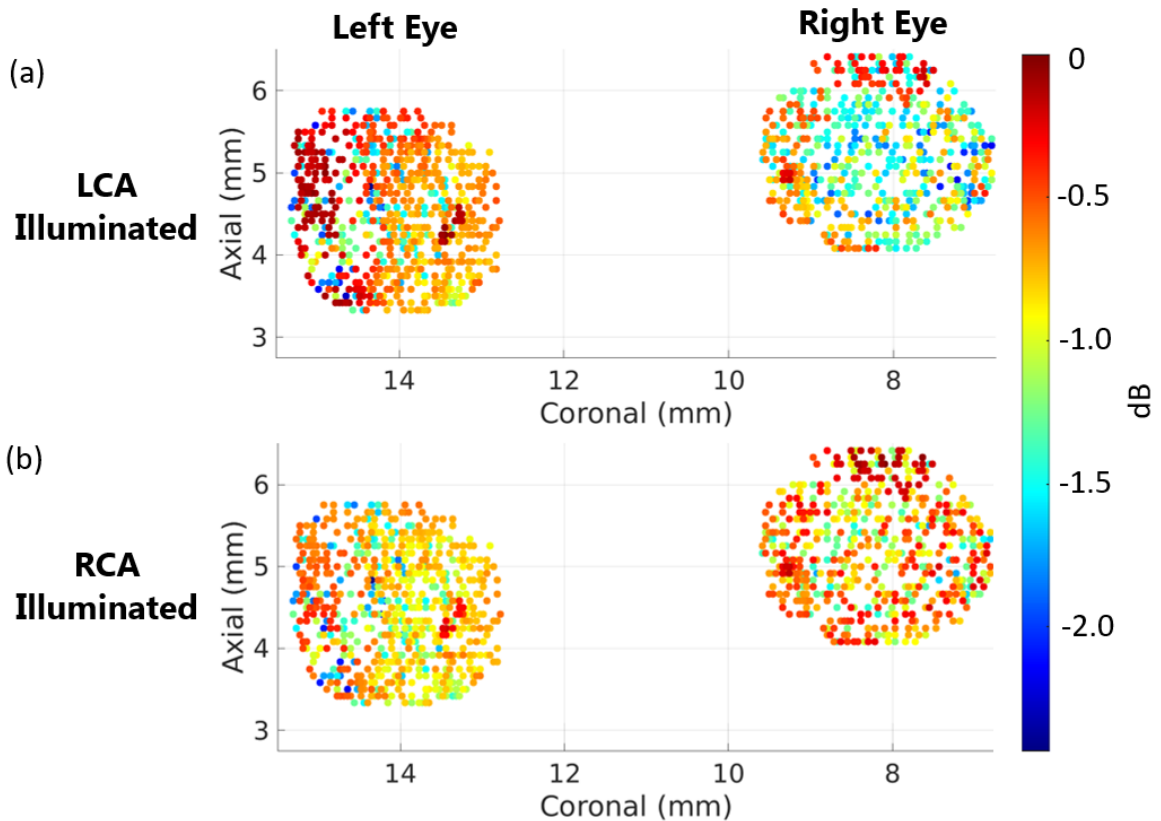


Figure 4.8: Visualization of k-Wave acoustic sensor data for sensors placed on the left and right eyelids of the fresh cadaver head when the photoacoustic source is (a) the LCA and (b) the RCA. The colors indicate the total signal energy received by each sensor at the completion of each simulation, normalized by the maximum of the total signal energy for each simulation.

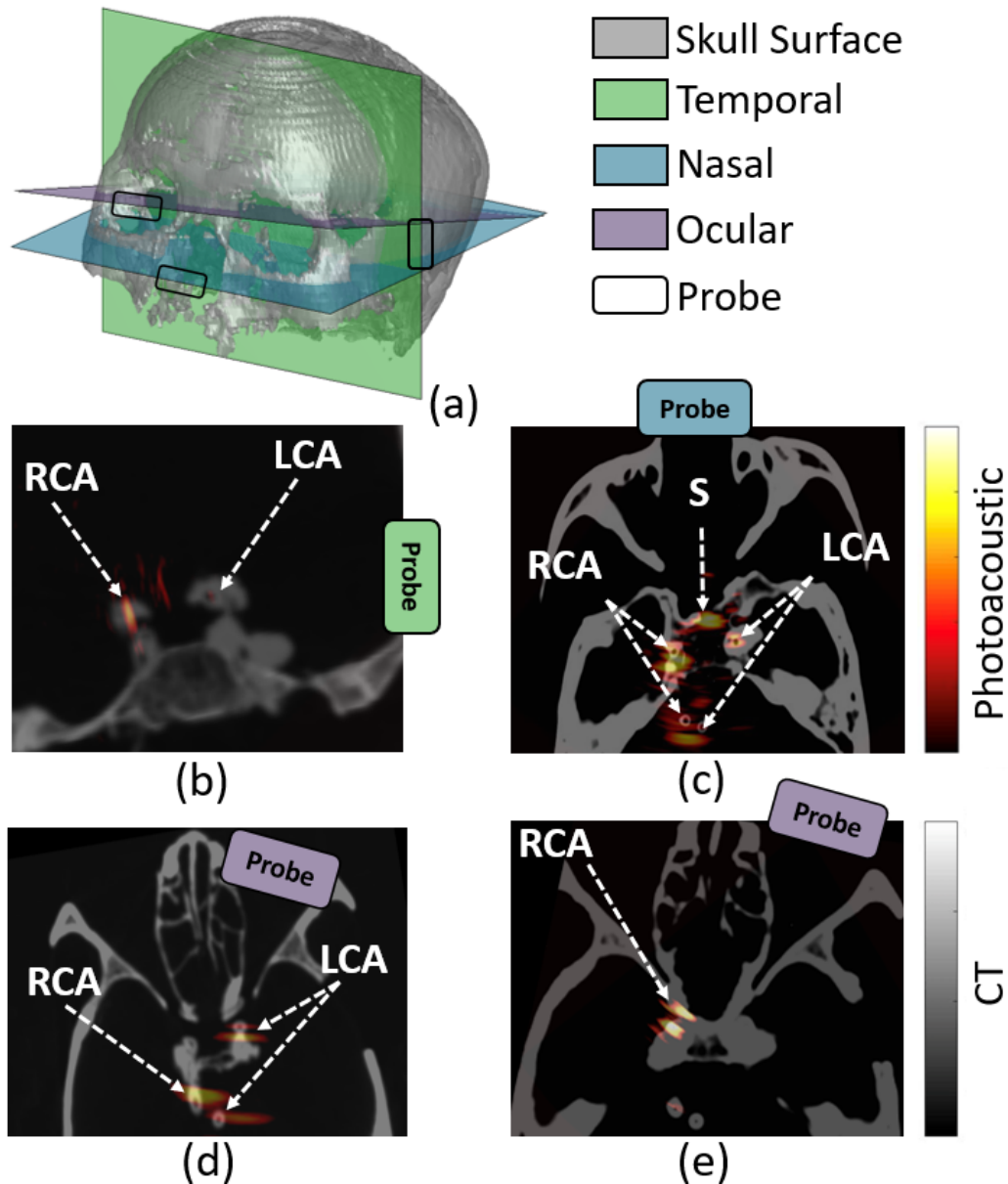


Figure 4.9: (a) 3D CT reconstruction of the empty skull highlighting the axial-lateral ultrasound imaging planes and lateral-elevation ultrasound probe locations used for the temporal region, nasal cavity, and ocular regions. Co-registered photoacoustic and CT images of the empty skull with the axial-lateral dimension of the ultrasound probe placed on the (b) temporal region (with no temple bone), (c) nasal cavity region, and (d) ocular region. (e) Co-registered photoacoustic and CT images of the skull filled with brain tissue and ultrasound probe placed on the right ocular region. The CT images are displayed in grayscale, and the photoacoustic images are displayed in color with 20 dB dynamic range. Photoacoustic targets include the LCA, RCA, and optical source (S). The Tygon tubing phantom ICAs appear as hollow circles on CT images.

for the 5 mm-core-diameter fiber bundle (as reported in Table 4.1). The ICA targets were visualized in DAS and SLSC images within this safety limit when the temporal bone was  $<1.3$  mm and  $\leq 1.3$  mm thick, respectively. However, the temporal bone of the human skull measures 1-4.4 mm thick [56]. Therefore, the temporal bone is considered as a less ideal ultrasound receiver location for photoacoustic imaging of the ICAs.

#### 4.3.3.2 Probe Location Comparison

Figs. 4.9(c) and 4.9(d) show the location of the ICA targets visualized when the ultrasound probe was placed in the nasal and ocular regions, respectively. The corresponding photoacoustic DAS and SLSC images overlaid on ultrasound images from the nasal and ocular probe locations are shown in Figs. 4.11(b) and 4.11(c), respectively. Similarly, Fig. 4.11(a) shows co-registered ultrasound and photoacoustic images that correspond to the temporal probe location shown in Fig. 4.9(b). In particular, Fig. 4.11(a) demonstrates that the LCA, RCA, and optical source was visualized when imaging through the nasal cavity. The RCA in Fig. 4.11(a) was additionally observed to cross the imaging plane in two locations with SLSC imaging, while the DAS image created from the same data shows only the portion of RCA that is closest to the light source.

The presence of bony anatomical landmarks to assist with registration is another detail to consider. Specifically, the co-registered ultrasound image obtained with the nasal probe location provides useful bony anatomical features, as observed in Fig. 4.11(a). The photoacoustic DAS and SLSC images in Fig. 4.11(b) show that both the LCA and RCA were visualized with the ocular probe position along with a bony anatomical reference, although the light source was not seen. When imaging through 1 mm of bone on the right temple, only the RCA was visualized in the photoacoustic DAS and SLSC images, as shown in Fig. 4.11(c). In addition, these images provide



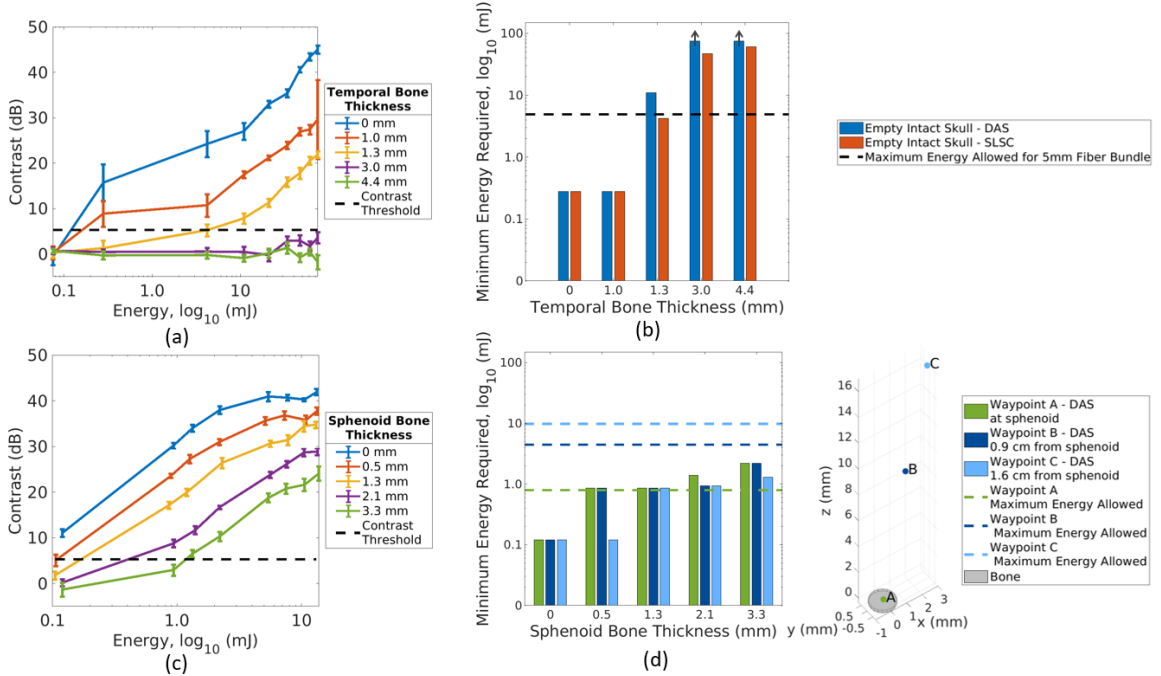


Figure 4.10: Empty skull experiments: (a) RCA contrast in DAS images with temporal bone thicknesses ranging 0-4.4 mm, and pulse energies ranging 0.08-75.0 mJ (displayed on a log scale). (b) Minimum energy required to visualize the RCA in DAS and SLSC images when the probe was placed on temple region. The dashed line represents the 4.95 mJ maximum allowable energy for the 5 mm-core-diameter fiber bundle, as reported in Table 4.1. Arrows ( $\uparrow$ ) represent minimum required energies which exceeded the maximum capable pulse energy of the optical source. Filled skull experiments: (c) RCA contrast in DAS images when the laser tip was located at waypoint C (1.64 cm away from sphenoid) for sphenoid bone thicknesses ranging 0-3.3 mm. Pulse energies ranged 0.10-13.8 mJ and are displayed on a log scale. (d) Minimum energy required to visualize the RCA in DAS images at waypoints A, B, and C when the probe was placed on the ocular region with sphenoid bone thicknesses ranging 0-3.3 mm. The dashed lines represent the maximum allowable energy calculated for the 2 mm-core-diameter fiber bundle without the quartz spacer attached, as reported in Table 4.2. A 3D visualization of waypoints A, B, and C with respect to the sphenoid bone surface is shown for reference.

no bony anatomical references (unlike the nasal and ocular images), and the temporal bone window cut-out was instead used as a landmark for registration in these cases. The bottom of Fig. 4.11 presents quantitative contrast measurements for comparison. Because the photoacoustic signal from the RCA was consistently present in the three tested ultrasound probe positions, this signal was used for the quantitative compar-

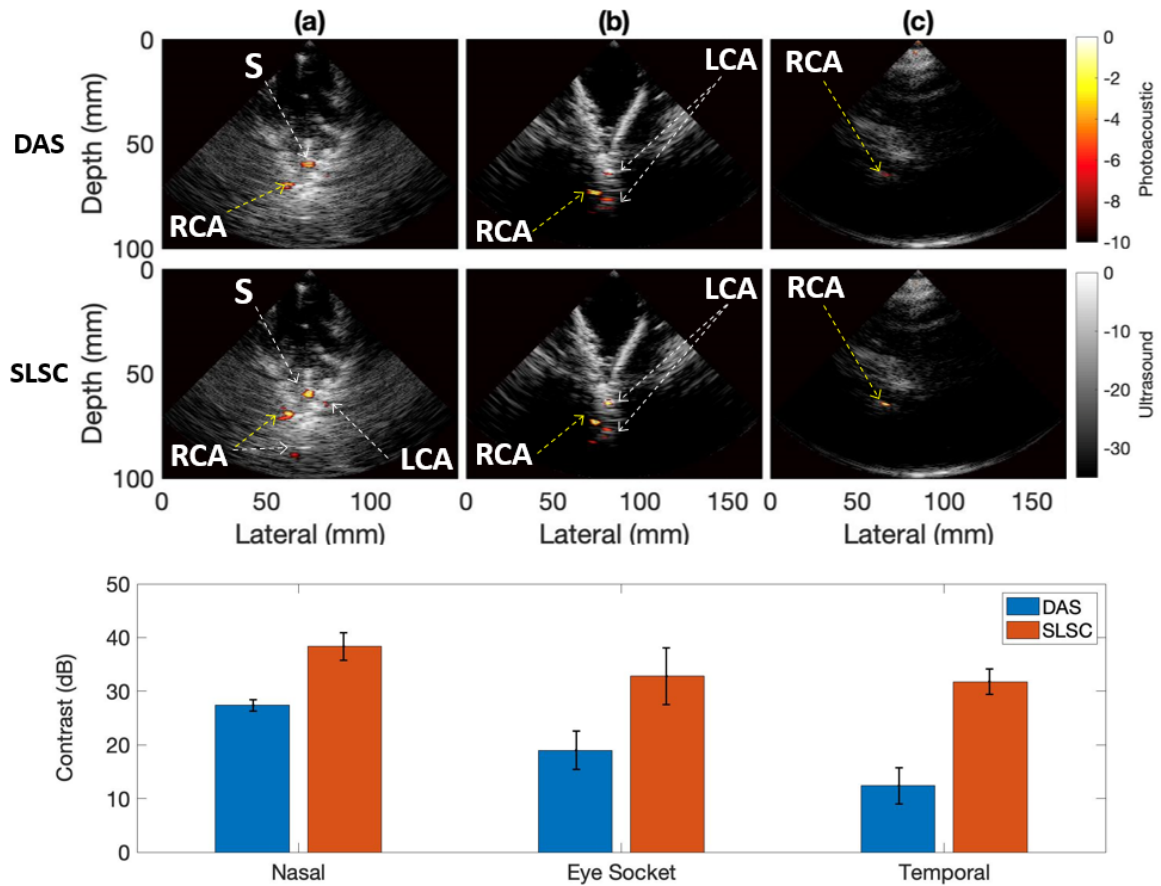


Figure 4.11: DAS and SLSC photoacoustic images of the empty skull overlaid on co-registered ultrasound images acquired with (a) nasal, (b) ocular, and (c) temporal probe locations. The optical source (S) emitted 3, 5, and 4 mJ per pulse, respectively. Each photoacoustic image was normalized to its brightest pixel and displayed with 10 dB dynamic range. The sphenoid and temporal bone thicknesses were 0 mm and 1 mm, respectively. The RCA signal labeled with the yellow arrow was used to compute contrast.

ison of photoacoustic image quality. The measured contrasts of the RCA in DAS photoacoustic images were 27 dB, 19 dB, and 12 dB for nasal, ocular and temporal regions, respectively. The corresponding contrasts in SLSC images were 41 dB, 35 dB, and 21 dB, respectively, resulting in a 9 - 16 dB improvement over DAS.

#### 4.3.4 Filled Skull Results and Spacer Design Requirements

Similar to Figs. 4.9(b)-(d), Fig 4.9(e) validates visualization of the RCA targets when brain tissue was present in the skull. For this setup, Fig. 4.10(c) shows RCA photoacoustic image contrast for one of the source-to-sphenoid distances (i.e., waypoint C). RCA contrast generally increased with increasing laser energy and decreased with increasing sphenoid bone thickness.

Fig. 4.10(d) shows the minimum energy required to visualize ICA targets with 5 dB contrast for waypoints A, B, and C. For waypoint A, the minimum energy was equivalent to or exceeded the maximum allowable energy with 0.5 mm or thicker sphenoid bone. For waypoints B and C, the minimum energies for the thickest sphenoid bone (i.e., 1.3 - 2.2 mJ at 3.3 mm thickness) were lower than the maximum allowable energies of 4.43 and 9.80 mJ per pulse, respectively. Therefore, the 2 mm-core-diameter fiber bundle must be positioned at least 0.89 cm (i.e., the distance of waypoint B from the bone surface) from the surface of the surgical workspace in order to visualize the ICAs within safety limits. Larger distances could also be used to increase the maximum allowed energy and improve image quality. These results motivated the quartz spacer design for the fresh cadaver head results presented in Section 4.3.5.

#### 4.3.5 Fresh Cadaver Head Results

Fig. 4.12 shows photoacoustic images from the ocular probe position overlaid on co-registered ultrasound or CT images of the fresh cadaver head. When imaging from the left eye, a significant level of background noise was present in the DAS image, which reduces the overall LCA contrast (Fig. 4.12(a)). Conversely, in the SLSC image, the background noise was significantly reduced, and the LCA was visualized with 30 dB contrast (Fig. 4.12(b)). When imaging from the right eye, the RCA was visualized with 18 dB and 33 dB contrast in DAS and SLSC images, respectively

(Figs. 4.12(c) and 4.12(d), respectively). Fig. 4.12(e) shows the photoacoustic-to-CT registration for the the RCA, visualized with the photoacoustic receiver located on the right cadaver eye. The photoacoustic signals originate from the same location as the RCA, which confirms visualization of the RCA.

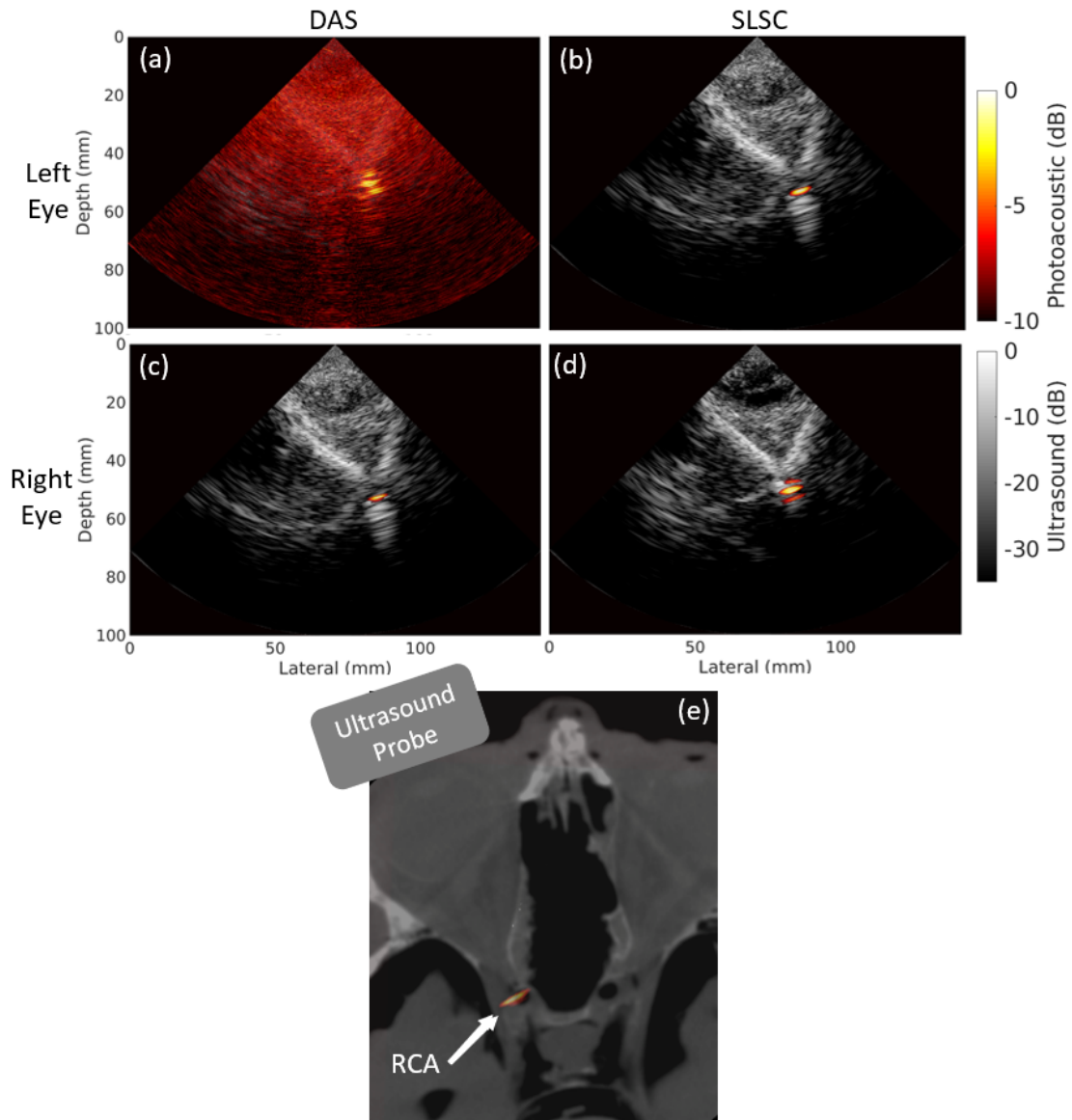


Figure 4.12: (a,c) DAS and (b,d) SLSC photoacoustic images from the fresh cadaver, overlaid on co-registered ultrasound images acquired with (a,b) left and (c,d) right ocular probe locations. The light source operated at 5.4 mJ per pulse and was placed on the LCA (visualized through the left eye) or RCA (visualized through the right eye). (e) Co-registered CT (gray scale) and photoacoustic image (color) images acquired with the ultrasound probe placed on the right eyelid of the cadaver head.

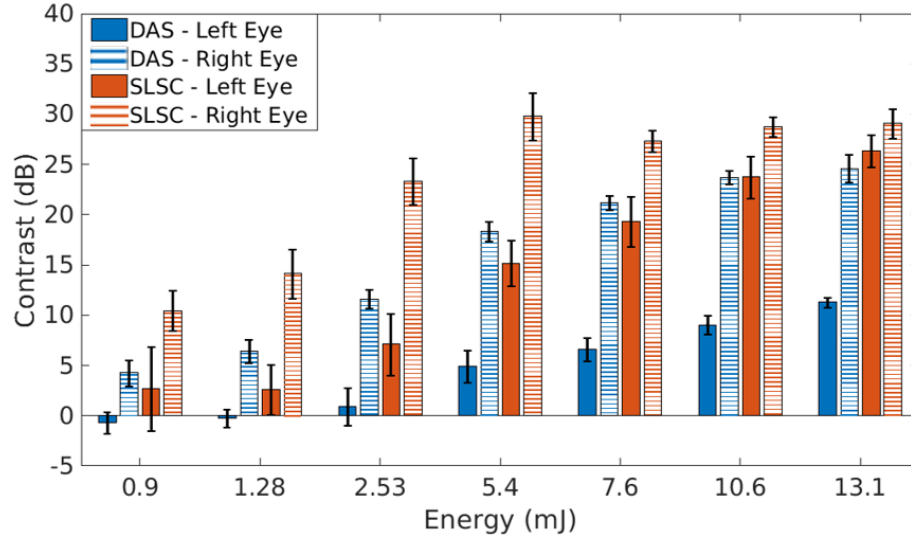


Figure 4.13: Contrast of the ICAs in DAS and SLSC photoacoustic images from the fresh cadaver head when the ultrasound probe was located on the left or right eye (as indicated in the legend), and the light source illuminated the ICA located on the same side as the probe.

Fig. 4.13 compares the contrast of photoacoustic DAS and SLSC images of the ICAs when the the light source was placed on the ICA of interest and viewed from the ocular region on the same side as the ICA. For this setup, the measured contrasts in DAS images obtained from the right ocular region were 5.0 - 14.7 dB greater than those obtained from the left ocular region. Therefore, the right eye was determined to be the preferable location for DAS photoacoustic imaging of the ICAs in this cadaver head.

This result also shows that SLSC imaging raised target contrasts and reduced the contrast difference between images obtained from the left and right eyes, when compared the differences observed with DAS imaging. For example, at energy levels 10.6 and 13.1 mJ per pulse, the SLSC images from the left and right eye experienced a 2 - 5 dB difference in contrast values with SLSC imaging (compared to 13 - 15 dB with DAS imaging). Therefore, SLSC beamforming can be used to reduce left-right asymmetries in the contrast of amplitude-based DAS photoacoustic images, which are likely caused by asymmetrical bone structures.

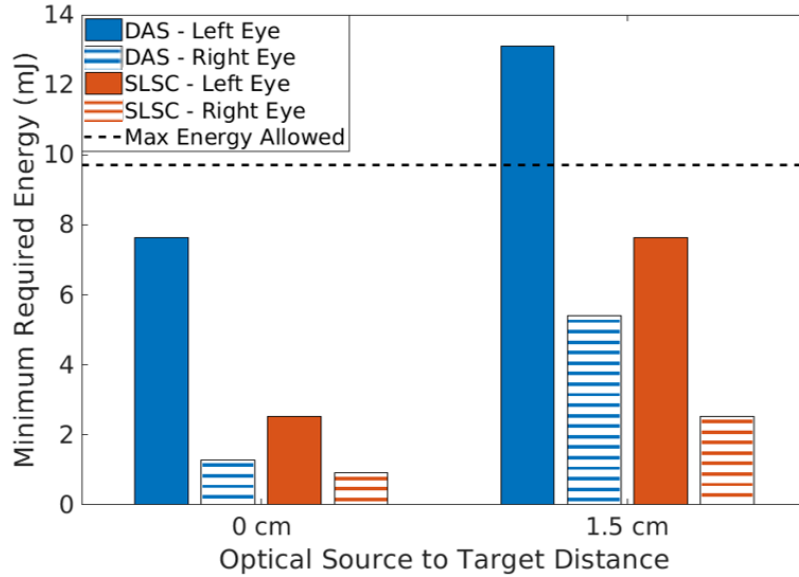


Figure 4.14: Minimum energy required to visualize the ICAs with 5 dB contrast with DAS and SLSC imaging when the optical source was placed at stationary distances of 0 cm and 1.5 cm away from the ICA target located on the same side as the probe (which is indicated in the legend).

Fig. 4.14 shows the minimum energy required to visualize the ICAs with at least 5 dB contrast at two different optical source-to-target distances (i.e., 0 and 1.5 cm). The 1.5 cm distance represents imaging capabilities when the ICA is difficult to locate during surgery. In both cases, SLSC imaging reduces the minimum required energy for ICA visualization compared to DAS imaging by 0.4 - 5.1 mJ and 3.9 - 5.5 mJ for the source-to-target distances of 0 cm and 1.5 cm, respectively. Although the LCA was not visualized with DAS imaging within safety limits when the source-to-target distance was 1.5 cm, SLSC imaging successfully visualized this target within safety limits.

Fig. 4.15 reports contrast as a function of multiple source-to-target distances for DAS and SLSC imaging. When the light source was placed on the RCA target (i.e., 0 mm distance), this target was visualized with 20 - 25 dB contrast with DAS imaging, with lower contrast observed at larger distances. When the light source was translated up to 9 mm away from the target, the RCA was visualized with 5 - 15

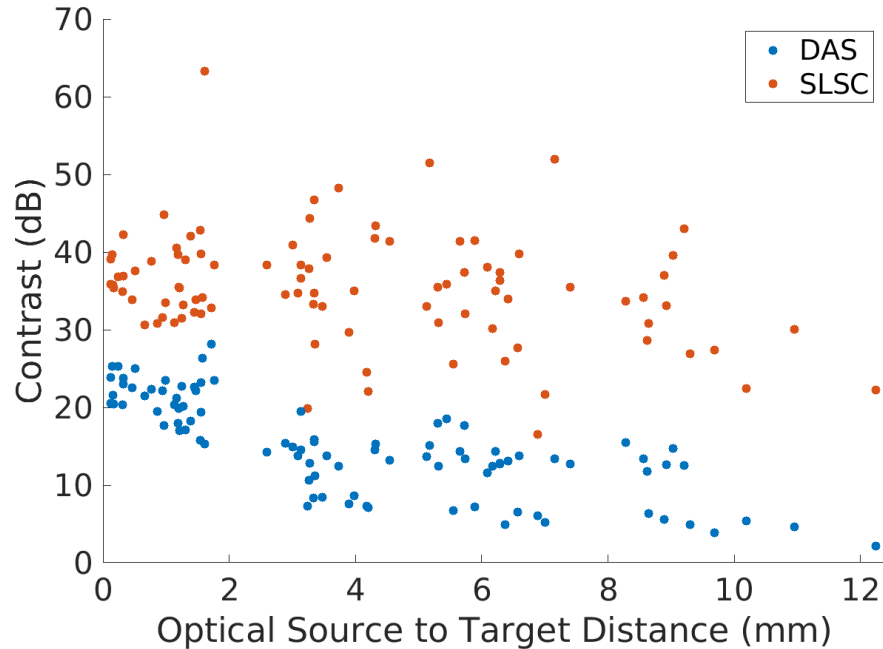


Figure 4.15: DAS contrast measurements from photoacoustic images of the right ocular region as the light source was navigated in the sphenoid sinus of the fresh cadaver head and the distance between the light source and RCA was increased.

dB contrast with DAS imaging. At distances  $>9$  mm, contrast drops below the 5 dB threshold with DAS imaging, while SLSC imaging continues to provide superior contrast at multiple source-to-target distances.

#### 4.4 Discussion

This work investigated the propagation of acoustic waves within human cadaveric skull specimens in simulation and experimental studies in order to determine the optimal ultrasound probe locations for photoacoustic imaging during minimally invasive surgeries of the skull base. The complex bony anatomy of the human skull significantly impacts the propagation of acoustic waves from internal photoacoustic sources to external acoustic receivers placed on the skull during a surgical procedure, as indicated by k-Wave simulations (Fig. 4.6). Concave bony surfaces trap acoustic signal in the frontal cranium which causes reverberations and increases the length of

the acoustic pathway from source to sensor. Therefore higher energy optical sources, advanced beamforming techniques, and strategic placement of the ultrasound probe are necessary to generate high contrast and interpretable transcranial photoacoustic images.

Although the temporal region was previously proposed as a possible location for ultrasound probe placement [16]–[19], this location performed more poorly when considering both simulation and experimental results (see Figs. 4.7 and 4.10(a,b), respectively). Specifically, when the temporal bone was thicker than 1.3 mm, it was not possible for the targets to be seen within energy safety limits. Considering that the adult human temporal bone measures 1-4.4 mm [56], the temporal bone is generally not a feasible location for placing the ultrasound probe in light of these results.

Both k-Wave simulations and empty skull experimental results agree that placing the ultrasound probe in the nasal cavity would receive the highest photoacoustic pressure and therefore produce the highest contrast photoacoustic images (Figs. 4.7 and 4.11). The nasal cavity also enabled simultaneous visualization of the LCA, RCA, and optical source. Simultaneous visualization of these three sources is advantageous to determine the proximity of the surgical tool to the ICAs when the optical source can be attached to the tool tip [16], [38] or when visualization of endonasal tool tips is otherwise needed. In addition, the corresponding nasal cavity ultrasound image has the potential to provide an intuitive imaging plane for surgeons.

Despite these benefits, placing the probe in the nasal cavity has three logistical barriers. First, a forward-looking endoscopic ultrasound probe is required. Second, space constraints limit the use of endoscopic probes in conjunction with light delivery systems and other surgical tools. Third, as the probe is inserted into the nasal cavity, an acoustic coupling medium such as water or gel would be required in the naturally air-filled pathway [57]. One potential solution to provide acoustic coupling is to attach a water-filled balloon to a re-designed nasal ultrasound probe, as previously



implemented for ultrasound endoscopy procedures [58]–[60]. Similar innovations could be implemented to address the remaining barriers. From this perspective, the work presented in this paper regarding nasal probe locations both demonstrates the need for novel photoacoustic and ultrasonic nasal probes and takes an additional step to outline preliminary design and energy requirements for these probes.

The ocular region was the second most optimal position based on the magnitude of the photoacoustic signal received in simulations and photoacoustic experiments (see Figs. 4.7 and 4.11), but we consider it to be the most optimal from a logistics perspective for the following two reasons. First, this position can be used with standard ultrasound probes and acoustic coupling gel and therefore can be more readily integrated in the surgical suite. Second, the absence of the ultrasound probe in the nasal cavity maintains sufficient space for the light delivery method, which is a critical component of the proposed photoacoustic imaging solution in cases where the ICAs cannot be located by endoscopy alone.

To demonstrate additional feasibility of the ocular ultrasound probe position, we created a setting in the cadaver head experiments mimicking a case where the surgeon would move the light source around the sphenoid sinus in search of the photoacoustic ICA signal (see Fig. 4.15). Results demonstrate visualization of the RCA with DAS and SLSC beamforming when the optical source-to-RCA distance was  $\leq 9$  mm, which is well within the bounds of the average 2 cm diameter surgical site [13]. To further improve maneuverability, we designed a light delivery system with a small form factor (see Table 4.1 and Fig. 4.4) to better fit the confined space of the nasal cavity while meeting the requirements of emitting sufficient energy and remaining within safety limits. This design has the potential to be improved in the future through incorporation of diffusers at the fiber bundle tip to reduce the device size, increase the beam divergence angle, and shorten the quartz spacer length.

There are three limitations introduced with the ocular probe reception of the

photoacoustic signals produced by this new light delivery design. First, the optical source is outside of the imaging plane, which can possibly be addressed by relying on the DAS contrast measurements to assess the source-to-target distance. Second, only one ICA will likely be present in the imaging plane at any given time (rather than both ICAs), as seen in the cadaver head experiment. Third, the ICA on the same side as the ocular region is likely to be visualized over the ICA on the opposite side (e.g., LCA when visualizing signals through the left ocular region). Although the RCA was visualized from the left ocular region in the filled skull experiment, it was not visible from the left ocular region in the cadaver head experiment. We suspect that the source of this discrepancy was the difference in acoustic coupling. Specifically, the water in the filled skull likely provided acoustic coupling for the acoustic waves traveling from the RCA, across the nasal cavity, to the probe on the left eye, while the air naturally contained within this acoustic pathway in the fresh cadaver head prevented acoustic coupling. The second and third limitations can possibly be addressed by simultaneously placing a novel ultrasound probe design on each eye.

Many of our observations about SLSC beamforming are consistent with previously reported advantages and disadvantages of this coherence-based beamformer [16], [19], [34]–[36]. For example, SLSC imaging is advantageous over DAS when the goal is to produce high contrast photoacoustic images of the ICAs in the presence of low laser fluence and attenuating tissues such as bone (Figs. 4.11, 4.12, 4.13). However, because coherence-based imaging is robust to changes in fluence, an amplitude-based beamformer such as DAS is more promising when the goal is to use image contrast to estimate source-to-target distances (Fig. 4.15). The results in Fig. 4.10(b) additionally demonstrate that SLSC images generally reduced the required energy to visualize the ICA targets when compared to requirements with DAS images.

One additional significant outcome of the studies presented in this paper is that

they indicate the promise of the simulation methodology for patient-specific pre-operative surgical planning of optimal receiver locations when using photoacoustic imaging as an intraoperative navigation technique. Variations in skull anatomy between individuals as well as asymmetry in skull anatomy within an individual alters the characteristics of the acoustic pathway from the ICA photoacoustic source to the externally placed acoustic receivers. We demonstrated that skull anatomy asymmetry within an individual has a potential on the quality of photoacoustic images. It is therefore probable that in extreme cases of asymmetry, one of the ocular regions may be eliminated as a feasible probe location. Conversely, it is also possible that in extreme cases of inter-patient variability, more feasible probe locations would be available.

#### **4.5 Conclusion**

The work presented in this paper details significant requirements for progression toward patient studies of transcranial intraoperative photoacoustic imaging of the internal carotid arteries. The nasal cavity and ocular regions were identified as feasible locations for the ultrasound probe. We then designed a custom light delivery method and demonstrated its use in a fresh cadaver head. In addition, we demonstrated that photoacoustic k-Wave simulations can potentially be used with preoperative CT scans as a patient-specific surgical planning tool to choose the most optimal probe position. Advanced beamforming techniques, such as SLSC, are preferable over DAS when the goal is to produce high contrast photoacoustic images of the ICAs during minimally invasive neurosurgeries. DAS is more promising when the goal is to use image contrast to estimate source-to-target distances. A single optical wavelength was used for these demonstrations, while future wavelength optimization has the potential to preferentially excite oxyghemoglobin in the ICAs over deoxyhemoglobin in the venous plexus surrounding the surgical site. Overall, this translational research

demonstrates that photoacoustic imaging is a promising technique for guidance of endonasal transsphenoidal surgeries.

#### 4.6 Acknowledgements

This research was financially supported by NIH Grant No. R00-EB018994 and the NSF Graduate Research Fellowship Program (Grant No. DGE1746891). The authors thank Peter Kazanzides for sharing the Mayfield clamp used in these studies and Mohammed Lehar for assistance with preparing the bone fragment samples. The study sponsors had no involvement with the study design, the data collection, analysis, and interpretation, the writing of research reports, nor the decision to submit this article for publication.

#### References

- [1] M. T. Graham, J. Huang, F. Creighton, and M. A. L. Bell, “Simulations and human cadaver head studies to identify optimal acoustic receiver locations for minimally invasive photoacoustic-guided neurosurgery,” *Photoacoustics*, p. 100 183, 2020.
- [2] R. J. Komotar, R. M. Starke, D. M. Raper, V. K. Anand, and T. H. Schwartz, “Endoscopic endonasal compared with microscopic transsphenoidal and open transcranial resection of giant pituitary adenomas,” *Pituitary*, vol. 15, no. 2, pp. 150–159, 2012.
- [3] M. Buchfelder and J. Kreutzer, “Transcranial surgery for pituitary adenomas,” *Pituitary*, vol. 11, no. 4, pp. 375–384, 2008.
- [4] P. F. Svider, M. J. Pines, M. D. Raikundalia, A. J. Folbe, S. Baredes, J. K. Liu, and J. A. Eloy, “Transsphenoidal surgery for malignant pituitary lesions:

- An analysis of inpatient complications,” in *International Forum of Allergy & Rhinology*, vol. 5, 2015, pp. 659–664.
- [5] P. Cappabianca, L. M. Cavallo, and E. de Divitiis, “Endoscopic endonasal transsphenoidal surgery,” *Neurosurgery*, vol. 55, pp. 933–941, 2004.
- [6] X. Zhang, Z. Fei, W. Zhang, J. Zhang, W. Liu, L. Fu, W. Cao, and S. Jiang XF and Song, “Endoscopic endonasal transsphenoidal surgery for invasive pituitary adenoma,” *Journal of Clinical Neuroscience*, vol. 15, pp. 241–245, 2008.
- [7] I. Ciric, A. Ragin, C. Baumgartner, and D. Pierce, “Complications of transsphenoidal surgery: Results of a national survey, review of the literature, and personal experience,” *Neurosurgery*, vol. 40, no. 2, pp. 225–237, 1997.
- [8] M. S. Agam, M. A. Wedemeyer, B. Wrobel, M. H. Weiss, J. D. Carmichael, and G. Zada, “Complications associated with microscopic and endoscopic transsphenoidal pituitary surgery: Experience of 1153 consecutive cases treated at a single tertiary care pituitary center,” *Journal of Neurosurgery*, vol. 130, no. 5, pp. 1576–1583, 2018.
- [9] M. O. Perry, W. H. Snyder, and E. R. Thal, “Carotid artery injuries caused by blunt trauma,” *Annals of Surgery*, vol. 192, no. 1, pp. 74–77, 1980.
- [10] J. Raymond, J. Hardy, R. Czepko, and D. Roy, “Arterial injuries in transsphenoidal surgery for pituitary adenoma; the role of angiography and endovascular treatment,” *American Journal of Neuroradiology*, vol. 18, no. 4, pp. 655–665, 1997.
- [11] R. Valentine and P.-J. Wormald, “Carotid artery injury after endonasal surgery,” *Otolaryngologic Clinics of North America*, vol. 44, no. 5, pp. 1059–1079, 2011.
- [12] L. C. Heringer, M. F. des de Oliveira, J. M. Rotta, and R. V. Botelho, “Effect of repeated transsphenoidal surgery in recurrent or residual pituitary adenomas: A

- systematic review and meta-analysis,” *Surgical Neurology International*, vol. 7, pp. 1–6, 2016.
- [13] M. A. Mascarella, R. Forghani, S. D. Maio, D. Sirhan, A. Zeitouni, G. Mohr, and M. A. Tewfik, “Indicators of a reduced intercarotid artery distance in patients undergoing endoscopic transsphenoidal surgery,” *Journal of Neurological Surgery, Part B, Skull Base*, vol. 76, no. 3, pp. 195–201, 2015.
- [14] K. Kitazawa, H. Okudera, T. Takemae, and S. Kobayashi, “CT guided transsphenoidal surgery: Report of nine cases,” *Neurological Surgery*, vol. 21, no. 147, 1993.
- [15] X. Wang, D. L. Chamberland, and G. Xi, “Noninvasive reflection mode photoacoustic imaging through infant skull toward imaging of neonatal brains,” *Journal of Neuroscience Methods*, vol. 168, no. 2, pp. 412–421, 2008.
- [16] M. A. L. Bell, A. K. Ostrowski, K. Li, P. Kazanzides, and E. M. Boctor, “Localization of transcranial targets for photoacoustic-guided endonasal surgeries,” *Photoacoustics*, vol. 3, no. 2, pp. 78–87, 2015.
- [17] ———, “Quantifying bone thickness, light transmission, and contrast interrelationships in transcranial photoacoustic imaging,” in *Proceedings of SPIE, Photons Plus Ultrasound: Imaging and Sensing*, vol. 9323, 2015.
- [18] M. A. L. Bell, A. B. Dagle, P. Kazanzides, and E. M. Boctor, “Experimental assessment of energy requirements and tool tip visibility for photoacoustic-guided endonasal surgery,” in *Proceedings of SPIE, Photons Plus Ultrasound: Imaging and Sensing*, vol. 9708, 2016, p. 97080D.
- [19] M. A. L. Bell, A. K. Ostrowski, P. Kazanzides, and E. M. Boctor, “Feasibility of transcranial photoacoustic imaging for interventional guidance of endonasal surgeries,” in *Proceedings of SPIE, Photons Plus Ultrasound: Imaging and Sensing*, vol. 8943, 2014, p. 894307.

- [20] T. Kirchner, J. Gröhl, N. Holzwarth, M. A. Herrera, A. Hernández-Aguilera, E. Santos, and L. Maier-Hein, “Photoacoustic monitoring of blood oxygenation during neurosurgical interventions,” in *Proceedings of SPIE, Photons Plus Ultrasound: Imaging and Sensing*, vol. 10878, 2019, pp. 14–18.
- [21] M. F. Kircher, A. De La Zerda, J. V. Jokerst, C. L. Zavaleta, P. J. Kempen, E. Mittra, K. Pitter, R. Huang, C. Campos, F. Habte, R. Sinclair, C. W. Brennan, I. K. Mellinghoff, E. C. Holland, and S. S. Gambhir, “A brain tumor molecular imaging strategy using a new triple-modality mri-photoacoustic-raman nanoparticle,” *Nature Medicine*, vol. 18, no. 5, pp. 829–834, 2012.
- [22] P. Beard, “Biomedical photoacoustic imaging,” *Interface Focus*, vol. 1, no. 4, pp. 602–631, 2011.
- [23] J. Yu, H. Nguyen, W. Steenbergen, and K. Kim, “Recent development of technology and application of photoacoustic molecular imaging toward clinical translation,” *Journal of Nuclear Medicine*, vol. 59, no. 8, pp. 1202–1207, 2018.
- [24] M. Kneipp, J. Turner, H. Estrada, J. Rebling, S. Shoham, and D. Razansky, “Effects of the murine skull in optoacoustic brain microscopy,” *Journal of Biophotonics*, vol. 9, no. 1-2, pp. 117–123, 2016.
- [25] G. Pinton, J.-F. Aubry, E. Bossy, M. Muller, M. Pernot, and M. Tanter, “Attenuation, scattering, and absorption of ultrasound in the skull bone,” *Medical Physics*, vol. 39, no. 1, pp. 299–307, 2012.
- [26] H. Estrada, J. Rebling, J. Turner, and D. Razansky, “Broadband acoustic properties of a murine skull,” *Physics in Medicine & Biology*, vol. 61, no. 5, p. 1932, 2016.
- [27] S. Golovynskiy, I. Golovynska, L. I. Stepanova, O. I. Datsenko, L. Liu, J. Qu, and T. Y. Ohulchansky, “Optical windows for head tissues in near-infrared

- and short-wave infrared regions: Approaching transcranial light applications,” *Journal of Biophotonics*, vol. 11, no. 12, e201800141, 2018.
- [28] L. Nie, X. Cai, K. I. Maslov, A. Garcia-Uribe, M. A. Anastasio, and L. V. Wang, “Photoacoustic tomography through a whole adult human skull with a photon recycler,” *Journal of Biomedical Optics*, vol. 17, no. 11, p. 110 506, 2012.
- [29] Q. Xu, B. Volinski, A. Hariri, A. Fatima, and M. Nasiriavanaki, “Effect of small and large animal skull bone on photoacoustic signal,” in *Proceedings of SPIE, Photons Plus Ultrasound: Imaging and Sensing*, vol. 10064, 2017, 100643S.
- [30] H. Estrada, X. Huang, J. Rebling, M. Zwack, S. Gottschalk, and D. Razansky, “Virtual craniotomy for high-resolution optoacoustic brain microscopy,” *Scientific Reports*, vol. 8, no. 1, p. 1459, 2018.
- [31] S. Govinahalli Sathyanarayana, B. Ning, R. Cao, S. Hu, and J. A. Hossack, “Dictionary learning-based reverberation removal enables depth-resolved photoacoustic microscopy of cortical microvasculature in the mouse brain,” *Scientific Reports*, vol. 8, no. 1, p. 985, 2018.
- [32] C. Huang, L. Nie, R. W. Schoonover, Z. Guo, C. O. Schirra, M. A. Anastasio, and L. V. Wang, “Aberration correction for transcranial photoacoustic tomography of primates employing adjunct image data,” *Journal of Biomedical Optics*, vol. 17, no. 6, p. 066 016, 2012.
- [33] S. Purkayastha and F. Sorond, “Transcranial doppler ultrasound: Technique and application,” *Seminars in Neurology*, vol. 32, no. 4, pp. 411–420, 2012.
- [34] M. A. L. Bell, N. Ku, D. Y. Song, and E. M. Boctor, “Short-lag spatial coherence beamforming of photoacoustic images for enhanced visualization of prostate brachytherapy seeds,” *Biomedical Optics Express*, vol. 4, no. 10, p. 1964, 2013.



- [35] M. A. L. Bell, N. P. Kuo, D. Y. Song, J. U. Kang, and E. M. Boctor, “In vivo visualization of prostate brachytherapy seeds with photoacoustic imaging,” *Journal of Biomedical Optics*, vol. 19, no. 12, p. 126 011, 2014.
- [36] M. A. L. Bell, X. Guo, D. Y. Song, and E. M. Boctor, “Transurethral light delivery for prostate photoacoustic imaging,” *Journal of Biomedical Optics*, vol. 20, no. 3, p. 036 002, 2015.
- [37] S. Kim, Y. Tan, P. Kazanzides, and M. A. L. Bell, “Feasibility of photoacoustic image guidance for telerobotic endonasal transsphenoidal surgery,” *IEEE International Conference on Biomedical Robotics and Biomechatronics (BioRob)*, vol. 6, 2016.
- [38] B. Eddins and M. A. L. Bell, “Design of a multifiber light delivery system for photoacoustic-guided surgery,” *Journal of Biomedical Optics*, vol. 22, no. 4, pp. 1–11, 2017.
- [39] B. E. Treeby and B. T. Cox, “K-Wave: MATLAB toolbox for the simulation and reconstruction of photoacoustic wave fields,” *Journal of Biomedical Optics*, vol. 15, no. 2, p. 021 314, 2010.
- [40] B. E. Treeby, B. T. Cox, and J. Jaros, *A matlab toolbox for the time domain simulation of acoustic wave field, user manual, (2016) manual version 1.1, toolbox release 1.1*, version Version 1.1, Toolbox Release 1.1, 2016, August 27, 2016.
- [41] M. Tabei, T. D. Mast, and R. Waag, “A k-space method for coupled first-order acoustic propagation equations,” *The Journal of the Acoustical Society of America*, vol. 111, no. 1, pp. 53–63, 2002.
- [42] N. Ugryumova, S. J. Matcher, and D. P. Attenburrow, “Measurement of bone mineral density via light scattering,” *Physics in Medicine & Biology*, vol. 49, no. 3, p. 469, 2004.

- [43] P. Van der Zee, M. Essenpreis, and D. T. Delpy, “Optical properties of brain tissue,” in *Proceedings of SPIE, Photon Migration and Imaging in Random Media and Tissues*, vol. 1888, 1993, pp. 454–465.
- [44] S. K. V. Sekar, I. Bargigia, A. Dalla Mora, P. Taroni, A. Ruggeri, A. Tosi, A. Pifferi, and A. Farina, “Diffuse optical characterization of collagen absorption from 500 to 1700 nm,” *Journal of Biomedical Optics*, vol. 22, no. 1, p. 015 006, 2017.
- [45] R. L. van Veen, H. Sterenborg, A. Pifferi, A. Torricelli, and R. Cubeddu, “Determination of vis-nir absorption coefficients of mammalian fat, with time-and spatially resolved diffuse reflectance and transmission spectroscopy,” in *Biomedical Topical Meeting*, Optical Society of America, 2004, SF4.
- [46] D. J. Segelstein, “The complex refractive index of water,” Ph.D. dissertation, University of Missouri–Kansas City, 1981.
- [47] S. Praul, *Tabulated molar extinction coefficient for hemoglobin in water*, <https://omlc.org/spectra/hemoglobin/summary.html>, Accessed: 2020-03-18.
- [48] S. L. Jacques, R. D. Glickman, and J. A. Schwartz, “Internal absorption coefficient and threshold for pulsed laser disruption of melanosomes isolated from retinal pigment epithelium,” in *Laser-Tissue Interaction VII*, International Society for Optics and Photonics, vol. 2681, 1996, pp. 468–477.
- [49] S. L. Jacques and D. J. McAuliffe, “The melanosome: Threshold temperature for explosive vaporization and internal absorption coefficient during pulsed laser irradiation,” *Photochemistry and Photobiology*, vol. 53, no. 6, pp. 769–775, 1991.
- [50] J. L. Su, R. R. Bouchard, A. B. Karpiouk, J. D. Hazle, and S. Y. Emelianov, “Photoacoustic imaging of prostate brachytherapy seeds,” *Biomedical Optics Express*, vol. 2, no. 8, pp. 2243–2254, 2011.

- [51] American National Standards Institute, *American national standard for the safe use of lasers*, 2007.
- [52] S. Ley, M. Stadthalter, D. Link, D. Laqua, and P. Husar, “Phantom materials mimicking the optical properties in the near infrared range for non-invasive fetal pulse oximetry,” *36th Annual International Conference of the IEEE Engineering in Medicine and Biology Society*, pp. 1432–1435, 2014.
- [53] A. I. Chen, M. L. Balter, M. I. Chen, D. Gross, S. K. Alam, T. J. Maguire, and M. L. Yarmush, “Multilayered tissue mimicking skin and vessel phantoms with tunable mechanical, optical, and acoustic properties,” *Medical Physics*, vol. 43, no. 6, pp. 3117–3131, 2016.
- [54] S. A. Filatova, I. A. Shcherbakov, and V. B. Tsvetkov, “Optical properties of animal tissues in the wavelength range from 350 to 2600 nm,” *Journal of Biomedical Optics*, vol. 22, no. 3, p. 035 009, 2017.
- [55] M. A. L. Bell, Trahey, G. E., Byran, B. C., and J. J. Dahl, “Short-lag spatial coherence of backscattered echoes: Imaging characteristics,” *IEEE Transactions on Ultrasonics, Ferroelectrics, and Frequency Control*, vol. 58, no. 7, pp. 1377–1388, 2011.
- [56] S. Ma, L. J. Baillie, and M. D. Stringer, “Reappraising the surface anatomy of the pterion and its relationship to the middle meningeal artery,” *Clinical Anatomy*, vol. 25, no. 3, pp. 330–339, 2012.
- [57] S. Yoshinaga, I. Oda, S. Nonaka, R. Kushima, and Y. Saito, “Endoscopic ultrasound using ultrasound probes for the diagnosis of early esophageal and gastric cancers,” *World Journal of Gastrointestinal Endoscopy*, vol. 4, no. 6, pp. 218–226, 2012.

- [58] A. Chung and V. Kwan, “Endoscopic ultrasound: An overview of its role in current clinical practice,” *Australasian Journal of Ultrasound in Medicine*, vol. 12, no. 2, pp. 21–29, 2009.
- [59] H. Inoue, T. Kawano, K. Takeshita, and T. Iwai, “Modified soft-balloon methods during ultrasonic probe examination for superficial esophageal cancer,” *Endoscopy*, vol. 30, no. S 1, A–41, 1998.
- [60] M. B. Wallace, B. J. Hoffman, A. S. Sahai, H. Inoue, A. Van Velse, and R. H. Hawes, “Imaging of esophageal tumors with a water-filled condom and a catheter us probe,” *Gastrointestinal Endoscopy*, vol. 51, no. 5, pp. 597–600, 2000.

# Chapter 5

## Validation of Patient-Specific Simulation Methods to Determine Acoustic Windows

*The work presented in this chapter was published in the following manuscript:*

M. T. Graham, F. X. Creighton, and M. A. L. Bell, “Validation of eyelids as acoustic receiver locations for photoacoustic-guided neurosurgery,” in *Photons Plus Ultrasound: Imaging and Sensing 2021*, International Society for Optics and Photonics, vol. 11642, 2021, p. 1 164 228.

### 5.1 Introduction

Endoscopic transsphenoidal surgery is a minimally invasive technique in which instruments are inserted through the nasal cavity to drill through sphenoid bone and remove pituitary tumors [2]. During this procedure, critical structures such as the internal carotid arteries (ICAs), cranial nerves, and dura lie within millimeters of each other. Iatrogenic injury to these structures causes surgical complications such as ICA injury, cerebral spinal fluid leak, hemorrhage, stroke, cranial nerve paresis, and death [3]. Patients with aggressive, reoccurring tumors often require revision surgeries

in which scarring, loss of natural anatomical markers, and disrupted ICA locations increase the risk of surgical complications in these revision surgeries to 11.4% [3].

Intraoperative techniques, such as stereotactic guidance and endoscopy, are the gold standard for navigation within the skull base. However, these techniques suffer from two primary limitations. First, stereotactic guidance is susceptible to registration errors as the anatomy is disrupted and deviates from preoperative x-ray computed tomography (CT) or magnetic resonance (MR) images. Second, although endoscopy offers real-time snapshots of the surgical site, it does not provide visualization of subsurface structures in the surgical path. To address these two well-known limitations, our group is pioneering transcranial photoacoustic imaging as a promising neurosurgical intraoperative imaging technique for real-time visualization of the ICAs [4]–[10], with supporting evidence of more general transcranial photoacoustic imaging additionally provided by other groups [11]–[13]. However, transcranial photoacoustic imaging is challenged by interactions with cranial bone, which degrade image quality [14]–[16].

We previously developed and demonstrated a simulation methodology to identify naturally occurring acoustic windows in the adult human skull, namely the temporal, nasal, and ocular regions [8], [9]. The ocular region was determined to be an optimal location and was subsequently used to successfully obtain images of the left carotid artery (LCA) and right carotid artery (RCA) within a fresh human cadaver head. The work presented in this paper utilizes these experimental cadaver imaging results in combination with simulations studies to further investigate the eyelid as an acoustic receiver location. In particular, this work validates that simulations can potentially model patient-specific asymmetries in the skull base and predict photoacoustic image quality when using the eyelids as the receiver location.

## 5.2 Methods

Three-dimensional photoacoustic simulations were performed using the k-Wave toolbox [17], [18], based on the CT volume of a human cadaver head. The CT volume was converted to heterogeneous density, speed of sound, and absorption prefactor volumes. Fig. 5.1 shows an axial slice of the heterogeneous speed of sound volume. The computational grid was defined with a symmetric voxel size of 0.3 mm x 0.3 mm x 0.3 mm. Acoustic wave propagation was simulated with a time increment of  $1.23^{-8}$  seconds. No shear waves were included in these simulations.

Spherical 0.3 mm-diameter photoacoustic targets were positioned in the locations of the LCA and RCA. Each source was simulated independently. Acoustic sensors were distributed across the eyelids to receive intracranial photoacoustic signals, as shown in Fig. 5.1(a). The signal energy,  $E_s$ , received by each sensor was calculated as:

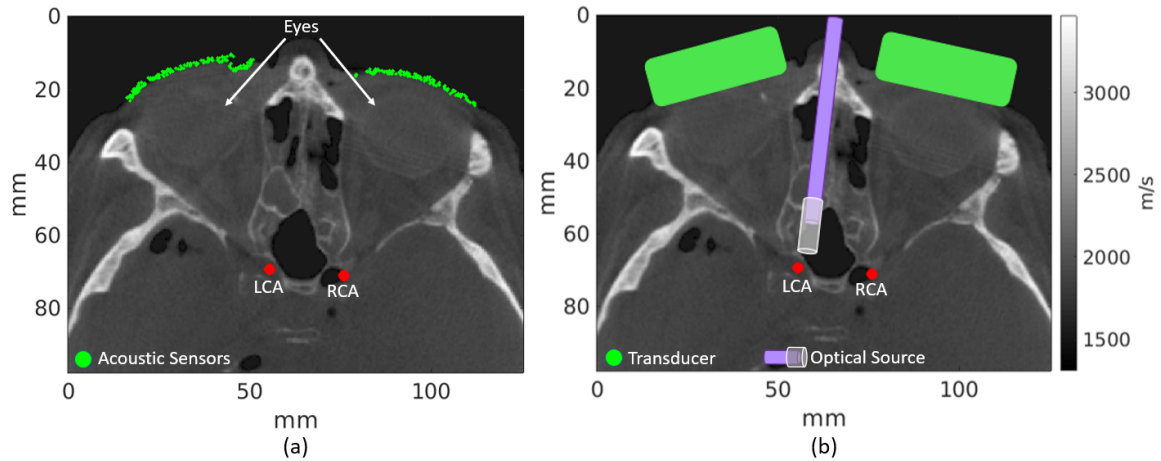


Figure 5.1: Annotated slices of the speed of sound distribution, derived from axial CT slices of the same human cadaver head. (a) The simulation consisted of acoustic sensors distributed across the eyelids and photoacoustic sources independently placed in the left carotid artery (LCA) or right carotid artery (RCA) position. (b) The corollary experimental setup consisted of transducers placed on the eyelids, an optical source inserted through the nasal cavity, and independently illuminated LCA and RCA photoacoustic sources.

$$E_s = \sum_{n=0}^N |x_s(n)|^2, \quad E \in \mathbb{R}^{1 \times S} \quad (5.1)$$

where  $s$  is the sensor index,  $S$  is the total number of sensors,  $x_s(n)$  is the time domain pressure signal,  $N_t$  is the total simulation time in seconds, and  $E$  is the vector containing all  $E_s$ . The log-compressed signal energy,  $\hat{E}_s$ , was calculated as:

$$\hat{E}_s = 20 \log_{10} \left( \frac{E_s}{\max(E)} \right) \quad (5.2)$$

Simulation outputs were validated with experimental channel data obtained from the experimental procedure described in our previous publication [9]. In particular, an ultrasound transducer was placed on the eyelids of the cadaver head and an optical source was inserted through the nasal cavity, as illustrated in Fig. 5.1(b). Ultrasound and photoacoustic delay-and-sum (DAS) images were generated from the channel data and each image was normalized to its brightest pixel. Prior to normalizing the displayed photoacoustic DAS images, the amplitudes of the image pixels,  $P_i$ , within an ellipsoidal region of interest (ROI) inside the photoacoustic source were measured and converted to a log-compressed amplitude as follows:

$$\hat{P}_i = 20 \log_{10} \left( \frac{P_i}{\max(P)} \right), \quad P \in \mathbb{R}^{1 \times I} \quad (5.3)$$

where  $i$  is the pixel index,  $I$  is the total number of pixels, and  $P$  is the vector containing all  $P_i$ .

### 5.3 Results

Fig. 5.2 shows the photoacoustic signal energy received by each simulated acoustic sensor on the left and right eyelids, as calculated by Eq. 5.2. When the LCA was simulated, the left eye sensors received a higher median signal energy of -27.94 dB when compared to -34.99 dB for the right eye sensors, as demonstrated in Fig.



5.2(a). When the RCA was simulated, the right eye sensors received a higher median signal energy of  $-21.53$  dB when compared to  $-36.33$  dB for the left eye sensors, as demonstrated in Fig. 5.2(b). Based on these results, it would be most ideal to image the LCA and RCA with sensors located on the left and right eye, respectively. Fig. 5.2(c) compares the relative probability distributions of the log-compressed signal energies received by the sensors placed in the ideal imaging locations defined above. Although the left and right distributions share energy values in similar ranges (i.e.,  $-41.81$  dB to  $-6.11$  dB and  $-44.05$  dB to  $0$  dB, respectively), the right distribution is skewed toward higher energy measurements than the left distribution. In particular, the median of the right eye energy distribution is  $6.41$  dB greater than the median of the left eye energy distribution.

Fig. 5.3 shows experimental photoacoustic results from the same human cadaver

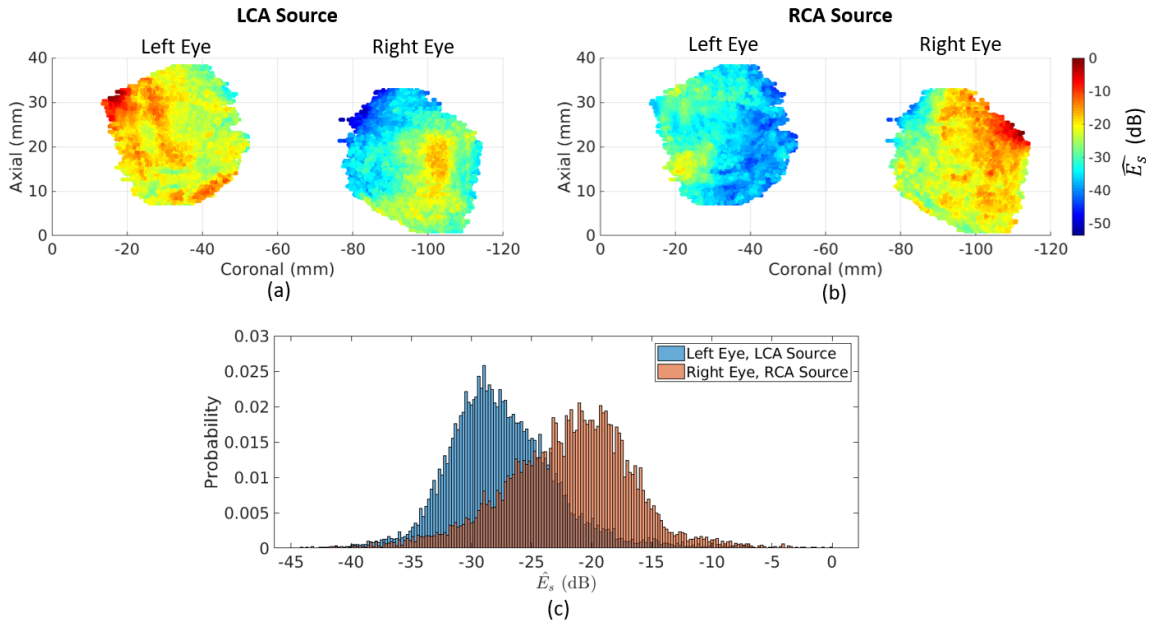


Figure 5.2: Visualization of k-Wave acoustic sensor data for sensors placed on the left and right eyelids of the cadaver head when the photoacoustic source is the (a) LCA and (b) RCA. (c) Histograms of the probability of a left or right eyelid sensor receiving a log-compressed total signal energy in the range 0 to  $-45$  dB. Each histogram represents energies from sensors on a singular eyelid when illuminating the corresponding carotid artery independently, calculated using Eq. 5.2.

head that was simulated to obtain the results in Fig. 5.2. Photoacoustic images obtained from each eyelid probe position were overlaid on co-registered ultrasound images. When imaging from the left eye, background noise was present in the photoacoustic image, reducing the overall LCA visibility (Fig. 5.3(a)). When imaging from the right eye, less background noise was present, enabling better RCA visibility (Fig. 5.3(b)). Fig. 5.3(c) compares the relative probability distributions of the log-compressed photoacoustic image amplitudes from ROIs within the photoacoustic targets in Figs. 5.3(a) and 5.3(b), as calculated by Eq. 5.3. The right distribution is skewed toward higher amplitude measurements than left distribution. In particular,

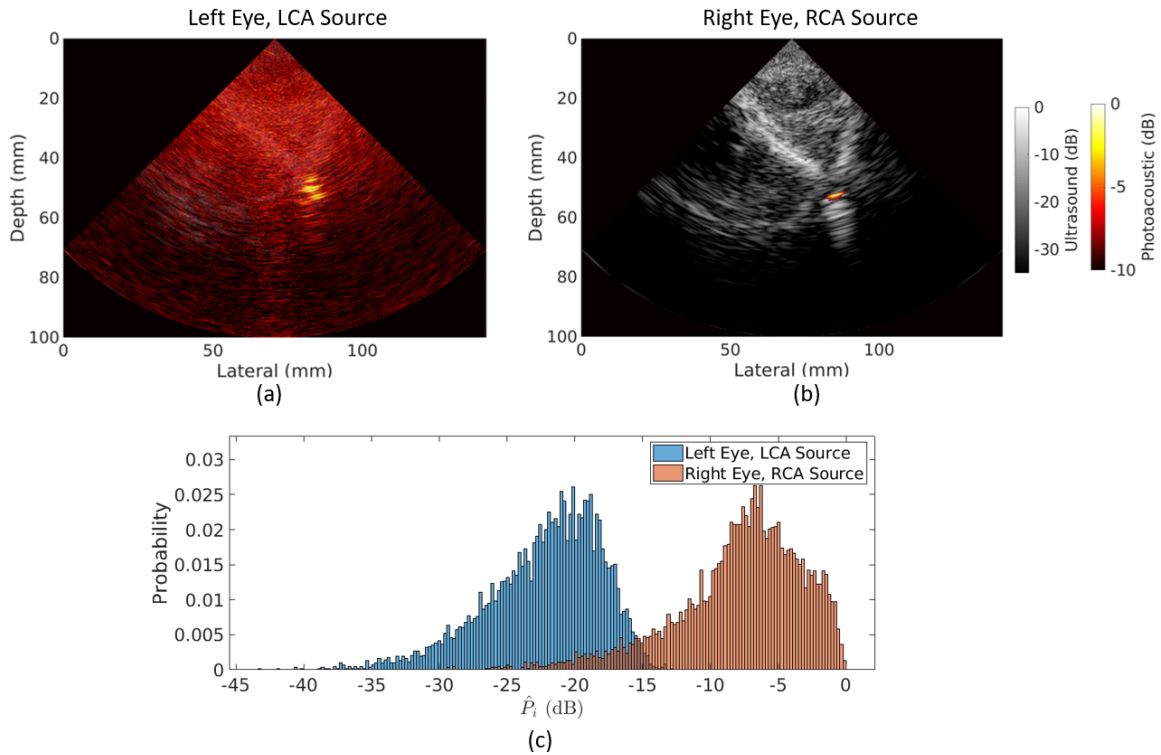


Figure 5.3: DAS photoacoustic images from the fresh cadaver, overlaid on co-registered ultrasound images when the transducer location and photoacoustic source are the (a) left eyelid and LCA and (b) right eyelid and RCA. The images were normalized to the brightest pixel within the image. (c) Histograms of the probability of an image pixel within a region of interest inside the photoacoustic source in the DAS images having an amplitude in the range 0 to -45 dB, calculated using Eq. 5.3.

the distributions have amplitude values in the range -43.12 dB to -12.86 dB and -29.41 dB to 0 dB, for the left and right eye images, respectively. The median of the left and right image amplitude distributions are -21.55 dB and -7.05 dB, respectively.

#### 5.4 Discussion

The work presented in this paper used experimental cadaver imaging to validate the predictions of simulation studies based on the same cadaver head. In particular, two predictions were made from the simulations results. First, it is optimal to place the acoustic receiver on the left and right eyelids when imaging the LCA and RCA, respectively (see Figs. 5.2(a) and 5.2(b)). Second, when using these optimal locations, there is a left-right asymmetry between the received energies for this particular patient (see Fig. 5.2(c)). The simulation study prediction of asymmetry was confirmed with experimental images, which demonstrated greater ICA visibility and greater pixel amplitudes in the image obtained with the right eyelid probe location when compared to that of the left eyelid probe location (see Fig. 5.3). The left-right asymmetry is most likely due to anatomical differences in the acoustic pathways from the ICA sources to their respective ocular cavity opening. Therefore, the agreement between cadaver and simulation results demonstrates that simulations can potentially provide patient-specific predictions of photoacoustic image quality based on a patient's unique skull base anatomy.

In addition, results demonstrate the promise of photoacoustic simulations as a tool for patient-specific preoperative surgical planning of optimal receiver locations when using photoacoustic imaging as an intraoperative navigation technique. Presurgical identification of receiver locations offers three primary benefits in photoacoustic image-guided surgery. First, this presurgical identification would eliminate wasting valuable operating room time to search for and find a suitable transducer location, thereby reducing the time the patient is under anesthesia, the total procedure du-

ration, and the medical cost. The second benefit is removal of the potential barrier that the surgeon may be unable to identify a viable transducer location and therefore unable to use photoacoustic image-guidance during the procedure. The third benefit is identification of transducer locations which would minimize image quality degradation from the presence of bone and thereby produce photoacoustic images of the ICAs with the best image quality possible for the patient.

## 5.5 Conclusion

This paper is the first to use photoacoustic amplitude distributions from a human cadaver to validate that simulations sufficiently model patient-specific asymmetries in the skull base. Experimental results also demonstrate that simulations can predict photoacoustic image quality when using the eyelids as the receiver location. Photoacoustic energy measurements from simulations and amplitude measurements from experiments revealed that the right eyelid receiver location outperformed the left eyelid receiver location. These results highlight the promise of simulations as a patient-specific presurgical planning tool when using photoacoustic imaging as an intraoperative navigation technique.

## 5.6 Acknowledgements

Funding was provided by National Science Foundation (NSF) CAREER Award ECCS-1751522, NSF SCH Award NSF IIS-2014088, and in part by NSF Graduate Research Fellowship DGE1746891.

## References

- [1] M. T. Graham, F. X. Creighton, and M. A. L. Bell, “Validation of eyelids as acoustic receiver locations for photoacoustic-guided neurosurgery,” in *Photons*

- Plus Ultrasound: Imaging and Sensing 2021*, International Society for Optics and Photonics, vol. 11642, 2021, p. 1 164 228.
- [2] P. Cappabianca, L. M. Cavallo, and E. de Divitiis, “Endoscopic endonasal transsphenoidal surgery,” *Neurosurgery*, vol. 55, pp. 933–941, 2004.
- [3] M. S. Agam, M. A. Wedemeyer, B. Wrobel, M. H. Weiss, J. D. Carmichael, and G. Zada, “Complications associated with microscopic and endoscopic transsphenoidal pituitary surgery: Experience of 1153 consecutive cases treated at a single tertiary care pituitary center,” *Journal of Neurosurgery*, vol. 130, no. 5, pp. 1576–1583, 2018.
- [4] M. A. L. Bell, A. K. Ostrowski, K. Li, P. Kazanzides, and E. M. Boctor, “Localization of transcranial targets for photoacoustic-guided endonasal surgeries,” *Photoacoustics*, vol. 3, no. 2, pp. 78–87, 2015.
- [5] —, “Quantifying bone thickness, light transmission, and contrast interrelationships in transcranial photoacoustic imaging,” in *Proceedings of SPIE, Photons Plus Ultrasound: Imaging and Sensing*, vol. 9323, 2015.
- [6] M. A. L. Bell, A. B. Dagle, P. Kazanzides, and E. M. Boctor, “Experimental assessment of energy requirements and tool tip visibility for photoacoustic-guided endonasal surgery,” in *Proceedings of SPIE, Photons Plus Ultrasound: Imaging and Sensing*, vol. 9708, 2016, p. 97080D.
- [7] M. A. L. Bell, A. K. Ostrowski, P. Kazanzides, and E. M. Boctor, “Feasibility of transcranial photoacoustic imaging for interventional guidance of endonasal surgeries,” in *Proceedings of SPIE, Photons Plus Ultrasound: Imaging and Sensing*, vol. 8943, 2014, p. 894 307.
- [8] M. T. Graham, F. X. Creighton, and M. A. L. Bell, “Investigation of acoustic windows for photoacoustic imaging of intracranial blood vessels,” in *2020 IEEE International Ultrasonics Symposium (IUS)*, IEEE, 2020, pp. 1–4.

- [9] M. T. Graham, J. Huang, F. Creighton, and M. A. L. Bell, “Simulations and human cadaver head studies to identify optimal acoustic receiver locations for minimally invasive photoacoustic-guided neurosurgery,” *Photoacoustics*, p. 100 183, 2020.
- [10] M. A. Lediju Bell, “Photoacoustic imaging for surgical guidance: Principles, applications, and outlook,” *Journal of Applied Physics*, vol. 128, no. 6, p. 060 904, 2020.
- [11] X. Wang, D. L. Chamberland, and G. Xi, “Noninvasive reflection mode photoacoustic imaging through infant skull toward imaging of neonatal brains,” *Journal of neuroscience methods*, vol. 168, no. 2, pp. 412–421, 2008.
- [12] T. Kirchner, J. Gröhl, N. Holzwarth, M. A. Herrera, A. Hernández-Aguilera, E. Santos, and L. Maier-Hein, “Photoacoustic monitoring of blood oxygenation during neurosurgical interventions,” in *Proceedings of SPIE, Photons Plus Ultrasound: Imaging and Sensing*, vol. 10878, 2019, pp. 14–18.
- [13] M. F. Kircher, A. De La Zerda, J. V. Jokerst, C. L. Zavaleta, P. J. Kempen, E. Mittra, K. Pitter, R. Huang, C. Campos, F. Habte, R. Sinclair, C. W. Brennan, I. K. Mellinshoff, E. C. Holland, and S. S. Gambhir, “A brain tumor molecular imaging strategy using a new triple-modality mri-photoacoustic-raman nanoparticle,” *Nature Medicine*, vol. 18, no. 5, pp. 829–834, 2012.
- [14] M. Kneipp, J. Turner, H. Estrada, J. Rebling, S. Shoham, and D. Razansky, “Effects of the murine skull in optoacoustic brain microscopy,” *Journal of Biophotonics*, vol. 9, no. 1-2, pp. 117–123, 2016.
- [15] G. Pinton, J.-F. Aubry, E. Bossy, M. Muller, M. Pernot, and M. Tanter, “Attenuation, scattering, and absorption of ultrasound in the skull bone,” *Medical Physics*, vol. 39, no. 1, pp. 299–307, 2012.

- [16] H. Estrada, J. Rebling, J. Turner, and D. Razansky, “Broadband acoustic properties of a murine skull,” *Physics in Medicine & Biology*, vol. 61, no. 5, p. 1932, 2016.
- [17] B. E. Treeby and B. T. Cox, “K-Wave: MATLAB toolbox for the simulation and reconstruction of photoacoustic wave fields,” *Journal of Biomedical Optics*, vol. 15, no. 2, p. 021 314, 2010.
- [18] B. E. Treeby, B. T. Cox, and J. Jaros, *A matlab toolbox for the time domain simulation of acoustic wave field, user manual, (2016) manual version 1.1, toolbox release 1.1*, version Version 1.1, Toolbox Release 1.1, 2016, August 27, 2016.

# Chapter 6

## Workflow and Vision for Clinical Translation of Acoustic Windows Identified with Presurgical, Patient-Specific Simulations

*The work presented in this chapter was published in the following manuscript:*

M. T. Graham, R. A. Dunne, and M. A. L. Bell, “Comparison of compressional and elastic wave simulations for patient-specific planning prior to transcranial photoacoustic-guided neurosurgery,” *Journal of Biomedical Optics*, vol. 26, no. 7, p. 076 006, 2021.

### 6.1 Introduction

The endonasal transsphenoidal approach to pituitary tumor resection is a minimally invasive technique that requires insertion of surgical instruments through the nose to remove sphenoid bone and underlying pituitary tumors [2]. Although the procedure is generally safe [3], morbidity and mortality rates rise to 14-23% and 24-26%, respectively, if iatrogenic injury to the internal carotid arteries (ICAs) occurs [4]–[6]. Current intraoperative guidance techniques, such as stereotactic guidance and endoscopy, enable monitoring of the ICAs in close proximity to the surgical site, how-



ever, they suffer from two primary limitations. First, stereotactic guidance is subject to registration errors which can become increasingly large as patient anatomy is disrupted during surgery and deviates from the anatomy in preoperative x-ray computed tomography (CT) or magnetic resonance (MR) images. Second, endoscopy is unable to identify the ICAs when they are obscured by bone or other tissues in the operative path. Our group is investigating the use of transcranial photoacoustic imaging as an intraoperative imaging technique for real-time visualization of the ICAs to address these two limitations, as detailed in our original research papers [7]–[12] and summarized in literature surveys on this topic [13], [14].

To achieve photoacoustic imaging for guidance of endonasal transsphenoidal surgery, we propose the insertion of light-transmitting fiber optic devices in the nasal cavity, similar to other surgical tools [7]–[13]. This light source will then excite the hemoglobin within the ICAs, converting the absorbed optical energy to acoustic energy that is received by an externally placed ultrasound receiver. The external ultrasound receiver placement results in a transcranial photoacoustic imaging scenario, which is challenged by acoustic interactions with bone and is known to degrade image quality [15]–[17]. Previous work from our group developed and demonstrated a simulation method to identify naturally occurring acoustic windows in the adult human skull in order to minimize acoustic interactions with bone and to provide high-contrast photoacoustic images of the ICAs [11], [12]. We demonstrated that patient-specific simulations have the potential to enable preoperative planning to determine appropriate placement of imaging system components [11], [12].

Our vision for a presurgical workflow with the use of simulations is shown in Fig. 6.1, in direct comparison to a workflow without access to presurgical simulations. Without simulations, a surgeon may need to search and find optimal locations to place an ultrasound receiver to best receive the acoustic signals within the skull. This intraoperative process may be prone to the expenditure of time that could in-

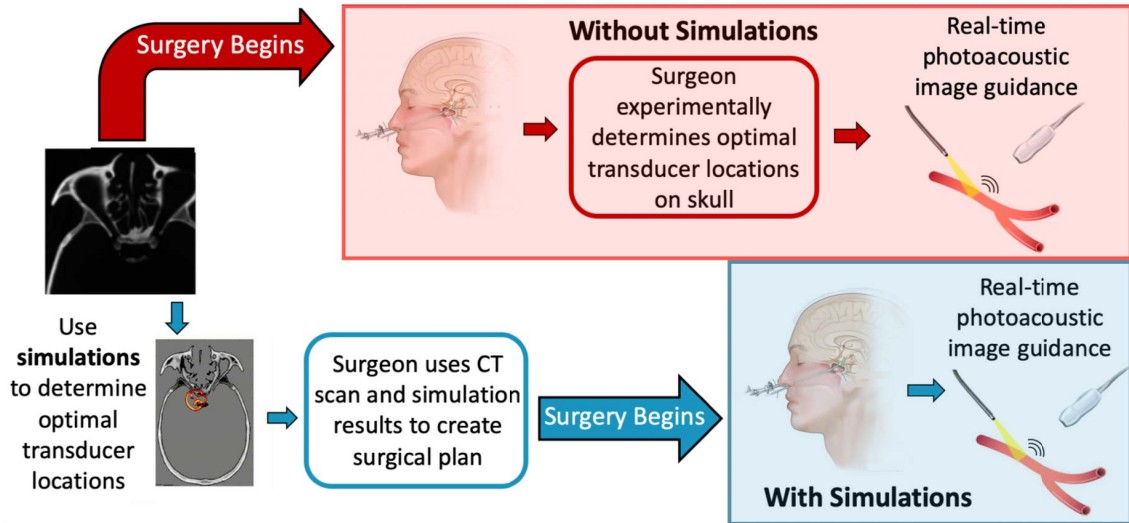


Figure 6.1: Surgical workflow with and without the use of patient-specific simulations. Without photoacoustic simulations, a surgeon will likely have to test multiple ultrasound receiver locations and their feasibility. Simulations have the potential to efficiently identify these locations before the surgical procedure.

stead be spent operating on the patient and would also increase the time that the patient is under anesthesia and on the operating table. In addition, the surgeon may have to abandon the use of intraoperative photoacoustic image guidance during the procedure if a viable receiver location is not determined in time, thereby sacrificing the benefits of real-time photoacoustic-based guidance during the surgery [12]. In contrast, the simulations that we propose have the potential to preoperatively identify patient-specific ultrasound receiver locations [12]. The surgeon may then use the simulation results and the patient’s preoperative CT scan to construct a time-efficient surgical plan for each operation. With this step completed, the neurosurgery may then be safely executed with the benefit of real-time, intraoperative photoacoustic image guidance.

Our group previously identified the ocular cavity, temporal region, and nasal cavity as three optimal ultrasound receiver locations, using compressional-wave-only simulations [11], [12]. However, the shear waves known to propagate within dense media

such as bone were excluded from our initial demonstrations. As an alternative, elastic wave simulations which include both compressional and shear waves, are expected to more accurately represent the physical acoustic process. However, elastic wave simulations, such as the k-Wave elastic simulations based on the classical Kelvin-Voigt absorption model, are time consuming and memory intensive [18]. Time and memory costs reduce the ease and likelihood of clinical translation.

This paper presents a comparison of compressional and elastic photoacoustic k-Wave simulations in order to investigate which simulation type (i.e., compressional or elastic) is required for preoperative surgical planning. The remainder of this paper is organized as follows. Section 6.2 details the simulation methods and quantitative metrics used for the comparison. Section 6.3 presents the resulting comparisons. Section 6.4 discusses the implications of the results with respect to the compressional wave simulations that were used in our experimental validation studies, with regard to the vision presented in Fig. 6.1, and with an eye toward reducing barriers to clinical translation. Finally, Section 6.5 concludes the manuscript.

## 6.2 Methods

### 6.2.1 Simulation Configuration

Three-dimensional photoacoustic k-Wave [18]–[20] simulations were performed after converting the CT volume of a human cadaver skull into heterogeneous, volumetric maps of corresponding density, compressional and shear wave sound speeds, and compressional and shear wave absorption prefactors. Fig. 6.2 shows an example axial slice from the CT volume of a human cadaver skull. Homogeneous volumes were additionally modeled as the average density, sound speed, and absorption values of brain tissue in order to provide baseline photoacoustic images that do not contain heterogeneous tissue effects, such as aberration, attenuation, scattering and reverber-

ation. The simulated tissue properties for the heterogeneous and homogeneous cases are reported in Table 6.2. A 2-D cross-section of the propagating wave at various time points for the homogeneous and heterogeneous cases is shown in Fig. 6.3, , with more details available in Video 1. The computational grid was defined with a symmetric voxel size of 0.3 mm x 0.3 mm x 0.3 mm. Acoustic wave propagation was simulated with a sampling frequency of 82 MHz (i.e., time increment of  $1.12^{-8}$  seconds) on a NVIDIA Quadro RTX 6000 GPU (Table 6.1).

Phased array ultrasound transducers with 0.3 mm pitch, 13.5 mm height, 0 mm kerf, and 64 elements (as reported in Table 6.1) were positioned to receive transcranial photoacoustic signals from three acoustic windows: (1) the left ocular cavity, (2) the left temple region, and (3) the nasal cavity, as shown in Fig. 6.2. A spherical photoacoustic source with a diameter of 0.3 mm (i.e., a point source) or 4 mm (i.e., the diameter of a typical adult carotid artery) was placed in the location of the left carotid artery (LCA), as shown in Fig. 6.2. Background absorption was not modeled in the photoacoustic source distributions for the following two reasons. First, background

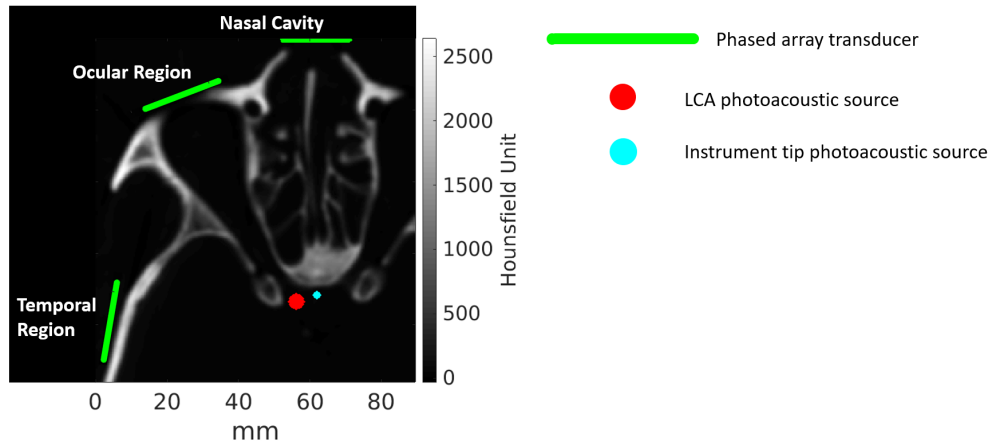


Figure 6.2: Axial slice from the CT volume of the human cadaver skull demonstrating a 2-D cross-section of the 3-D simulation configuration. Spherical photoacoustic sources were placed within the left internal carotid artery (LCA) and at distances of 6-13 mm from the LCA to represent a the tip of a surgical instrument (a distance of 6 mm is shown). Green lines illustrate locations of independently placed ultrasound transducers.

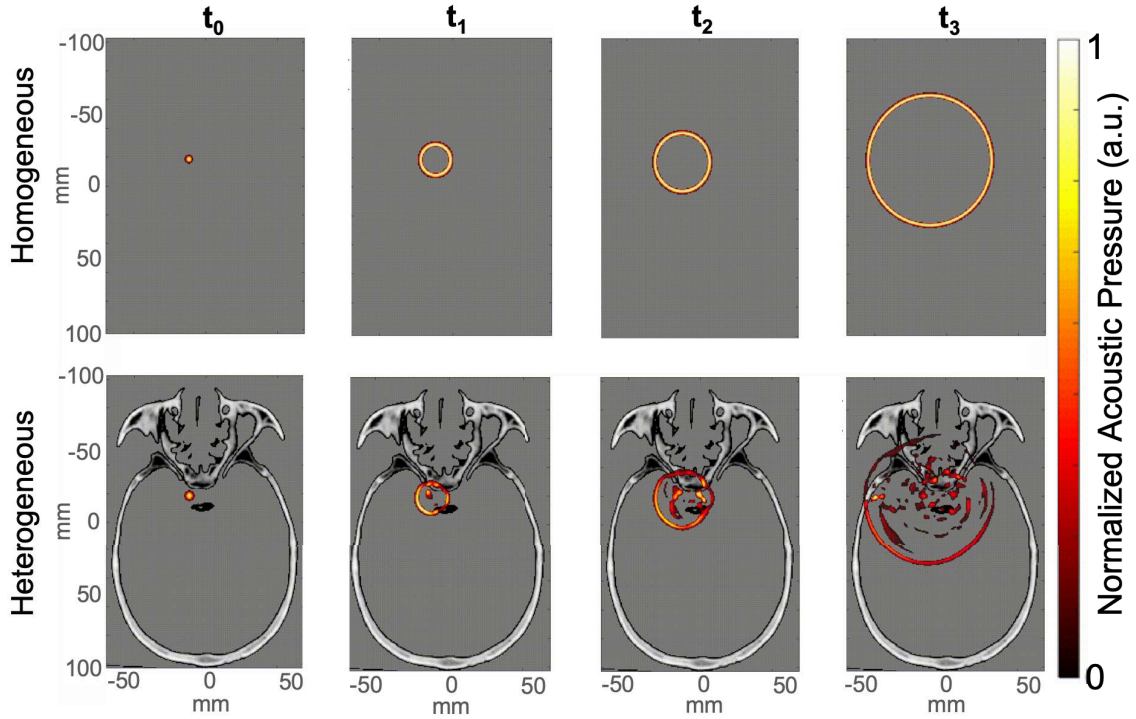


Figure 6.3: Two-dimensional cross-section of acoustic wave propagation at various time points (i.e.,  $t_0$  through  $t_3$ ) during the homogeneous (top) and heterogeneous (bottom) three-dimensional simulations. There is no bone present in the homogeneous simulation, as represented by the greyscale background. In both cases, the acoustic wave propagates spherically outward from the initial pressure distribution (location of left ICA). In the heterogeneous simulations, acoustic interactions with cranial bone cause distortions (i.e., aberrations, attenuation, scattering, reverberations) in the waveform which ultimately degrade image quality. See Video 1 for the evolution of wave propagation for these two simulations.

absorption can be mitigated by carefully selecting the illumination wavelength to preferentially excite the oxygenated hemoglobin over surrounding tissues [29]. Second, our previous observations in transcranial photoacoustic imaging of the cadaveric ICAs did not display evidence of background absorption [12].

To investigate photoacoustic image characteristics when the tip of a surgical instrument is also in the imaging plane, a 2 mm-diameter spherical photoacoustic source was positioned within the surgical site at distances of 6-13 mm from the 4 mm-diameter LCA target. These distances were measured from the centers of the LCA

Table 6.1: Transcranial photoacoustic simulation parameters.

Simulation Parameter	Values
<b>Transducer</b>	
Pitch	0.3 mm
Height	13.6 mm
Kerf	0.0 mm
Elements	64
Bandwidth	84.5%
Center Frequency	3.6 MHz
Field of View	90°
<b>Simulation Grid</b>	
Voxel Size	$0.3 \times 0.3 \times 0.3 \text{ mm}^3$
Sampling Frequency	82 MHz

Table 6.2: Simulated tissue properties of the homogeneous and heterogeneous volumetric maps [19], [21]–[26]. The two shear wave properties of sound speed in brain and absorption power law prefactors in bone and brain are not explicitly known. However, these properties can be estimated as approximately half the corresponding compressional speed of sound and approximately double the corresponding compressional absorption power law prefactor [25], [27].

		Speed of Sound (m/s)	Absorption Power Law Prefactor (dB MHz <sup>1.18</sup> /cm) [20], [28]	Density (kg/m <sup>3</sup> )
<b>Bone</b>	Compression	1300-3492 [19], [21]	1.36-2.50 [23]	812-2770 [19], [22]
	Shear	650-1746 [25]	2.71-5.00*	
<b>Brain</b>	Compression	1519 [26]	0.21 [23], [24]	1045 [26]
	Shear	800*	0.75*	

\*Estimated shear wave values

and instrument targets. Considering this measurement and the best possible system resolution described in Section 6.2.2, the minimum distance simulated was 6 mm. The distances of the LCA source relative to the center of the transducers located on the ocular, nasal, and temple regions were 7.40 cm, 8.02 cm, and 5.03 cm, respectively.

### 6.2.2 Image Formation and Analysis

Received transducer channel data were bandpass filtered to contain -6 dB frequencies in the range 1-5 MHz. Randomly distributed Gaussian noise was added to the received channel data obtained with the transducer located in the temporal region in order to model the electronic noise of an imaging system, resulting in a 15 dB channel signal-to-noise ratio (SNR). The same noise distribution was then added to the received channel data obtained with the remaining transducer locations (i.e., nasal and temple regions) in order to simulate the same noise floor for the three transducer locations, each viewing photoacoustic signals of the same 4 mm target.

Photoacoustic delay-and-sum (DAS) images were generated from the filtered channel data with additive noise. Although advanced beamforming techniques exist to compensate for acoustic heterogeneity [30]–[32], the DAS beamformer is a more standard choice that was selected to compare acoustic heterogeneity effects between the two simulation types. DAS image quality (i.e., resolution, target visibility, and target detectability) was measured for each transducer location. Resolution was assessed by calculating the area of the -6 dB contour of the point spread function (PSF), measured from images of the point target. The best possible system resolution was also measured as the distance of the minimum cross-section through the center of the -6 dB contour with the smallest area. Target visibility was assessed using images of the the 4 mm-diameter LCA target to measure contrast, signal-to-noise ratio (SNR), and contrast-to-noise ratio (CNR), while target detectability was assessed using the generalized contrast-to-noise ratio (gCNR) [33], [34]. These image quality metrics are defined as follows:

$$\text{Contrast} = 20 \log_{10} \left( \frac{\mu_t}{\mu_b} \right), \quad (6.1)$$

$$\text{SNR} = \frac{\mu_t}{\sigma_b}, \quad (6.2)$$

$$\text{CNR} = \frac{|\mu_t - \mu_b|}{\sqrt{\sigma_t^2 + \sigma_b^2}}, \quad (6.3)$$

$$\text{gCNR} = 1 - \sum_{k=0}^{N_h-1} \min\{h_t(x_k), h_b(x_k)\}, \quad (6.4)$$

where  $\mu_t$  and  $\mu_b$  are the means,  $\sigma_t$  and  $\sigma_b$  are the standard deviations, and  $h_t$  and  $h_b$  are the histograms of the signal amplitudes within ellipsoidal regions of interest (ROIs) placed within the photoacoustic target (denoted by subscript  $t$ ) or within the background of the photoacoustic image (denoted by subscript  $b$ ),  $N_h$  is the number of bins in the histogram, and  $k$  is the index of the bin. A total of  $N_h = 145$  bins were used to create the histograms for the gCNR measurements. For each image, a singular target ROI was centered on the brightest pixel in the image. For the images obtained with the ocular and nasal transducer locations, six background ROIs were located around the target ROI to calculate means and standard deviations of image quality metrics. For the images obtained with the temple region transducer location, only five background ROIs were used because the sixth was outside the field of view of the transducer. The area of the target ROI and each background ROI were equivalent.

Target-to-instrument tip distances were measured from DAS photoacoustic images of the LCA and the instrument tip, calculated as the Euclidean distance between the centroid from each source. The distance error was calculated as the absolute difference between the measured target-to-instrument tip distance and the known target-to-instrument distance.

### 6.3 Results

Table 6.3 compares the execution time and memory usage of the three-dimensional compressional and elastic simulations, performed with the three independently placed transducers illustrated in Fig. 6.2. The last row of this table reports the mean time



and memory usage across the three simulations to demonstrate that elastic simulations required approximately 4.6x more time and 2.7x more memory than compressional simulations.

Figs. 6.4(a) and 6.4(b) show simulated photoacoustic channel data from the heterogeneous compressional and elastic simulations of the 0.3 mm-diameter LCA source obtained from the temple acoustic window. Although the initial wavefront shapes across elements look similar between the two simulation types, the compressional simulation has greater reverberations in the photoacoustic signal subsequent to the initial wavefront. To further appreciate the differences in the wavefronts between the simulation types, Fig. 6.4(c) shows the difference image of the elastic channel data subtracted from the compressional channel data. The wavefront in the compressional simulation has a greater amplitude than the wavefront in the elastic simulation, as indicated by the positive values along the wavefront in the difference image. Specifically the maximum amplitudes of the wavefronts were  $9e^{-5}$  Pa and  $6e^{-5}$  Pa for the compressional and elastic simulations, respectively.

Fig. 6.5(a) shows simulated photoacoustic images generated from the heterogeneous simulations of the 4 mm-diameter LCA source. The shape, location, and visibility of the targets generally agree between the compressional and elastic simulation pairs for each transducer location. Fig. 6.5(b) quantifies the target visibility and detectability of the heterogeneous simulated images displayed in Fig. 6.5(a). There were minimal differences in contrast, SNR, and CNR measurements, and the gCNR

Table 6.3: Comparison of execution times and memory usage for the compressional and elastic k-Wave simulations.

	<b>Time (minutes)</b>		<b>Memory (GB)</b>	
	Compressional	Elastic	Compressional	Elastic
<b>Ocular</b>	9.26	43.73	3.02	8.10
<b>Nasal</b>	10.24	47.79	3.22	8.65
<b>Temporal</b>	10.65	46.80	3.75	10.13
<b>Mean</b>	10.05	45.85	3.33	8.96

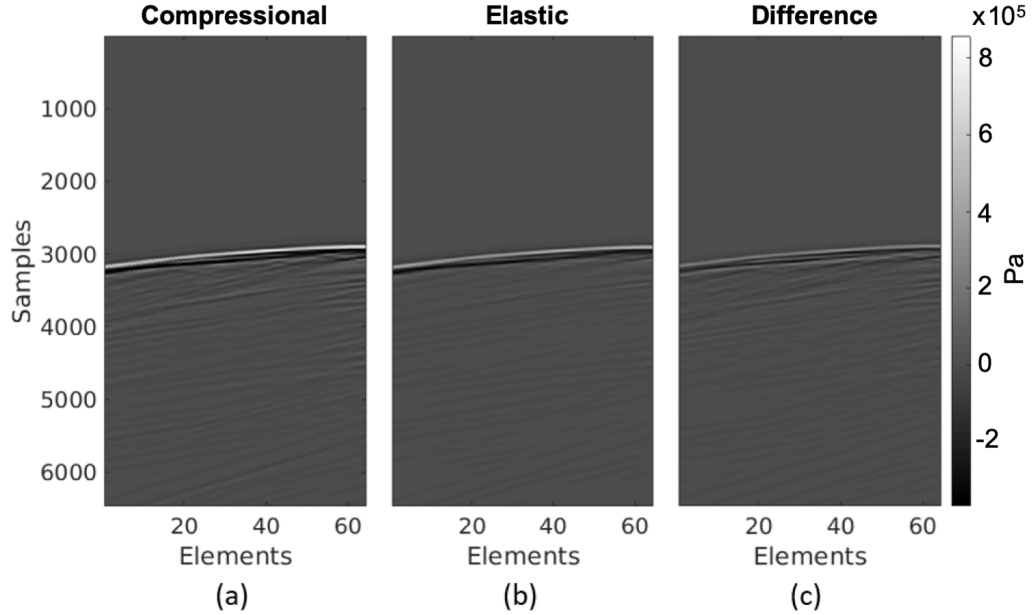
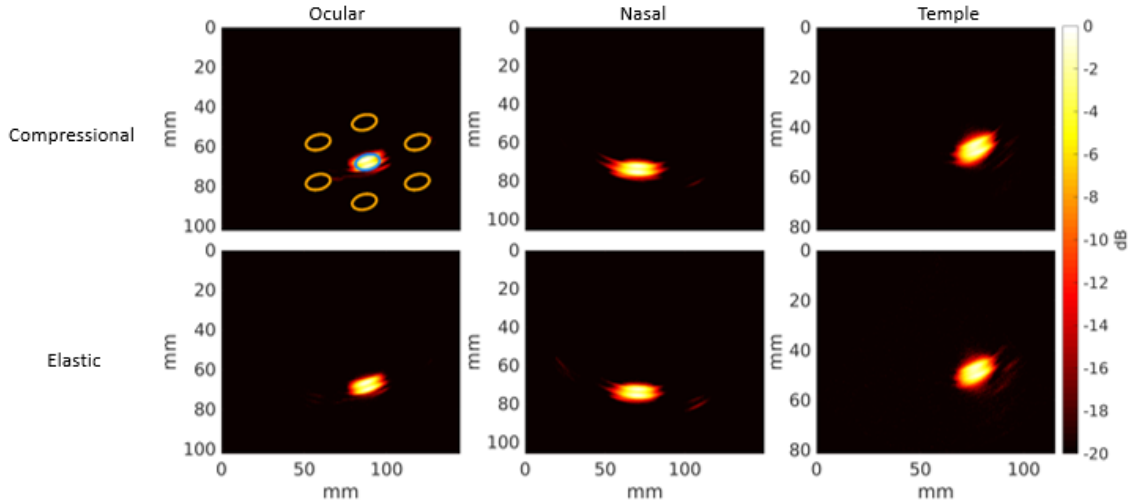


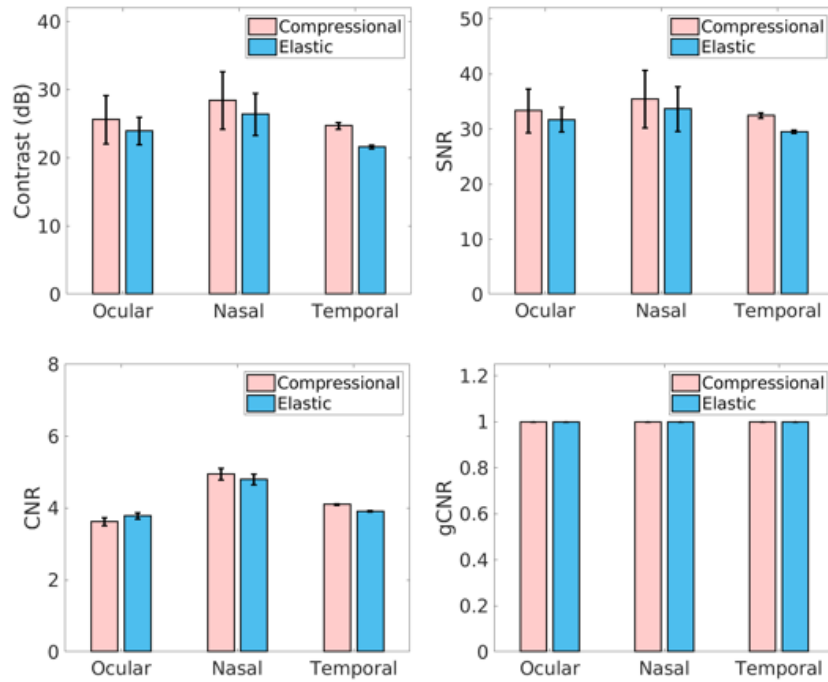
Figure 6.4: Simulated (a) compressional and (b) elastic photoacoustic channel data of the left internal carotid artery obtained with the temporal acoustic window. (c) Difference image of the elastic channel data subtracted from the compressional channel data.

measurements were equivalent. Therefore, the visibility and detectability of these photoacoustic image targets ranges from similar to equivalent for compressional and elastic wave simulations. As noted by Kempinski *et al.*[34], there is no benefit to improving particular methods when the gCNR is already near its maximum value of 1.0, and in this case the method is the type of simulation used for presurgical planning.

Figs. 6.6(a) and 6.6(b) show the -6 dB contours of the point target images from the homogeneous and heterogeneous simulations, respectively. The best resolution of the system was 1.4 mm, obtained from the shortest cross-section of the -6 dB contour of the homogeneous compressional simulation image obtained from the temporal region. Fig. 6.6(c) shows the calculated areas of the contours. The contour areas of the baseline homogeneous simulated images were  $9.33 \text{ mm}^2$ ,  $9.80 \text{ mm}^2$ , and  $6.60 \text{ mm}^2$  for the ocular, nasal, and temple acoustic windows, respectively, for compressional simulations and  $10.27 \text{ mm}^2$ ,  $11.05 \text{ mm}^2$ ,  $7.08 \text{ mm}^2$ , respectively, for elastic simulations. The areas of the corresponding simulated images obtained with the heterogeneous



(a)



(b)

Figure 6.5: (a) Simulated photoacoustic images of the left internal carotid artery obtained with the ocular, nasal, and temporal acoustic windows, from left to right respectively. The top and bottom rows show compressional and elastic simulation results, respectively. The single target and multiple background ellipsoidal regions of interest are outlined in blue and orange, respectively. Images are displayed with 10 dB dynamic range. (b) Corresponding mean  $\pm$  one standard deviation of contrast, signal-to-noise ratio (SNR), contrast-to-noise ratio (CNR), and generalized contrast-to-noise ratio (gCNR)[33], [34] measurements.

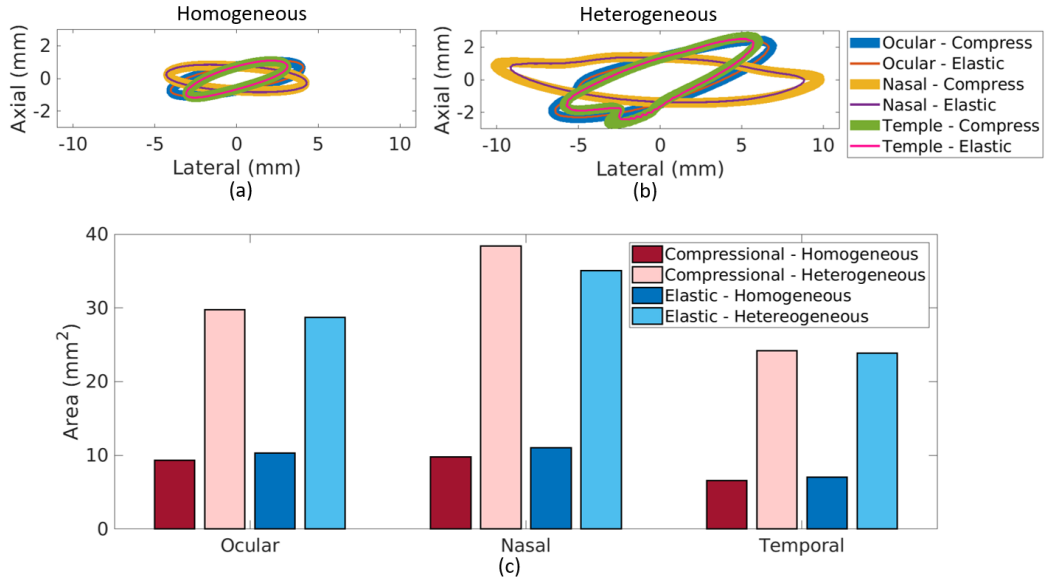


Figure 6.6: Point spread function -6 dB contours for the (a) homogeneous and (b) heterogeneous point target simulations. (c) Corresponding areas of the point spread function -6 dB contours. Homogeneous simulation measurements provide baseline resolution measurements without the negative effects of tissue heterogeneity.

skull model were  $29.78 \text{ mm}^2$ ,  $38.26 \text{ mm}^2$ ,  $24.22 \text{ mm}^2$ , respectively, for compressional simulations and  $28.76 \text{ mm}^2$ ,  $35.29 \text{ mm}^2$ ,  $24.21 \text{ mm}^2$ , respectively, for elastic simulations. Therefore, the resolution of these photoacoustic images is  $0.45\text{-}1.24 \text{ mm}^2$  better for the homogeneous compressional wave simulations than the homogeneous elastic wave simulations. However, in the presence of bone, the elastic wave simulations have  $0.33\text{-}3.35 \text{ mm}^2$  better resolution than compressional wave simulations for the heterogeneous case.

Fig. 6.7(a) shows an annotated photoacoustic image from a heterogeneous simulation of the LCA and a surgical instrument tip, obtained with the ocular acoustic window. The ground truth target-to-instrument distance is 11.27 mm and the measured target-to-instrument distance is 11.18 mm in this image. Fig. 6.7(b) displays image-based measurements of multiple target-to-instrument distances as a function of ground truth distances. The largest distance error between measurements and ground truth was obtained with the nasal cavity images, measuring 1.24 mm and 1.16 mm

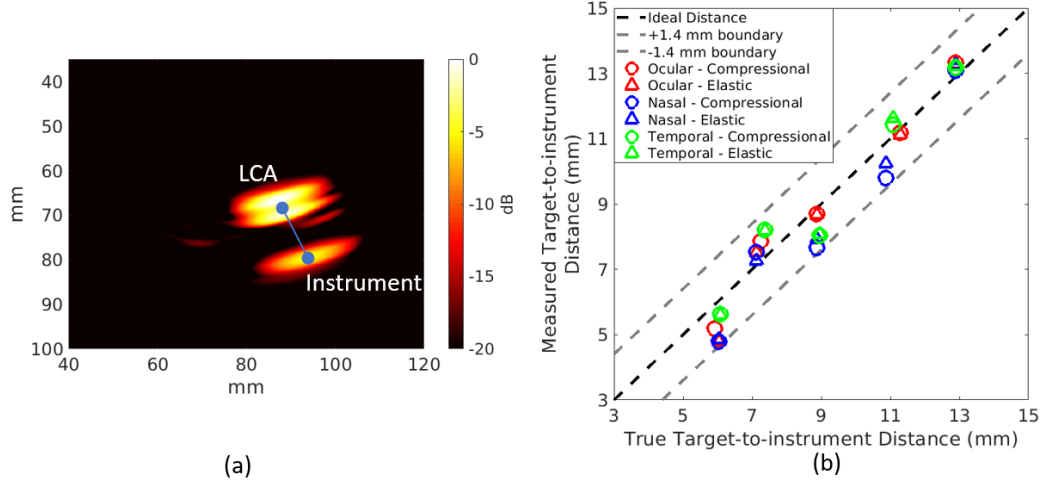


Figure 6.7: (a) Heterogeneous simulated photoacoustic images of the two sources representing the LCA and instrument tip, obtained with the ocular acoustic window at a relative distance of 11.27 mm. The target-to-instrument distance is the length of the line between the source centers in the image. (b) Comparison of measured target-to-instrument distances as a function of the true target-to-instrument distances for compressional ( $\circ$ ) and elastic ( $\triangle$ ) measurements in the ocular, nasal, and temporal acoustic windows. The ideal 1:1 relationship is shown as the dashed black line, with  $\pm 1.4$  mm boundaries, representing the best possible resolution of the system, indicated by the dashed gray lines.

for the compressional and elastic wave simulations, respectively.

The errors for the ocular and temporal regions ranged 0.09-0.91 mm and 0.14-0.88 mm for the compressional and elastic simulations, respectively. When comparing the target-to-instrument distance errors between the compressional and elastic simulations, the differences in errors were 0.03-0.09 mm, 0.07-0.45 mm, and 0.03-0.22 mm for the ocular, nasal, and temporal regions, respectively. Therefore, the relative target-to-instrument distances can be measured with accuracy within the 1.4 mm best possible resolution of the system from both compressional and elastic wave simulations.

## 6.4 Discussion

This paper details our investigations of k-Wave elastic wave simulations as a method for presurgical planning of transducer placement during transcranial photoacoustic-

guided neurosurgery. In particular, we assessed comparative differences in wave propagation, image quality (i.e., target visibility, target detectability, and target size estimation), and target-to-instrument tip distances (i.e., distances between a critical blood vessel and surgical instrument tip) using photoacoustic channel data and images generated from compressional and elastic transcranial simulations, resulting in three key observations. First, wavefronts in the channel data were similar in terms of general wavefront shape, but differed in amplitude and reverberations between the compressional and elastic simulations, as shown in Fig. 6.4. Second, target visibility and detectability were qualitatively and quantitatively similar between the compressional and elastic simulations for the three acoustic windows tested, as shown in Fig. 6.5. Third, the accuracy of target-to-instrument tip distances measured using either compressional or elastic simulations were generally similar between elastic and compressional simulations and were within the best possible resolution of the system, as shown in Fig. 6.7. Although the latter two observations (based on results presented in Figs. 6.5 and 6.7) may seem counterintuitive with respect to shear waves being the primary acoustic component during acoustic propagation in bone, we hypothesize that the similarity of target visibility, target detectability, and target-to-instrument distances between the two simulation types are due to the strategic choice of transducer location [12] (i.e., the length of acoustic interaction with bone is minimized along the pathway from the LCA source to transducers) and the relatively minimal thickness of bone with respect to the distance between the source and each transducer.

Our three key observations indicate that it is likely sufficient to utilize the less time-consuming, less memory-intensive k-Wave compressional simulations for presurgical planning, confirming that appropriate complexity was included when comparing simulation to experimental results from a human cadaver[12]. The arguably minimal 0.33-3.35 mm<sup>2</sup> area differences in point spread functions between k-Wave compressional and elastic simulations indicate that future investigations surrounding the ef-

fects of point spread function differences could be useful prior to completely eliminating elastic simulations from the presurgical planning process. In particular, for the three acoustic windows tested, the areas of the -6 dB contours of the point spread functions achieved with the compressional wave simulations was up to  $1.24 \text{ mm}^2$  better than that of the elastic wave simulations for the homogeneous case and up to  $3.35 \text{ mm}^2$  worse than that of the elastic simulations for the heterogeneous case, as shown in Fig. 6.6. A neurosurgeon user study could possibly be performed to determine if these differences in image resolution would substantially alter a neurosurgeon’s presurgical plan.

Note that our observations are specifically catered to simulation results obtained with the k-Wave Toolbox software package. A comparison with multiple other simulation packages [35]–[37] was beyond the scope of this paper. Using the k-Wave simulation package, we demonstrated for the first time that it is likely sufficient to sacrifice the accuracy of elastic wave simulations by solely relying on compressional wave simulations for presurgical planning. Although this sacrifice affects the photoacoustic waveforms sensed by the simulated receivers (as shown in Fig. 6.4) and image resolution (as shown in Fig. 6.6), it may not impact the image quality needed to make surgical decisions based on target detectability and target-to-instrument distance. Thus, we now have a better understanding of this pathway to advance intra-operative transcranial photoacoustic imaging of the internal carotid arteries toward surgical use.

Regarding the benefit of shorter simulation times, though minimally invasive neurosurgeries are rarely emergency procedures, surgeons waiting on simulations to complete before operating on a patient might create bottlenecks in presurgical planning. This issue could be a barrier to entry for this technology in hospitals which might not have access to or financial resources for powerful GPUs. Without the GPUs that we used to accelerate our simulations, elastic wave simulations could take several

hours to complete and ultimately disrupt the presurgical workflow. When utilizing compressional wave simulations, which require approximately 4.6x less time to simulate, surgeons can avoid these presurgical bottlenecks, regardless of their accessibility to GPUs. In addition, reduced computational memory places less strain on computational resource requirements for presurgical simulations and can enable surgeons to perform multiple patient-specific simulations at once. Thus, when implemented with compressional wave simulations, our proposed presurgical planning step has the potential to rapidly identify patient-specific optimal transducer locations for incorporation into the surgical plan, in support of our vision outlined in Fig. 6.1.

In summary, presurgical identification of optimal photoacoustic imaging system component locations with compressional wave simulations offers three primary benefits. First, this presurgical identification would eliminate wasting valuable operating room time to search for and find a suitable transducer location, thereby reducing the time the patient is under anesthesia, the total procedure duration, and the medical cost. The second benefit is removal of the potential barrier that the surgeon may be unable to identify a viable transducer location and therefore unable to use photoacoustic image-guidance during the procedure. The third benefit is identification of transducer locations which would minimize image quality degradation from the presence of bone and thereby produce photoacoustic images of the ICAs with the best image quality possible for the patient. Possible future work includes comparison of simulation types when modeling more complex source distributions, such as the possibility for optical absorption from the deoxygenated blood in the endothelial tubes of the cavernous sinus, and follow up neurosurgeon user studies.

## 6.5 Conclusion

The work presented in this paper is the first to reveal that the less time-consuming and less memory-intensive compressional k-Wave simulations are likely sufficient for



identification of optimal transducer locations for transcranial photoacoustic-guided surgery. This assessment is based on target visibility and detectability (e.g., target contrast, SNR, CNR, and gCNR) and relative source-to-instrument distance producing similar or identical quantitative measurements for compressional and elastic simulations. These results have multiple implications for reducing barriers for clinical translation of simulation-based photoacoustic-guided surgery.

## 6.6 Acknowledgements

This work was supported by the Computational Sensing and Medical Robotics Research Experience for Undergraduates Program (Grant No. EEC 1852155), NIH Grant No. R00EB018994, NSF CAREER Award Grant No. ECCS 1751522, and the NSF Graduate Research Fellowship Program (Grant No. DGE 1746891).

## References

- [1] M. T. Graham, R. A. Dunne, and M. A. L. Bell, “Comparison of compressional and elastic wave simulations for patient-specific planning prior to transcranial photoacoustic-guided neurosurgery,” *Journal of Biomedical Optics*, vol. 26, no. 7, p. 076 006, 2021.
- [2] P. Cappabianca, L. M. Cavallo, and E. de Divitiis, “Endoscopic endonasal transsphenoidal surgery,” *Neurosurgery*, vol. 55, pp. 933–941, 2004.
- [3] I. Ciric, A. Ragin, C. Baumgartner, and D. Pierce, “Complications of transsphenoidal surgery: Results of a national survey, review of the literature, and personal experience,” *Neurosurgery*, vol. 40, no. 2, pp. 225–237, 1997.
- [4] M. O. Perry, W. H. Snyder, and E. R. Thal, “Carotid artery injuries caused by blunt trauma,” *Annals of Surgery*, vol. 192, no. 1, pp. 74–77, 1980.

- [5] J. Raymond, J. Hardy, R. Czepko, and D. Roy, “Arterial injuries in transsphenoidal surgery for pituitary adenoma; the role of angiography and endovascular treatment,” *American Journal of Neuroradiology*, vol. 18, no. 4, pp. 655–665, 1997.
- [6] R. Valentine and P.-J. Wormald, “Carotid artery injury after endonasal surgery,” *Otolaryngologic Clinics of North America*, vol. 44, no. 5, pp. 1059–1079, 2011.
- [7] M. A. L. Bell, A. K. Ostrowski, K. Li, P. Kazanzides, and E. M. Boctor, “Localization of transcranial targets for photoacoustic-guided endonasal surgeries,” *Photoacoustics*, vol. 3, no. 2, pp. 78–87, 2015.
- [8] —, “Quantifying bone thickness, light transmission, and contrast interrelationships in transcranial photoacoustic imaging,” in *Proceedings of SPIE, Photons Plus Ultrasound: Imaging and Sensing*, vol. 9323, 2015.
- [9] M. A. L. Bell, A. B. Dagle, P. Kazanzides, and E. M. Boctor, “Experimental assessment of energy requirements and tool tip visibility for photoacoustic-guided endonasal surgery,” in *Proceedings of SPIE, Photons Plus Ultrasound: Imaging and Sensing*, vol. 9708, 2016, p. 97080D.
- [10] M. A. L. Bell, A. K. Ostrowski, P. Kazanzides, and E. M. Boctor, “Feasibility of transcranial photoacoustic imaging for interventional guidance of endonasal surgeries,” in *Proceedings of SPIE, Photons Plus Ultrasound: Imaging and Sensing*, vol. 8943, 2014, p. 894307.
- [11] M. T. Graham, F. X. Creighton, and M. A. L. Bell, “Investigation of acoustic windows for photoacoustic imaging of intracranial blood vessels,” in *2020 IEEE International Ultrasonics Symposium (IUS)*, IEEE, 2020, pp. 1–4.
- [12] M. T. Graham, J. Huang, F. Creighton, and M. A. L. Bell, “Simulations and human cadaver head studies to identify optimal acoustic receiver locations for min-

- minally invasive photoacoustic-guided neurosurgery,” *Photoacoustics*, p. 100 183, 2020.
- [13] M. A. Lediju Bell, “Photoacoustic imaging for surgical guidance: Principles, applications, and outlook,” *Journal of Applied Physics*, vol. 128, no. 6, p. 060 904, 2020.
- [14] A. Wiacek and M. A. L. Bell, “Photoacoustic-guided surgery from head to toe,” *Biomedical Optics Express*, vol. 12, no. 4, pp. 2079–2117, 2021.
- [15] M. Kneipp, J. Turner, H. Estrada, J. Rebling, S. Shoham, and D. Razansky, “Effects of the murine skull in optoacoustic brain microscopy,” *Journal of Biophotonics*, vol. 9, no. 1-2, pp. 117–123, 2016.
- [16] G. Pinton, J.-F. Aubry, E. Bossy, M. Muller, M. Pernot, and M. Tanter, “Attenuation, scattering, and absorption of ultrasound in the skull bone,” *Medical Physics*, vol. 39, no. 1, pp. 299–307, 2012.
- [17] H. Estrada, J. Rebling, J. Turner, and D. Razansky, “Broadband acoustic properties of a murine skull,” *Physics in Medicine & Biology*, vol. 61, no. 5, p. 1932, 2016.
- [18] K. Firouzi, B. Cox, B. Treeby, and N. Saffari, “A first-order k-space model for elastic wave propagation in heterogeneous media,” *The Journal of the Acoustical Society of America*, vol. 132, no. 3, pp. 1271–1283, 2012.
- [19] B. E. Treeby and B. T. Cox, “K-Wave: MATLAB toolbox for the simulation and reconstruction of photoacoustic wave fields,” *Journal of Biomedical Optics*, vol. 15, no. 2, p. 021 314, 2010.
- [20] B. E. Treeby, B. T. Cox, and J. Jaros, *A matlab toolbox for the time domain simulation of acoustic wave field, user manual, (2016) manual version 1.1, toolbox release 1.1*, version Version 1.1, Toolbox Release 1.1, 2016, August 27, 2016.

- [21] T. D. Mast, “Empirical relationships between acoustic parameters in human soft tissues,” *Acoustics Research Letters Online*, vol. 1, no. 2, pp. 37–42, 2000.
- [22] U. Schneider, E. Pedroni, and A. Lomax, “The calibration of ct hounsfield units for radiotherapy treatment planning,” *Physics in Medicine & Biology*, vol. 41, no. 1, p. 111, 1996.
- [23] F. A. Duck, *Physical properties of tissues: a comprehensive reference book*. Academic press, 2013.
- [24] D. White, G. Curry, and R. Stevenson, “The acoustic characteristics of the skull,” *Ultrasound in Medicine & Biology*, vol. 4, no. 3, pp. 225–252, 1978.
- [25] P. J. White, G. T. Clement, and K. Hynynen, “Longitudinal and shear mode ultrasound propagation in human skull bone,” *Ultrasound in Medicine & Biology*, vol. 32, no. 7, pp. 1085–1096, 2006.
- [26] B. A. Lloyd, “Tissue properties,” *IT’IS Foundation*, 2020.
- [27] G. T. Clement, P. J. White, and K. Hynynen, “Enhanced ultrasound transmission through the human skull using shear mode conversion,” *The Journal of the Acoustical Society of America*, vol. 115, no. 3, pp. 1356–1364, 2004.
- [28] B. E. Treeby and B. T. Cox, “Modeling power law absorption and dispersion for acoustic propagation using the fractional laplacian,” *The Journal of the Acoustical Society of America*, vol. 127, no. 5, pp. 2741–2748, 2010.
- [29] P. Beard, “Biomedical photoacoustic imaging,” *Interface Focus*, vol. 1, no. 4, pp. 602–631, 2011.
- [30] H. Estrada, X. Huang, J. Rebling, M. Zwack, S. Gottschalk, and D. Razansky, “Virtual craniotomy for high-resolution optoacoustic brain microscopy,” *Scientific Reports*, vol. 8, no. 1, p. 1459, 2018.

- [31] S. Govinahalli Sathyanarayana, B. Ning, R. Cao, S. Hu, and J. A. Hossack, “Dictionary learning-based reverberation removal enables depth-resolved photoacoustic microscopy of cortical microvasculature in the mouse brain,” *Scientific Reports*, vol. 8, no. 1, p. 985, 2018.
- [32] C. Huang, L. Nie, R. W. Schoonover, Z. Guo, C. O. Schirra, M. A. Anastasio, and L. V. Wang, “Aberration correction for transcranial photoacoustic tomography of primates employing adjunct image data,” *Journal of Biomedical Optics*, vol. 17, no. 6, p. 066 016, 2012.
- [33] A. Rodriguez-Molares, O. M. H. Rindal, J. D’hooge, S.-E. Måsøy, A. Austeng, M. A. L. Bell, and H. Torp, “The generalized contrast-to-noise ratio: A formal definition for lesion detectability,” *IEEE Transactions on Ultrasonics, Ferroelectrics, and Frequency Control*, vol. 67, no. 4, pp. 745–759, 2019.
- [34] K. M. Kempinski, M. T. Graham, M. R. Gubbi, T. Palmer, and M. A. L. Bell, “Application of the generalized contrast-to-noise ratio to assess photoacoustic image quality,” *Biomedical Optics Express*, vol. 11, no. 7, pp. 3684–3698, 2020.
- [35] F. Gao, X. Feng, and Y. Zheng, “Photoacoustic elastic oscillation and characterization,” *Optics Express*, vol. 23, no. 16, pp. 20 617–20 628, 2015.
- [36] J. Poudel, S. Na, L. V. Wang, and M. A. Anastasio, “Iterative image reconstruction in transcranial photoacoustic tomography based on the elastic wave equation,” *Physics in Medicine & Biology*, vol. 65, no. 5, p. 055 009, 2020.
- [37] S. Kang and J. Hwang, “Tuning the characteristics of photoacoustic pressure in a laser-induced photoacoustic generator: A numerical study,” *Applied Mathematical Modelling*, vol. 94, pp. 98–116, 2021.

# Chapter 7

## Conclusions and Future Directions

### 7.1 Summary

In this dissertation, theoretical, simulated, and experimental approaches were implemented to address challenges facing photoacoustic detection of the ICAs in the presence of bone. First, we derived a novel photoacoustic-specific spatial coherence theory and validated this theory for photoacoustic targets similar in size to adults ICAs (Chapter 2). This foundational theory justifies the implementation of advanced coherence-based techniques for improved ICA detection in bony environments, as well as detection of nearby surgical instruments illuminated with the photoacoustic effect. To maximize the full potential of our theoretical derivation, we developed an open-source toolbox to simulate and characterize coherence-based photoacoustic image investigations for clinical applications such as blood vessel and instrument tip detection (Chapter 3).

Next, we utilized SLSC imaging for ICA detection in a human cadaver head and differentiated intraoperative ICA tracking tasks most beneficial for coherence-based beamforming from those better suited to more traditional amplitude-based DAS beamforming (Chapter 4). Additionally, we presented a novel simulation-based

approach to identify naturally occurring acoustic windows within an adult cranium (Chapter 4). These windows reduce the attenuating, reverberating, and aberrating acoustic interactions with bone. We demonstrated the feasibility of these newly identified acoustic windows with human cadaver experiments. Our simulation-based approach is a promising tool for patient-specific pre-operative surgical planning of optimal receiver locations (Chapter 5). Finally, we fine-tuned this presurgical simulation method to reduce implementation barriers for clinical translation of intraoperative photoacoustic detection of the ICAs (Chapter 6).

From presurgical to intraoperative use, our contributions demonstrate a new paradigm for photoacoustic detection of the ICAs during minimally invasive neurosurgery, as illustrated in Fig. 7.1. In particular, preoperative CT scans may serve as inputs to both acoustic propagation (e.g., k-Wave) and photoacoustic spatial coherence simulations (e.g., PhocoSpace). Insights from these simulations enable strategic selection of photoacoustic imaging system parameters (e.g., acoustic windows, lag value for SLSC image display, and illuminating beam width) such that robust intraoperative detection of the ICAs with amplitude- and coherence-based photoacoustic images can be achieved.

## 7.2 From ICA detection to nerve detection

### 7.2.1 Rationale

As presented in Chapter 4 for the ICAs, both amplitude-based DAS beamforming and coherence-based SLSC beamforming are each uniquely suited to accomplish different intraoperative tasks. SLSC beamforming improves target detection in highly attenuating environments and changes in fluence measured by DAS image amplitudes can provide optical source-to-target distance measurements 4. These benefits can be extended beyond blood vessel detection, towards the prevention of iatrogenic injury

to other critical structures, such as nerves [1].

Similar to ICA injury, nerve injury has severe consequences (e.g., motor dysfunction, sensory dysfunction, decreased dexterity, chronic pain, and varying degrees of long-term disability) [2]–[6]. Similar to ICA detection, photoacoustic imaging of nerves is challenged by optical attenuation due to the presence of tissues along the optical pathway (e.g, muscle, tumor, and blood). In addition, photoacoustic detection of nerves is further challenged by the comparable optical absorption properties of nerves and surrounding tissue at isolated wavelengths [7]–[10]. These similar properties reduce target contrast and impede photoacoustic monitoring of nerves.

The benefits of SLSC and DAS beamforming can be exploited to overcome the two challenges noted above. Specifically when translating the benefits of DAS beamforming to the concept of nerve imaging, differences in tissue optical absorption as a function of the illuminating wavelength can be measured by DAS image amplitude to generate DAS image amplitude spectral measurements. These photoacoustic amplitude spectra can be exploited to differentiate nerve from background tissue. Our preliminary experiments with *ex vivo* external carotid artery and sciatic nerve

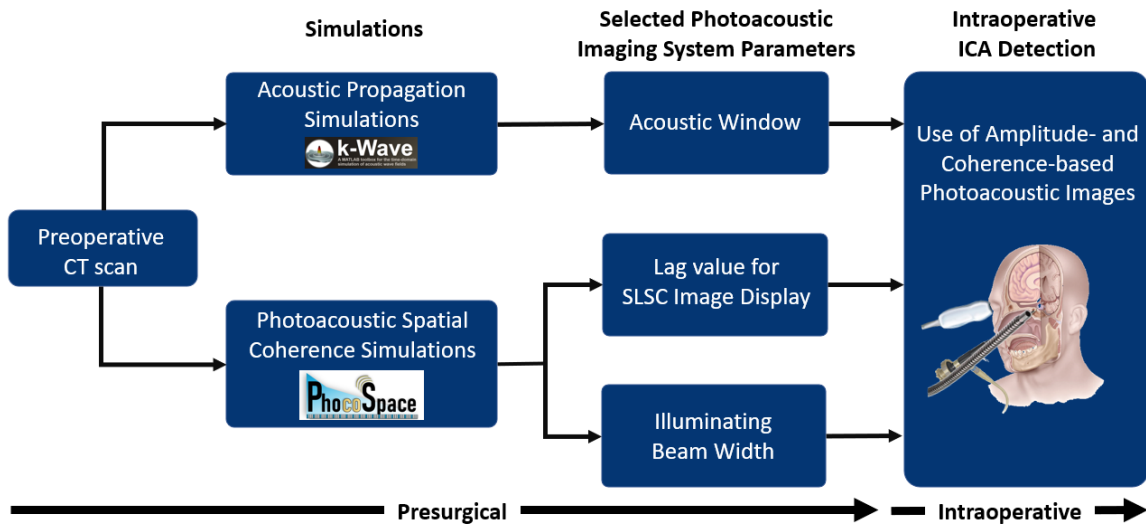


Figure 7.1: New paradigm for photoacoustic detection of the ICAs during minimally invasive neurosurgery.



tissue correlated changes in DAS image contrast with changes in the optical absorption spectrum of hemoglobin and lipids [1]. In particular, this work was the first to quantitatively differentiate between blood vessel and nerve specimens when excited with wavelengths in the ranges 690 - 800 nm (which resides in the NIR-I window) and 1200 - 1260 nm (which resides in the NIR-II window). Therefore, we propose a combined amplitude- and coherence-based multispectral imaging methodology for photoacoustic nerve imaging.

### 7.2.2 *Experimental methods*

Fig. 7.2 outlines a novel method for combined amplitude- and coherence-based multispectral photoacoustic imaging and detection of nerves. An *in vivo* porcine ulnar nerve was embedded in a plastisol phantom.<sup>†</sup> Two 3.9 mm-diameter fiber bundles (Armadillo SIA, Sunnyvale, CA, USA) coupled to an OPO (Opotek, Carlsbad, CA, USA) emitted pulse energies of 10.6 mJ/pulse and 4.1 mJ/pulse for wavelengths ranging 1200-1420 nm and 1600-1820 nm, respectively. Photoacoustic data were received with an Alpinion L8-17 transducer coupled to an Alpinion E-CUBE 12R ultrasound scanner (Alpinion Medical Systems, Seoul, South Korea). SLSC and DAS photoacoustic images were generated from the received data. SLSC images obtained with 1200 nm wavelength were used to locate ROIs indicating the nerve and background signals, indicated by the green and purple regions in the images in Fig. 7.2. The amplitude of each DAS image pixel within these SLSC-identified ROIs were measured as a function of wavelength to generate photoacoustic amplitude spectra. The photoacoustic amplitude spectra of a single pixel in each region is demonstrated in Fig. 7.2. Ground truth absorptivity measurements of the ulnar and plastisol phantom were obtained with a Cary 5000 dual beam spectrophotometer and external diffuse reflectance accessory (Agilent Technologies, Santa Clara, CA). Absorptivity

---

<sup>†</sup>Thanks to Sami Tuffaha, Nick von Guionneau, and Visakha Suresh for their assistance with *in vivo* data collection.

measurements of water and cholesterol, the primary optical absorbers in nerve, were also obtained.<sup>‡</sup>

### 7.2.3 Results from multispectral measurements of nerve tissue

Fig. 7.3 compares the ground truth absorptivity spectra and *in vivo* photoacoustic amplitude spectra. Figs. 7.3(a) and 7.3(b) show the absorptivity spectra measured at wavelengths 1200-1420 nm and 1600-1820 nm, respectively. The absorptivity spectra

<sup>‡</sup>Thanks to Susanna Thon and Arlene Chiu for their assistance with absorptivity data collection.

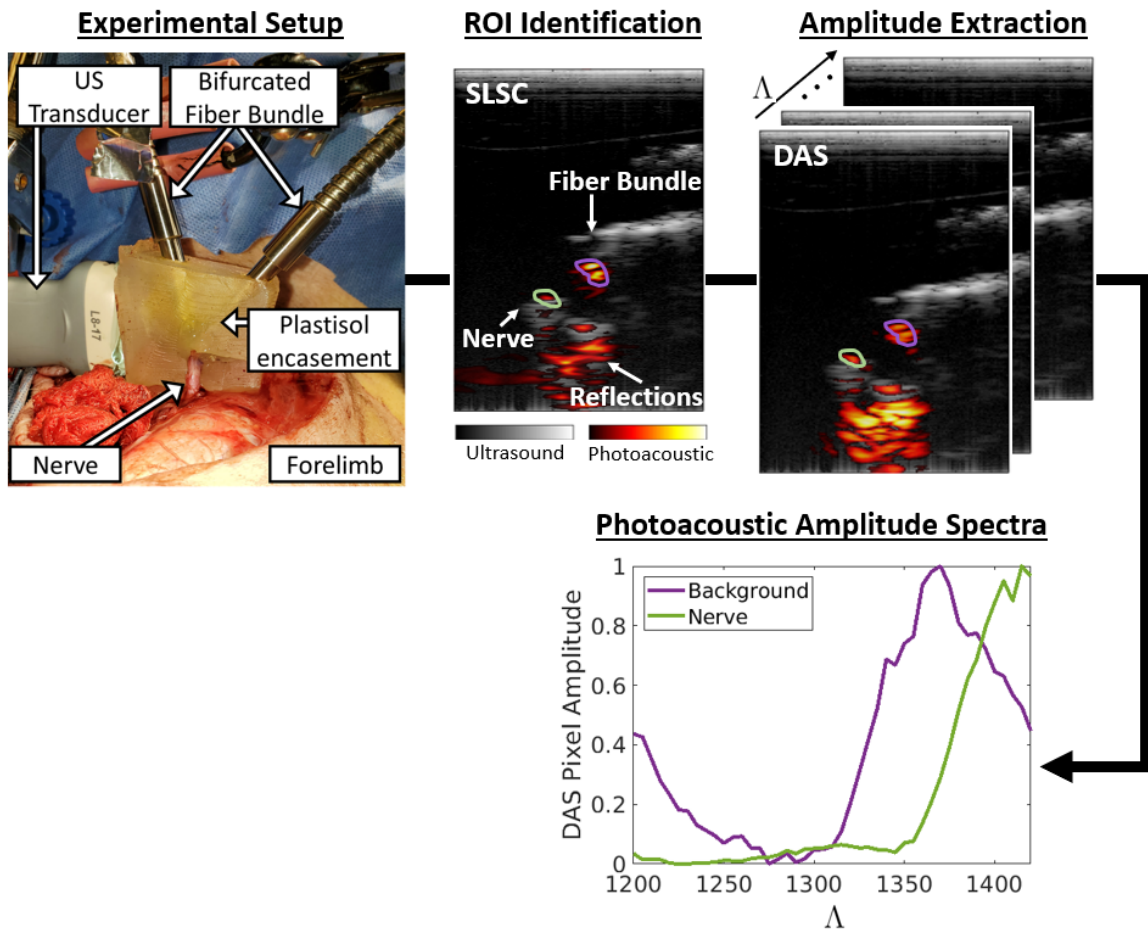


Figure 7.2: Schematic of the combined amplitude- and coherence-based multispectral imaging methodology indicating four key phases (1) experimental setup for data acquisition, (2) ROI identification with SLSC imaging (3) extraction of DAS pixel amplitude with SLSC-identified ROIs, and (4) generation of photoacoustic amplitude spectra.

of nerve and plastisol intersect at multiple wavelengths including 1290, 1360, 1405, 1645, and 1750 nm. Nerve and plastisol absorptivity measurements generally agree with the water and cholesterol absorptivity measurements, respectively. For example, both nerve and water exhibit local absorption peaks at 1420 nm and 1600 nm, and they both plateau above 1790 nm. Similarly, both plastisol and cholesterol exhibit local absorption peaks at 1200, 1395, and 1720 nm, with a slowed monotonic decrease in the range 1735-1765 nm.

Figs. 7.3(c) and 7.3(d) show *in vivo* photoacoustic amplitude spectra of nerve and plastisol, measured at wavelengths 1200-1420 nm and 1600-1820 nm, respectively. Similar to the corresponding absorptivity measurements, segments of these *in vivo* spectra overlap. However, two major discrepancies are observed between the absorptivity measurements and the photoacoustic amplitude spectra. First, the photoacoustic amplitude spectra have a 20 to 25 nm decrease in wavelength relative to the corresponding absorptivity measurements. For example, the plastisol absorptivity peaks at 1395 nm and 1720 nm occur at 1375 and 1695 nm, respectively, in the photoacoustic amplitude spectra. Second, the nerve photoacoustic amplitude spectra do not demonstrate the positive slope in absorption in the range 1680-1740 nm that is demonstrated in the corresponding absorptivity measurements.

#### 7.2.4 Interpretation of preliminary application to nerves and proposed next steps

The results presented in Section 7.2.3 demonstrate a possible combined amplitude- and coherence-based multispectral photoacoustic imaging methodology for visualizing and differentiating nerves from surrounding tissues. Although the absorptivity and photoacoustic amplitude spectra are equivalent between nerve and plastisol (i.e., target and background) at isolated wavelengths, each of these components also exhibit unique spectral features (Fig. 7.3). The presence or absence of these unique features in multispectral photoacoustic measurements can be exploited to identify the

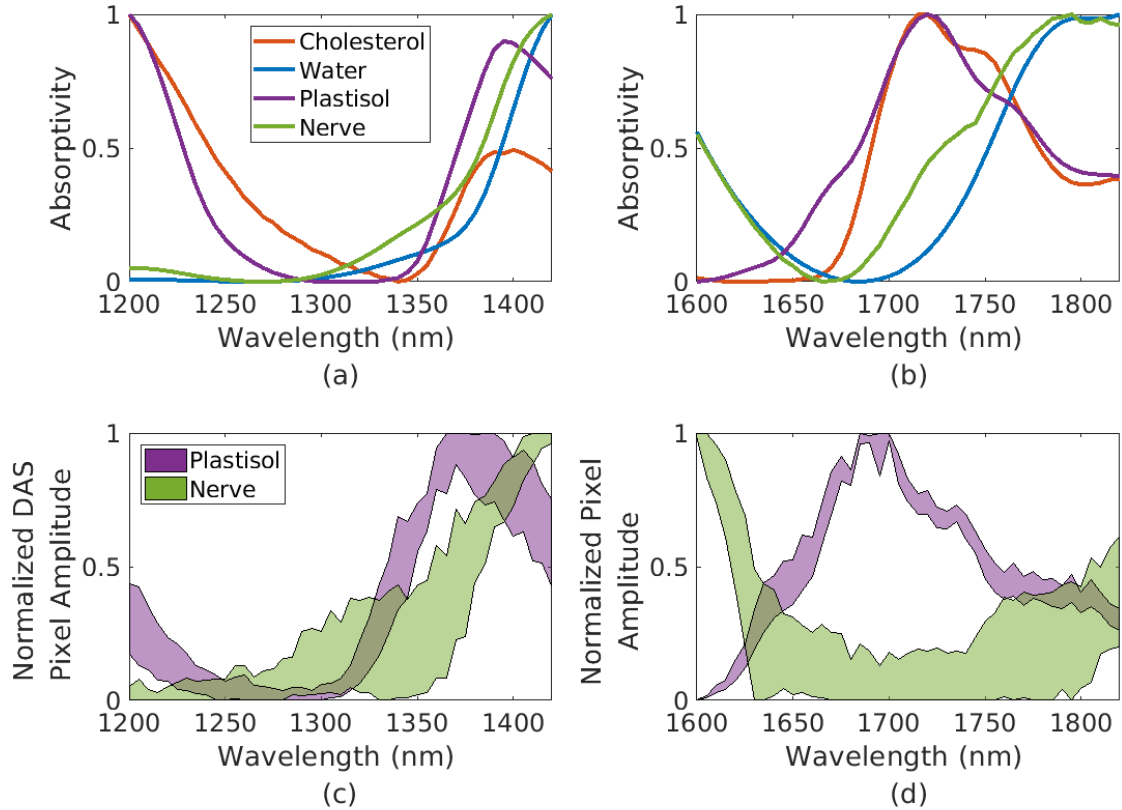


Figure 7.3: Absorptivity spectra of cholesterol, water, nerve, and plastisol measured at wavelengths (a) 1200-1420 nm and (b) 1600-1820 nm . (c,d) Corresponding photoacoustic amplitude spectra measured from SLSC-indicated regions in DAS images at wavelengths (c) 1200-1420 nm and (d) 1600-1820 nm. The top and bottom boundaries of the shaded regions represent the maximum and minimum, respectively, amplitude measured from the DAS image pixels within the SLSC-identified region at that wavelength.

photoacoustic signal as originating from nerve or plastisol. Additionally, these results demonstrate the unique benefits of SLSC and DAS beamforming. In particular, SLSC was beneficial for localizing signals of interest, followed by DAS being beneficial for differentiating the content of these identified signals of interest. A similar approach and finding was reported in [11], [12] to distinguish surgical biomarkers and in [13] to visualize and distinguish the uterine blood vessel from the ureter in a laparoscopic hysterectomy procedure. These benefits further highlight the necessity of strategically choosing between a coherence- or amplitude-based beamformer, based on the

goal of the intraoperative photoacoustic imaging task.

Future work will explore nerve tissue localization and differentiation in more complex imaging environments such as nerves embedded in tissue or nerves adjacent to major blood vessels. Future studies will also explore the identified discrepancies between the absorptivity measurements and photoacoustic amplitude spectra. For example, the absence of the positive slope in the range 1680-1740 nm of the *in vivo* nerve measurements can potentially be explained by DAS measurements capturing changes in fluence (as demonstrated in Chapter 4). In particular, the presence of an absorption peak for plastisol in the range 1680-1740 nm indicates a corresponding decay in fluence incident on the nerve in this range. A multispectral fluence correction technique could potentially eliminate the fluence changes and isolate the optical absorption characteristics in the photoacoustic measurements.

### 7.3 Additional Possible Directions

#### 7.3.1 Novel transducer designs

Novel transducer designs have the potential to augment methods for ICA and nerve visualization. Designs such as 3D transducers or 2D transducers translated with robotic control [14], [15], can generate volumetric photoacoustic reconstructions of the complex paths of the ICAs or nerves within the surgical area. Additionally, these volumes can enable localization of multiple targets of interest, such as an instrument tip and critical blood vessel or nerves, which do not simultaneously intersect a single imaging plane. For example, as mentioned in Chapter 4, only the ICA (and not the instrument tip) will be visualized at a given time when imaging a single plane through the identified ocular window [16]. Also as shown in Chapter 4, the anatomical relationship between the LCA and RCA within the surgical site indicates that they are unlikely to be simultaneously visualized through a singled acoustic window, even

with volumetric imaging. Alternatively, multiple transducers can be placed on separate acoustic windows to visualize targets separated by distances outside the feasible volumetric range encompassed by the proposed transducer designs.

### *7.3.2 Comparison to alternative image quality improvement solutions*

The advanced coherence-based beamforming techniques presented in this dissertation are one signal processing solution to improve photoacoustic image quality in the presence of bone. Competing solutions, such as complex time-reversal techniques [17]–[19] and machine learning techniques [20], [21], demonstrate reduction of reverberation artifacts, correction of signal aberration, improved resolution, and increased target contrast. Future studies can compare the image quality improvements, reconstruction accuracy, computational complexity, and clinical translatability between coherence-based beamforming and these alternative solutions. This multifaceted comparison would provide a comprehensive assessment of the advantages, disadvantages, and indications for use of each technique for photoacoustic imaging within bony environments.

### *7.3.3 Photoacoustic spatial coherence theory applied to brachytherapy seed detection*

Our photoacoustic spatial coherence theory in Chapter 2 can be extended beyond this dissertation to other clinical applications. One possibility is the visualization of brachytherapy seeds for prostate cancer treatment [22]–[26]. In particular, we applied the theoretical approach to the results in [22], where brachytherapy seeds, which have a cylindrical geometry and are made of metal, were embedded in a phantom and visualized with photoacoustic SLSC imaging.

The top row in Fig. 7.4 shows the dimensions of the seed targets with outlines showing the cross section of the target visualized within each column of the figure. When imaging the 0.8 mm diameter cross section of the seed, the experimental results

in the bottom row of Fig. 7.4 show that a higher lag value of  $M = 10$  provided better resolution than that at the lower lag value of  $M = 2$ . By modeling a similar target geometry with our theory (middle row), we see a trend that agrees with previous reports [22], [27]. In particular, the increase in  $M$  includes higher spatial frequency content and improves target boundary delineation.

When imaging the 4.5 mm length of the seeds, the experimental results show that the target appeared more uniform and more accurately reconstructed with a lower lag value of  $M = 2$  than a higher lag value of  $M = 10$ . After modeling this geometry with our theory, we are able to explain this trend that was previously unexplainable. In particular, the results in Chapter 2 demonstrate that larger targets have shorter

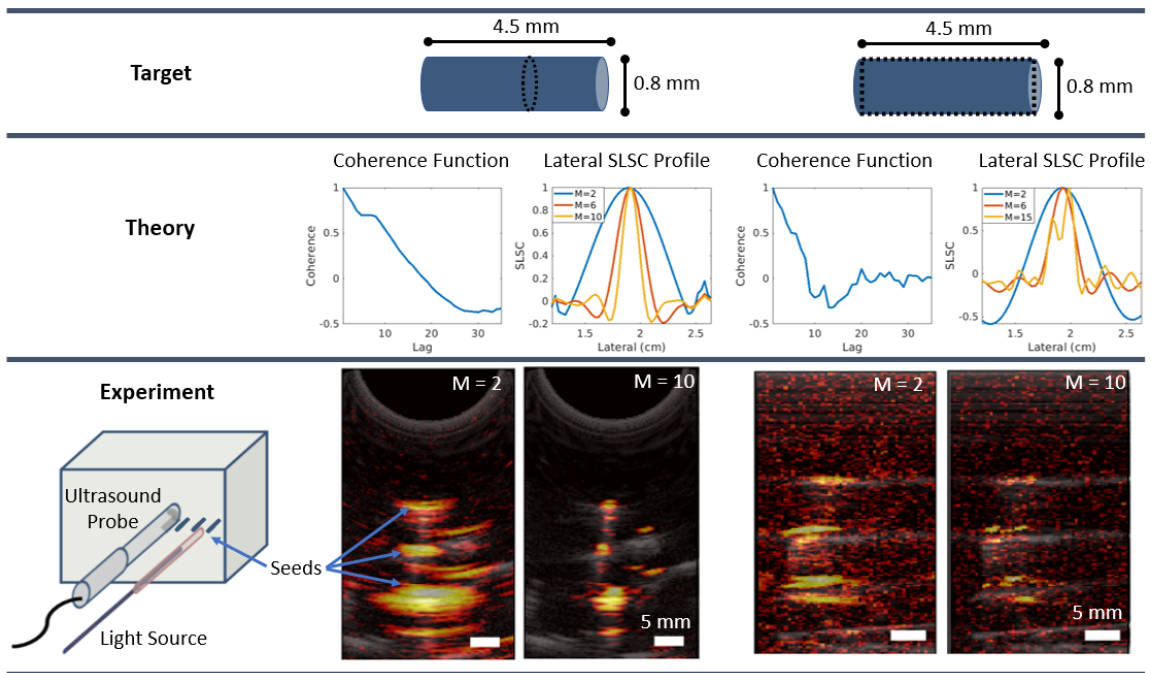


Figure 7.4: Theoretical explanation of the effect of  $M$  value in the experimental visualization of two cross sections of brachytherapy seeds with SLSC imaging. (top row) Schematic diagrams of a brachytherapy seed, showing seed dimensions and outlines of the cross sections imaged within each column. (middle row) Theoretical spatial coherence functions and lateral profiles from the corresponding theoretical SLSC image when the indicated cross section of the brachytherapy seed was simulated. (bottom row) Experimental images of the brachytherapy seeds displayed with  $M=2$  and  $M=10$  [22].

coherence lengths, and the maximum value for optimal image display is limited by the coherence length. Therefore, our recently developed theory provides a fundamental understanding of photoacoustic spatial coherence principles that enabled strategic usage and optimization of SLSC image display for brachytherapy seed visualization. It is likely that this theory can be extended to additional clinical applications with similar benefits.

## 7.4 Outlook

This dissertation introduces novel theoretical, simulated, and experimental photoacoustic approaches to address the challenges surrounding intraoperative monitoring of the ICAs. Focusing on theoretical foundations of photoacoustic spatial coherence theory, exploitation of naturally occurring cranial acoustic windows, and benefits of amplitude- and coherence-based beamforming, the developed approaches establish a new paradigm for photoacoustic detection of the ICAs during endonasal transsphenoidal surgery. Beyond ICA detection, these contributions advance photoacoustic imaging as a viable intraoperative image-guidance technique for surgical instrument tip detection, nerve detection, brachytherapy seed detection, and other possible clinical applications which occur within optically and acoustically challenging environments.

## References

- [1] M. T. Graham, J. Y. Guo, and M. A. L. Bell, “Simultaneous visualization of nerves and blood vessels with multispectral photoacoustic imaging for intraoperative guidance of neurosurgeries,” in *Advanced Biomedical and Clinical Diagnostic and Surgical Guidance Systems XVII*, International Society for Optics and Photonics, vol. 10868, 2019, 108680R.



- [2] M. Siemionow and G. Brzezicki, "Current techniques and concepts in peripheral nerve repair," *International Review of Neurobiology*, vol. 87, pp. 141–172, 2009.
- [3] G. Rangavajla, N. Mokarram, N. Masoodzadehgan, S. B. Pai, and R. V. Belamkonda, "Noninvasive imaging of peripheral nerves," *Cells Tissues Organs*, vol. 200, no. 1, pp. 69–77, 2014.
- [4] C. B. Novak, D. J. Anastakis, D. E. Beaton, S. E. Mackinnon, and J. Katz, "Relationships among pain disability, pain intensity, illness intrusiveness, and upper extremity disability in patients with traumatic peripheral nerve injury," *The Journal of Hand Surgery*, vol. 35, no. 10, pp. 1633–1639, 2010.
- [5] M. Ahmed-Labib, J. D. Golan, and L. Jacques, "Functional outcome of brachial plexus reconstruction after trauma," *Neurosurgery*, vol. 61, no. 5, pp. 1016–1023, 2007.
- [6] P. Ciaramitaro, M. Mondelli, F. Logullo, S. Grimaldi, B. Battiston, A. Sard, C. Scarinzi, G. Migliaretti, G. Faccani, D. Cocito, and I. N. for Traumatic Neuropathies, "Traumatic peripheral nerve injuries: Epidemiological findings, neuropathic pain and quality of life in 158 patients," *Journal of the Peripheral Nervous System*, vol. 15, no. 2, pp. 120–127, 2010.
- [7] S. K. V. Sekar, I. Bargigia, A. Dalla Mora, P. Taroni, A. Ruggeri, A. Tosi, A. Pifferi, and A. Farina, "Diffuse optical characterization of collagen absorption from 500 to 1700 nm," *Journal of Biomedical Optics*, vol. 22, no. 1, p. 015 006, 2017.
- [8] R. R. Anderson, W. Farinelli, H. Laubach, D. Manstein, A. N. Yaroslavsky, J. Gubeli III, K. Jordan, G. R. Neil, M. Shinn, W. Chandler, G. P. Williams, S. V. Benson, D. R. Douglas, and H. F. Dylla, "Selective photothermolysis of lipid-rich tissues: A free electron laser study," *Lasers in Surgery and Medicine*:

- The Official Journal of the American Society for Laser Medicine and Surgery*, vol. 38, no. 10, pp. 913–919, 2006.
- [9] D. J. Segelstein, “The complex refractive index of water,” Ph.D. dissertation, University of Missouri–Kansas City, 1981.
- [10] V. Tuchin, “Tissue optics and photonics: Light-tissue interaction ii,” *Journal of Biomedical Photonics and Engineering*, vol. 2, no. 3, p. 030201, 2016.
- [11] E. A. Gonzalez, C. A. Graham, and M. A. Lediju Bell, “Acoustic frequency-based approach for identification of photoacoustic surgical biomarkers,” *Frontiers in Photonics*, vol. 2, 2021.
- [12] E. A. Gonzalez, C. A. Graham, and M. A. L. Bell, “Optimization of a dual wavelength atlas technique to differentiate methylene blue from hemoglobin in photoacoustic signals,” in *Photons Plus Ultrasound: Imaging and Sensing 2022*, SPIE, vol. 11960, 2022, pp. 51–58.
- [13] A. Wiacek, K. C. Wang, H. Wu, and M. A. L. Bell, “Photoacoustic-guided laparoscopic and open hysterectomy procedures demonstrated with human cadavers,” *IEEE transactions on medical imaging*, vol. 40, no. 12, pp. 3279–3292, 2021.
- [14] J. Shubert and M. A. L. Bell, “Photoacoustic imaging of a human vertebra: Implications for guiding spinal fusion surgeries,” *Physics in Medicine and Biology*, 2018.
- [15] K. Kempinski, A. Wiacek, M. Graham, E. Gonzalez, B. Goodson, D. Allman, J. Palmer, H. H. S. Beck, J. He, and M. A. L. Bell, “In vivo photoacoustic imaging of major blood vessels in the pancreas and liver during surgery,” *Journal of Biomedical Optics*, vol. 24, no. 12, 2019.

- [16] M. T. Graham, J. Huang, F. Creighton, and M. A. L. Bell, “Simulations and human cadaver head studies to identify optimal acoustic receiver locations for minimally invasive photoacoustic-guided neurosurgery,” *Photoacoustics*, p. 100 183, 2020.
- [17] H. Estrada, X. Huang, J. Rebling, M. Zwack, S. Gottschalk, and D. Razansky, “Virtual craniotomy for high-resolution optoacoustic brain microscopy,” *Scientific Reports*, vol. 8, no. 1, p. 1459, 2018.
- [18] C. Huang, L. Nie, R. W. Schoonover, Z. Guo, C. O. Schirra, M. A. Anastasio, and L. V. Wang, “Aberration correction for transcranial photoacoustic tomography of primates employing adjunct image data,” *Journal of Biomedical Optics*, vol. 17, no. 6, p. 066 016, 2012.
- [19] R. Manwar, K. Kratkiewicz, and K. Avanaki, “Investigation of the effect of the skull in transcranial photoacoustic imaging: A preliminary ex vivo study,” *Sensors*, vol. 20, no. 15, p. 4189, 2020.
- [20] S. Govinahalli Sathyanarayana, B. Ning, R. Cao, S. Hu, and J. A. Hossack, “Dictionary learning-based reverberation removal enables depth-resolved photoacoustic microscopy of cortical microvasculature in the mouse brain,” *Scientific Reports*, vol. 8, no. 1, p. 985, 2018.
- [21] L. Mohammadi, H. Behnam, J. Tavakkoli, and K. Avanaki, “Skull acoustic aberration correction in photoacoustic microscopy using a vector space similarity model: A proof-of-concept simulation study,” *Biomedical Optics Express*, vol. 11, no. 10, pp. 5542–5556, 2020.
- [22] M. A. L. Bell, N. Ku, D. Y. Song, and E. M. Boctor, “Short-lag spatial coherence beamforming of photoacoustic images for enhanced visualization of prostate brachytherapy seeds,” *Biomedical Optics Express*, vol. 4, no. 10, p. 1964, 2013.

- [23] M. A. L. Bell, N. P. Kuo, D. Y. Song, J. U. Kang, and E. M. Boctor, “In vivo visualization of prostate brachytherapy seeds with photoacoustic imaging,” *Journal of Biomedical Optics*, vol. 19, no. 12, p. 126 011, 2014.
- [24] M. A. L. Bell, D. Y. Song, and E. M. Boctor, “Coherence-based photoacoustic imaging of brachytherapy seeds implanted in a canine prostate,” in *Medical Imaging 2014: Ultrasonic Imaging and Tomography*, SPIE, vol. 9040, 2014, pp. 166–171.
- [25] M. A. L. Bell, X. Guo, H. J. Kang, and E. Boctor, “Improved contrast in laser-diode-based photoacoustic images with short-lag spatial coherence beamforming,” in *2014 IEEE International Ultrasonics Symposium*, IEEE, 2014, pp. 37–40.
- [26] B. Pourebrahimi, S. Yoon, D. Dopsa, and M. C. Kolios, “Improving the quality of photoacoustic images using the short-lag spatial coherence imaging technique,” in *Photons Plus Ultrasound: Imaging and Sensing 2013*, International Society for Optics and Photonics, vol. 8581, 2013, 85813Y.
- [27] K. M. Kempinski, M. T. Graham, M. R. Gubbi, T. Palmer, and M. A. L. Bell, “Application of the generalized contrast-to-noise ratio to assess photoacoustic image quality,” *Biomedical Optics Express*, vol. 11, no. 7, pp. 3684–3698, 2020.

---

# Michelle T. Graham

---

## Education

*Johns Hopkins University, Baltimore, MD*

Ph.D. in Electrical Engineering, 2022

M.S.E. in Electrical Engineering, 2019

*The University of Scranton, Scranton, PA*

B.S. in Biophysics, 2015

Minor in Mathematics

Summa Cum Laude GPA: 3.90

## Awards & Honors

2021	National Institutes of Health Blueprint MedTech Program awardee and incubator participant
2018-2022	National Science Foundation Graduate Student Research Fellowship
2018	Johns Hopkins Center for Bioengineering Innovation and Design Humanitarian Hackathon 1st Place
2016-2017	Virginia and Edward M. Wysocki, Sr. Memorial Fellowship Awardee
2015	Joseph P. Harper Award for Excellence in Physics
2011	University of Scranton Full Tuition Presidential Scholarship

## Publications

### *Peer-reviewed Journal Publications*

1. M. T. Graham, R. A. Dunne, and M. A. L. Bell, "Comparison of compressional and elastic wave simulations for patient-specific planning prior to transcranial photoacoustic-guided neurosurgery," *Journal of Biomedical Optics*, vol. 26, no. 7, p. 076 006, 2021
2. M. T. Graham and M. A. L. Bell, "Photoacoustic spatial coherence theory and applications to coherence-based image contrast and resolution," *IEEE Transactions on Ultrasonics, Ferroelectrics, and Frequency Control*, vol. 67, no. 10, pp. 2069–2084, 2020
3. M. T. Graham, J. Huang, F. Creighton, and M. A. L. Bell, "Simulations and human cadaver head studies to identify optimal acoustic receiver locations for minimally invasive photoacoustic-guided neurosurgery," *Photoacoustics*, p. 100 183, 2020

4. K. M. Kempfski, M. T. Graham, M. R. Gubbi, T. Palmer, and M. A. L. Bell, "Application of the generalized contrast-to-noise ratio to assess photoacoustic image quality," *Biomedical Optics Express*, vol. 11, no. 7, pp. 3684–3698, 2020
5. M. Graham, F. Assis, D. Allman, A. Wiacek, E. Gonzalez, M. Gubbi, J. Dong, H. Hou, S. Beck, J. Chrispin, and M. A. L. Bell, "In vivo demonstration of photoacoustic image guidance and robotic visual servoing for cardiac catheter-based interventions," *IEEE Transactions on Medical Imaging*, vol. 39, no. 4, pp. 1015–1029, 2020
6. K. Kempfski, A. Wiacek, M. Graham, E. Gonzalez, B. Goodson, D. Allman, J. Palmer, H. H. S. Beck, J. He, and M. A. L. Bell, "In vivo photoacoustic imaging of major blood vessels in the pancreas and liver during surgery," *Journal of Biomedical Optics*, vol. 24, no. 12, 2019
7. B. Stephanian, M. T. Graham, H. Hou, and M. A. L. Bell, "Additive noise models for photoacoustic spatial coherence theory," *Biomedical Optics Express*, vol. 9, no. 11, 2018
8. M. Naser, M. T. Graham, K. Pierre, and N. N. Boustany, "Label-free classification of bax/bak expressing vs. double-knockout cells," *Annals of Biomedical Engineering*, vol. 44, no. 11, pp. 3398–3407, 2016
9. N. P. Truncale and M. T. Graham, "Visualizing sound with an electro-optical eardrum," *The Physics Teacher*, vol. 52, no. 2, pp. 76–79, 2014

#### *Conference Proceedings*

1. M. Graham and M. Bell, "PhocoSpace: An open-source simulation package to implement photoacoustic spatial coherence theory," in *2022 IEEE International Ultrasonics Symposium (IUS)*, accepted, IEEE, 2022
2. M. T. Graham, N. von Guionneau, S. Tuffaha, and M. A. L. Bell, "Design and optimization of simulated light delivery systems for photoacoustic assessment of peripheral nerve injury," in *Photons Plus Ultrasound: Imaging and Sensing 2022*, SPIE, vol. 11960, 2022, pp. 275–281
3. K. M. Kempfski, M. T. Graham, A. Wiacek, M. Gubbi, and M. A. L. Bell, "Generalized contrast-to-noise ratio as a metric of photoacoustic image quality," in *Photons Plus Ultrasound: Imaging and Sensing 2021*, International Society for Optics and Photonics, vol. 11642, 2021, p. 116421C
4. M. T. Graham, F. X. Creighton, and M. A. L. Bell, "Validation of eyelids as acoustic receiver locations for photoacoustic-guided neurosurgery," in *Photons Plus Ultrasound: Imaging and Sensing 2021*, International Society for Optics and Photonics, vol. 11642, 2021, p. 1164228

5. M. T. Graham, R. A. Dunne, and M. A. L. Bell, “Investigating the effects of compressional and elastic photoacoustic waves to predict transcranial photoacoustic image quality for guidance of minimally invasive neurosurgeries,” in *Advanced Biomedical and Clinical Diagnostic and Surgical Guidance Systems XIX*, International Society for Optics and Photonics, vol. 11631, 2021, 116310Q
6. M. T. Graham, F. X. Creighton, and M. A. L. Bell, “Investigation of acoustic windows for photoacoustic imaging of intracranial blood vessels,” in *2020 IEEE International Ultrasonics Symposium (IUS)*, IEEE, 2020, pp. 1–4
7. M. T. Graham, F. Assis, D. Allman, A. Wiacek, E. Gonzalez, M. R. Gubbi, J. Dong, H. Hou, S. Beck, J. Chrispin, and M. A. L. Bell, “Photoacoustic image guidance and robotic visual servoing to mitigate fluoroscopy during cardiac catheter interventions,” in *Advanced Biomedical and Clinical Diagnostic and Surgical Guidance Systems XVIII*, International Society for Optics and Photonics, vol. 11229, 2020, 112291E
8. M. T. Graham, J. Y. Guo, and M. A. L. Bell, “Simultaneous visualization of nerves and blood vessels with multispectral photoacoustic imaging for intraoperative guidance of neurosurgeries,” in *Advanced Biomedical and Clinical Diagnostic and Surgical Guidance Systems XVII*, International Society for Optics and Photonics, vol. 10868, 2019, 108680R
9. M. T. Graham and M. A. L. Bell, “Development and validation of a short-lag spatial coherence theory for photoacoustic imaging,” in *Photons Plus Ultrasound: Imaging and Sensing 2018*, International Society for Optics and Photonics, vol. 10494, 2018, 104945K
10. M. T. Graham and M. A. L. Bell, “Theoretical application of short-lag spatial coherence to photoacoustic imaging,” in *2017 IEEE International Ultrasonics Symposium (IUS)*, IEEE, 2017, pp. 1–4
11. M. Naser, M. T. Graham, K. Pierre, J. A. Hostettler, H. Sierra, and N. N. Boustany, “Quantification of bax/bak-dependent morphological changes by textural analysis of optical scatter images,” in *Biomedical Optics*, Optical Society of America, 2014, BT3A–37

## Presentations

1. M. T. Graham, N. von Guionneau, S. Tuffaha, and M. A. L. Bell, “Design and optimization of simulated light delivery systems for photoacoustic assessment of peripheral nerve injury,” in *Photons Plus Ultrasound: Imaging and Sensing 2022*, poster presentation, SPIE, vol. 11960, 2022, pp. 275–281
2. M. T. Graham, R. A. Dunne, and M. A. L. Bell, “Investigating the effects of compressional and elastic photoacoustic waves to predict transcranial photoacoustic image quality for guidance of minimally invasive neurosurgeries,” in *Advanced Biomedical and Clinical Diagnostic and Surgical Guidance Systems XIX*,

- oral presentation, International Society for Optics and Photonics, vol. 11631, 2021, 116310Q
3. M. T. Graham, F. X. Creighton, and M. A. L. Bell, "Validation of eyelids as acoustic receiver locations for photoacoustic-guided neurosurgery," in *Photons Plus Ultrasound: Imaging and Sensing 2021*, oral presentation, International Society for Optics and Photonics, vol. 11642, 2021, p. 1164228
  4. M. T. Graham, F. X. Creighton, and M. A. L. Bell, "Investigation of acoustic windows for photoacoustic imaging of intracranial blood vessels," in *2020 IEEE International Ultrasonics Symposium (IUS)*, poster presentation, IEEE, 2020, pp. 1–4
  5. M. T. Graham, F. Assis, D. Allman, A. Wiacek, E. Gonzalez, M. R. Gubbi, J. Dong, H. Hou, S. Beck, J. Chrispin, and M. A. L. Bell, "Photoacoustic image guidance and robotic visual servoing to mitigate fluoroscopy during cardiac catheter interventions," in *Advanced Biomedical and Clinical Diagnostic and Surgical Guidance Systems XVIII*, oral presentation, International Society for Optics and Photonics, vol. 11229, 2020, 112291E
  6. M. T. Graham, J. Y. Guo, and M. A. L. Bell, "Simultaneous visualization of nerves and blood vessels with multispectral photoacoustic imaging for intraoperative guidance of neurosurgeries," in *Advanced Biomedical and Clinical Diagnostic and Surgical Guidance Systems XVII*, oral presentation, International Society for Optics and Photonics, vol. 10868, 2019, 108680R
  7. M. T. Graham and M. A. L. Bell, "Development and validation of a short-lag spatial coherence theory for photoacoustic imaging," in *Photons Plus Ultrasound: Imaging and Sensing 2018*, poster presentation, International Society for Optics and Photonics, vol. 10494, 2018, 104945K
  8. M. T. Graham and M. A. L. Bell, "Implications of theoretical photoacoustic spatial covariance for short-lag spatial coherence imaging," in *2018 International Symposium on Ultrasonic Imaging and Tissue Characterization*, oral presentation, 2018
  9. M. T. Graham and M. A. L. Bell, "Theoretical application of short-lag spatial coherence to photoacoustic imaging," in *2017 IEEE International Ultrasonics Symposium (IUS)*, poster presentation, IEEE, 2017, pp. 1–4
  10. M. T. Graham and M. A. L. Bell, "Theoretical application of short-lag spatial coherence to photoacoustic imaging," in *2017 International Symposium on Ultrasonic Imaging and Tissue Characterization*, oral presentation, 2017